

# UNCLASSIFIED

AD NUMBER
AD862483
NEW LIMITATION CHANGE
TO Approved for public release, distribution unlimited
FROM Distribution authorized to U.S. Gov't. agencies and their contractors; Specific Authority; Sep 1969. Other requests shall be referred to U.S. Army Missile Command, Attn: AMSMI-RDK, Redstone Arsenal, AL.
AUTHORITY
USAMC ltr, 29 Nov 1972

THIS PAGE IS UNCLASSIFIED

AD

REPORT NO. RD-TR-69-21

SEPTEMBER 1969

**JET INTERACTION CONTROL  
EFFECTIVENESS FOR SUBSONIC  
AND SUPERSONIC FLIGHT**

**FINAL REPORT**

by

L. A. CASSEL  
N. A. DURANDO  
C. W. BULLARD  
J. M. KELSO

Research and Development Directorate  
McDonnell Douglas Astronautics Company  
Western Division  
Santa Monica, California  
for

Advanced Systems Laboratory  
Research and Development Directorate  
Army Missile Command  
under Contract No. DAAH01-68-C-1919

This document is subject to special report controls and each transmittal to foreign governments or foreign nationals may be made only with prior approval of this command, Attn: AMSMI-RDK



**U.S. ARMY MISSILE COMMAND**  
*Redstone Arsenal, Alabama*

The findings in this report are not to be construed as an official Department of the Army position unless so designated by other authorized documents

D D C

DEC 16 1969

REPORT NO. RD-TR-69-21

SEPTEMBER 1969

**JET INTERACTION CONTROL  
EFFECTIVENESS FOR SUBSONIC  
AND SUPERSONIC FLIGHT****FINAL REPORT**

by

**L. A. CASSEL  
N. A. DURANDO  
C. W. BULLARD  
J. M. KELSO****Research and Development Directorate  
McDonnell Douglas Astronautics Company  
Western Division  
Santa Monica, California  
for****Advanced Systems Laboratory  
Research and Development Directorate  
Army Missile Command  
under Contract No. DAAH01-68-C-1919**

This document is subject to special report controls and each transmittal to foreign governments or foreign nationals may be made only with prior approval of this command, Attn: AMSMI-R

**U.S. ARMY MISSILE COMMAND**  
**Redstone Arsenal, Alabama**

The findings in this report are not to be construed as an official Department of the Army position unless so designated by other authorized documents

DA Project No. 1M2623XXA206  
and AMC Management Structure Code No. 522C.11.178  
McDonnell Douglas Report No. MDC-G1164

## ABSTRACT

Interference effects between a highly underexpanded, sonic or supersonic jet in a subsonic or supersonic crossflow, and the surface from which the jet exhausts are examined. For subsonic freestream Mach numbers, existing data is examined and correlated. Various semi-empirical models to represent the interference pressure distribution on flat plates are then developed. For supersonic freestream Mach numbers, a computer program for calculating jet interference effects on axisymmetric bodies at angle of attack is described. Interference effects between the jet plume and control fins on a cruciform missile are analyzed. A semi-empirical model of the jet in a crossflow, valid at large distances from the nozzle is developed. The results of this model are then used to compute interference forces and moments on fins located aft of the nozzle, both for subsonic and for supersonic freestream Mach numbers.

A-6	Comparison of Theory and Data for $M_j = 3.00$	153
B-1	Integration Contour for Equation (B-12)	159
B-2	Search for Solutions to Set of Five Simultaneous Equations for Vortex Model	167
B-3	Result of Search for Solutions to Vortex Model	168
C-1	Vehicle Profile Description Options	176

## FOREWORD

This report describes results of an analysis conducted by the McDonnell Douglas Astronautics Company--Western Division (MDAC-WD), under United States Army Contract DAAH01-68-C-1919. The contract was initiated under DA Project No. 1M2623XXA206 and AMC Management Structure Code No. 522C.11.148. The technical effort was conducted between 1 June 1968 and 31 August 1969. The project was administered under the direction of the Aerodynamics Branch, Advanced Systems Laboratory, U. S. Army Missile Command, Redstone Arsenal, Alabama. The Army technical monitors for the study were Mr. D. J. Spring and Mr. T. A. Street.

In addition to the authors, Mr. J. G. Davis and Dr. R. Rosen of MDAC-WD made significant contributions to the boundary layer separation analysis and subsonic flow modeling, respectively.

## CONTENTS

	LIST OF FIGURES	ix
	LIST OF SYMBOLS	xv
Section 1	INTRODUCTION	1
Section 2	SUBSONIC MAINSTREAM JET INTERACTION DESCRIPTION AND SCALING	3
	2.1 Description of the Jet	3
	2.2 Underexpanded Jet Interaction Pressure Distributions	7
	2.3 Empirical Modeling of the Interference Pressure Distribution	19
Section 3	FLOWFIELD MODELS FOR THE INTERACTION REGION	29
	3.1 Models Proposed in the Literature	29
	3.2 Phenomenological Models	32
	3.3 Pressure Models	48
	3.4 Pressure Model Computer Programs	62
Section 4	CONTROL EFFECTIVENESS PREDICTION FOR SUPERSONIC FLIGHT	67
	4.1 General Description of the Program	67
	4.2 Vehicle Geometry	68
	4.3 Angle of Attack Determination	69
	4.4 Equivalent Body Sizing	75
	4.5 Vehicle Surface Pressure Integration	76
	4.6 Equivalent Obstacle Program Results	86
Section 5	JET-FIN INTERFERENCE EFFECTS	93
	5.1 General Considerations	93
	5.2 Jet Properties at Large Distances From the Nozzle	96
	5.3 Jet-Fin Interference Forces and Moments	113
	5.4 Results of Jet-Fin Interference Calculations	132

Section 6	CONCLUSIONS	141
Appendix A	TERMINAL SHOCK LOCATION FOR SUPERSONIC NOZZLES	143
	A. 1 Sonic Nozzle	143
	A. 2 Supersonic Nozzle	147
	A. 3 Comparison with Data	150
Appendix B	SINGULARITY STRENGTHS FOR VORTEX MODEL	155
	B. 1 Derivation of Fourier Coefficients	155
	B. 2 Solution of the Equations	162
	B. 3 Numerical Results	166
Appendix C	EQUIVALENT SOLID OBSTACLE ANALOGY COMPUTER PROGRAM	171
	C. 1 Main Program	171
	C. 2 Vehicle Geometry	175
	C. 3 Local Flow Subroutine (LOCFLO)	177
	C. 4 Pressure Integration Subroutine	177
	REFERENCES	183



## FIGURES

1	Jet in Subsonic Cross Flow with Barrel Shock System	4
2	Jet in Subsonic Cross Flow with Diamond Shock System	6
3	Flat Plate Model Dimension and Orifice Locations	8
4	Army Missile Command Model	9
5	Reference Coordinate System for Interference Pressure on an Ogive-Cylinder	10
6	Pressure Distribution Along Plane of Symmetry of an Ogive Cylinder	12
7	Correlated Pressure Distribution Along Plane of Symmetry of an Ogive Cylinder, $M_\infty = 0.8$	13
8	Correlated Pressure Distribution Along Plane of Symmetry of an Ogive Cylinder, $M_\infty = 0.2$	14
9	Correlated Circumferential Pressure Distribution at the Jet Station, $M_\infty = 0.2$	15
10	Reference Coordinate System for Describing Interference Pressure Distribution on a Flat Plate	16
11	Correlated Pressure Distribution Along Plane of Symmetry of a Flat Plate	17
12	Correlation of Flat-Plate Data off the Centerline	18
13	Jet Thrust Amplification Factor Based on Data From AMICOM-CAL Tests of an Ogive-Cylinder, $M_\infty < 1.0$	20
14a	Comparison of Vogler's Data and Fourier Series, $r = 1.5$	22
14b	Comparison of Vogler's Data and Fourier Series, $r = 2.0$	22
14c	Comparison of Vogler's Data and Fourier Series, $r = 3.0$	23
14d	Comparison of Vogler's Data and Fourier Series, $r = 4.0$	23

15	Variation of Zeroth Fourier Coefficient with Distance from the Nozzle and Velocity Ratio	25
16	Variation of First Fourier Coefficient With Distance From the Nozzle and Velocity Ratio	26
17	Variation of Second Fourier Coefficient with Distance from the Nozzle and Velocity Ratio	27
18	Comparison of Data and Theory of Reference 36	31
19	Diagram for Solution of Equation (21), $U_{\infty}/U_j = 0.4$	38
20	Results of Doublet-Vortex and Doublet Model Compared With Data ( $\theta = 0^\circ$ )	40
21	Results of Doublet-Vortex and Doublet Models Compared to Data ( $\theta = 30^\circ$ )	41
22	Results of Doublet-Vortex and Doublet Model Compared With Data ( $\theta = 60^\circ$ )	42
23	Results of Doublet-Vortex and Doublet Model Compared With Data ( $\theta = 90^\circ$ )	43
24	Results of Doublet-Vortex and Doublet Models Compared With Data ( $\theta = 120^\circ$ )	44
25	Results of Doublet-Vortex and Doublet Model Compared With Data ( $\theta = 150^\circ$ )	45
26	Results of Doublet-Vortex and Doublet Model Compared With Data ( $\theta = 180^\circ$ )	45
27	Location of Vortex Model Singularities	46
28	Results of Source and Orifice Models Compared With Data ( $\theta = 0^\circ$ )	50
29	Results of Source and Orifice Models Compared With Data ( $\theta = 30^\circ$ )	51
30	Results of Source and Orifice Models Compared With Data ( $\theta = 60^\circ$ )	52
31	Results of Source and Orifice Models Compared With Data ( $\theta = 90^\circ$ )	53
32	Results of Source and Orifice Models Compared With Data ( $\theta = 120^\circ$ )	54
33	Results of Source and Orifice Models Compared With Data ( $\theta = 150^\circ$ )	55

34	Results of Source and Orifice Models Compared With Data ( $\theta = 180^\circ$ )	56
35	$A_0$ , $A_1$ and $k$ as Functions of the Velocity Ratio	58
36	Streamlines and Equipotential Lines for Flow Through an Orifice	59
37	Coordinate System For Cylinder Projection of Exit Plane	64
38	Coordinate System For Vehicle Geometry	70
39	Coordinate System For Equivalent Body Flowfield	7
40	Bow Shock/Boundary Layer Interaction Approximation	82
41	Correlation of Pressure at $X_S$ for Turbulent Separation	84
42	AMICOM Reaction Jet Force Model	85
43	Equivalent Obstacle Analogy Prediction of Normal Force	87
44	Equivalent Obstacle Analogy Prediction of Pitching Moment	88
45	Equivalent Obstacle Analogy Prediction of $K_F$ Versus $\alpha$	89
46	Equivalent Obstacle Analogy Prediction of $K_M$ Versus $\alpha$	89
47	Equivalent Obstacle Analogy Prediction of $K_F$ Versus $P$	90
48	Equivalent Obstacle Analogy Prediction of $K_M$ Versus $P$	90
49	Equivalent Obstacle Analogy Prediction of $K_F$ Versus $M_\infty$	91
50	Equivalent Obstacle Analogy Prediction of $K_M$ Versus $M_\infty$	91
51	Scale of Fin Interference With Penetration Height	95
52	Jet Wake in Free Stream Flow Field at Mach 0.9 and Zero Angle of Attack	97
53	Jet-Oriented Coordinate System	97
54	Jet-Induced Vortices in the Crossflow Plane	100

55	Scale Constants for Equivalent Subsonic Jet Diameters	108
56	Constant Product of Vortex Strength and Separation	109
57	Constant Ratio of Vortex Separation to Height Above the Nozzle Plane	111
58	Comparison of Predicted and Experimental Vortex Strengths	112
59	Reference Axes for Fin Interference Calculations	114
60	Actual Jet Plume and Theoretical Model for Calculating Induced Velocities at the Fin Location	119
61	Upwash and Sidewash Produced by a Single Vortex	120
62	Vortex System Contributing to Total Induced Velocities	122
63	Fin Geometry	124
64	Flowchart for Fin Interference Force and Moment Computations	133
65	Fin Interference Normal Force Coefficient ( $M_\infty = 0.8$ , $\alpha = 2^\circ$ )	134
66	Fin Interference Side Force Coefficient ( $M_\infty = 0.8$ , $\alpha = 2^\circ$ )	134
67	Fin Interference Rolling Moment Coefficient ( $M_\infty = 0.8$ , $\alpha = 2^\circ$ )	135
68	Schematic Diagram of Vortex Locations and Interference Forces for Various Roll Angles	136
69	Comparison of Interference Normal Force Coefficient With Data $P = 60$	138
70	Comparison of Interference Normal Force Coefficient With Data $P = 100$	138
A-1	Mach Disk Height for a Supersonic Nozzle Based on Sonic Nozzle Results	144
A-2	Mach Number Distribution for Sonic Nozzle Plume	146
A-3	Mach Number Upstream of the Mach Disk	147
A-4	Comparison of Theory and Data for $M_j = 1.00$	151
A-5	Comparison of Theory and Data for $M_j = 2.00$	152

A-6	Comparison of Theory and Data for $M_j = 3.00$	153
B-1	Integration Contour for Equation (B-12)	159
B-2	Search for Solutions to Set of Five Simultaneous Equations for Vortex Model	167
B-3	Result of Search for Solutions to Vortex Model	168
C-1	Vehicle Profile Description Options	176

## LIST OF SYMBOLS

$a_0, a_1, a_2$	Variables defined in Equations (B. 6a, b, c), respectively
$a_t$	Speed of sound at nozzle throat
$a_\infty$	Free stream speed of sound
$A_j$	Integration constant in Equation (45)
$A_j$	Jet exit area
$A_j^*$	Jet throat area
$A_n (U_\infty/U_j)$	Nondimensional model flow parameters
$A_n^* (U_\infty/U_j)$	Dimensional model flow parameters
$b_0, b_1, b_2$	Variables defined in Equations (B. 11a, b, c), respectively
$c(\eta)$	Local fin chord
$c_n(r, U_\infty/U_j)$	Coefficients in Fourier series representation for data
$c_r$	Fin root chord
$c_t$	Fin tip chord
$C(\eta)$	Normalized local fin chord, $C = c/R$
$C_p$	Pressure coefficient
$C_r$	Normalized root chord, $C_r = c_r/R$
$C_x$	Equivalent body drag coefficient
$C_{\ell_i}$	Two-dimensional flat plate lift coefficient
$C_L$	Interference rolling moment coefficient
$C_M$	Interference pitching moment coefficient
$C_N$	Interference yawing moment coefficient

$C_Y$	Interference side force coefficient
$C_Z$	Interference normal force coefficient
$d_e$	Equivalent jet diameter
$d_j$	Jet exit diameter
$d_t$	Jet throat diameter
$F(\theta)$	Function defined by Equation (B-5)
$h$	Distance from nozzle plane to Mach disk, or to first intersection of diamond shock pattern
$h^*$	Mach disk height for sonic jet (Appendix A)
$h_s$	Jet penetration height
$h_1$	Jet penetration height for jet exit local flow conditions
$H(\alpha)$	Function defined by Equation (74) (Section 4)
$I_{o1}$	Integral defined by Equation (B-9)
$I_{o2}$	Integral defined by Equation (B-8)
$k$	Scale factor in orifice model
$K$	Jet thrust amplification factor (Section 2) Constant defined by Equation (69) (Section 4) Universal constant in jet vortex model (Section 5)
$K'$	Constant in jet vortex model
$l$	Distance between nozzle centerline and midpoint of fin mean geometric chord
$L_R$	Reference length
$L$	Normalized distance between nozzle centerline and midpoint of fin mean geometric chord, $L = (\sigma_e l)/d_e$
$M_f$	Mach number immediately upstream of the Mach disk
$M_f^*$	Mach number immediately upstream of the Mach disk for sonic jet
$M_j$	Jet exit Mach number

$M_1$	Mach number on vehicle surface at jet location
$M_\infty$	Freestream Mach number
$p$	Pressure
$p_{oj}$	Jet chamber pressure
$p_\infty$	Freestream pressure
$P$	$p_{oj}/p_\infty$ Static pressure ratio ( $p/p_\infty$ ) (Section 4)
$p_1$	Local pressure on vehicle surface at jet location
$p_{t1}$	Total pressure on vehicle surface
$q_\infty$	Freestream dynamic pressure
$\mathbf{q}^*$	Dimensional velocity vector
$\mathbf{q}$	Nondimensional velocity vector
$r^*$	Sonic radius for compressible source flow
$R$	Cross-sectional radius of axisymmetric body
$s$	Fin semispan
$S$	Arc length along circular cross-section of ogive-cylinder (Section 2) Arc length defined in Figure 37 (Section 3) Radius of equivalent obstacle (Section 4) Normalized fin semispan, $S = s/R$ (Section 5)
$S_R$	Reference area
$T_\infty$	Freestream static temperature
$T_{o_\infty}$	Freestream stagnation temperature
$U_j$	Jet exit velocity
$U_\infty$	Freestream velocity
$U'_\infty$	Model freestream velocity
$V$	Volume flow rate for orifice model
$w^*(\zeta)$	Dimensional complex potential



$w(\zeta)$	Nondimensional complex potential
$Y_v$	Vortex spreading parameter in jet vortex model
$\alpha$	Missile angle of attack
$\alpha_i$	Induced angle of attack at fin location
$\alpha_L$	Local angle of attack defined by Equation (70)
$\beta$	$\sqrt{ 1 - M_\infty^2 }$
$\beta_i$	Induced angle of sideslip at fin location
$\gamma$	Specific heat ratio
$\gamma_j$	Jet specific heat ratio
$\Gamma$	Vortex strength
$\Gamma^*$	Normalized vortex strength $\Gamma^* = (\Gamma \sigma) / (4\pi U_\infty d_j)$
$\delta$	Cone half-angle (Section 4) Universal constant in jet vortex model (Section 5)
$\Delta A_{ij}$	Area element
$\epsilon$	Universal constant in jet vortex model
$\zeta_o$	Complex vortex position vector
$\eta$	Coordinate along confocal hyperboloidal system (Section 3) Distance determined by evaluating integral Equation (60) (Section 3)
$\theta_c$	Effective cone half-angle
$\theta_s$	Shock angle
$\theta_M$	Maximum effective cone half-angle for attached shock
$\kappa$	$K^2$ (Section 4)
$\lambda$	Taper ratio ( $c_t/c_r$ )
$\mu$	$\cos \xi$ (Section 3) Angle between jet centerline and freestream velocity (Section 5)
$\nu$	$\sinh \eta$ (Section 3)

$\rho$	Density
$\sigma$	Subsonic jet velocity ratio, $\sigma = U_\infty/U_j$
$\sigma_e$	Equivalent jet mass flux ratio, $\sigma_e = (\rho_\infty U_\infty)/(\rho_e U_e)$
$\underline{\tau}$	Kelvin impulse defined by Equation (100)
$\phi$	Roll angle (Section 5)
$\phi_j$	Jet nozzle inclination angle relative to surface
$\Phi$	Velocity potential
$\psi$	Meridional angle defined in Figure 5

## Section 1

### INTRODUCTION

The problem of analyzing the effectiveness of reaction jet control systems on flight vehicles operating in the atmosphere has received considerable interest in the past several years (e. g., References 1 to 11). It is well known that the interaction between a reaction control jet and flow around the jet on a vehicle surface generates a force on the vehicle which is often larger than the jet thrust. Consequently the problem of analyzing reaction jet control effectiveness usually reduces to one of determining the magnitude and behavior of the force due to this interaction. The presence, and frequent dominance, of the force due to interaction leads to the term "jet interaction" (JI) control which is usually applied to endoatmospheric reaction control systems.

Reports of both experimental and analytical studies of JI are common in the literature. These studies are generally classified according to mainstream flow conditions and the jet configuration. The case of widest interest (e. g., References 5, 12, 13, 14, 15) has been that of two-dimensional interaction between the jet from an infinite sonic slot and a uniform supersonic stream over a flat plate. The interaction is considered to be three-dimensional whenever a velocity component exists normal to the plane of intersection of the mainstream velocity and the jet centerline in the interaction flow region. The three-dimensional interaction between a jet from an orifice or nozzle in a flat plate and a uniform supersonic stream has received attention from various investigators (e. g., References 2, 16, 17, 18). More complex JI problems involving variously configured sonic and supersonic jets exhausting transverse to axisymmetric or three-dimensional supersonic flows are more infrequently discussed in the unclassified literature (e. g., References 1, 2, 3, 6, 8). Finally, studies of underexpanded sonic or supersonic jets interacting with subsonic mainstreams are comparatively rare for any flow geometry (e. g., References 8, 9, 10, 19).

Some success in scaling experimental data for JI control forces has been demonstrated in the literature, notably for two-dimensional flows. However, JI control force prediction techniques for complex flow geometries typical of those encountered in application are rare and generally very limited in range of applicability. The blast wave analogy methods proposed by various investigators, as discussed in Reference 19, have been most commonly applied.

The objective of the study reported here has been to develop approximate JI control force prediction techniques applicable to JI in three-dimensional subsonic and supersonic flows. In the initial phase of the study (Reference 19), emphasis was placed on devising a technique applicable to JI controls on axisymmetric missiles in supersonic flight, and a lesser effort was devoted to the subsonic flight problem. In the second phase of the study, emphasis has been placed on the development of a technique for analyzing the JI problem when the mainstream is subsonic. A secondary effort in the second phase has been devoted to expanding the range of applicability of the supersonic mainstream analysis technique developed in the initial phase.

The general complexity of three-dimensional JI flows is well known, particularly with regard to their boundary layer separation and jet plume aspects. Consequently, approaches to interaction force prediction methods are usually through analogies to the interaction flow field rather than descriptions of it. This has been the case in the present study. Based on experimental data available in the literature, or provided by the U. S. Army Missile Command (AMICOM) from recent experiments, the significant governing aspects of the flow field have been identified. Then inviscid flow analogies have been developed to represent the various aspects of the flow field. This approach has been taken with both supersonic and subsonic mainstream JI with various degrees of success as discussed in Reference 19 and this report.

Since the second phase of the study has been strongly oriented toward JI in a subsonic mainstream, the bulk of this report is devoted to this subject. The general nature of the JI flow field in a subsonic mainstream is discussed along with empirical models of its behavior in Section 2. Various incompressible, potential flow models of the subsonic mainstream JI flow are discussed in Section 3. The expanded equivalent body analogy JI effectiveness prediction program for three-dimensional jets on axisymmetric missiles in supersonic flight is described in Section 4. Methods of calculating the effects of jet-to-fin interference when fins are located aft of JI controls in subsonic or supersonic flight are discussed in Section 5.

## Section 2

### SUBSONIC MAINSTREAM JET INTERACTION DESCRIPTION AND SCALING

The development of mathematical models of JI in a subsonic mainstream requires a basic understanding of the fluid mechanics involved which can only be derived from detailed experiments. In this section the physical aspects of the interaction flow will be described, based on available experimental data. Empirical scaling of interference pressures in the interaction region will also be described.

Reaction control jet systems typically employ very high chamber pressures, so that downstream of the nozzle, the jet exhibits the internal shock system characteristic of highly underexpanded plumes (see Figure 1). It will be shown later that a characteristic dimension of this shock system is an important scaling length for the interference pressure distribution.

No experiments were conducted by MDAC-WD during the study. However, previously unpublished experimental data taken by AMICOM was made available for use in the study. To the knowledge of the authors, the experimental data concerning an underexpanded jet in a subsonic mainstream which is being provided by AMICOM is the only reasonably detailed data in existence (References 10 and 20 contain limited data). The more detailed experiments by AMICOM are not yet complete; consequently, experimental data regarding a subsonic jet in a crosswind have been relied on heavily during the present study. Existing data may be classified into two categories: (1) Flow field surveys in the vicinity of the jet plume, along the jet trajectory and (2) pressure distribution on the surface from which the jet exhausts or forces and moments on the body from which the jet exhausts.

#### 2.1 DESCRIPTION OF THE JET

The flow field of interest is illustrated in the schlieren photograph in Figure 1. Reaction control jets are typically highly underexpanded, causing a shock engulfed plume at the jet exit similar to that evident in the figure. The existence of this plume differentiates the subsonic mainstream JI flow field from that often studied in reference to the vertical take-off and landing (VTOL) aircraft transitional flight problem. VTOL related studies typically deal with low subsonic jet velocities.

To the authors' knowledge, no surveys of the flow in a highly underexpanded rocket plume exhausting normal to a subsonic free stream have been conducted. Examination of flow visualization photographs

LEGEND:

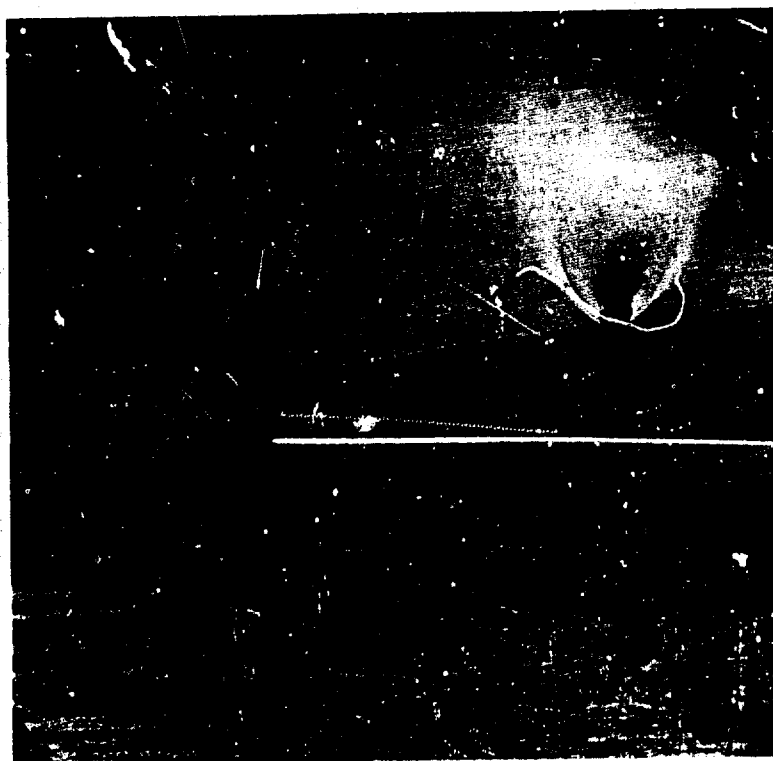
$$M_{\infty} = 0.50$$

$$p_{O_j}/p_{\infty} = 81.00$$

$$\alpha = 0.00$$

$$d_t = 0.44 \text{ IN.}$$

$$M_j = 1.00$$



(a)

LEGEND:

$$M_{\infty} = 0.20$$

$$p_{O_j}/p_{\infty} = 40.17$$

$$\alpha = 0.00$$

$$d_t = 0.44 \text{ IN.}$$

$$M_j = 1.00$$



(b)

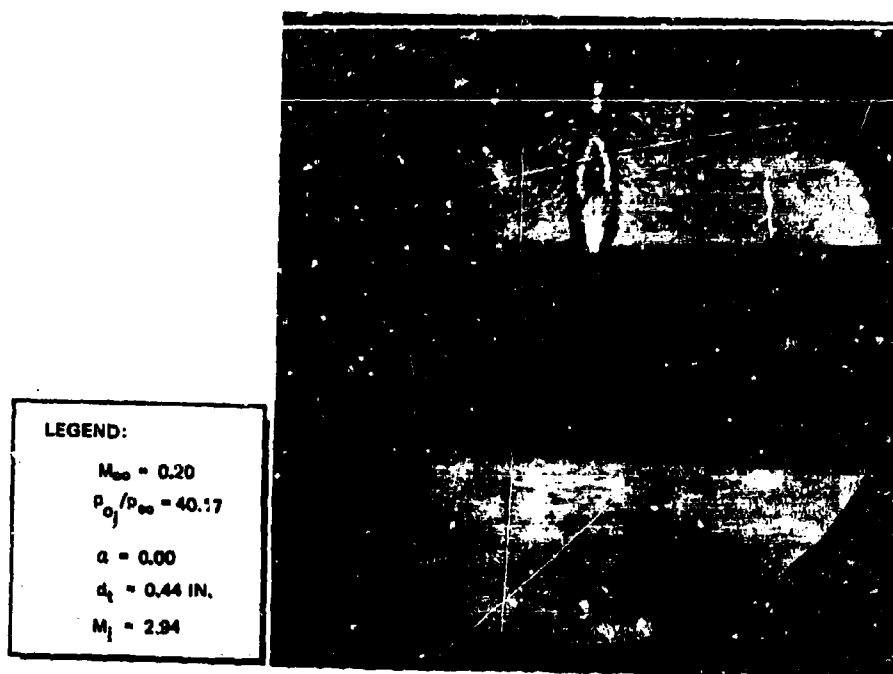
Figure 1. Jet in Subsonic Cross Flow with Barrel Shock System

such as Figure 1 indicates that the plume shape is not influenced too strongly by the crossflow. Indeed, since the flow within the barrel shock system is highly supersonic, most of the flow field in this portion of the jet core would be unaffected by any changes in the plume boundary. Near the nozzle exit, a highly underexpanded plume in a subsonic crossflow might therefore be expected to behave approximately as a jet plume exhausting into still air.

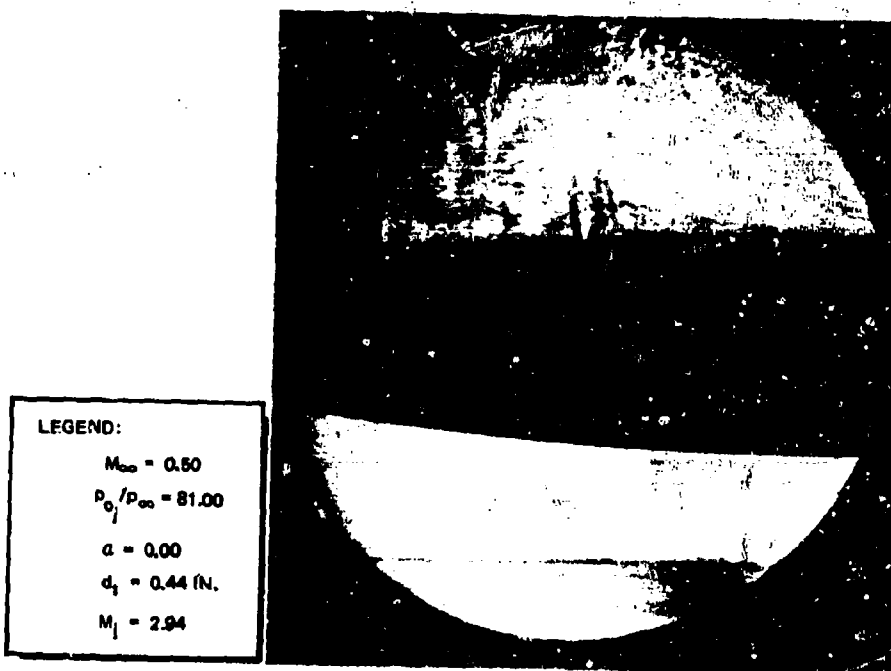
The jet plume, however, has a blockage and entrainment effect on the mainstream, in the neighborhood of the nozzle exit. Some aspects of this behavior can be surmised. A shear layer forms around the jet plume and mixing between the jet and the mainstream begins in this region where the jet axial velocity is relatively low. The mainstream flow past the plume and shear layer is believed to behave in a manner similar to flow over a cylinder at low Reynolds number with separation and the formation of vortices on the leeward side. The behavior of the mixing region is more evident in Figure 2 where the underexpanded jet is supersonic at the exit and the plume exhibits the familiar diamond shock pattern. Since the supersonic jet shown has an expansion ratio of 4.0, it is less underexpanded than the sonic jet in Figure 1, and the shock bounding the plume is not as strong.

At some distance from the nozzle exit, the jet eventually becomes subsonic, probably before significant bending occurs. From this point, more definitive descriptions of the jet are possible based on the more detailed experimental data for a subsonic jet in a crosswind.

Several excellent observations of the qualitative behavior of subsonic jets in a subsonic crossflow exist in the literature, such as those in References 21 and 22. The remarks in this paragraph are based mainly on these references. Beginning at the nozzle and progressing along the jet axis, the first region encountered consists of a potential core surrounded by a turbulent mixing layer. The low momentum flow in the mixing layer is deflected downstream by the crossflow, causing a deformation of the jet cross-section into a kidney shape. The flow separates near the edges of the jet and two counter-rotating vortices are formed on the leeward side, as in low Reynolds number flow about a circular cylinder. The potential core is consumed in a shorter distance than if the jet were exhausting into still air, but its centerline remains undeflected, except in the case of relatively low jet velocities compared to free stream velocities. After the jet has become fully turbulent, vigorous mixing with the free stream occurs. The vortices on the leeward side apparently enhance the entrainment of external air. This mixing causes the jet axial velocity to decay much more rapidly than for a jet in still air, as illustrated by Figure 11 of Reference 23. The entrainment of free stream momentum causes the jet to bend quickly to a direction which is almost aligned with the free stream. It is evident from experimental data such as that in Reference 23 that mixing or momentum entrainment and not a "cross-flow pressure drag" causes most of the jet bending. Some analogies between the cross flow pressure drag on a solid obstacle and the jet bending have been drawn, but experiments seem to indicate that the pressure in the jet soon adjusts to the free stream value and any pressure drag influence is



(a)



(b)

Figure 2 Jet in Subsonic Cross Flow with Diamond Shock System



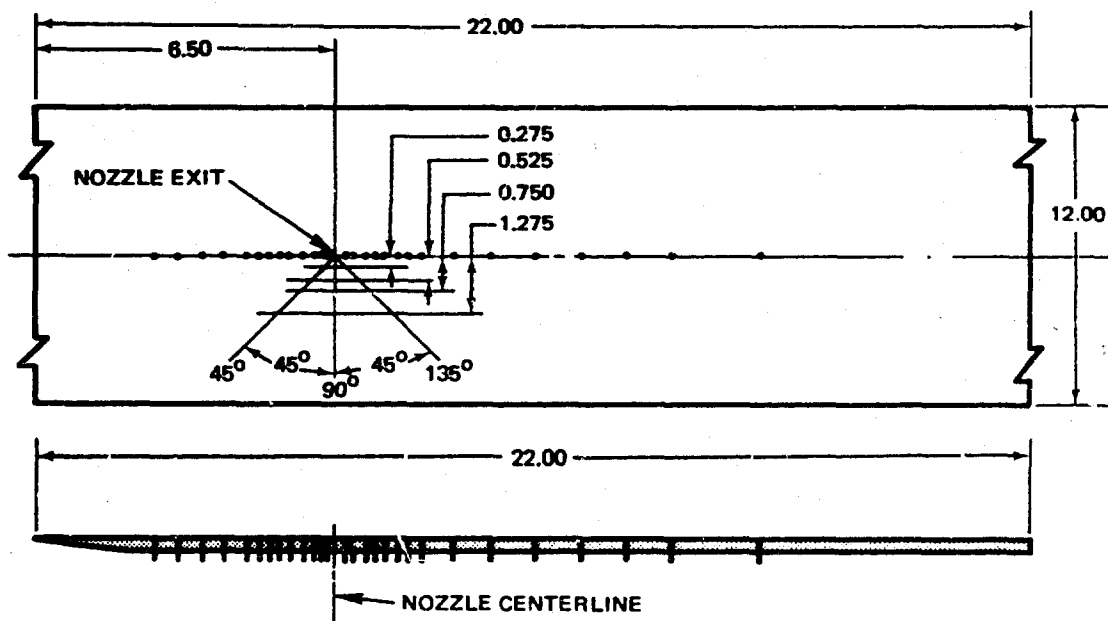
confined to the immediate neighborhood of the orifice. For example, Jordison states in Reference 21 that surveys show that the pressure in the jet is everywhere equal to the free stream pressure a few diameters from the orifice. Some more evidence of the rapid decay to free stream pressure is shown in Reference 24. In the zone of maximum bending, the leeward vortices have been absorbed into the jet and continue to grow in strength. The final state in the jet appears to be a long region where the jet direction differs little from the free stream, and where the axial jet velocity is practically the same as the free stream velocity. This last region is called the "vortex zone" in Reference 22 because the counter-rotating vortices still persist, although with diminishing strength.

## 2.2 UNDEREXPANDED JET INTERACTION PRESSURE DISTRIBUTIONS

Several experiments have been conducted, by the Advanced Systems Laboratory, Research and Engineering Directorate, AMICOM, where pressure distributions due to interaction between an under-expanded jet and a subsonic stream were measured. Except for the data presented by Spring and Street in Reference 8, results of these experiments are not yet generally available. In the present study, data from wind tunnel tests conducted by AMICOM at Cornell Aeronautical Laboratory (CAL) and Arnold Engineering Development Center (AEDC) were made available to the authors by Spring and Street. These data, some of which will be presented in this section, are contained in References 25 to 28, which are not generally available except through AMICOM. Schematic drawings of the test models are shown in Figures 3 and 4.

References 25 and 26 have limited pressure data for a highly under-expanded jet exhausting from a flat plate. The tests of Reference 25 were conducted with several different nozzle configurations of slightly different exit Mach numbers. Different jet gases were also used in order to investigate the effect of changing the jet specific heat ratio,  $\gamma_j$ . The free stream Mach number was varied from 0.6 to 1.2, and the jet chamber-to-free-stream pressure was varied. The experiment reported in Reference 26 was conducted with essentially the same model, but included tests of hot gas effects.

References 27 and 28 contain extensive interference pressure data for an underexpanded jet exhausting just forward of the nose juncture from an ogive-cylinder missile configuration. The ogive-cylinder model of Reference 27 had interchangeable circular and slot nozzles. The two circular nozzles had different exit diameters but the same exit Mach number. The model of Reference 28 was tested with one circular nozzle and one slot nozzle, both of which were sonic. During these tests, the free stream Mach number varied from 0.20 to 1.25 and the jet chamber-to-free-stream pressure ratio ranged from 0 to 120. The pressure distribution in the neighborhood of the nozzle was measured with a large number of taps distributed on the surface. Total forces and moments on the model were also



CENTERLINE PRESSURE TAP LOCATIONS (INCHES FROM JET CENTERLINE)	
FORWARD	AFT
0.275	0.275
0.40	0.40
0.525	0.65
0.75	0.90
1.00	1.15
1.275	1.40
1.50	1.65
1.75	1.90
2.00	2.65
2.50	3.40
3.00	4.40
3.50	5.40
4.00	6.40
6.50	7.40
	9.40

Figure 3. Flat Plate Model Dimension and Orifice Locations

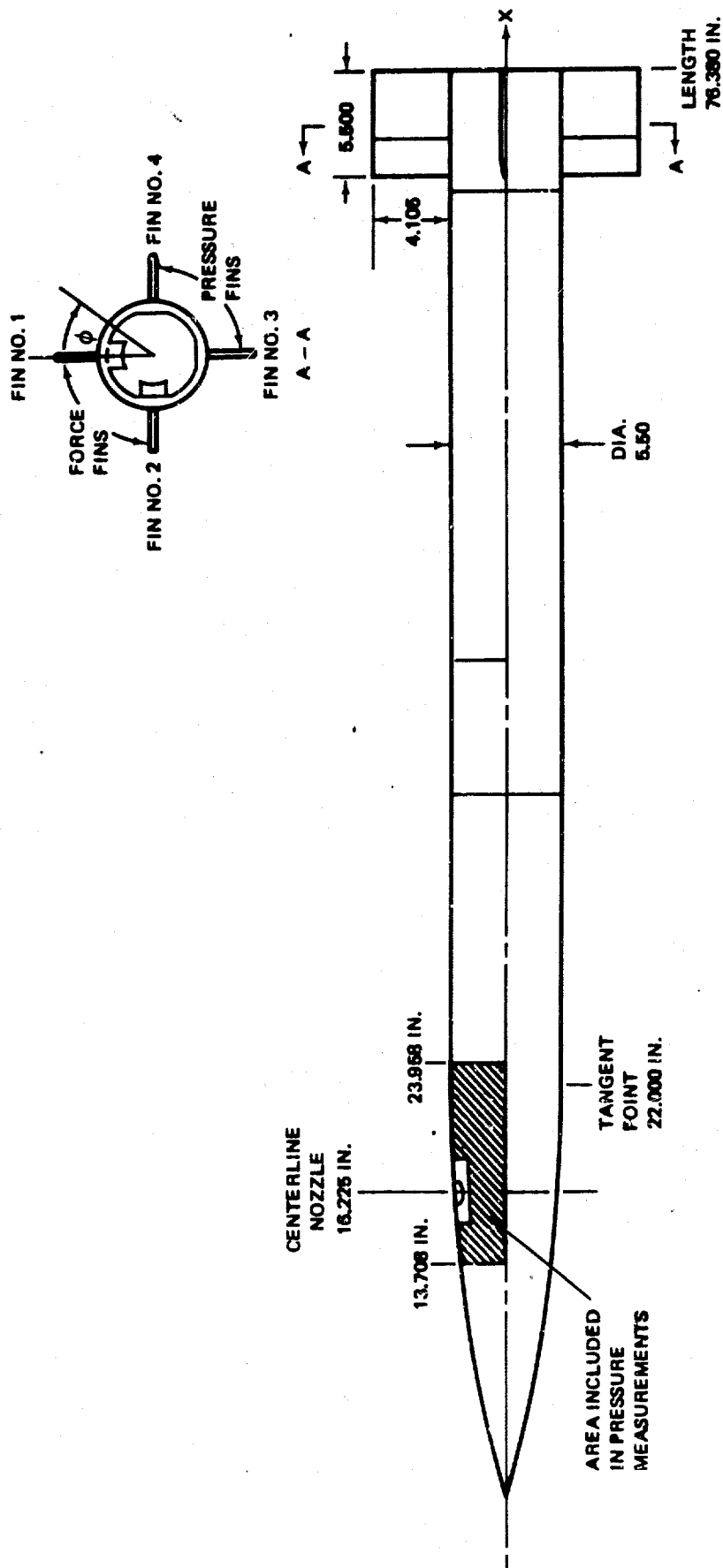


Figure 4. Army Missile Command Model

measured through a sting balance system. During some of the experiments rectangular, cruciform stabilizing fins were placed on the model. Two of the fins were instrumented with pressure taps, and the other two had their own internal balances to measure forces and moments.

Generally, the pressure distributions measured in References 25 to 28 exhibit the same behavior as those observed for a supersonic mainstream. There is a limited region of positive pressure coefficient on the windward side of the jet and a larger negative  $C_p$  region on the leeward side. It has been found that it is possible to correlate some of the experimental results by properly choosing the scaling length. The ogive-cylinder data of References 27 and 28 will be discussed first, since the pressure distributions were measured in greater detail.

Using the coordinate system shown in Figure 5, pressure coefficients along the plane of symmetry  $S = 0$  are plotted in Figure 6 for one value of the free stream Mach number and various pressure ratios. The pressure coefficient has been defined in the conventional manner:

$$C_p = \frac{p - p_\infty}{q_\infty}$$

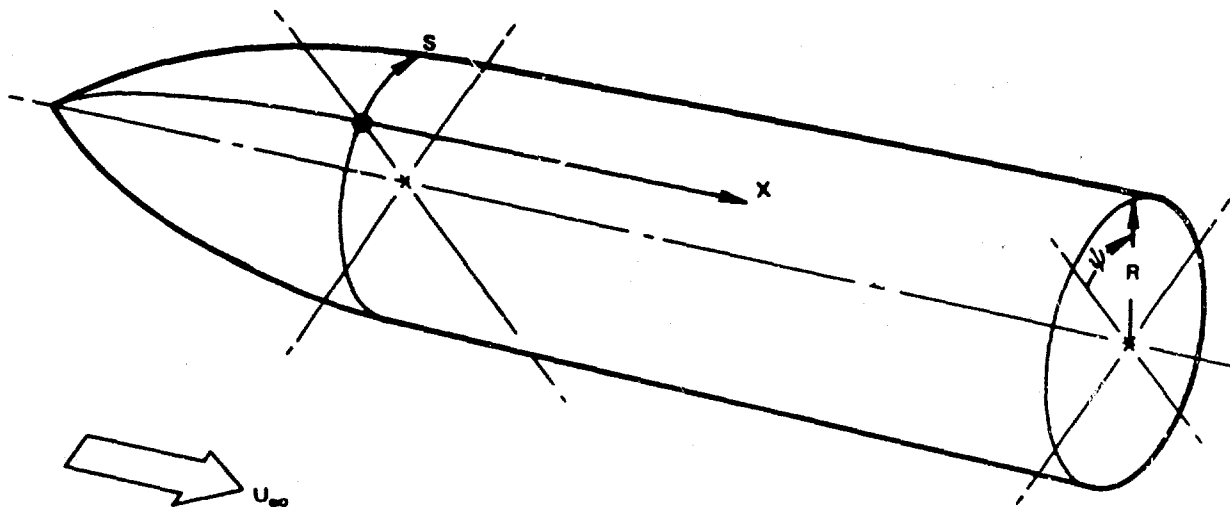


Figure 5. Reference Coordinate System for Interference Pressure on an Ogive-Cylinder

Although the nozzle was not quite located on the cylindrical portion of the model, the effects of curvature have been neglected and  $x$  has been assumed to be equal to the distance along the model axis in inches. Also, the jet-off pressure distribution has not been subtracted out, so that the  $C_p$  shown in Figure 6 is not strictly an interference pressure coefficient. The data shows, however, that the jet-off  $C_p$  is very small and has a negligible effect on the curves of Figure 6. These curves exhibit the characteristic positive pressure coefficients on the windward ( $x < 0$ ) side, with large negative pressure coefficients on the leeward ( $x > 0$ ) side.

The jets used in References 27 and 28 are highly underexpanded and possess the internal shock structure characteristics shown in Figure 2. It has been found that a significant dimension of this shock structure provides a reasonably valid scaling length for pressure distributions in the neighborhood of the jet exit. Based on flow visualization data such as shown in Figures 1 and 2 it can be assumed that, insofar as internal shocks are concerned, jets penetrating a subsonic cross flow behave as if they were exhausting into still air. Let  $h$  denote the distance from the nozzle exit to the Mach disk or to the first intersection of the "diamond" shock pattern when this configuration exists. The data of Love et al in Reference 29 indicate that, for both shock configurations, the ratio of  $h$  to the jet exit diameter can be correlated as a function of the jet exit to free stream pressure ratio at a fixed value of the jet exit Mach number. For sonic nozzles, Crist, Sherman, and Glass have correlated experimental values of  $h$  for a wide range of conditions by plotting  $(h/d_j)$  vs the jet stagnation to ambient static pressure ratio  $P$ , as shown in Reference 30. Based on experimental data, they obtain the empirical equation:

$$\frac{h}{d_j} = (0.645) \sqrt{P} \quad (1)$$

Although this equation does not strictly apply to a diamond shock pattern and a supersonic nozzle, it will be used to calculate  $h$  for scaling purposes with the nozzle throat diameter  $d_t$  substituted for  $d_j$ . A length,  $h$ , thus calculated, permits correlation of interference pressure data for different pressure ratios and nozzle diameters for an underexpanded jet in a subsonic crossflow.

Figure 7 shows the same data as Figure 6, but with  $x$  scaled by the shock intersection height  $h$ . Evidently, the data for all pressure ratios fall on a single curve. Data for larger diameter nozzle ( $d_t = 0.33$  in.) are also included in the figure, and the points correlate well with  $d_t = 0.22$  in. data. Figure 8 shows the same data correlation for cases when the free stream Mach number is 0.20. Note that in this case  $C_p$  is negative upstream as well as downstream of the nozzle. The data for  $M_\infty = 0.20$  has also been correlated along the line  $x = 0$ , as shown in Figure 9. The abscissa represents the arc length:

$$S = R\psi$$

normalized by  $h$ .

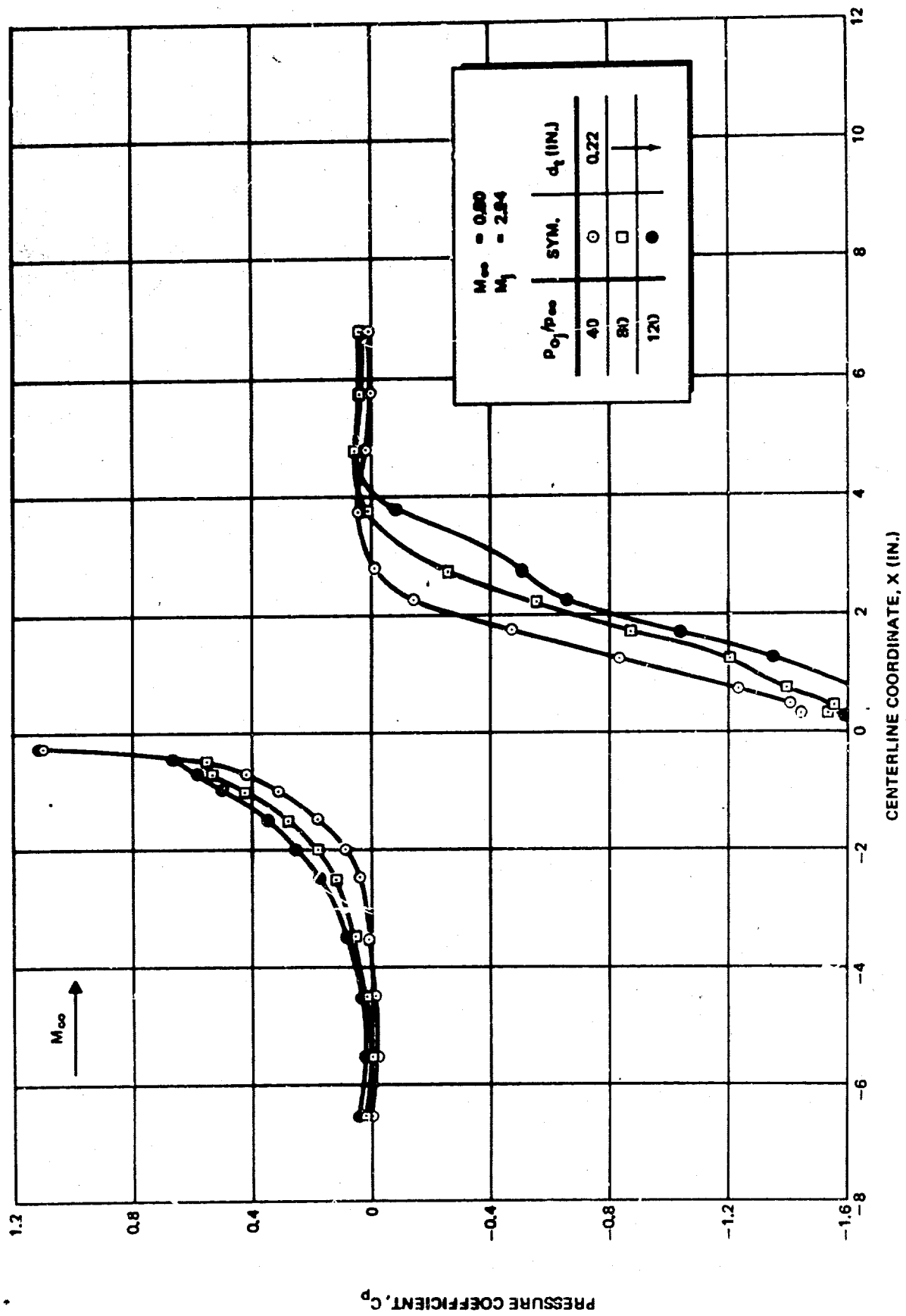


Figure 6. Pressure Distribution Along Plane of Symmetry of an Ogive Cylinder

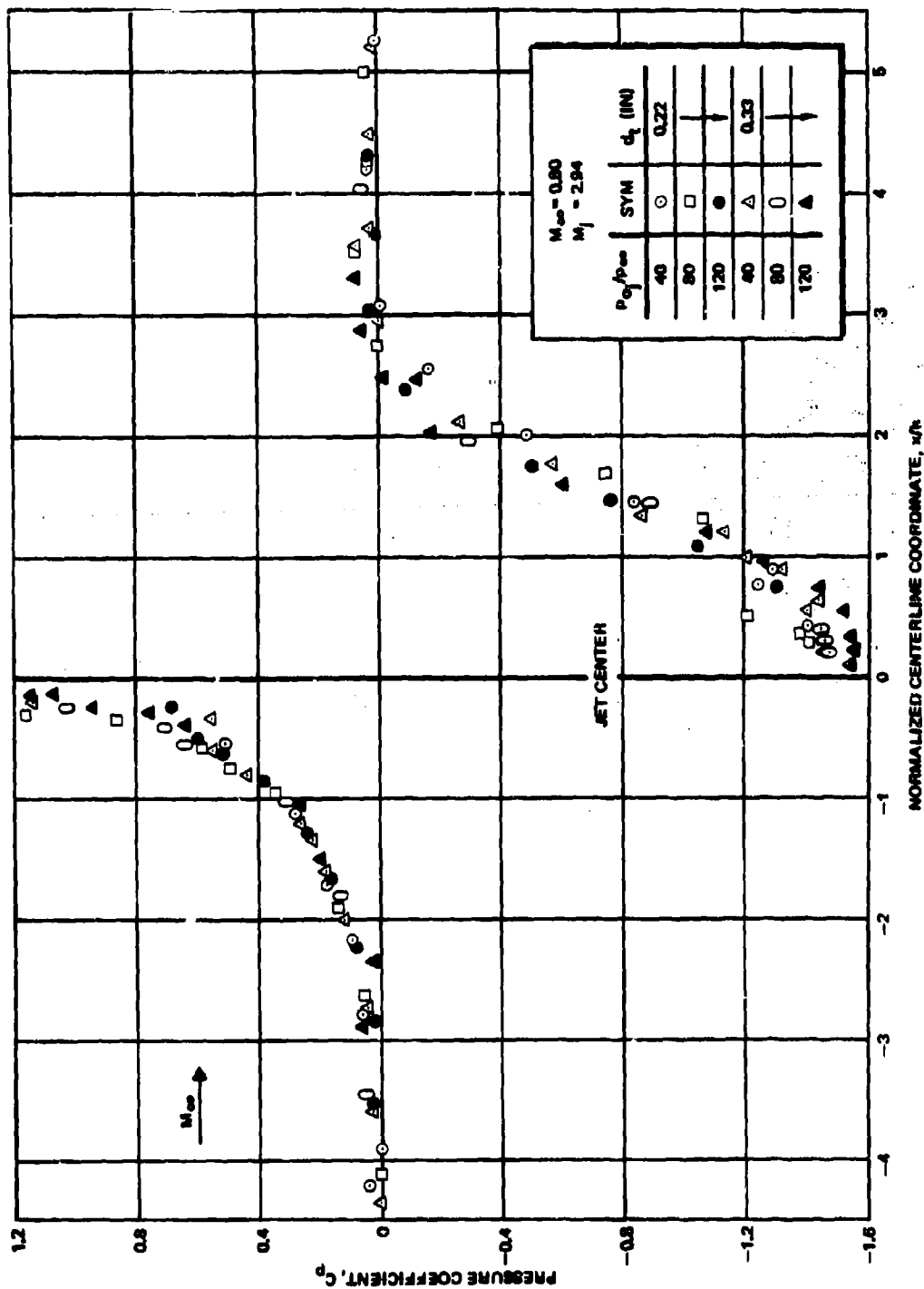


Figure 7. Correlated Pressure Distribution Along Plane of Symmetry of an Ogive Cylinder,  $M_\infty = 0.8$

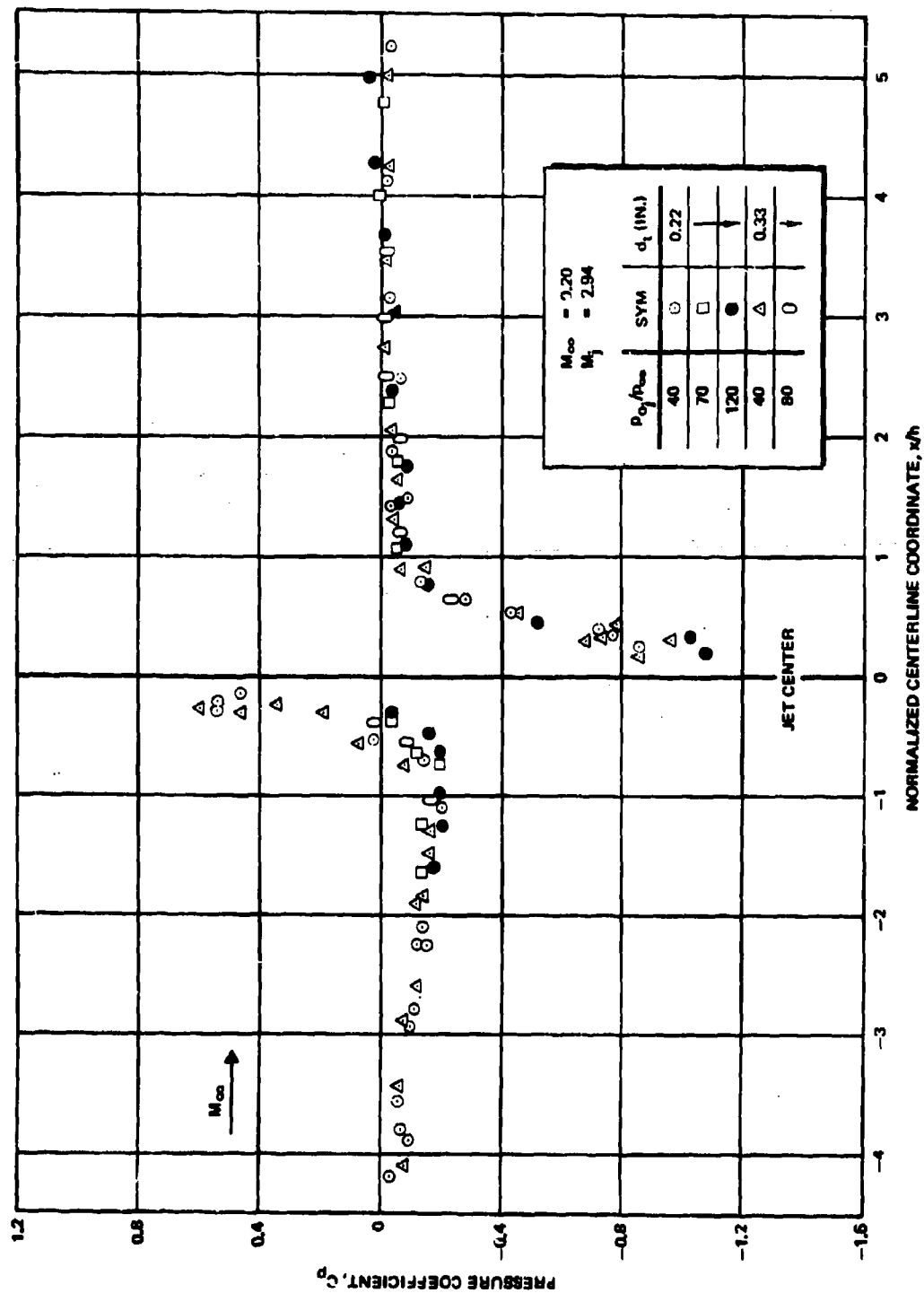


Figure 8. Correlated Pressure Distribution Along Plane of Symmetry of an Ogive Cylinder,  $M_\infty = 0.2$



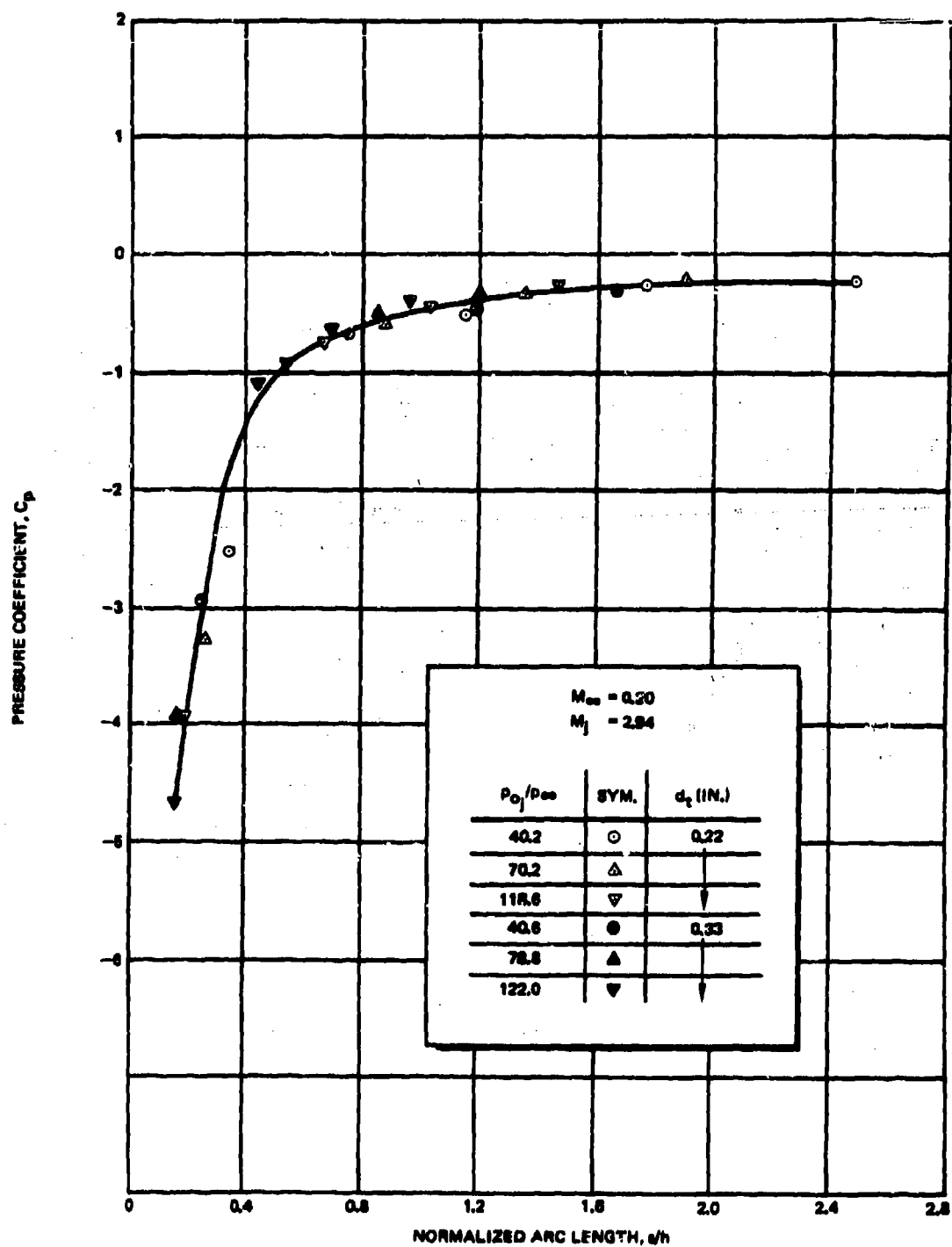


Figure 9. Correlated Circumferential Pressure Distribution at the Jet Station,  $M_\infty = 0.2$

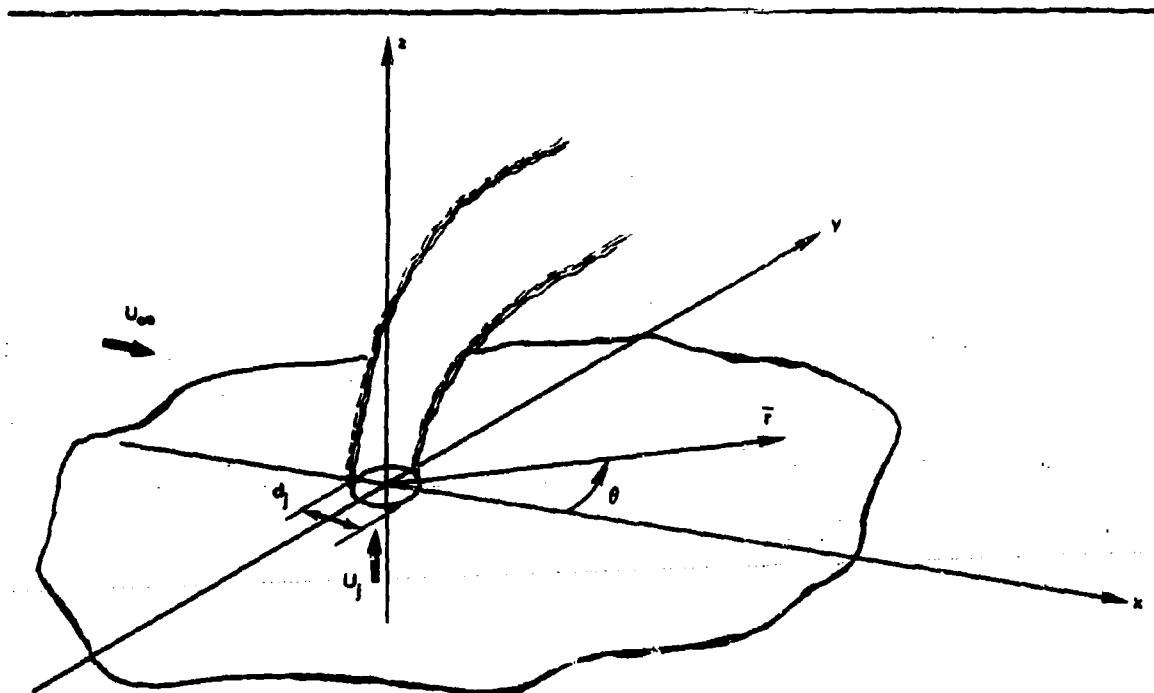


Figure 10. Reference Coordinate System for Describing Interference Pressure Distribution on a Flat Plate

When the flat plate interference pressure measurements of Reference 25 are evaluated, it is found that the scale,  $h$ , correlates this data also. The coordinate system used is shown schematically in Figure 10. Figure 11 is a plot of correlated data along the centerline of the plate, and Figure 12 shows a limited amount of data at intermediate values of  $\theta$ . It must be pointed out that the results shown in Figures 11 and 12 are not as conclusive as those on the previous graphs because the pressure ratios are not very different. Furthermore, the jet exit Mach numbers in the cases shown are not exactly the same, and it appears that the correlation only holds for a fixed exit Mach number, as discussed below.

In sum, it has been found that a scale which is characteristic of the internal shock structure in a highly underexpanded jet and varies directly as the square root of the pressure ratio correlates the interference pressure distribution for fixed  $M_\infty$  and  $M_j$ . A striking feature of the correlated data is the limited extent of the disturbance in the flat plate as well as the ogive-cylinder cases. It appears that the induced pressures reduce to zero within four to five lengths,  $h$ , from the nozzle.

Pressure coefficients from Reference 28 for tests with a sonic nozzle were compared to the  $M_j = 2.94$  data at equal values of  $M_\infty$ . The curves did not agree. Consideration was given to improving the calculation of Mach disk height to include the dependence on nozzle Mach

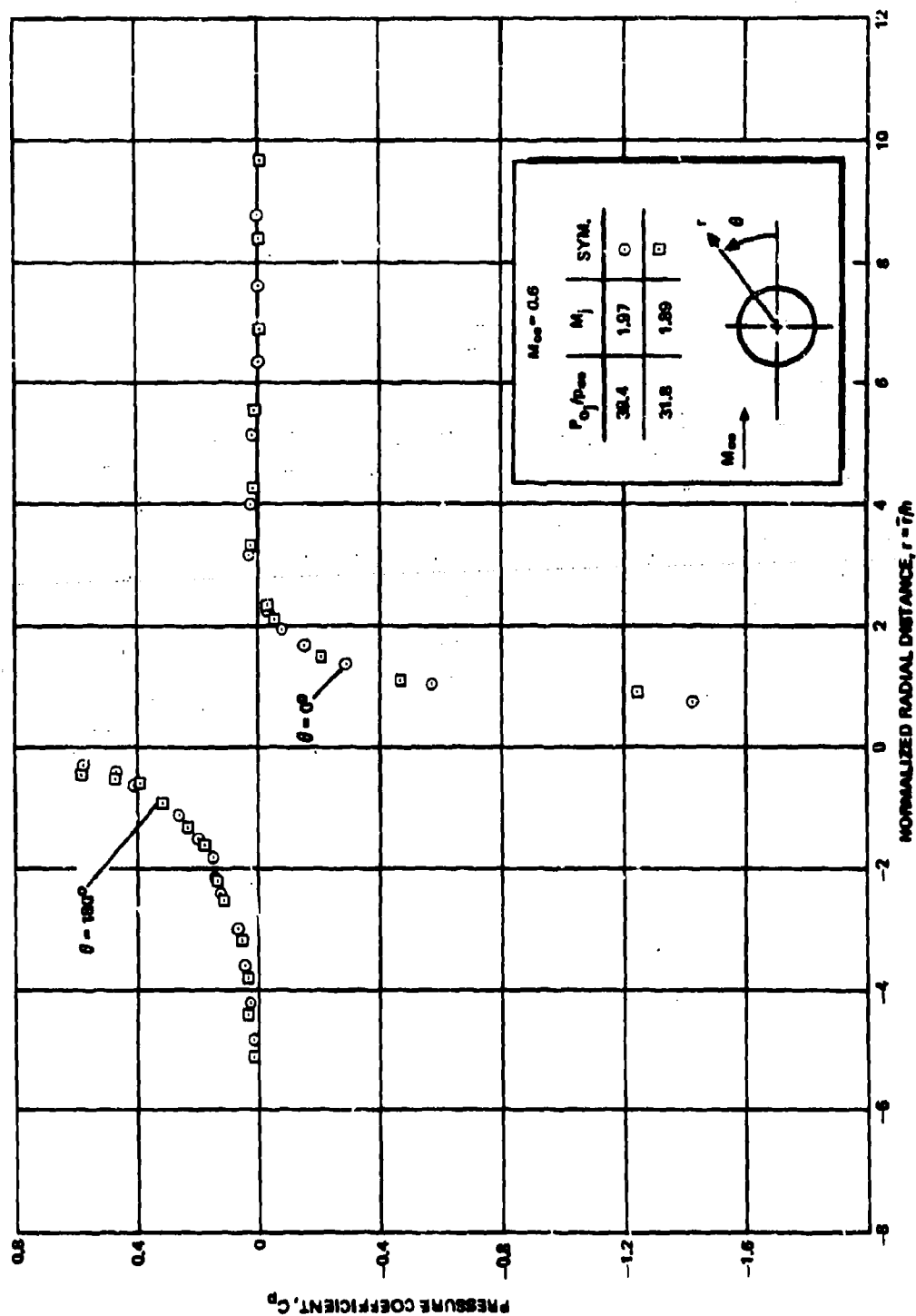


Figure 11. Correlated Pressure Distribution Along Plane of Symmetry of a Flat Plate

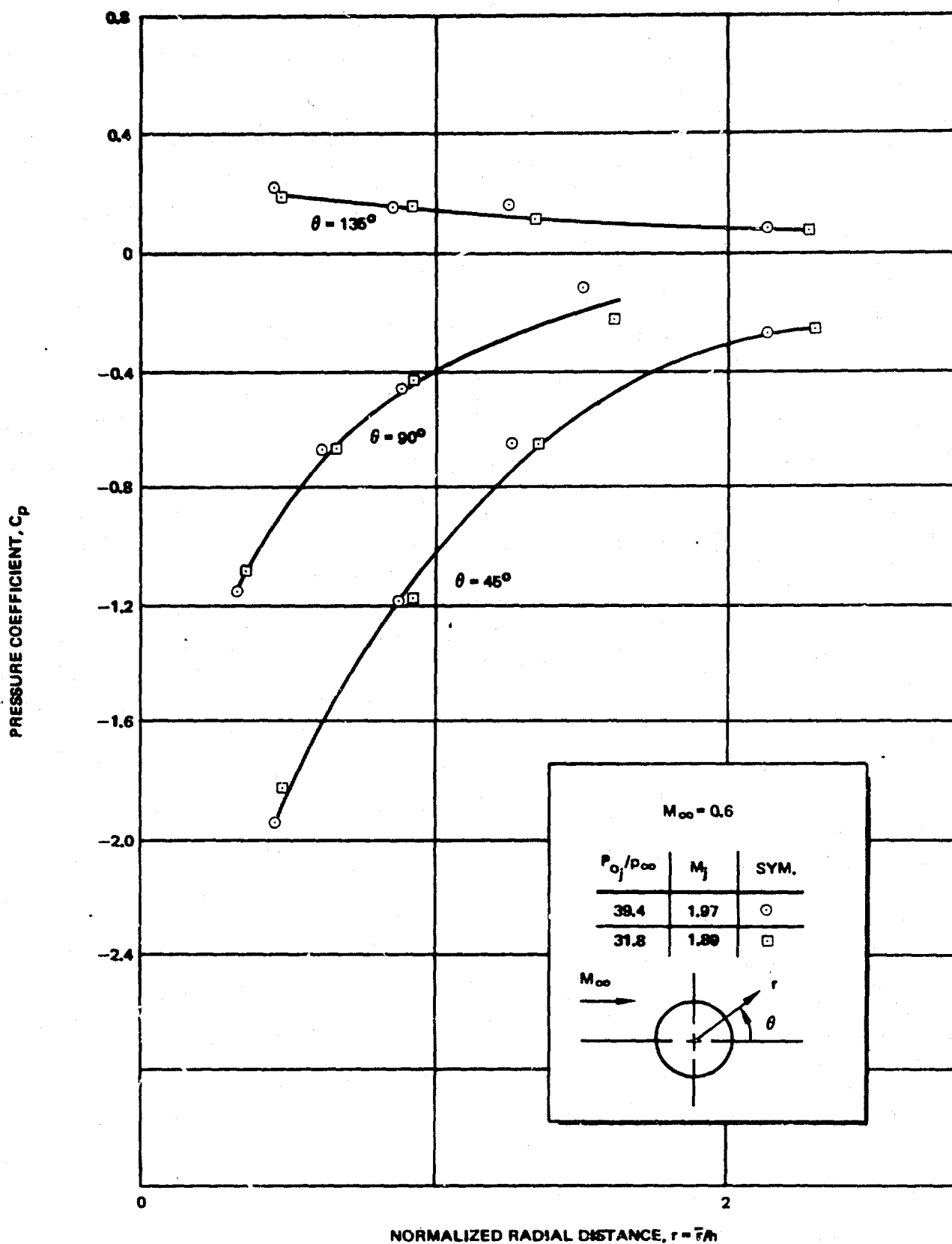


Figure 12. Correlation of Flat-Plate Data off the Centerline

number,  $M_j$ , in order to extend the correlation to other nozzle Mach numbers. A method for computing  $h$  in a highly underexpanded supersonic plume exhausting into still air was developed, as discussed in Appendix A. However, this still failed to correlate the effects of nozzle exit Mach number.

The interaction forces and moments produced by the interference pressures due to the underexpanded jet in a subsonic stream were measured as noted above in the tests described in References 27 and 28. For the ogive-cylinder configuration shown in Figure 4, the jet thrust amplification factor, defined

$$K = \frac{\text{Thrust} + \text{Interaction Force}}{\text{Thrust}}$$

is shown in Figure 13 as a function of the momentum ratio parameter described in Reference 19. It is evident that the amplification factor scales reasonably well with the momentum ratio parameter, even when jet throat area and free stream Mach number are varied. In fact, for these low subsonic Mach numbers the correlation is better than the same correlation for a similar configuration at the transonic and supersonic Mach numbers shown in Reference 31. The effect of exit Mach number on amplification factor is not correlated by the momentum ratio, just as its effect on pressure distribution was not correlated by the plume dimension, as described above.

### 2.3 EMPIRICAL MODELING OF THE INTERFERENCE PRESSURE DISTRIBUTION

Since the objective of the study reported here has been to expeditiously develop reliable engineering analysis techniques, the first analysis models developed were empirical. The empirical models are not only of direct use, they are also of considerable value in the development of more analytical analysis models, as will be described in Section 3. In this section, experimental interference pressure distributions on a flat plate are represented by means of a Fourier series in the azimuthal angle,  $\theta$ , defined in Figure 10.

The principal difficulty encountered in the development of empirical models of the interference pressure distribution was the lack of sufficiently detailed experimental data. The data in References 27 and 28 are representative of the level of detail required; however, the three-dimensional nature of the undisturbed flow leads to a special case in the interference pressure distribution. The data in References 25 and 26 for the jet exhausting into a uniform stream are ideal for differentiating the effects of interaction; however, the pressure distributions were not measured in sufficient detail to provide data for empirical modeling. Experiments are presently being conducted by AMICOM to provide more detailed data for the behavior of an underexpanded jet exhausting from a flat plate in uniform subsonic crossflow. In the interim, data for interference pressures due to a subsonic jet as reported in Reference 32 by Vogler have been used. Comparison of the limited data from Reference 25 with the data from Reference 32 indicates that the general shape and levels of the interference pressure distribution are approximately the same in both cases.

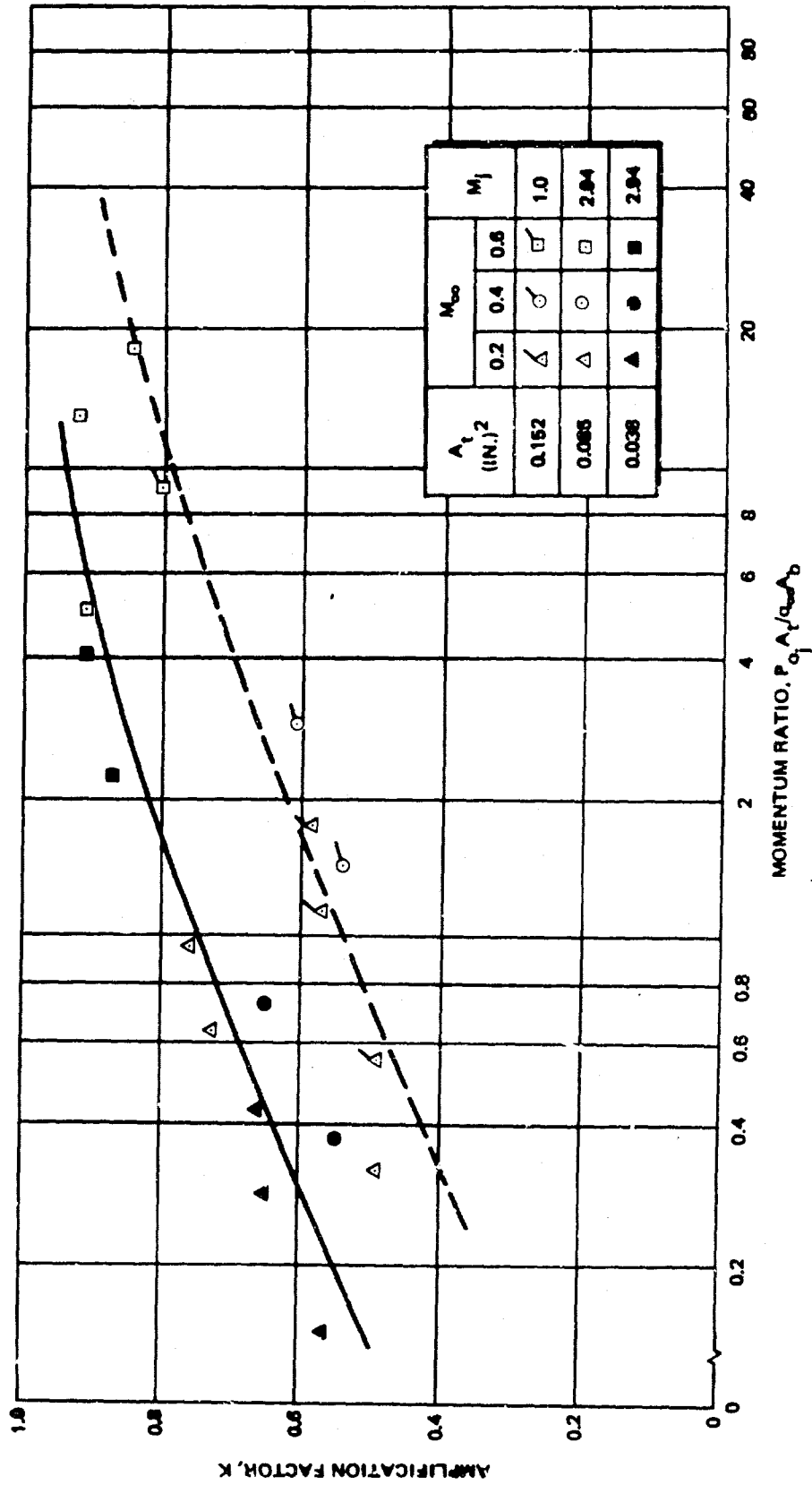


Figure 13. Jet Thrust Amplification Factor Based on Data From AMICOM-CAL Tests of an Ogive-Cylinder,  $M_\infty < 1.0$

For subsonic jets, References 32 to 34 indicate that the significant correlating parameter is the ratio of free stream to jet velocity ( $U_\infty/U_j$ ). Geometrical similarity also exists, so that data for the same velocity ratio, normalized by the nozzle diameter, falls approximately on a single curve. Plots of Vogler's data at a fixed value of  $r$  (where  $r$  has been normalized by the jet diameter) reveal that for a fixed value of ( $U_\infty/U_j$ ) the data varies regularly with  $\theta$ . It appears therefore that a truncated Fourier series of the form

$$C_p(r, \theta; U_\infty/U_j) = \sum_{n=0}^m c_n \left( r, \frac{U_\infty}{U_j} \right) \cos n\theta \quad (2)$$

should represent the data quite well with relatively few terms. The coordinates used in Equation (1) are depicted in Figure 10. Due to the symmetry of the flow about the lines  $\theta = 0$  and  $\theta = \pi$ , the series will not contain any sine terms. The coefficients,  $c_n$ , may be evaluated at a fixed value of  $r$  by numerically integrating the data and using the orthogonality of the cosine function. That is, the expressions

$$c_0 \left( r; U_\infty/U_j \right) = \frac{1}{\pi} \int_0^\pi C_p d\theta \quad (3)$$

and

$$c_n \left( r; U_\infty/U_j \right) = \frac{2}{\pi} \int_0^\pi C_p \cos n\theta d\theta \quad (4)$$

for  $n > 0$

can be used.

Some difficulty was encountered in using Vogler's data, principally because the measured pressure coefficient does not decay to zero as it should. As mentioned in Reference 32, this fact is probably caused by misalignment of the plate with respect to the free stream or possibly by warping of the plate under the loads induced by the jet. The data was therefore adjusted along each ray  $\theta = \text{constant}$  so that the pressure coefficient would be zero at  $r = 10$ . The results of plotting the data for  $U_\infty/U_j = 0.3$  as a function of  $\theta$  for various values of the normalized radius  $r$  are shown in Figures 14a-14d. Using Equations (3) and (4), the data has been integrated numerically to obtain the coefficients  $c_n$ . Two- and three-term series representations

$$C_p = c_0(r) + c_1(r) \cos \theta$$

and

$$C_p = c_0(r) + c_1(r) \cos \theta + c_2(r) \cos 2\theta$$

are also plotted in Figures 14a-14d. Evidently, three terms in the series are sufficient to represent the pressure distribution quite well.

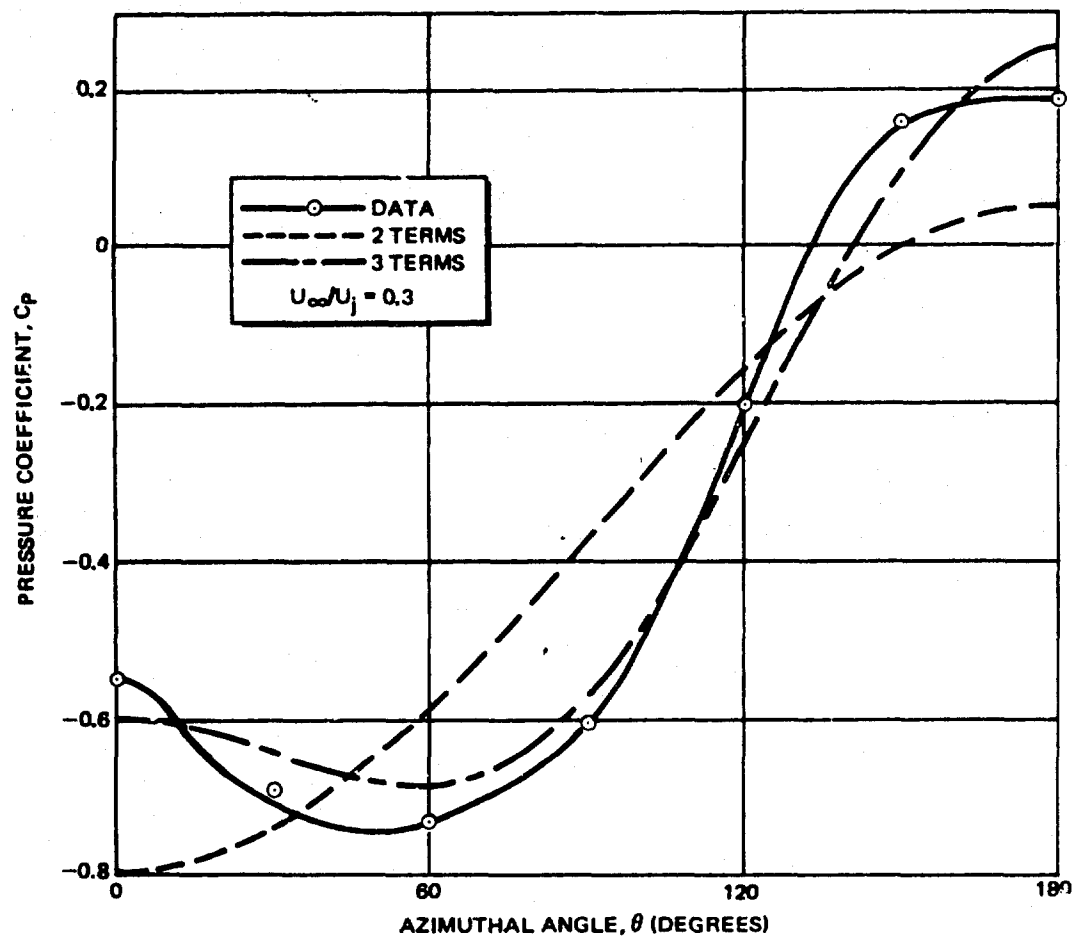


Figure 14a. Comparison of Vogler's Data and Fourier Series,  $r = 1.5$

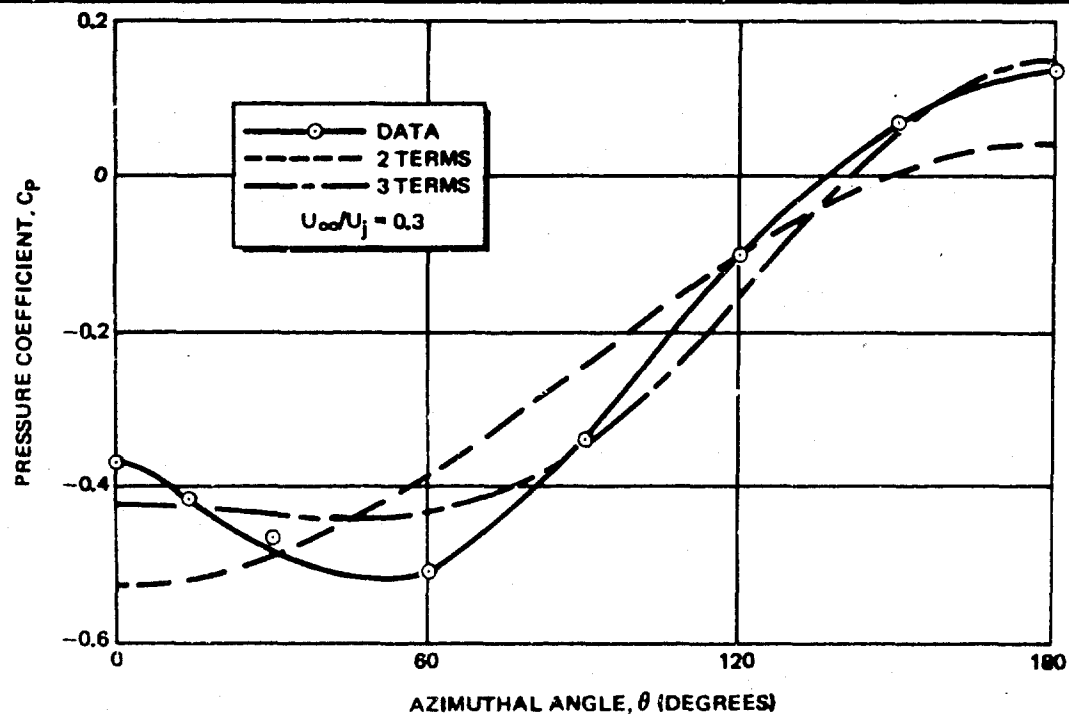


Figure 14b. Comparison of Vogler's Data and Fourier Series,  $r = 2.0$



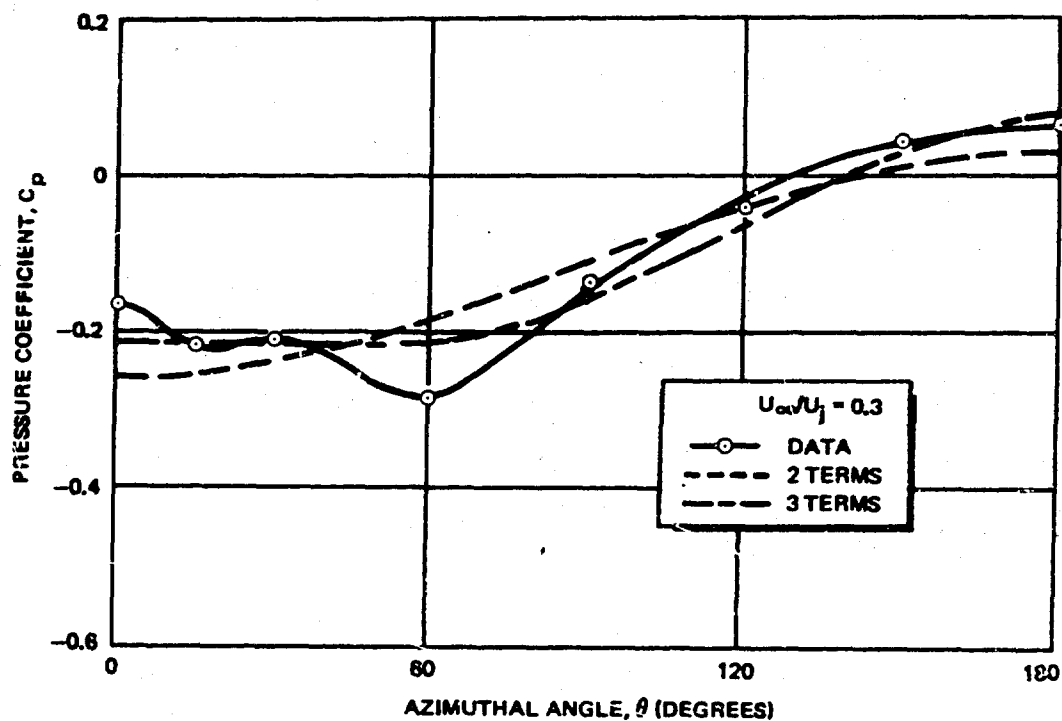


Figure 14c. Comparison of Vogler's Data and Fourier Series,  $r = 3.0$

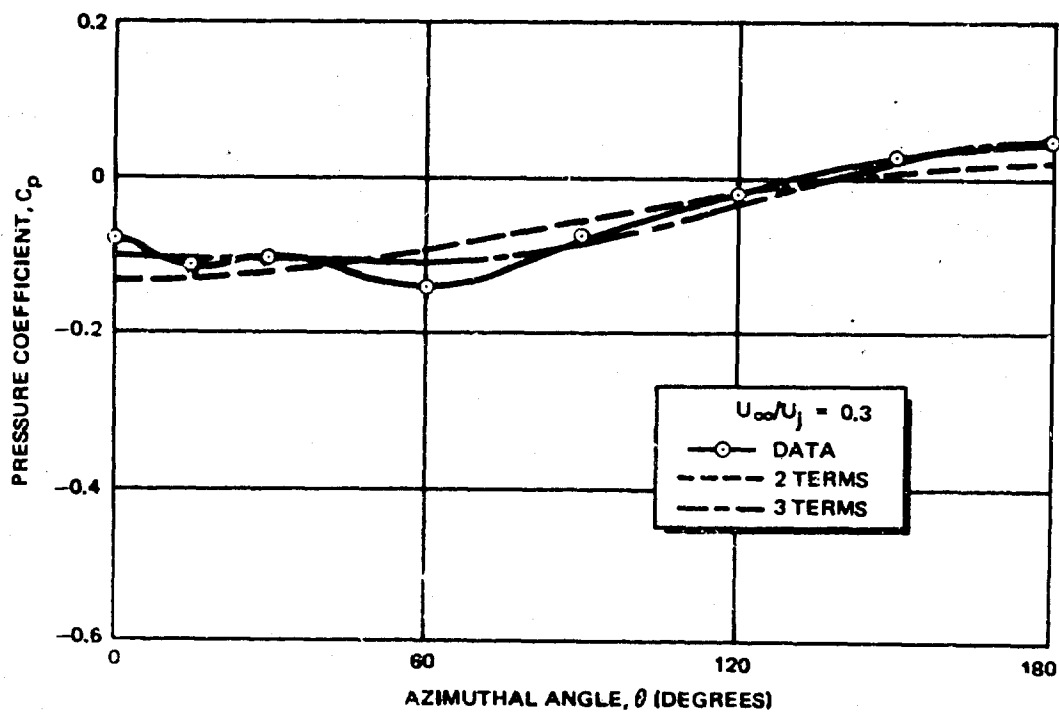


Figure 14d. Comparison of Vogler's Data and Fourier Series,  $r = 4.0$

There is one other distinct advantage to this truncated Fourier series technique. The force or moment on the plate due to the interaction can be calculated from the equation

$$F \text{ or } M = q_{\infty} \int_{r_j}^{\infty} \int_0^{2\pi} C_p \cos n\theta r^{(n+1)} dr d\theta \quad (5)$$

where the force is obtained if  $n$  equals 0 and the moment results if  $n$  equals 1. If the pressure coefficient is written in the form of Equation (2), the integral becomes

$$\int_{r_j}^{\infty} \int_0^{2\pi} \cos n\theta \sum_{n=0}^{n=m} c_n \cos m\theta r^{(1+n)} dr d\theta$$

or

$$\sum_{n=0}^m \int_{r_j}^{\infty} \int_0^{2\pi} c_n \cos n\theta \cos m\theta r^{(1+n)} dr d\theta$$

Due to the orthogonality of the cosine, this now becomes

$$F = q_{\infty} \int_0^{\infty} c_0 r dr d\theta$$

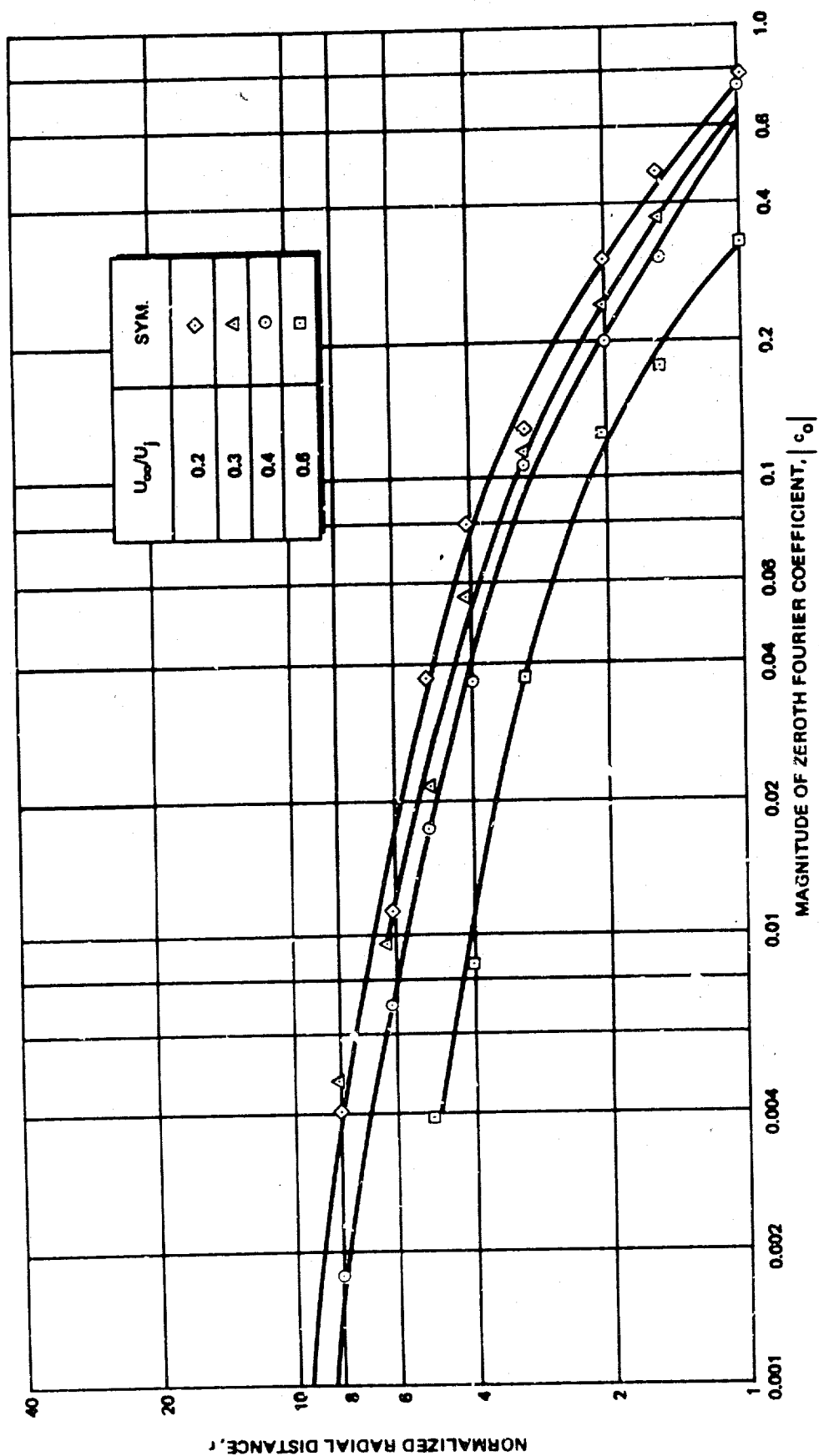
and

$$M = q_{\infty} \int_0^{\infty} \int_0^{2\pi} c_1 \cos^2 \theta r^2 dr d\theta$$

Thus, the total contribution to the forces comes from the first term of the Fourier series (truncated or complete) and the total contribution to the moment comes from the second. Matching the first couple of terms of a Fourier series takes on a new significance in the light of this result. If analytical models could be found that would have very close agreement in these terms for all values of  $r$ , then the two most important quantities could be predicted quite well.

Figures 15 and 16 show the first two Fourier coefficients obtained from all of Vogler's data as functions of  $r$  for various values of  $U_{\infty}/U_j$ . The variation in the third coefficient,  $c_2$ , is much more irregular, as shown in Figure 17.

From the above results, it is evident that Fourier series techniques will yield a simple and efficient empirical description of interference pressure distributions on a flat plate. In addition, this means of data analysis has been helpful in the development of semi-empirical flowfield models, as described in the next section.



Figures 15. Variation of Zeroth Fourier Coefficient with Distance from the Nozzle and Velocity Ratio

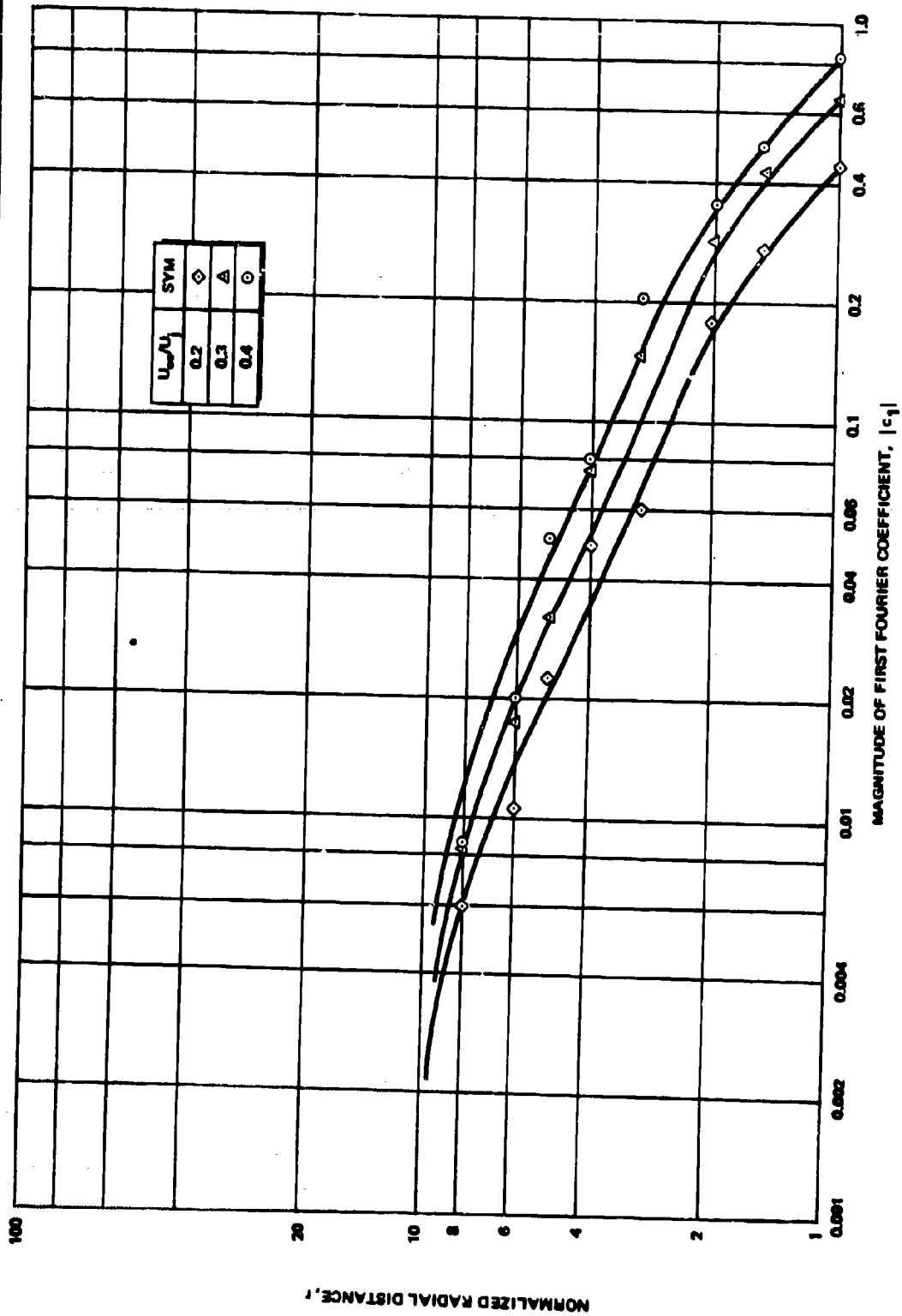


Figure 16. Variation of First Fourier Coefficient With Distance From the Nozzle and Velocity Ratio

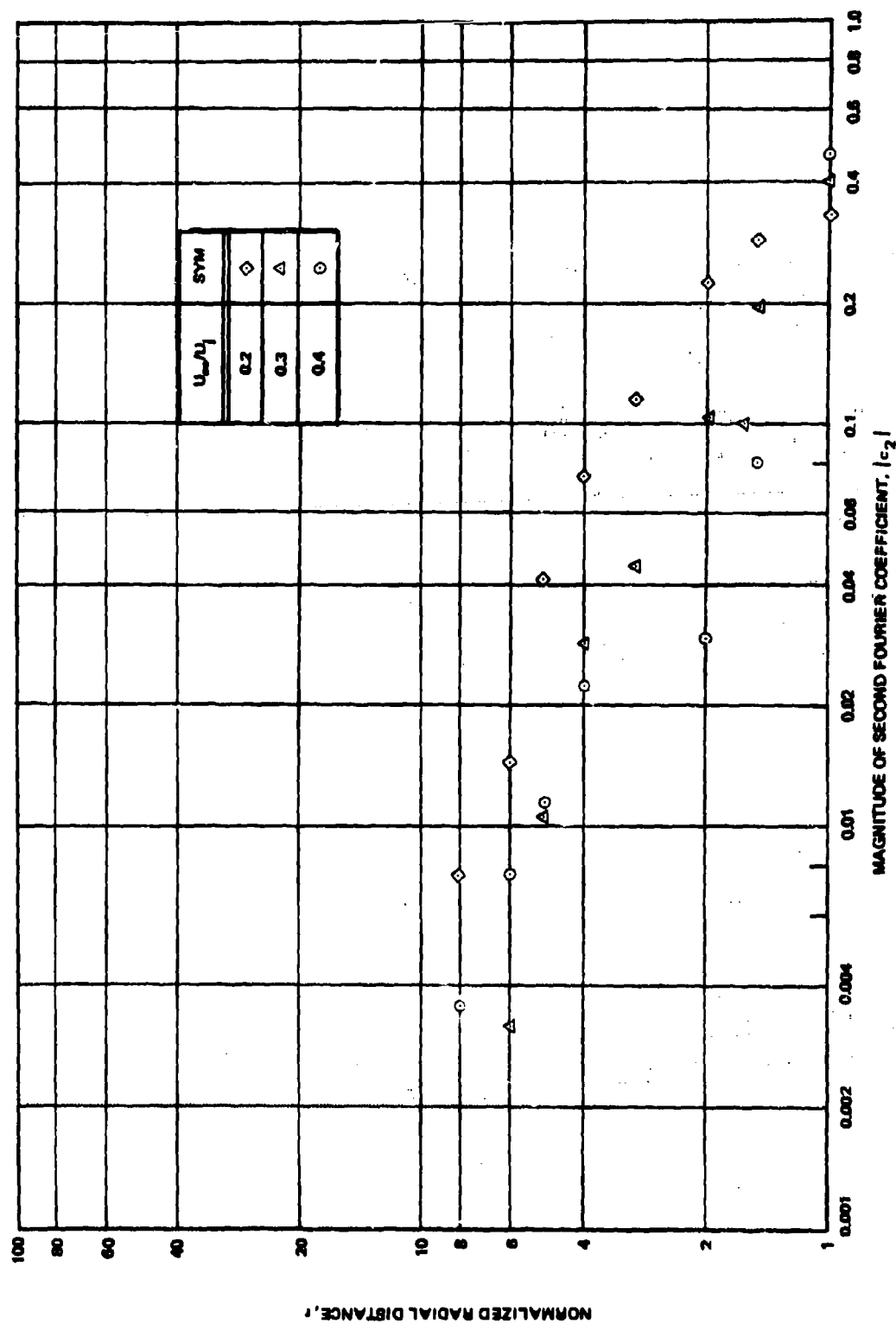


Figure 17. Variation of Second Fourier Coefficient with Distance from the Nozzle and Velocity Ratio

### Section 3

## FLOWFIELD MODELS FOR THE INTERACTION REGION

The subsonic mainstream JI flowfield is characterized by complex phenomena, including mixing of turbulent and laminar, compressible and comparatively incompressible flows, as well as three-dimensional flow-separation phenomena. Consequently, detailed mathematical modeling of the flow represents a task of considerably higher magnitude than that intended in the study reported here. In this study, the approach taken to mathematical modeling was indirect. Analogies to the actual flowfield were postulated that could be expected to yield pressure distributions in the region of the jet exit which would behave as those derived from experiment. The model flows were assumed to be incompressible and inviscid, and mathematical models were developed to allow maximum use of empirical data. The amenability of pressure distribution data to empirical description, as described in Section 2, provides some degree of flexibility in combining analytical and empirical methods.

The models developed may be divided into two general categories: phenomenological and pressure. The former introduce in some form the gross physical effects that the jet may be expected to induce on the surrounding stream, such as blockage and entrainment. The latter postulate a flow field intended only to give the proper qualitative pressure distribution. All the models contain arbitrary constants which are adjusted by matching the resultant pressures to experimental data, in most cases by means of the Fourier series representation described in Section 2. Due to the lack of sufficient detailed interference pressure distributions on flat plates with highly under-expanded jets, the data of Vogler has been used throughout. It is expected that the techniques developed may also be used to describe interference pressures when the jet is highly underexpanded.

### 3.1 MODELS PROPOSED IN THE LITERATURE

Various attempts have been made at theoretically predicting the interference pressure distribution on a flat plate from which a transverse jet exhausts. The main concern has been with the VTOL problem, so that the discussion applies to jets of relatively low velocity whose exit pressure is roughly equal to the free stream pressure.

Numerous investigators (References 19, 32, 33 and 35) have attempted to represent the interference pressure on the plate by the inviscid flow

about an infinite solid circular cylinder normal to the cross flow. While for some velocity ratios the agreement is not unreasonable on the windward side of the jet, it is not good on the downstream portion of the plate.

In Reference 33, Bradbury and Wood have represented the interference effects produced by the jet by means of an entrainment and a blockage contribution to the velocity on the plate surface. It is assumed that the entrainment contribution is axisymmetric about the nozzle centerline, whereas the blockage term is not. Entrainment is assumed to vary with the ratio  $(U_\infty/U_j)$ , whereas the blockage term is taken to be independent of this ratio. Bradbury and Wood show that along the centerline of the plate, the pressure coefficient should then have the form

$$\sqrt{1 - C_p} = \frac{f(r)}{(U_\infty/U_j)} + \text{blockage term}$$

where the blockage term is independent of  $(U_\infty/U_j)$ . Consequently, a plot of  $(1 - C_p)$  vs  $(U_j/U_\infty)$  should be a straight line for large values of  $(U_j/U_\infty)$ . Bradbury and Wood show that this is the case. The entrainment function  $f(r)$  is calculated by postulating a sink distribution along the axis of the jet which will yield the same entrainment as calculated from a turbulent mixing analysis. However, it is shown that the contribution of this entrainment function to the overall pressure coefficient is extremely small so that most of the observed pressure coefficient would have to come from the blockage term. In Reference 33, Bradbury and Wood indicated that they had been unable to develop such a blockage term.

Wooler, et al, describe, in Reference 36, a very complete model which they have formulated for predicting interference pressures on wings with lift fans. Their method includes a scheme for predicting jet trajectories, provided that some constants can be adjusted empirically. These constants fix the entrainment rate and the growth of the jet in cross-section, and they are evaluated by matching theoretical and experimental jet trajectories. With the entrainment and blockage of the jet thus obtained, Wooler, et al, represent the effect of the jet on the surrounding fluid by distributing sinks and doublets along the jet trajectory. In particular, the upwash on the plane of the wing is calculated, from which the interference pressure is then found. The authors compare their theoretical results to measured pressure coefficients on a rectangular wing which they have tested. They show satisfactory agreement at fairly large distances from the jet orifice, but the agreement near the nozzle is not good. Figure 18 is a comparison made from the results of Reference 36. The pressure coefficient is plotted in the coordinates of Figure 10 for  $\theta = 90^\circ$ , by cross-plotting the chordwise  $C_p$  distribution given in Reference 36 for the midpoint on the chord.

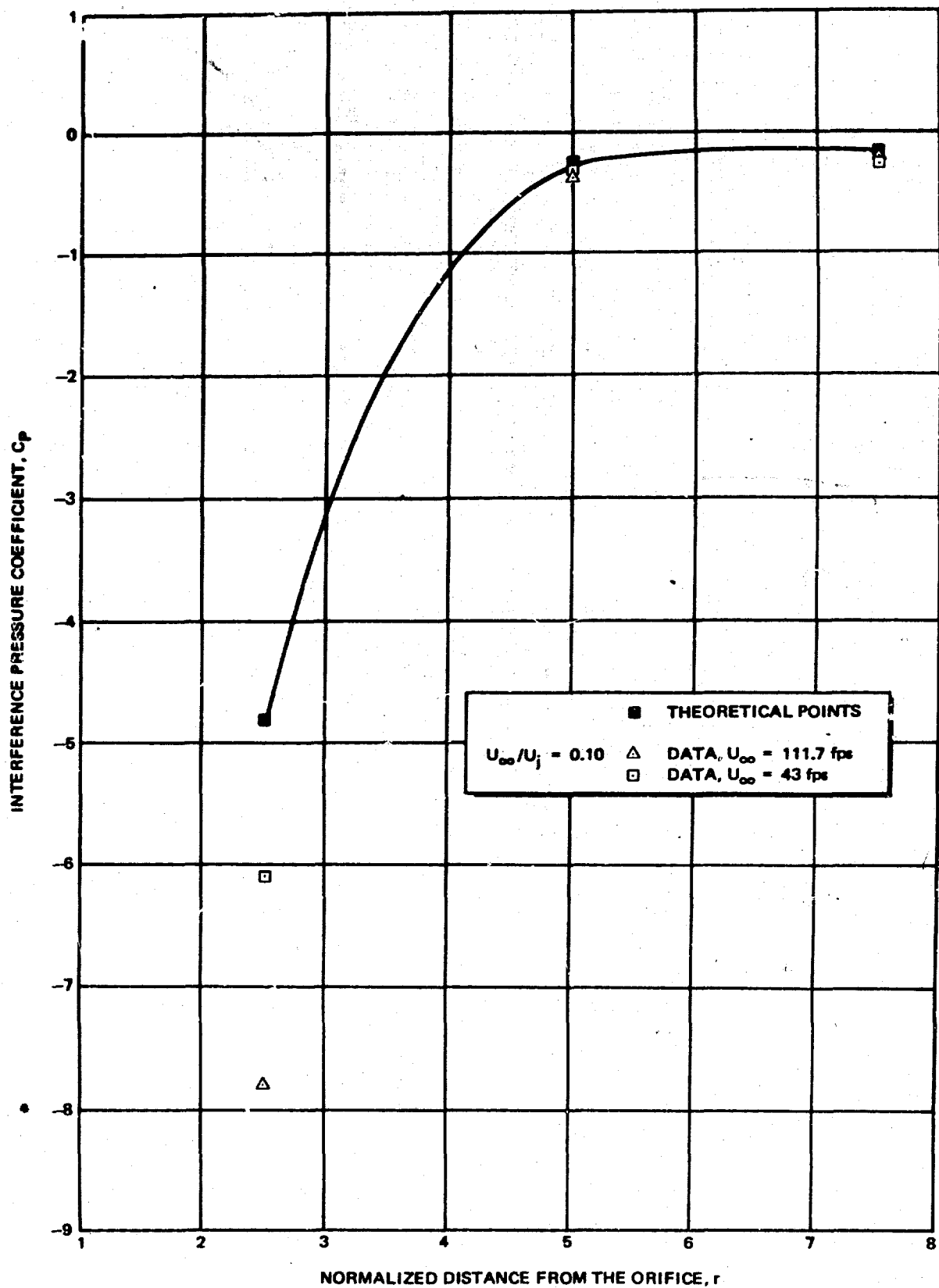


Figure 18. Comparison of Data and Theory of Reference 36



Another model for predicting interference pressures is proposed by Kuiper in Reference 9. He represents the blockage produced by the jet by the potential flow about a three-dimensional source in a uniform stream. The source is located at some distance from the exit plane of the nozzle, and this distance is adjusted to match the data of Reference 32. In Reference 9, however, the jets are considered to be located on the aft end of the vehicle, so that Kuiper is only concerned with the  $\theta$  range

$$90^\circ \leq \theta \leq 270^\circ.$$

### 3.2 PHENOMENOLOGICAL MODELS

Two models will be considered under this heading. Referring to Figure 10, it is assumed that the flowfield is two dimensional in planes  $z = \text{constant}$ , and that the free stream is incompressible, inviscid, and irrotational so that flow in the  $(x, y)$  plane obeys the two-dimensional Laplace's equation. The first model, called the doublet model, consists of the superposition of a free stream, source or sink, and a doublet. The doublet attempts to account for the blockage effects of the jet, while the sink would represent the entrainment caused by turbulent mixing. The second flow model, called the vortex model, is the same as the first, except for the addition of two counter-rotating vortices downstream of the origin. It is known experimentally that these vortices exist, and that the flow bears some similarity to separated flow behind a cylinder.

It has been shown in Section 2 that a truncated Fourier series in  $\theta$  succeeds in representing the data with reasonable accuracy. Consequently, the following procedure has been adopted for completely determining the models. Once the number and types of singularities have been chosen, the complex potential for the flowfield is written in terms of the singularity strengths. From this, an expression for the pressure coefficient is obtained and put in the form of a Fourier series in  $\theta$ , as in Equation (2). By setting each coefficient at a given value of  $r$  equal to the corresponding one obtained from the data, equations are obtained which may then be solved simultaneously for the unknown singularity strengths. This may be done for several values of the velocity ratio, using the data of Reference 32, and the singularity strengths obtained as functions of this velocity ratio. The benefits of this technique are twofold. First, its use will allow the extension of limited amounts of data to other velocity ratios. Second, by determining which singularities are strongest, the dominant factors in the flowfield can be inferred. This information could be extremely important in trying to relate the results obtained from flat plate data to an axisymmetric body. The model will yield results at one value of  $r$  which are as close to the data as the Fourier series representation is. The accuracy of results at other values of the radius will depend upon how closely the model depicts the actual situation and will determine whether the model is valid. Also, as discussed in Section 2, any model that accurately reproduces the  $r$  dependence of the first two terms in the Fourier series will accurately predict integrated forces and moments.

### 3. 2. 1 Doublet Model

The doublet model is a two-dimensional, potential flow model derived from the superposition of complex potentials for a uniform flow, a doublet, and a source (or sink) which are described in Reference 37.

Let  $\zeta$  denote the complex variable

$$\zeta = x + iy$$

where  $x$  and  $y$  have been normalized by the jet diameter, and let  $w(\zeta)$  denote the complex potential. Then the complex potential for flow about a doublet and a source may be described by the Equation

$$w^* = A_0^* \zeta + A_1^* \log \zeta + \frac{A_2^*}{\zeta} \quad (6)$$

where the coefficients  $A_n$  are purely real. If the model and actual flows are to have the same velocity at large distances,  $A_0^*$  must be chosen equal to  $U_\infty$ , and the pressure coefficient

$$C_p = \frac{p - p_\infty}{\frac{\rho_\infty}{2} U_\infty^2}$$

is given by:

$$C_p = 1 - \frac{1}{U_\infty^2} \left( \frac{dw^*}{d\zeta} \right) \overline{\left( \frac{dw^*}{d\zeta} \right)} \quad (7)$$

where a bar denotes the complex conjugate, as described in Reference 37. The above choice of  $A_0^*$ , however, creates a problem in matching the model and the experimental pressure coefficients. It may be shown that the Equations (6) and (7), when combined and transformed to real variables, lead to a three-term Fourier series for the pressure coefficient (up to and including a  $\cos 2\theta$  term). Equating coefficients in that series term by term to the experimentally determined coefficients,  $c_n(r)$ , would lead to three equations for the two unknowns  $A_1^*$  and  $A_2^*$ . This over specification can be avoided by leaving  $A_0^*$  unspecified and obtaining its value from a matching of the coefficients for all three terms. Since the resulting value of  $A_0^*$  will differ from  $U_\infty$ , the uniform stream specified in the model will not have the same velocity as the actual free stream flow. Since the objective of the model is to match pressures, it is of course desirable that the model and actual flows have the same free stream static pressure. Consequently, differing free stream velocities require that their stagnation pressures be different. By allowing different stagnation pressures in the flow and the model, the pressure at any stagnation points which arise in the model flow may be adjusted for

better agreement with data. This may prove to be necessary, since the data of Vogler shows that, even on the windward side, the measured pressures never reach the value of the free stream stagnation pressure.

Bernoulli's equation for the model flow can be written

$$p + \frac{\rho}{2} |\underline{q}^*|^2 = p_\infty + \frac{\rho_\infty}{2} U_\infty'^2$$

where

$|\underline{q}^*|$  = magnitude of the dimensional velocity vector

$U_\infty'$  = uniform flow velocity in the model

The pressure coefficient can be written in terms of the actual free stream velocity as

$$C_p = \frac{p - p_\infty}{\frac{\rho_\infty}{2} U_\infty'^2} = \left( \frac{U_\infty'}{U_\infty} \right)^2 - \frac{|\underline{q}^*|^2}{U_\infty'^2} \quad (8)$$

where it has been assumed that the model and actual flow densities are the same. Now, in Equation (6)  $A_0^* = U_\infty'$ , so that normalizing Equation (6) by  $U_\infty'$  yields

$$w = A_0 \zeta + A_1 \log \zeta + \frac{A_2}{\zeta} \quad (9)$$

where

$$A_0 = \frac{U_\infty'}{U_\infty}$$

and therefore the pressure coefficient is

$$C_p = A_0^2 - \left( \frac{dw}{d\zeta} \right) \left( \frac{dw}{d\zeta} \right) \quad (10)$$

Substituting Equation (9) into Equation (10) gives

$$C_p = -\frac{A_1^2}{\zeta \bar{\zeta}} - \frac{A_2^2}{(\zeta \bar{\zeta})^2} - A_0 A_1 \left( \frac{\zeta + \bar{\zeta}}{\zeta \bar{\zeta}} \right) + A_0 A_2 \left( \frac{\zeta^2 + \bar{\zeta}^2}{\zeta^2 \bar{\zeta}^2} \right)$$

This expression for the pressure coefficient is now to be written as a Fourier series in the azimuthal angle  $\theta$ . It can be done directly in this case by the substitution:

$$\zeta = re^{i\theta} \quad \bar{\zeta} = re^{-i\theta}$$

or for more complex models by the integral definitions, Equations (3, 4). After performing the substitution and equating the resulting expression term by term to the series

$$C_p(r, \theta) = \sum_{n=0}^{\infty} c_n(r) \cos n\theta$$

the following three equations result:

$$c_0(r) = - \left[ \frac{A_1^2}{r^2} + \frac{A_2^2}{r^4} \right] \quad (11)$$

$$c_1(r) = - \frac{2A_1}{r} \left[ A_0 - \frac{A_2}{r^2} \right] \quad (12)$$

$$c_2(r) = 2 \frac{A_0 A_2}{r^2} \quad (13)$$

These expressions for the coefficients,  $c_n$ , are to be set equal to experimentally determined values at a fixed value of  $r$ .

The value of  $r$  chosen for matching data is to some extent arbitrary. The circle  $r = 1$  was selected because this is the region with the highest values of  $C_p$  for which data were consistently available. Equations (11, 12, 13) then become

$$A_1^2 + A_2^2 = -c_0(1) \quad (14)$$

$$2A_1(A_0 - A_2) = -c_1(1) \quad (15)$$

$$2A_0 A_2 = c_2(1) \quad (16)$$

These may be solved as follows:

Adding Equations (14) and (15) yields

$$(A_1 - A_2)^2 + 2A_1 A_0 = -(c_0 + c_1),$$

and subtracting Equation (15) from Equation (14) yields

$$(A_1 + A_2)^2 - 2A_1 A_0 = -(c_0 - c_1)$$

Now, subtracting Equation (16) from each of these leads to

$$(A_1 - A_2)^2 + 2A_0(A_1 - A_2) + (c_0 + c_1 + c_2) = 0 \quad (17)$$

$$(A_1 + A_2)^2 - 2A_0(A_1 + A_2) + (c_0 - c_1 + c_2) = 0 \quad (18)$$

The quadratics in Equations (17, 18) may now be solved for  $(A_1 - A_2)$  and  $(A_1 + A_2)$  in terms of  $A_0$  and the coefficients,  $c_n$ . Then the resulting linear equations can be solved for  $A_1$  and  $A_2$ . The results are

$$A_1 = \pm \frac{1}{2} \left\{ \left[ A_0^2 - (c_0 - c_1 + c_2) \right]^{\frac{1}{2}} + \left[ A_0^2 - (c_0 + c_1 + c_2) \right]^{\frac{1}{2}} \right\} \quad (19)$$

$$A_2 = A_0 \pm \frac{1}{2} \left\{ \left[ A_0^2 - (c_0 - c_1 + c_2) \right]^{\frac{1}{2}} - \left[ A_0^2 - (c_0 + c_1 + c_2) \right]^{\frac{1}{2}} \right\} \quad (20)$$

Finally, substitution of (20) into (16) yields a single equation for  $A_0$  in the form

$$A_0 = \frac{c_2}{2A_0 \pm \left\{ \left[ A_0^2 - (c_0 - c_1 + c_2) \right]^{\frac{1}{2}} - \left[ A_0^2 - (c_0 + c_1 + c_2) \right]^{\frac{1}{2}} \right\}} \quad (21)$$

Equation (21) must be solved numerically for  $A_0$ , and once  $A_0$  is known,  $A_1$  and  $A_2$  can be determined by substituting into Equations (19, 20). As the equations indicate, it is possible in principle to have more than one solution. This is not surprising as it is caused by the fact that in matching pressures, a nonlinearity is introduced through the use of Bernoulli's equation. For a specific case, however, there has been no difficulty in choosing the solution which is physically significant.

For a velocity ratio ( $U_\infty/U_j$ ) = 0.4, the coefficients  $c_n$  calculated from Vogler's data have the following values:\*

$$c_0(1) = -0.619 \quad (22)$$

$$c_1(1) = -0.843 \quad (23)$$

$$c_2(1) = 0.287 \quad (24)$$

A graphical solution of Equation (21) is shown in Figure 19. With the numerical values given in Equations (22, 23, 24), the left hand side (L. H. S.), the right-hand side for positive sign (R. H. S. +), and right-hand side for negative sign (R. H. S. -) of Equation (21) are shown in Figure 19. This figure contains the restriction that  $A_0$  be real, and also that it be positive, so that actual and model free stream velocities will be in the same direction. Evidently, only one solution is possible, and it lies in the neighborhood enclosed by the circle labeled "solution" in the figure. Further iterations in this neighborhood yield the value

$$A_0 = 0.745, \quad (25)$$

and substitution in Equations (19, 20) (using the + sign) then gives

$$A_1 = 0.762 \quad (26)$$

$$A_2 = 0.192 \quad (27)$$

These results indicate that the model free stream velocity amounts to approximately 3/4 of the actual velocity, so that the model stagnation pressure is smaller than that in the actual stream. Furthermore, since  $A_1$  is positive, the source is indeed a source, and not a sink. It is possible to show that the radial velocity at  $r = 1/2$ , (which corresponds to the rim of the jet), is positive. This is contrary to what would be expected physically since the jet entrains free stream air and the net effect should be that of a mass sink.

The real test of the model is the agreement with data at values of  $r$  other than unity. Comparisons of pressures predicted by the model with data for seven rays ( $\theta = \text{const.}$ ) are shown in Figures 20 through 26. Examination of these figures shows disagreement around the

---

\*It has been mentioned in Section 2 that due to difficulties with Vogler's data at large distances from the orifice, this data has in some cases been adjusted so that  $C_p$  will decay to zero. This adjustment has not been made for the data used with the phenomenological models.

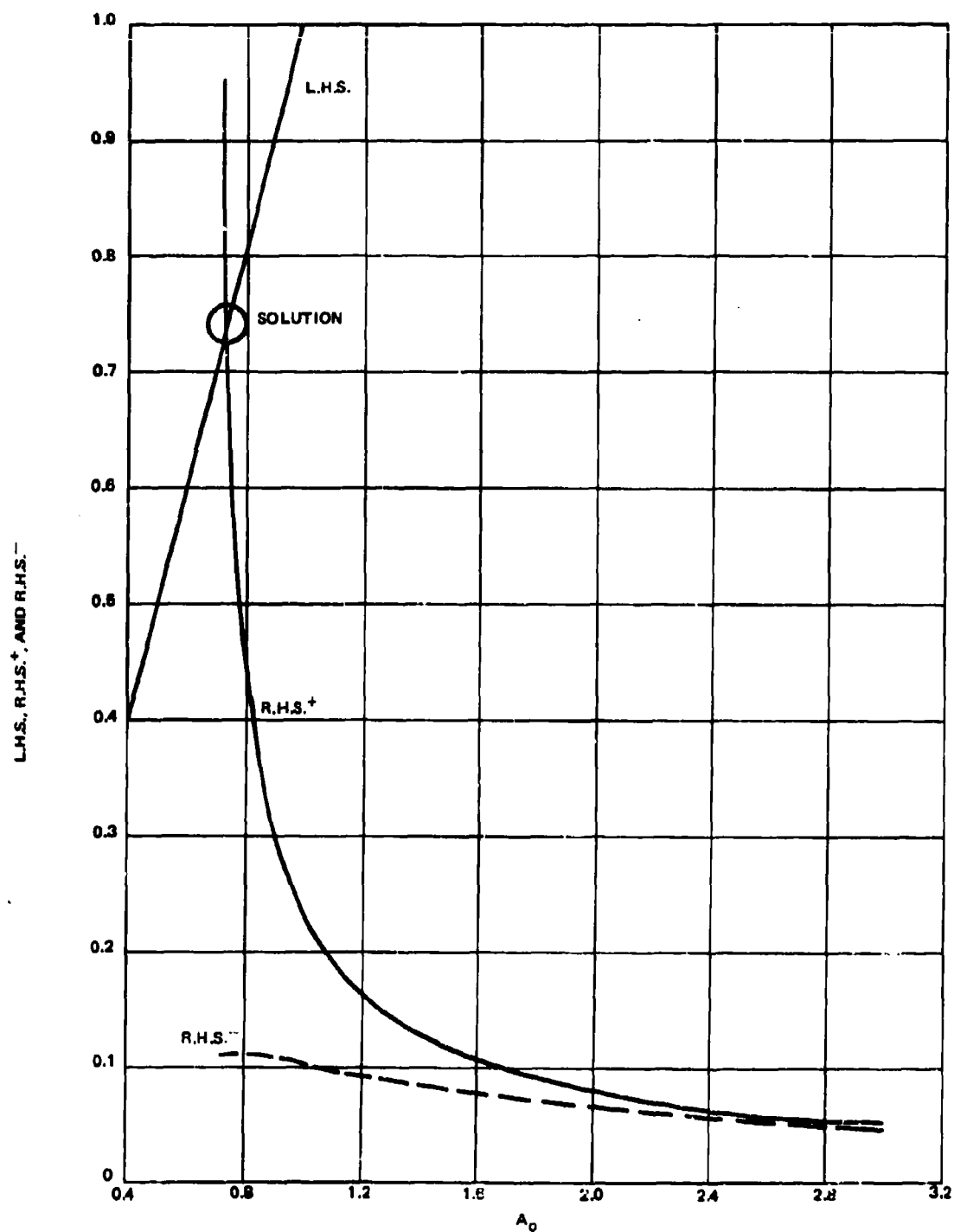


Figure 19. Diagram for Solution of Equation (21),  $U_\infty/U_i = 0.4$

upstream and downstream rays and good agreement only near the ray  $\theta = \pi/2$ . The accuracy of other results obtained from this model at different velocity ratios are similar to those described above. Thus, it can be concluded that this choice of singularities will not yield very accurate pressure distributions. Also, the velocities obtained do not behave in the way which would be expected physically.

### 3. 2. 2 Vortex Model

The second phenomenological model studied consists of a free stream, a source or sink, a doublet, and, in addition, two vortices of equal strength but opposite sign located symmetrically in the leeward quadrants. The latter are included to represent the vortex motion that is known to exist in the flow. The location of the singularities is shown in Figure 27.

In this case, model and free stream velocities are left equal since two additional unknowns are introduced by the vortex locations. Normalizing coordinates by the nozzle diameter  $d_j$ , and velocities by the free stream value  $U_\infty$ , the complex potential for the flow is

$$w(\zeta) = \zeta + A_1 \log \zeta + \frac{A_2}{\zeta} + iA_3 \log \left[ \frac{\zeta - \zeta_0}{\zeta - \bar{\zeta}_0} \right] \quad (28)$$

where  $\zeta_0$ ,  $\bar{\zeta}_0$  are the complex vortex position vector and its conjugate

$$\zeta_0 = r_0 e^{i\theta_0} \quad \bar{\zeta}_0 = r_0 e^{-i\theta_0}$$

The pressure coefficient is in this case given by

$$C_p = 1 - \left( \frac{dw}{d\zeta} \right) \left( \frac{d\bar{w}}{d\bar{\zeta}} \right) \quad (29)$$

Differentiating (28), taking its complex conjugate, and substituting in (29) gives the result

$$\begin{aligned} -C_p = & -A_2 \left[ \frac{1}{\zeta^2} + \frac{1}{\bar{\zeta}^2} \right] + \left[ A_1 \left( 1 - \frac{A_2}{\zeta \bar{\zeta}} \right) \right] \left[ \frac{1}{\zeta} + \frac{1}{\bar{\zeta}} \right] + \left[ \frac{A_1^2}{\zeta \bar{\zeta}} + \frac{A_2^2}{\zeta^2 \bar{\zeta}^2} \right] \\ & + iA_3 (\zeta_0 - \bar{\zeta}_0) \left\{ \frac{\bar{\zeta}^2 + A_1 \bar{\zeta} - A_2}{\bar{\zeta}^2 (\zeta - \zeta_0) (\zeta - \bar{\zeta}_0)} + \frac{\zeta^2 + A_1 \zeta - A_2}{\zeta^2 (\bar{\zeta} - \zeta_0) (\bar{\zeta} - \bar{\zeta}_0)} \right\} \\ & - A_3^2 \frac{(\zeta_0 - \bar{\zeta}_0)^2}{\zeta_0 \bar{\zeta}_0} \left\{ \frac{\zeta^2}{(\zeta - \zeta_0) (\zeta - \bar{\zeta}_0) \left( \zeta - \frac{r^2}{\zeta_0} \right) \left( \zeta - \frac{r^2}{\bar{\zeta}_0} \right)} \right\} \quad (30) \end{aligned}$$



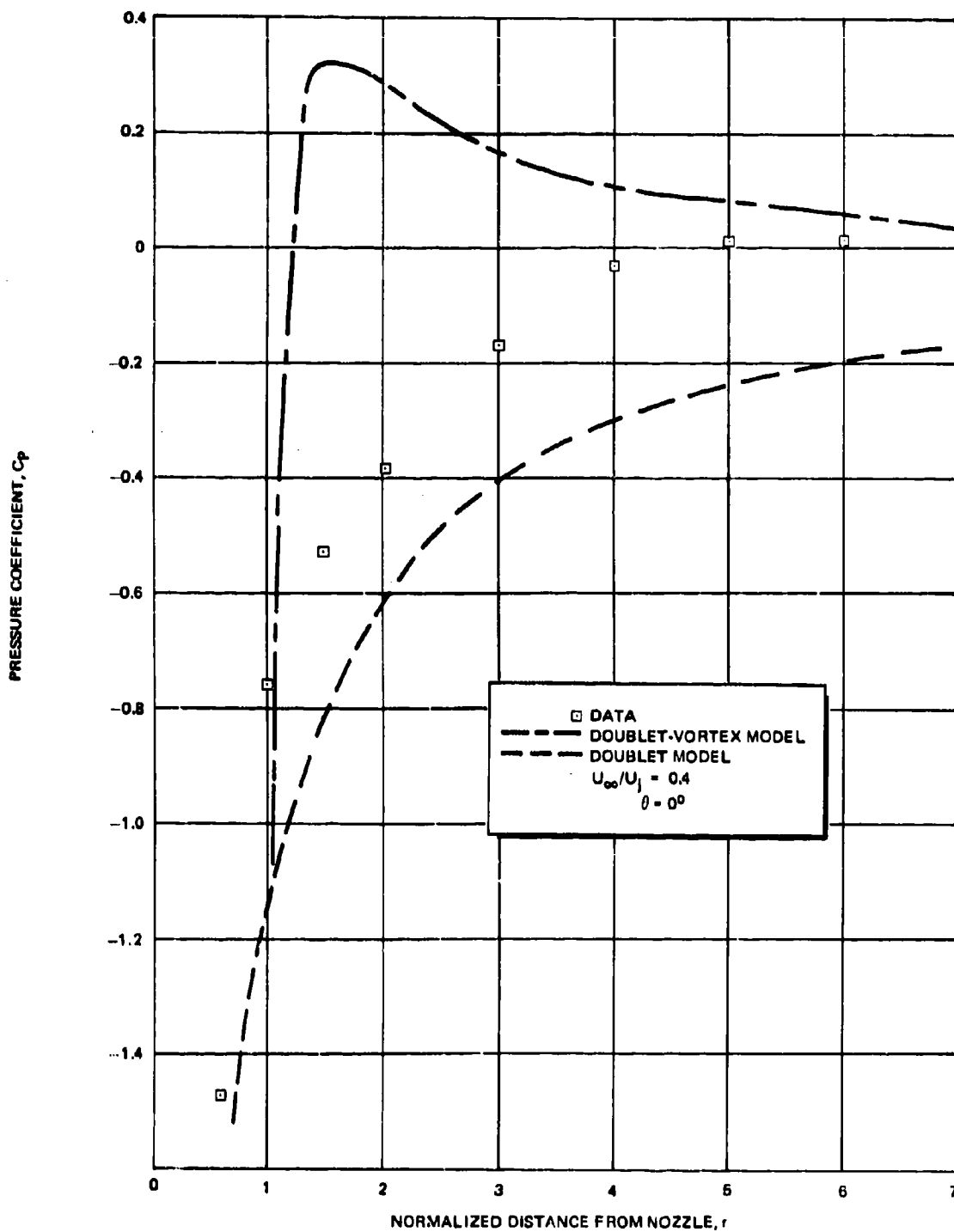


Figure 20. Results of Doublet-Vortex and Doublet Model Compared With Data ( $\theta = 0^\circ$ )

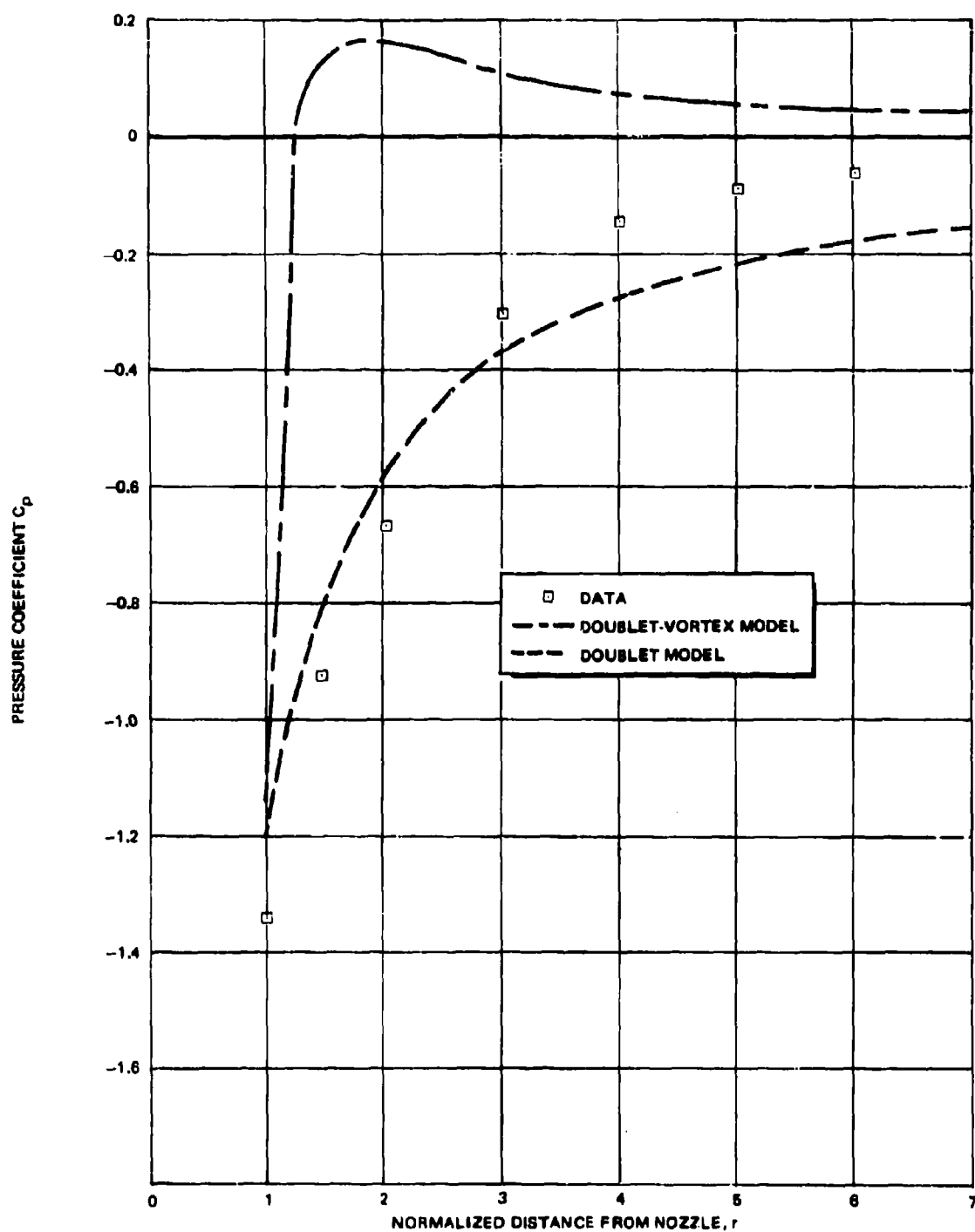


Figure 21. Results of Doublet-Vortex and Doublet Models Compared with Data ( $\theta = 30^\circ$ )

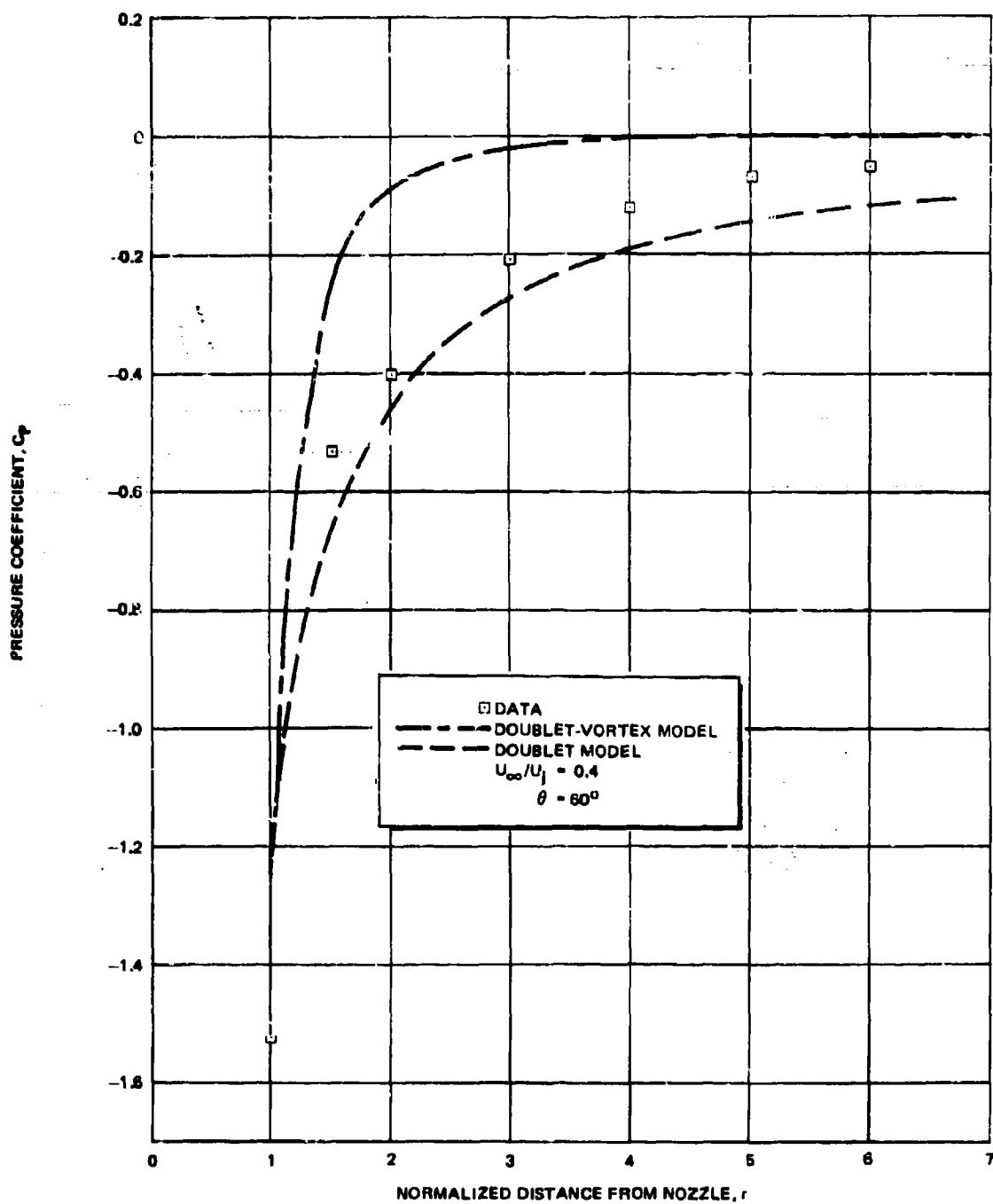


Figure 22. Results of Doublet-Vortex and Doublet Model Compared With Data ( $\theta = 60^\circ$ )

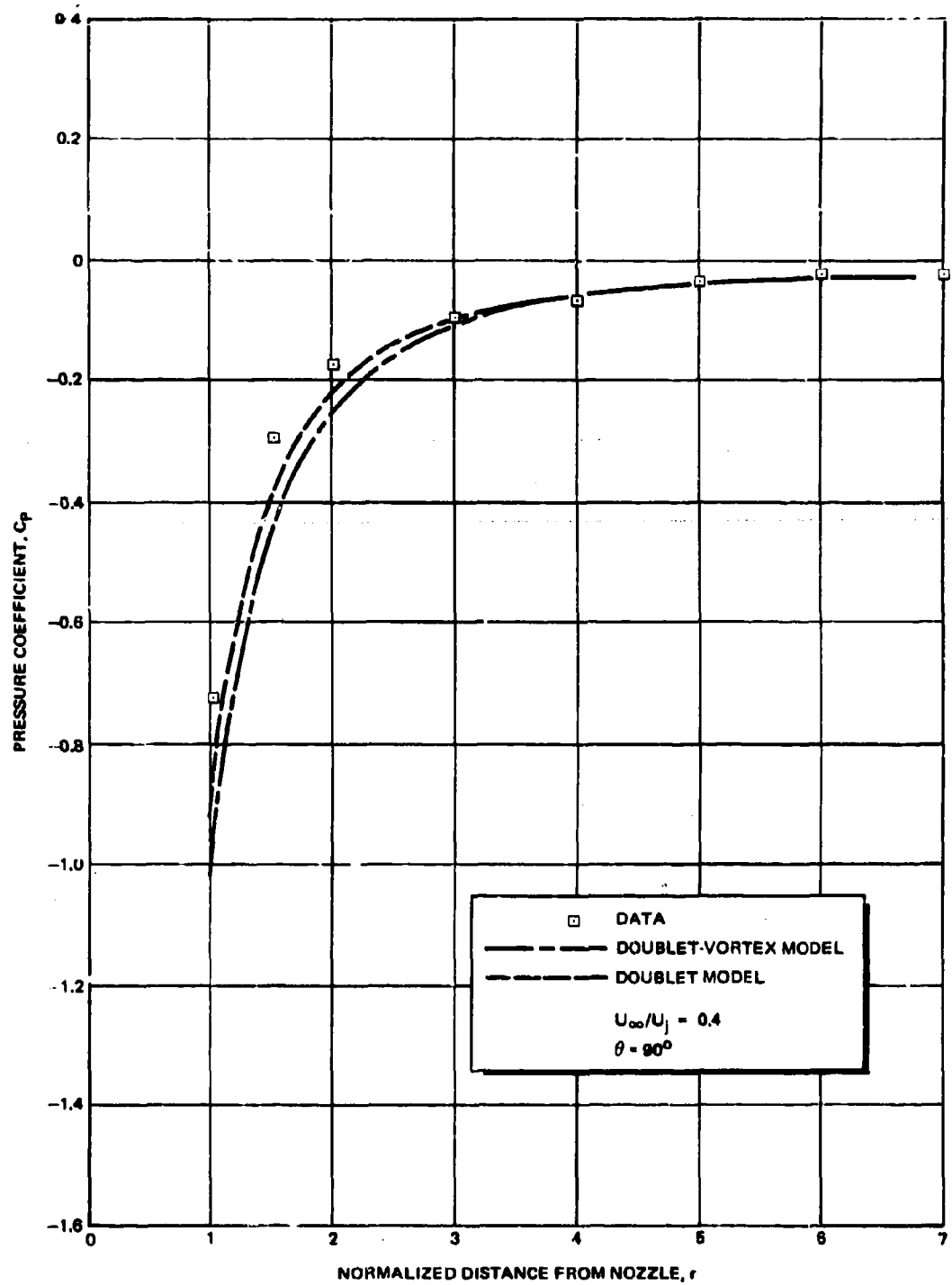


Figure 23. Results of Doublet-Vortex and Doublet Model Compared With Data ( $\theta = 90^\circ$ )

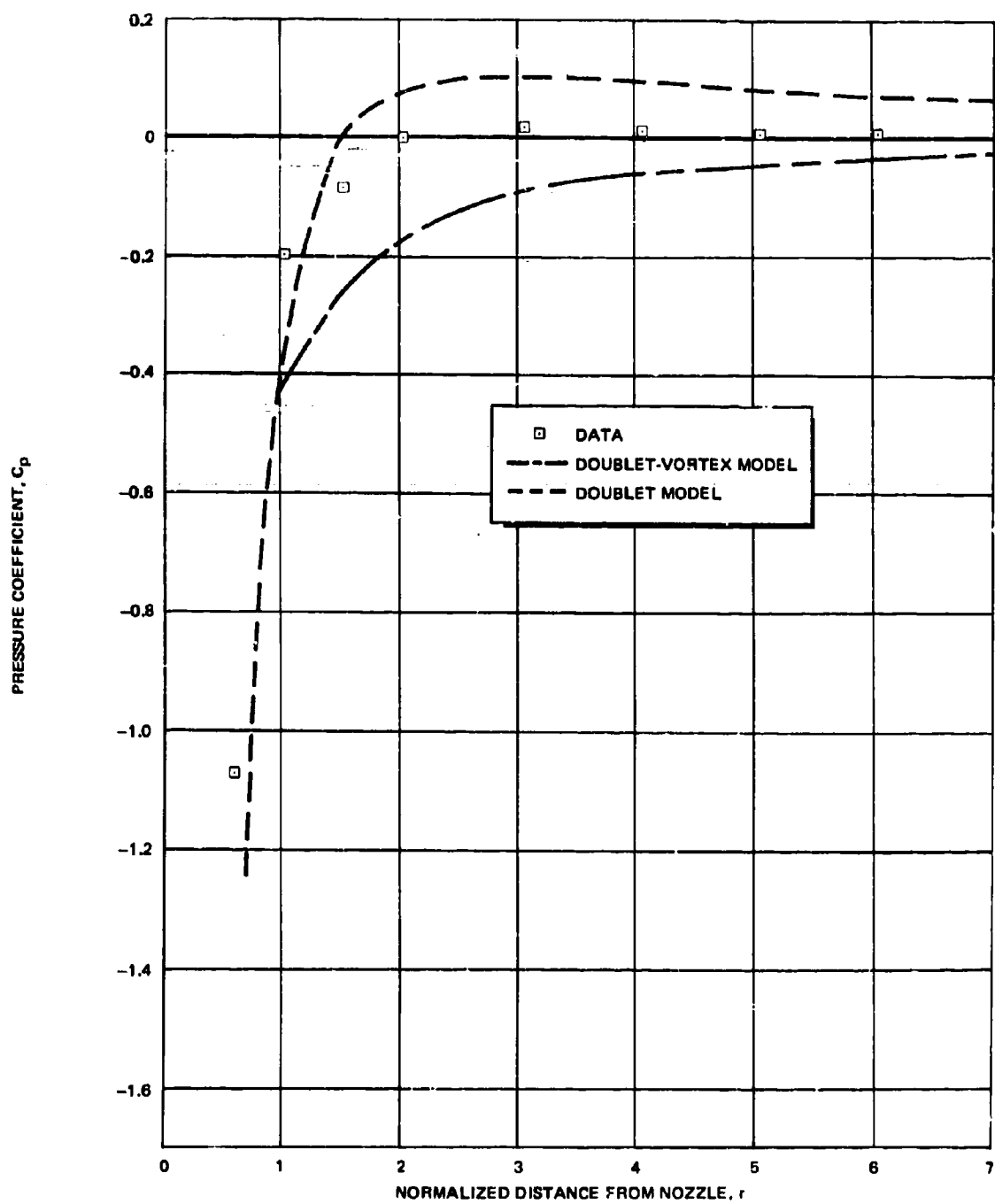


Figure 24. Results of Doublet-Vortex and Doublet Models Compared With Data ( $\theta = 120^\circ$ )

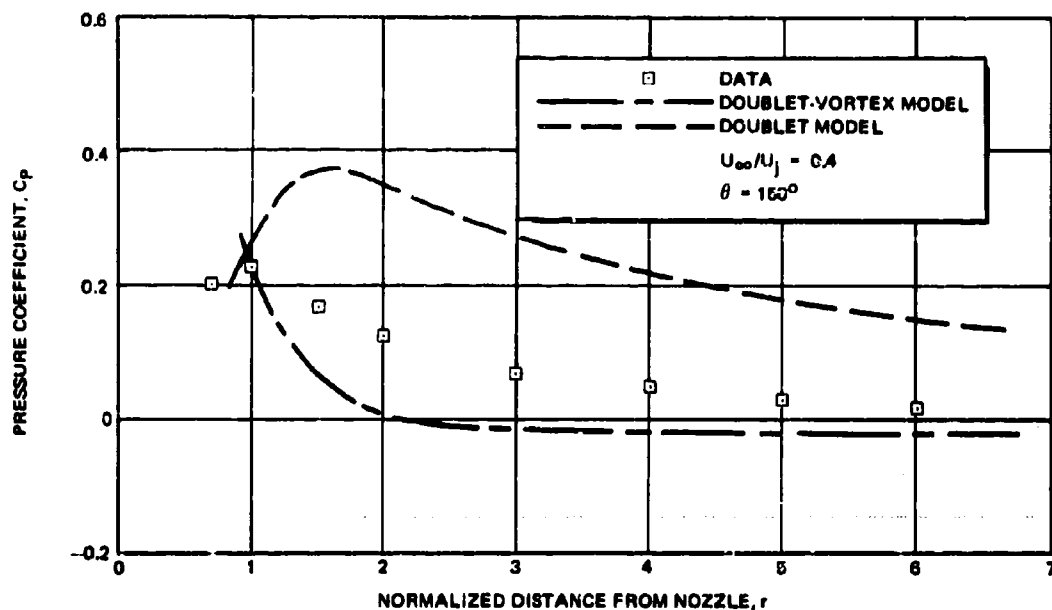


Figure 25. Results of Doublet-Vortex and Doublet Model Compared With Data ( $\theta = 150^\circ$ )

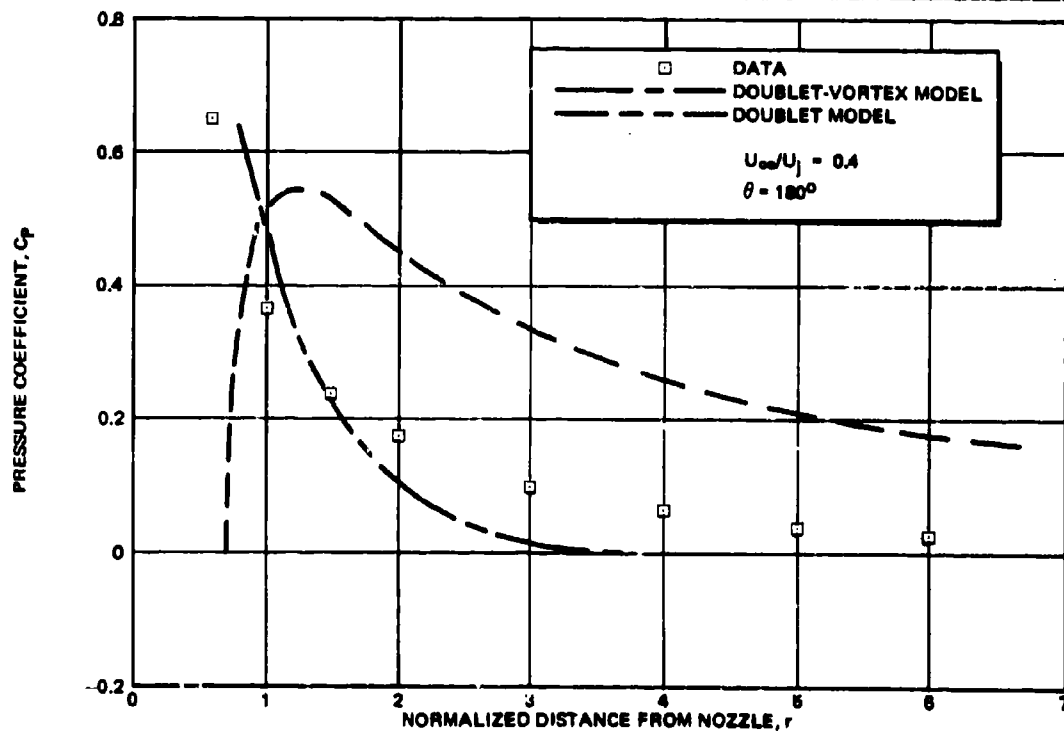


Figure 26. Results of Doublet-Vortex and Doublet Model Compared With Data ( $\theta = 180^\circ$ )

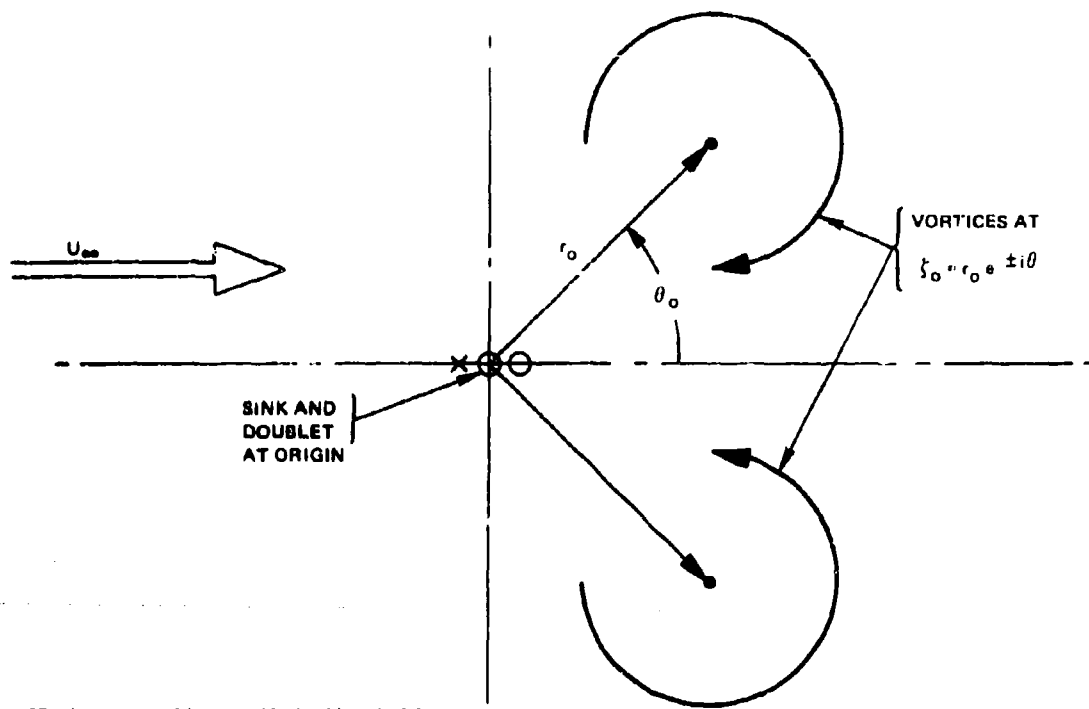


Figure 27. Location of Vortex Model Singularities

This expression contains the five unknowns,  $A_1$ ,  $A_2$ ,  $A_3$ ,  $r_0$ , and  $\theta_0$ . These unknowns can be determined in several ways. One would be to express the pressure coefficient as a five-term cosine series in  $\theta$  and equate the coefficients to a five-term series for the data. Another way would be to use a three-term series and equate the coefficients at two values of  $r$  (i. e., equate three coefficients at one  $r$  and two at another). A third option is to use physical considerations to provide two equations, and match a three-term series to determine the other three. This third option was taken as being more compatible with the physical reasoning which motivated selection of the model. The physical consideration used is that the vortices should remain stationary in the  $x, y$  plane, and consequently that the vector sum of the velocities induced at the location of a vortex by all other singularities be zero. For instance, removing the vortex at  $\zeta_0$  from the complex potential in Equation (28) and differentiating the result yields, at  $\zeta = \zeta_0$ ,

$$\left(\frac{dw'}{d\zeta}\right)_{\zeta_0} = 1 + \frac{A_1}{\zeta_0} - \frac{A_2}{\zeta_0^2} - \frac{iA_3}{(\zeta_0 - \zeta_0)}$$

Equating real and imaginary parts of this expression to zero yields two relations between the five unknowns, which may be written in the following form

$$\frac{\cos \theta_o}{r_o} = \frac{A_1}{2A_2} \quad (31)$$

$$\tan^3 \theta_o - \left(\frac{A_3}{A_1}\right) \tan^2 \theta_o + \left[\frac{4A_2}{A_1^2} + 1\right] \tan \theta_o - \left(\frac{A_3}{A_1}\right) = 0 \quad (32)$$

The next step is to write Equation (30) as a Fourier series in  $\theta$ . Due to the presence of singularities which are not at the origin, the Fourier series will in this case have an infinite number of terms, instead of terminating as it did for the doublet model. Of these terms, only the first three are matched to experimental values of the pressure coefficient at  $r = 1$ . This procedure leads to three nonlinear equations which are to be solved simultaneously with Equations (31) and (32) for the five unknowns  $A_1$ ,  $A_2$ ,  $A_3$ ,  $r_o$ , and  $\theta_o$ .

The derivation of the Fourier series for Equation (30) and the solution of the set of five nonlinear algebraic equations are quite complicated, as described in Appendix B. There are a great number of possible solutions, but one is again chosen on physical grounds. Calculations were carried out using the coefficients,  $c_n$ , obtained from Vogler's data at  $(U_\infty/U_1) = 0.4$  (as for the doublet model, the data was not adjusted). The numerical results obtained for this case are only approximate, and further iterations would have been necessary to obtain more exact numbers. Nevertheless, it was felt that they were sufficiently accurate for purposes of comparing the model to data in order to determine its validity. The numerical values found are listed below:

$$A_1 = -0.121 \quad (33)$$

$$A_2 = -0.048 \quad (34)$$

$$A_3 = 0.668 \quad (35)$$

$$r_o = 0.64 \quad (36)$$

$$\theta_o = 36.3^\circ \quad (37)$$

Note that in this case  $A_1$  is negative so that the second term in Equation (28) corresponds to a sink. The doublet is also negative, so that it pulls in fluid from the upstream side.  $A_3$  is positive, and the vortices have the sense of rotation shown in the sketch above. This agrees with the sense of rotation of the vortices which have been observed experimentally.



The values of pressure coefficient determined from the three-term Fourier series representation of Equation (30), using the numerical values listed in Equations (33)-(37), are compared to data in Figures 20-26. Evidently, the agreement is not good. For much of the  $\theta$  range, the agreement is worse than for the simpler doublet model. Thus, even though the singularities representing the jet have approximately the correct behavior expected on physical grounds, the predicted pressures are not realistic.

The failure of the vortex model along the leeward ray is especially significant, because it points to a fundamental difficulty of all inviscid models which attempt to simulate the observed velocities near the plate surface, including three-dimensional models. It is known from experiment (Reference 21), that immediately behind the jet the fluid velocity is inward toward the orifice. The presence of vortices in the vortex model was supposed to account for this fact. Because of symmetry and the condition of no flow through the plate, the velocity vector in the plane of the plate, along the  $x$  axis, must be aligned with the  $x$  axis (see Figure 10). Consequently, if far downstream perturbations are to decay and the velocity along the  $x$  axis is to become equal to  $U_\infty$ , the flow must reverse direction and have a stagnation point. If no account is taken of viscous dissipation, the pressure at this stagnation point will be equal to the free stream stagnation pressure, and the pressure coefficient will be unity. This difficulty will be encountered with any inviscid model that attempts to represent the inward velocity observed experimentally, no matter how complicated. As a matter of fact, the failure of the doublet model to approximate the experimental velocities on the surface may be traced to the same sources. As the doublet model was originally envisioned, the blockage of the jet would be accounted for by the doublet, and the entrainment by the sink. As it turned out, the negative pressure coefficient on the leeward side of the jet so influenced the sink strength that the sink became a source.

### 3.3 PRESSURE MODELS

Since the general shape of the interference pressure on a flat plate is known, model flows are constructed which will yield, approximately, this pressure distribution. At this point, free parameters are adjusted to obtain best agreement with data. No attempt is made to qualitatively reproduce the velocities observed on the surface. With this viewpoint, it is clear that the results obtained from the model should have a high pressure region on the windward side of the jet and a low pressure region on the leeward side. These both asymptotically decay to free stream pressure at infinity. To avoid the difficulties encountered with inviscid models in the previous section, the velocity induced by whatever represents the jet must be in the same direction as the free stream on the leeward side.

The simplest model that will meet these criteria is a source in a free stream. Two models of this type have been developed. The first uses the same assumption of two dimensional flow in the  $x, y$  plane (Figure 10) and consists of a two-dimensional source and a free stream, adjusted by the same methods employed for the phenomenological

models. It is referred to as the "source model." The second model is fully three dimensional, and it consists of a free stream superimposed on axisymmetric flow through an orifice. It is referred to as the "orifice model."

### 3.3.1 Source Model

The source model is derived from the potential for a two dimensional source in a uniform stream. This model is similar to the doublet model discussed in Section 3.2.1. It is simpler than the doublet model, but it yields pressures which agree better with data than those calculated from the doublet model. The complex potential for a source in a uniform stream is simply

$$w = A_0 \zeta + A_1 \log \zeta \quad (38)$$

As in Section 3.2.1, the model and actual flows are here assumed to have different stagnation pressure and free stream velocities. The above potential has again been normalized by the actual free stream velocity and by the nozzle diameter. Using Equations (10) and (38), the pressure coefficient can be written in real variables in the form

$$C_p = -\frac{A_1^2}{r^2} - 2A_0 A_1 \frac{\cos \theta}{r} \quad (39)$$

Note that in this case the Fourier series contains only two terms. As before,  $A_0$  and  $A_1$  are calculated by equating (39) term by term to a two-term Fourier series representation of the data at  $r = 1$ . For this case, however, the data of Reference 32 has been adjusted at each value of  $\theta$  so that  $C_p$  will be zero at  $r = 10$ . For  $U_\infty/U_j = 0.4$ , the first two Fourier coefficients thus obtained are:

$$-A_1^2 = c_0(1) = -0.725$$

$$-2A_0 A_1 = c_1(1) = -0.823$$

These yield:

$$A_0 = 0.483$$

$$A_1 = 0.851$$

Comparison of this model with experimental data is shown on Figures 28-34. As before, these are plots of the pressure coefficient as a function of the radial distance from the center of the nozzle for several values of  $\theta$ . As can be seen, this model gives quite good agreement in the vicinity of  $\theta = 90^\circ$ . The agreement near  $\theta = 0^\circ$  or

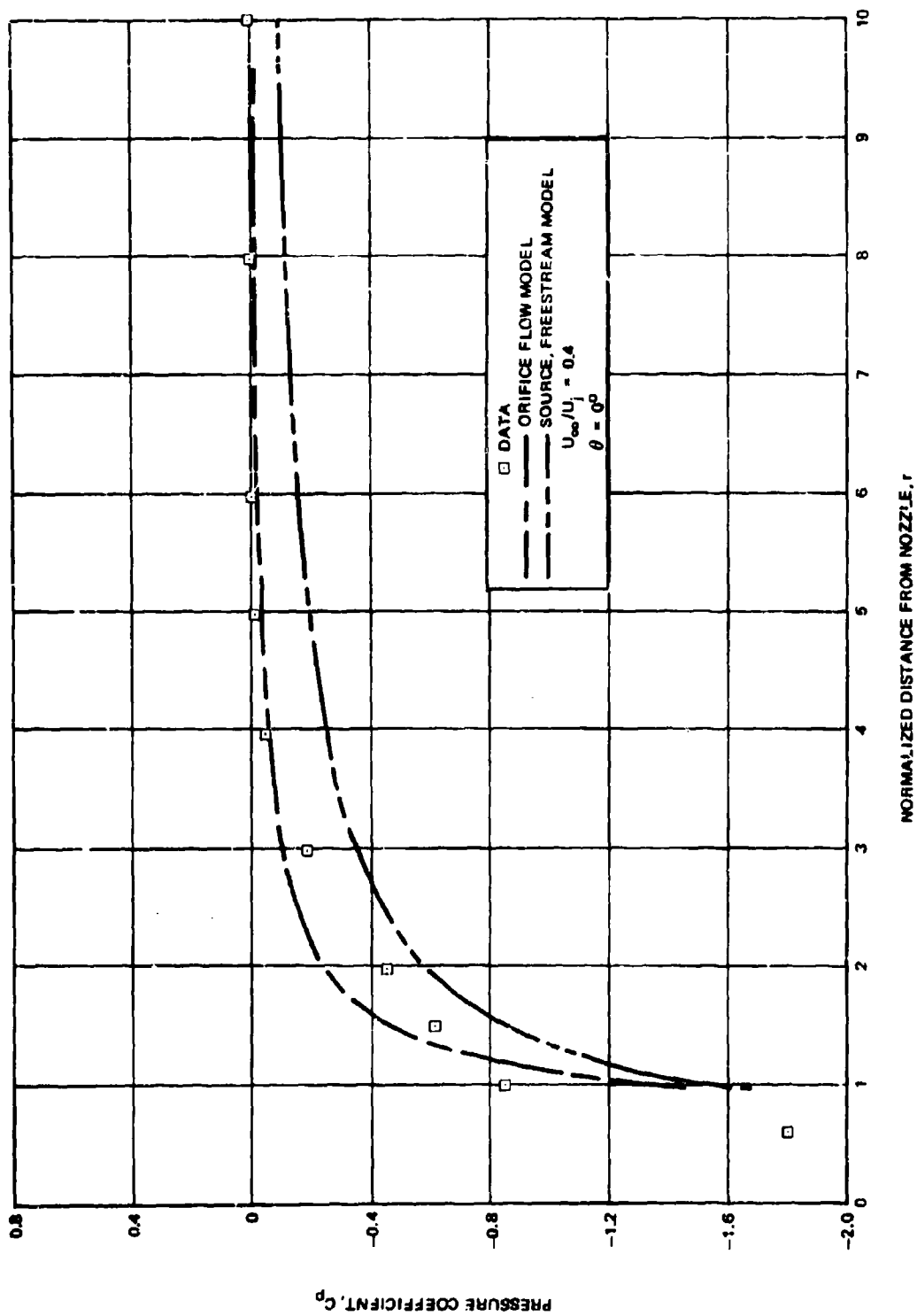


Figure 28. Results of Source and Orifice Models Compared With Data ( $\theta = 0^\circ$ )

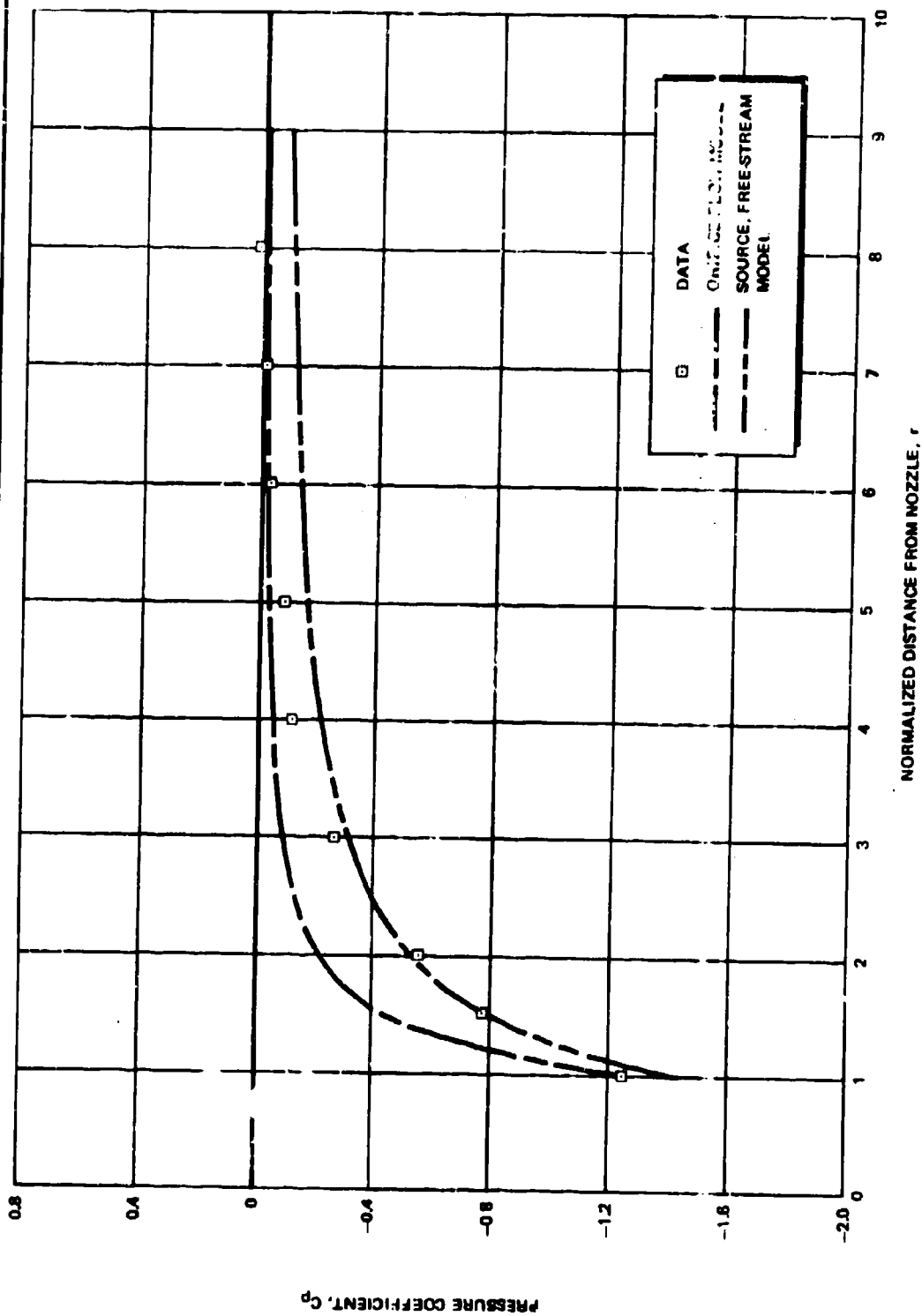


Figure 29. Results of Source and Orifice Models Compared With Data ( $\theta = 30^\circ$ )

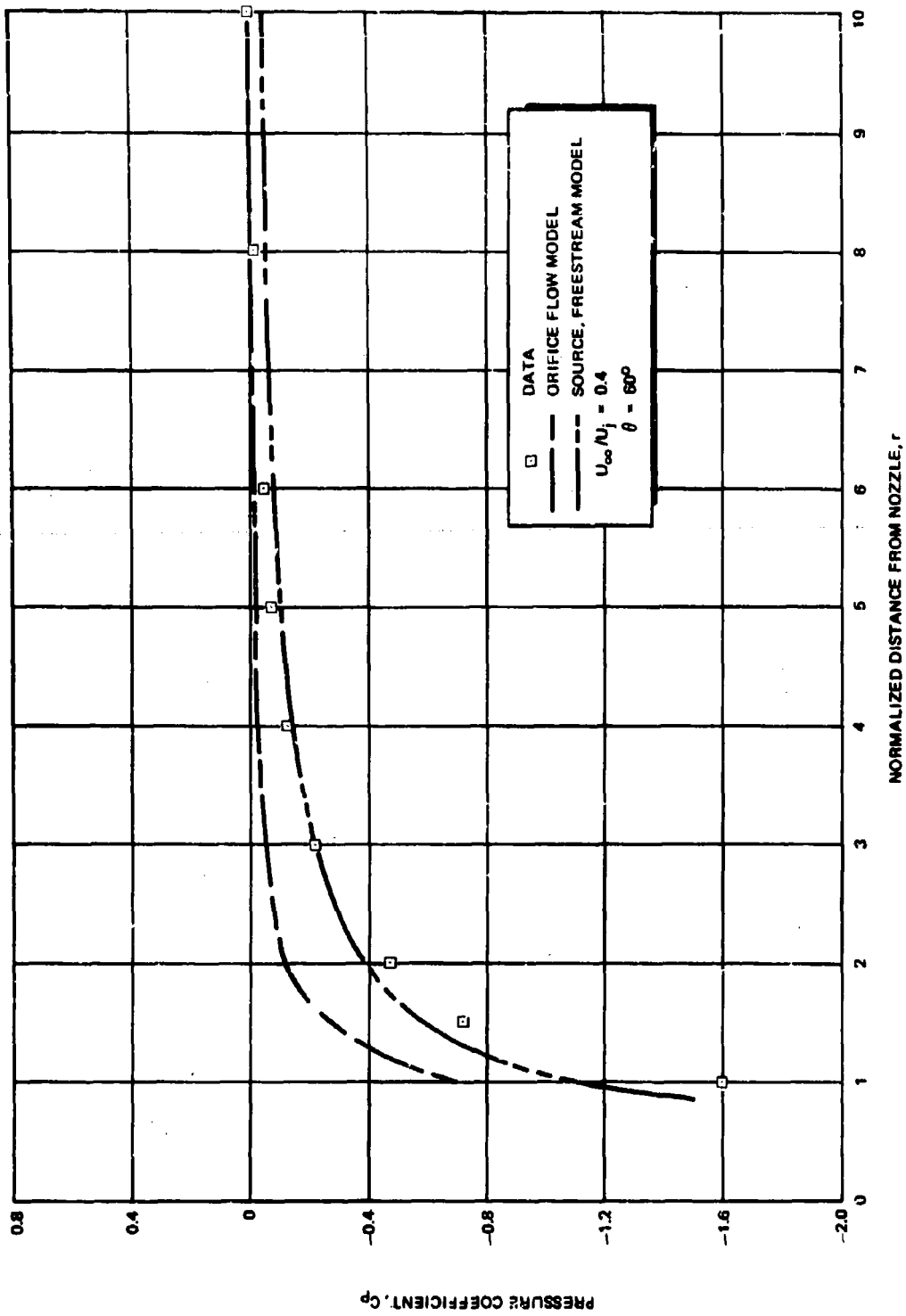


Figure 30. Results of Source and Orifice Models Compared With Data ( $\theta = 60^\circ$ )

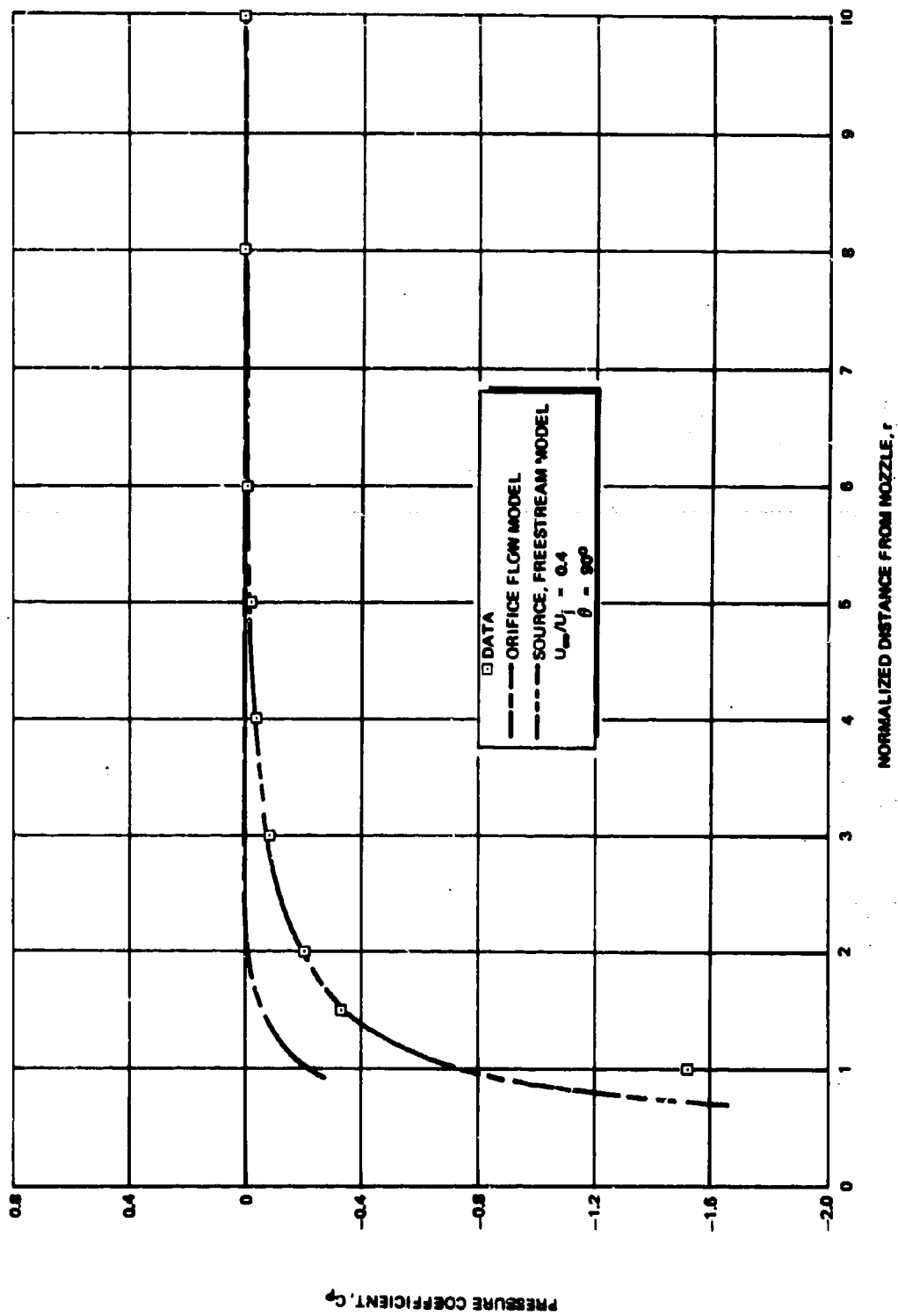


Figure 31. Results of Source and Orifice Models Compared With Data ( $\theta = 90^\circ$ )

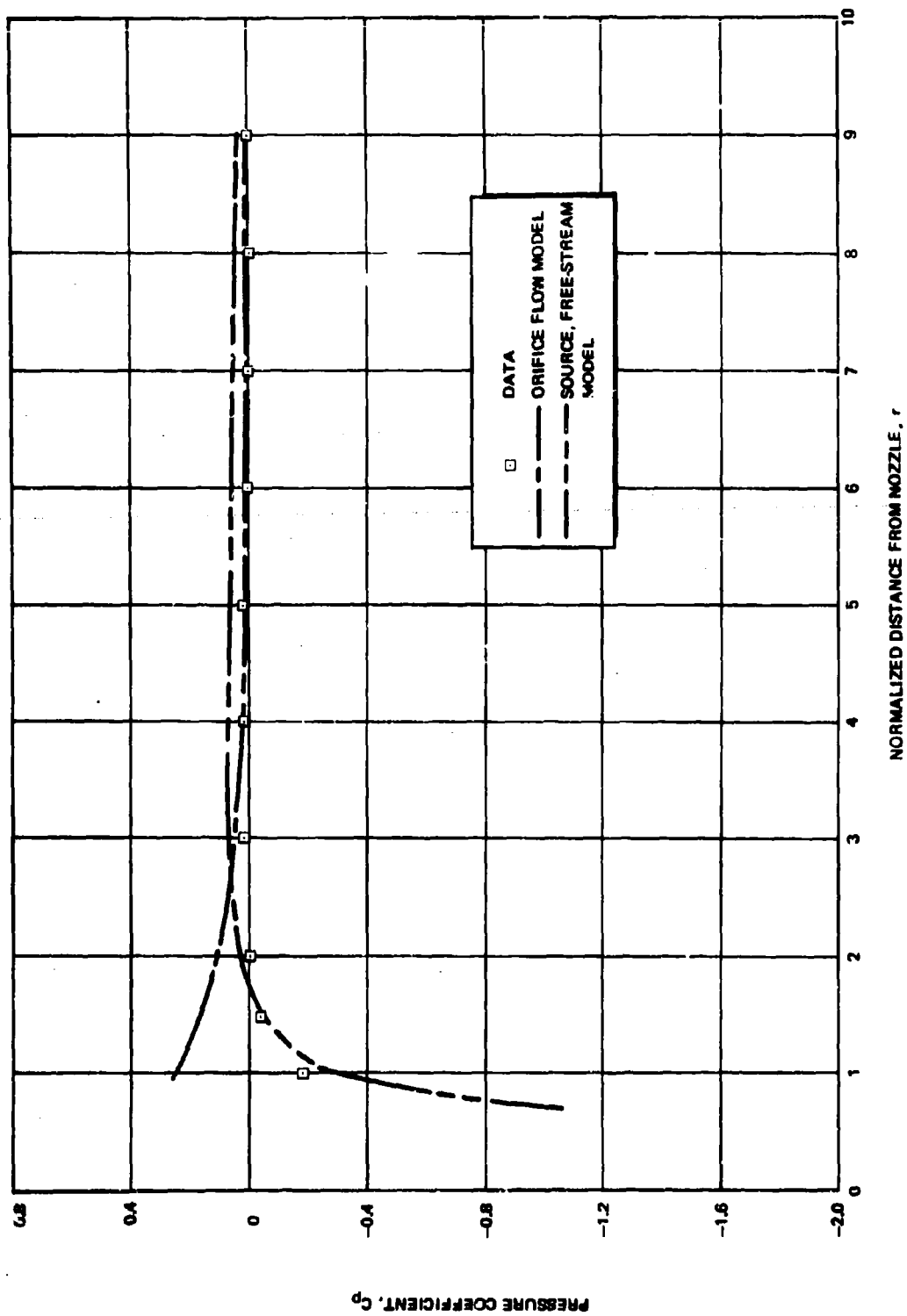


Figure 32. Results of Source and Orifice Models Compared With Data ( $\theta = 120^\circ$ )

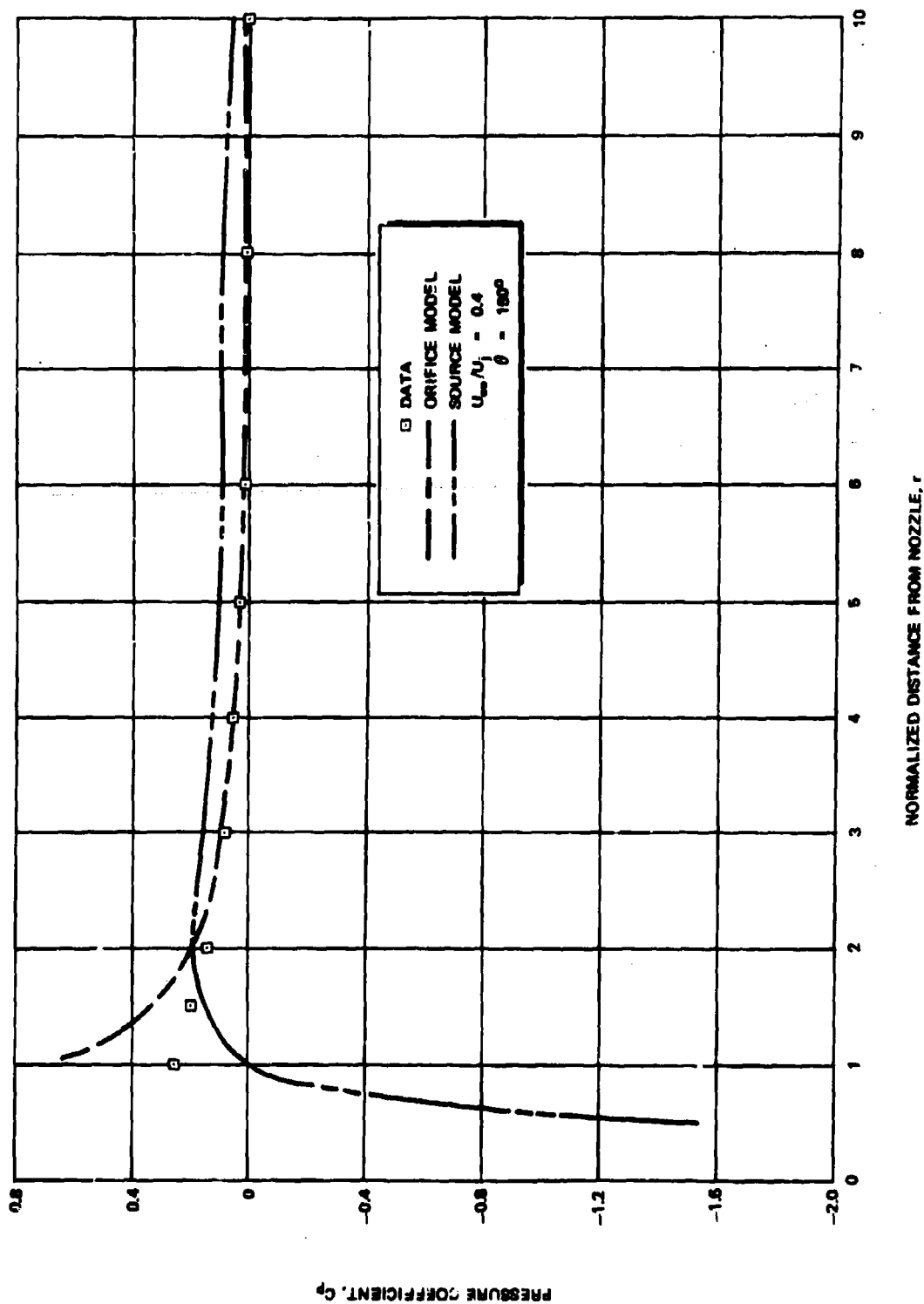


Figure 33. Results of Source and Orifice Models Compared With Data ( $\theta = 150^\circ$ )



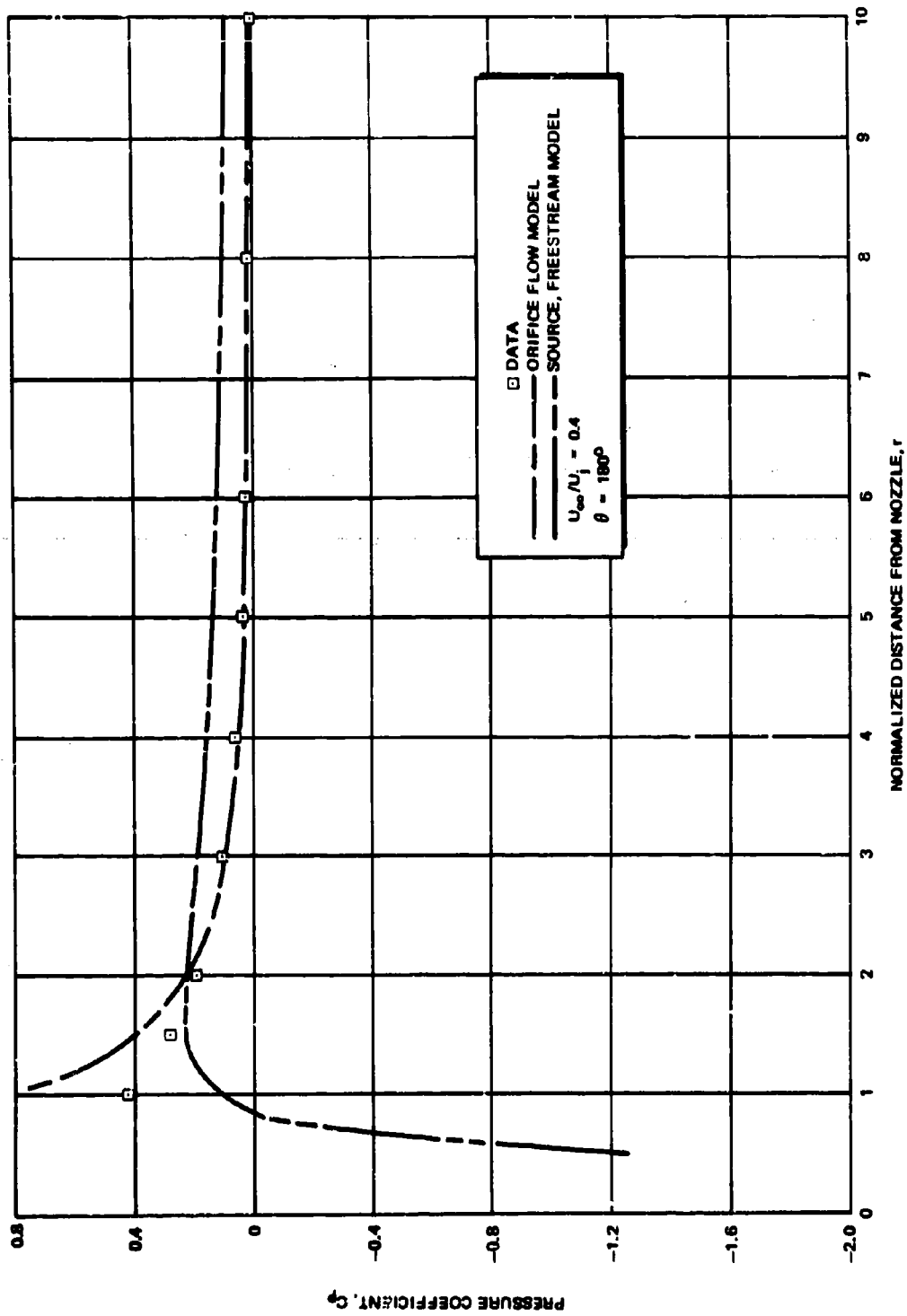


Figure 34. Results of Source and Orifice Models Compared With Data ( $\theta = 180^\circ$ )

$\theta = 180^\circ$  is not as good, but it is better than that obtained with the doublet model. The curves are typical of results obtained for other velocity ratios. Curves of the values of  $A_0$  and  $A_1$  as functions of the velocity ratio are shown in Figure 35.

### 3.3.2 Orifice Model

The orifice model consists of the three-dimensional potential flow derived by superimposing a transverse, uniform flow on axisymmetric flow through an orifice. First the velocity potential for flow through a circular orifice is derived. Then the components of the velocity in the plane of the orifice are determined. A uniform stream normal to the orifice axis of symmetry is then superimposed on the orifice flow by adding velocity components. Bernoulli's equation is then employed to calculate pressure distributions in the plane of the orifice.

A derivation of the potential for flow through an orifice is described by Lamb in Reference 37. The derivation of the orifice flow model follows basically from Lamb's solution. The coordinate system of interest is given by

$$\bar{z} = k \cos \xi \sinh \eta \quad (40)$$

$$\bar{r} = k \sin \xi \cosh \eta \quad (41)$$

where the variables  $\bar{z}$  and  $\bar{r}$  correspond to dimensional coordinates as defined in Figure 10. The constant  $k$  is an as yet unspecified scale length. Squaring and combining Equations (40), (41) yields

$$\frac{\bar{r}^2}{k^2 \sin^2 \xi} - \frac{\bar{z}^2}{k^2 \cos^2 \xi} = 1 \quad (42)$$

Equation (42) represents a family of hyperboloids of revolution (since it is independent of  $\theta$ ). The hyperboloids have foci on the circle  $\bar{r} = k$ ,  $\bar{z} = 0$ . The variable  $\xi$  is a parameter that varies from hyperboloid to hyperboloid. The value  $\xi = 0$  corresponds to the line  $\bar{r} = 0$ . The value  $\xi = \pi/2$  corresponds to the plane  $\bar{z} = 0$  with the circular region  $\bar{r} < k$  removed. Values of  $\xi$  between 0 and  $\pi/2$  correspond to hyperboloids between these two limiting cases. Negative values of  $\xi$  are not considered since  $\bar{r}$  is always positive. Combining Equations (40) and (41) in a different manner yields

$$\frac{\bar{r}^2}{k^2 \cosh^2 \eta} + \frac{\bar{z}^2}{k^2 \sinh^2 \eta} = 1 \quad (43)$$

so that lines  $\eta = \text{constant}$  correspond to confocal ellipsoids of revolution with foci on the circle  $\bar{r} = k$ . The coordinates are shown in Figure 36. From this figure it can be seen that a solution of Laplace's Equation in the  $(\xi, \eta)$  system in which lines  $\xi = \text{constant}$  correspond to the streamlines will transform under Equations (40) and (41) to the flow out

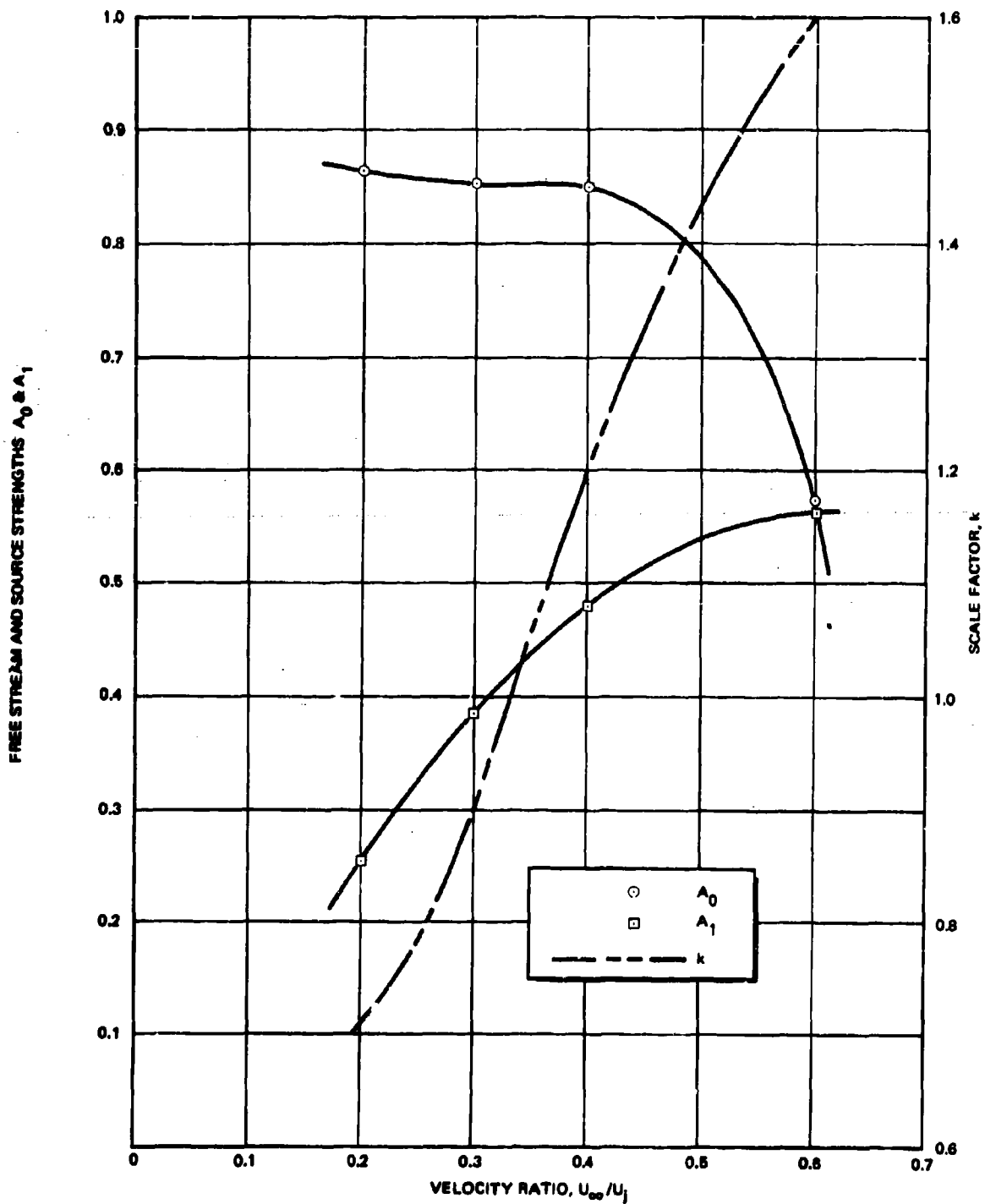


Figure 35.  $A_0$ ,  $A_1$ , and  $k$  as Functions of the Velocity Ratio

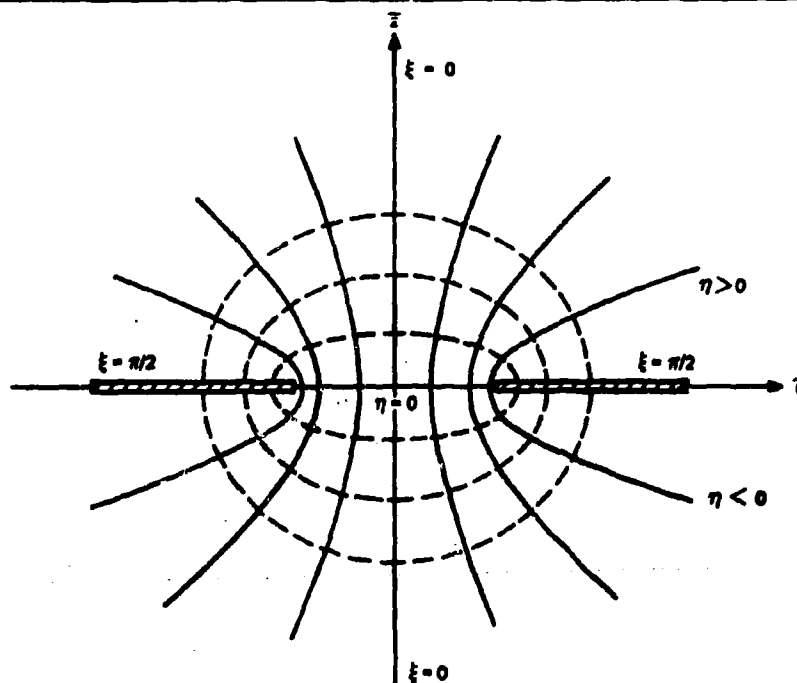


Figure 36. Streamlines and Equipotential Lines for Flow Through an Orifice

of (or into) an orifice. In terms of  $(\xi, \eta)$  coordinates, the equation of continuity becomes:

$$\frac{\partial}{\partial \mu} \left\{ (1 - \mu^2) \frac{\partial \Phi}{\partial \mu} \right\} + \frac{\partial}{\partial \nu} \left\{ (1 + \nu^2) \frac{\partial \Phi}{\partial \nu} \right\} = 0 \quad (44)$$

where:

$$\mu = \cos \xi$$

$$\nu = \sinh \eta$$

$$\Phi = \text{velocity potential}$$

Any dependence on  $\theta$  drops out since the flow is axisymmetric about the  $\bar{z}$ -axis. Since the coordinate system is orthogonal, and so are the streamlines and equipotential lines, it follows that if  $\xi = \text{constant}$  is to be a streamline, then  $\eta = \text{const}$  should correspond to an equipotential line. Therefore  $\Phi$  must be only a function of  $\eta$ --and consequently only a function of  $\nu$ . With  $\Phi$  a function of  $\nu$  only, Equation (44) may be integrated once to yield:

$$(1 + \nu^2) \frac{d\Phi}{d\nu} = \text{const.} = -A \quad (45)$$

which can be integrated again to yield:

$$\Phi = A \cot^{-1} \nu \quad (46)$$

The orifice flow velocity components parallel to the plane of the orifice are given by

$$\bar{v}_z = - \frac{\partial \Phi}{\partial z}$$

and

$$\bar{v}_r = - \frac{\partial \Phi}{\partial r}$$

Equations (40), (41), (46) are combined with these equations to yield the velocity components

$$\bar{v}_r = \frac{(A/k) \sin \xi \tanh \eta}{\sin^2 \xi \sinh^2 \eta + \cos^2 \xi \cosh^2 \eta} \quad (47)$$

and

$$\bar{v}_z = \frac{(A/k) \cos \xi}{\sin^2 \xi \sinh^2 \eta + \cos^2 \xi \cosh^2 \eta} \quad (48)$$

It may be shown that these velocities satisfy the boundary conditions of the problem. It may also be shown that for very large distances from the aperture the velocity decays like the flow from a three dimensional source, as would be expected.

Although it is evident from Equation (42) that the constant  $k$  corresponds to the radius of the orifice, the constant  $A$  in Equations (47), (48) is still to be determined. It can be fixed in terms of the volume flow rate out of the orifice. Defining  $V$  as the volume flow rate

$$V = 2\pi \int_0^k \bar{v}_z(\bar{r}, \theta) \bar{r} d\bar{r} \quad (49)$$

and substituting from Equations (40), (41), (48) gives

$$A = \frac{V}{2\pi k} \quad (50)$$

The effects of the free stream can be introduced by adding appropriate components of  $U_\infty$  vectorially to the velocity components on the plate surface. Since as shown in Figure 36, the plate surface corresponds to  $\xi = \pi/2$ , the radial velocity component due to the orifice flow is, according to Equation (47)

$$\bar{v}_{\bar{r}}\left(\frac{\pi}{2}, \eta\right) = \frac{(V/2\pi k^2)}{\sinh \eta \cosh \eta}$$

The transformation Equations (40), (41) become, at  $\xi = \pi/2$ ,

$$\bar{r} = k \cosh \eta$$

so that the above may be written

$$\bar{v}_{\bar{r}} = \frac{(A/2\pi k^2)}{r' \sqrt{r'^2 - 1}}$$

where  $r' \equiv r/k$ .

Referring to the polar coordinates of Figure 10, the free stream velocity vector has the following components along the  $\bar{r}$  and  $\theta$  directions, respectively:

$$\bar{v}_{\bar{r}\infty} = U_{\infty} \cos \theta$$

$$\bar{v}_{\theta\infty} = -U_{\infty} \sin \theta$$

The velocities can be substituted in Bernoulli's equation,

$$C_p = 1 - \frac{\bar{v}_{\bar{r}}^2 + \bar{v}_{\theta}^2}{(\rho_{\infty} U_{\infty}^2 / 2)}$$

to yield the interference pressure coefficient in the form

$$C_p = 1 - \frac{(V/2\pi k^2 U_{\infty})^2}{r'^2 (r'^2 - 1)} - \frac{(V/\pi k^2 U_{\infty}) \cos \theta}{r' \sqrt{r'^2 - 1}} \quad (51)$$

In Equation (51), the pressure coefficient for the orifice model contains two undetermined parameters. These are the volume flow  $V$  and the scale factor  $k$ . In considering ways to match Equation (51) to data for obtaining  $V$  and  $k$  it was found, in this instance, that it was best to assume that the model and actual jets have the same volume flow given by

$$V = \pi k^2 U_j$$

Equation (51) then becomes,

$$C_p = -\frac{1}{4} \frac{(U_j/U_\infty)^2}{r'^2(r'^2-1)} - \frac{(U_j/U_\infty)\cos\theta}{r'\sqrt{r'^2-1}} \quad (52)$$

The scale factor  $k$ , however, should not necessarily be set equal to the radius of the actual jet exit, but left to be determined as an effective orifice radius.

The data of Vogler in Reference 32 show positive pressure coefficients in the region upstream of the orifice, which indicate the predominance of blockage effects for velocity ratios  $U_\infty/U_j$  greater than 0.2. For velocity ratios close to unity, where the effect of the jet is primarily blockage, and in the underexpanded jet case of interest there is probably a large separated region behind the jet. Thus, the jet appears to the subsonic free stream as an obstacle considerably larger than the size of the orifice. As the velocity ratio decreases the entrainment increases and the apparent obstacle size of the jet decreases. It is to be expected then that  $(k/d_j)$  will decrease as the velocity ratio  $(U_\infty/U_j)$  decreases. The numerical values for  $k$  are found by comparing Equation (52) to the data of Vogler along the rays  $\theta = 0^\circ$ , and  $\theta = 180^\circ$ . At a fixed value of  $(U_\infty/U_j)$ , the scale was adjusted for an approximate best fit, and a value for  $(k/d_j)$  deduced. The relationship between  $(k/d_j)$  and  $(U_\infty/U_j)$  which yields consistently good results in the application of Equation (52) is shown in Figure 35. The curve may also be represented empirically by the relation

$$\frac{k}{d_j} = 0.876 - 1.874\left(\frac{U_\infty}{U_j}\right) + 12.153\left(\frac{U_\infty}{U_j}\right)^2 - 10.813\left(\frac{U_\infty}{U_j}\right)^3$$

A comparison of Equation (52) with the data of Vogler (Reference 6) for the specific case  $U_\infty/U_j = 0.4$  is made in Figures 28-34. It is recalled that the data has been adjusted at each value of  $\theta$ .

Agreement is good near the windward and leeward planes of symmetry, but not too good near  $\theta = \pi/2$ . In this neighborhood the decay predicted by Equation (52) is too fast to properly represent the data.

### 3.4 PRESSURE MODEL COMPUTER PROGRAMS

A computer program has been developed which calculates pressure distribution, interaction forces, and interaction moments on flat plates and cylindrical shapes, using the pressure models described in Section 3.3. The program is coded in the FORTRAN IV programming language for use on the IBM 7094 computer.

### 3.4.1 Flat Plate Interaction Forces

The data analysis and calculations of pressures by the computer program are carried out for the plane of the jet exit. The program requires either a set of pressure data in that plane, or the values for the empirical data fit Fourier coefficients and singularity strengths for the source model.

Three different methods of calculating the pressure distributions can be accomplished by the program. The first is either an empirical fit of the data which was input, based on a five-term Fourier series, or the pressure distribution calculated by the same resulting equation

$$C_p = \sum_{n=0}^2 c_n \cos(n\theta) \quad (53)$$

based on the input Fourier coefficients,  $c_n$ . The second alternative is to calculate the pressure distribution by the source and uniform stream model, as given by Equation (39). The third alternative is to calculate the pressure distribution based on the orifice flow in a uniform stream model according to Equation (52).

After the pressure distribution is calculated, it is integrated in the plane of the jet exit to yield interaction force and moment coefficients. The integration of the input pressure distributions is accomplished numerically in the coordinate system shown in Figure 10. In that coordinate system, the numerical integration scheme is given by

$$C_N = \frac{1}{S_R} \sum_i \sum_\ell C_p(r_i, \theta_\ell) \cdot \Delta A_{i\ell} \quad (54)$$

and

$$C_{M_i} = \frac{1}{S_R} \sum_i \sum_\ell r_i C_p(r_i, \theta_\ell) \cos(\theta_\ell) \Delta A_{i\ell} \quad (55)$$

where

$$\Delta A_{i\ell} = \frac{1}{2} \left[ \frac{\theta_{\ell+1} - \theta_{\ell-1}}{2} \right] \left[ \frac{r_{i+1} - r_{i-1}}{2} \right] \left[ \frac{r_{i+1} + r_{i-1}}{2} + r_o \right] \quad (56)$$

The pressure integration for the source model can be accomplished analytically by integrating Equation (39). The orifice flow model interference pressures are integrated numerically to smooth effects of the singularity at  $r' = 1$ .



### 3.4.2 Interaction Forces on a Cylinder

The mathematical models developed for subsonic mainstream JI provide pressure distributions only in the plane of the jet exit. However, an approximation and coordinate transformation have been introduced in order to calculate pressures on a cylindrical body and integrate them. The pressure distribution on the cylinder is approximated by wrapping the plane of the jet exit into a cylinder. This transformation is made in such a manner as to maintain constant distance on the surface between the jet exit and the point  $(S, \theta)$  in the plane located by the polar angle  $\theta$  as shown in Figure 37. The transformation is given by the equations

$$x - x_j = \eta \sin \theta \quad (57)$$

$$y = \eta \cos \theta \quad (58)$$

$$z = \sqrt{R^2 - \eta^2 \sin^2 \theta} \quad (59)$$

where the distance  $\eta$  is determined by numerically evaluating the integral

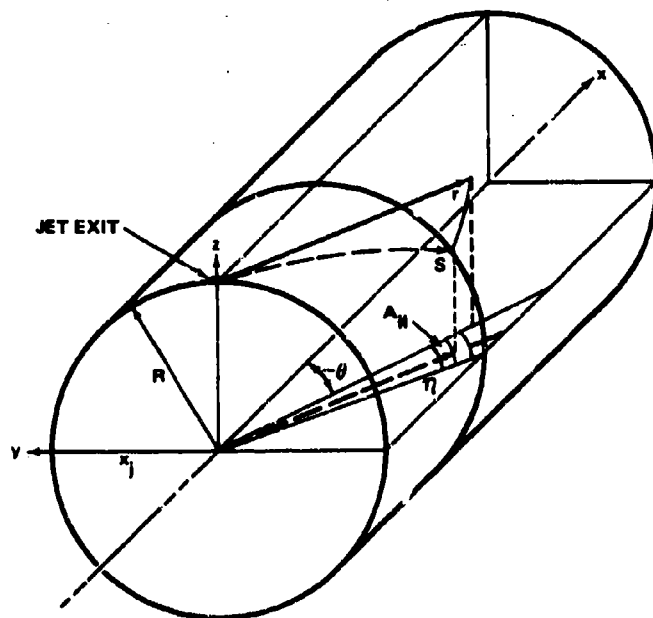


Figure 37. Coordinate System For Cylinder Projection of Exit Plane

$$S = r = \int_0^\eta \left[ \frac{R^2 - \eta'^2 \sin^2 \theta \cos^2 \theta}{R^2 - \eta'^2 \sin^2 \theta} \right]^{1/2} d\eta' \quad (60)$$

to determine the upper limit,  $\eta$ .

The pressure coefficient at the point  $(S, \theta)$  on the cylinder surface is given by the pressure coefficient in the plane of the jet exit, as the average value

$$C_{P_{il}} = \frac{1}{4} \left[ C_p(\theta_i, r_\ell) + C_p(\theta_i, r_{\ell+1}) + C_p(\theta_{i+1}, r_{\ell+1}) + C_p(\theta_{i+1}, r_\ell) \right] \quad (61)$$

The associated area increment,  $\Delta A_{il}$ , is the projection in the  $x, y$  plane shown in Figure 37.

In the program, the pressure coefficients given by Equation (61) are integrated numerically to yield the interaction force and moment coefficients

$$C_N = \frac{1}{S_R} \sum_i \sum_\ell C_{P_{il}} \Delta A_{il} \quad (62)$$

and

$$C_M = \frac{1}{S_R L_R} \sum_i \sum_\ell C_{P_{il}} \Delta A_{il} (x_j - x_{cg} + x_{il}) \quad (63)$$

where the moment is referred to the point  $x_{cg}$ .

The output of the program includes the coefficients  $C_N$  and  $C_M$  as well as the pressure distribution on the cylinder.

**BLANK PAGE**

## Section 4

### CONTROL EFFECTIVENESS PREDICTION FOR SUPERSONIC FLIGHT

One major objective of the study reported here has been to develop a computer program for predicting JI control effectiveness for axisymmetric missiles in supersonic flight. The analysis method employed in the computer program which has been developed is based on the equivalent solid obstacle in inviscid flow analogy. The analogy and its basis are described in detail in Reference 19. In this section, improvements and increases in capability and flexibility of the program are described. A description of the program and instructions concerning its use are contained in Appendix C.

#### 4.1 GENERAL DESCRIPTION OF THE PROGRAM

The final version of the equivalent solid obstacle program calculates static stability derivatives and JI amplification factors for axisymmetric missiles with circular lateral jets. The jet location on the vehicle is arbitrary and all parameters are calculated as functions of angle of attack.

The equivalent solid-obstacle analogy was described in Reference 19 and is based on a momentum balance criterion that is independent of viscous or geometric effects. It is required that the free stream exert a drag force on the jet plume as it accelerates the jet fluid downstream. The equivalent circular cross-sectional area of the plume is calculated by the method of Reference 19 and the jet plume is replaced by a solid obstacle, a hemisphere-cylinder having the same frontal area.

The key assumption involved in the equivalent-body analogy is that the jet plume can be replaced by a solid obstacle. It is further assumed that the shock-wave pattern caused by the equivalent body alone is unaltered by the presence of the vehicle surface, and the pressures on the vehicle surface are altered by a factor equal to the pressure ratio at the corresponding point in the equivalent-body flow field. The analysis of Reference 19 showed satisfactory agreement of shock shapes caused by a jet and an equivalent hemisphere-cylinder aligned with the free stream when these analyses were restricted to jets exhausting from flat plates. The method has now been extended to include arbitrary bodies of revolution at angle of attack. It is not to be expected that the shock shape or details of the pressure field behind the shock wave will match experimental data, but the integrated value of

the interaction force should be related to the wave drag of the equivalent body if the flow field is indeed shock dominated. Empirical data can be introduced to shape and scale the geometry of the disturbed region.

Although the analysis described herein is based entirely on nonviscous aerodynamics, an effort has been made to simulate the effects of boundary-layer separation resulting from the impingement on the vehicle surface of the bow shock wave caused by the jet plume. The resulting pressure distributions produce more realistic control moment increments for a given interaction force. The secondary viscous effects altering the pressure distribution in regions of high velocity gradients have been neglected.

The equivalent solid obstacle analogy has been combined with an existing surface pressure integration technique currently operational at MDAC-WD. The integration technique, described by Timmer and Stokes in Reference 38, is based on local inclination pressure laws and is used to predict and integrate surface pressures on bodies of revolution at angle of attack. On that portion of the vehicle in the region of influence of the jet, the surface pressures are multiplied by pressure ratios determined independently by a method of characteristics analysis of the axisymmetric equivalent body flow field.

The complete analysis method has been automated and is currently available in the form of a MDAC-WD FORTRAN IV computer program. Equivalent body flow fields (i. e., pressure distributions and shock shapes) for a unit hemisphere-cylinder have been calculated. These flow fields were calculated for the local undisturbed (jet off) Mach numbers  $\{M_1\}$  at the jet location on the vehicle surface. The jet penetration height is then calculated and the equivalent body flow field is scaled accordingly. Finally, the pressures are integrated over the vehicle surface taking into account the presence of the jet. In this manner, the angle of attack variation of force and moment amplification factors and vehicle aerodynamic coefficients can be determined for any combination of jet location and jet pressure ratio.

In this section the application of the equivalent body analogy to simulate the presence of control jets on bodies of revolution at angle of attack is described. Appendix C contains detailed flow charts and specific instructions for using the computer program.

#### 4.2 VEHICLE GEOMETRY

The vehicle surface is described with respect to body-fixed axes  $(x, y, z)$  with the origin at the nose and the positive  $x$ -axis as the axis of symmetry. The vehicle may be made up of one to eight components which are described in the  $x$ - $z$  plane as straight lines, circular arcs, or arbitrary curves. Each component is then subdivided into eight patches, each subtending a  $45^\circ$  angle on the surface. A 16 rectangle-per-patch integration mesh is constructed on all patches upstream

of the jet. Aft of and including the patch on which the jet is located the mesh fineness is increased to 64 rectangles per patch. As indicated in Figure 38, the free stream velocity vector is specified to be in the x-z plane, so consideration of the half-space  $y < 0$  (and therefore only 4 patches per component) is sufficient for vehicle geometry considerations.

### 4.3 ANGLE-OF-ATTACK DETERMINATION

The operational method of the program requires that calculations only be made for vehicle angles of attack which correspond to specific local Mach numbers at the jet location, with the jet off. These local Mach numbers correspond to those for which equivalent solid obstacle pressure distributions, as obtained from method of characteristic calculations, are stored on magnetic tapes.

The determination of the vehicle angles of attack  $\alpha_i$  which produce the specified local Mach numbers  $M_i$  at the jet location requires a numerical solution of the isentropic flow relations. Different methods of calculation are used depending on whether relatively sharp or blunt nosed vehicles are considered.

#### 4.3.1 Blunt-Nosed Vehicles

The basic assumption involved in determining the angle of attack for a specific local Mach number on blunt vehicles is that the fluid wetting the vehicle, at the jet location, passed through a normal shock at the nose and expanded isentropically to the local Mach number  $M_i$ . The local static-to-stagnation pressure is given by the isentropic relation

$$\frac{P_1}{P_{t_1}} = \left(1 + \frac{\gamma-1}{2} M_1^2\right)^{-\frac{\gamma}{\gamma-1}} \quad (64)$$

Combining this with the Rayleigh pitot formula,

$$\frac{P_{t_1}}{P_\infty} = \left[ \frac{(\gamma+1) M_\infty^2}{2} \right]^{\frac{\gamma}{\gamma-1}} \left[ \frac{\gamma+1}{2\gamma M_\infty^2 - \gamma + 1} \right]^{\frac{1}{\gamma-1}} \quad (65)$$

the static pressure ratio

$$P = \frac{P_1}{P_\infty} \quad (66)$$

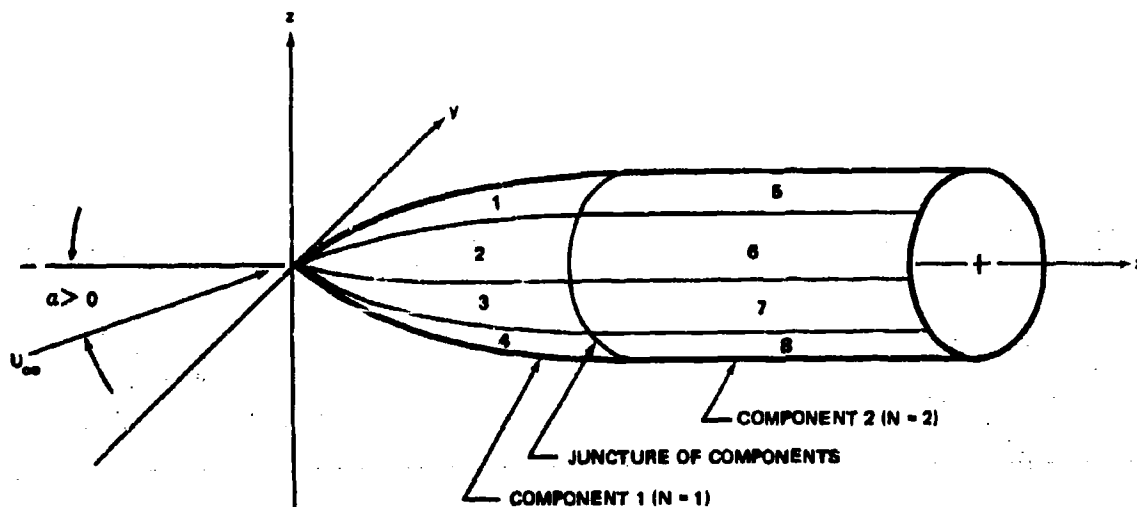


Figure 38. Coordinate System For Vehicle Geometry

can be determined. The vehicle angle of attack that produces this pressure is determined using one of the following local inclination laws:

Tangent Cone (windward surfaces)

$$P = 1 + \frac{\gamma}{2} K^2 \left\{ 1 + \left[ \frac{(\gamma + 1) K^2 + 2}{(\gamma - 1) K^2 + 2} \right] \ln \left( \frac{\gamma + 1}{2} + \frac{1}{K^2} \right) \right\} \quad (67)$$

Prandtl-Meyer (lee side hypersonic small disturbance)

$$P = \left\{ 1 + \frac{\gamma - 1}{2} K^2 \right\}^{\frac{2\gamma}{\gamma - 1}} \quad (68)$$

In the above expressions,

$$K = \sqrt{M_\infty^2 - 1} \sin \alpha_L \quad (69)$$

where  $\alpha_L$  is the local angle of attack and is given by the scalar product

$$\sin \alpha_L = -\underline{U}_\infty \cdot \underline{n} \quad (70)$$

where  $\underline{U}_\infty$  is the free-stream velocity unit vector and  $\underline{n}$  is the unit outer normal at the jet location,

$$\underline{n} = n_x \underline{i} + n_y \underline{j} + n_z \underline{k} \quad (71)$$

If the jet is on the lee side, the Prandtl-Meyer equation is used and can be solved for  $K$  explicitly. Then, since

$$\underline{V}_\infty = \underline{i} \sin \alpha + \underline{k} \cos \alpha$$

the appropriate angle of attack is the root of the equation

$$T(\alpha) \equiv n_x \sin \alpha + n_z \cos \alpha + \frac{K}{\sqrt{M_\infty^2 - 1}} = 0 \quad (72)$$

The root can be found by numerical solution in the interval

$$-\frac{\pi}{2} < \alpha < \frac{\pi}{2}$$

If, however, the jet is on the windward side, the tangent cone equation must be used. Since this cannot be solved explicitly for  $K$ , an iterative method is used. In the program, this method is used to find the root of the function:

$$G(\kappa) = 1 - P + \frac{\gamma}{2} \kappa \left\{ 1 + \left[ \left( \frac{\gamma+1}{\gamma-1} \right) \frac{\kappa+2}{\kappa-2} \right] \ln \left( \frac{\gamma+1}{2} + \frac{1}{\kappa} \right) \right\} = 0 \quad (73)$$



where  $\kappa \equiv K^2$ . Using the value of  $K$  thus obtained, the angle of attack  $\alpha_i$  is found using the same method as described above for the lee side case.

#### 4.3.2 Sharp-Nosed Vehicles

The problem of determining the angle of attack for a specific local Mach number on sharp nosed vehicles is slightly more complicated because of the presence of the attached shock on the nose of the vehicle. In the case of a blunt nosed vehicle (Subsection 4.3.1), calculation of the pressure ratio  $P$  was straightforward and independent of the angle of attack. For the sharp nosed vehicle, the total pressure on the vehicle changes as the angle of attack (and, hence, the strength of the attached shock) changes. It is assumed that the fluid wetting the vehicle surface is that fluid which passed through the oblique shock at the nose on the windward ray. Thus, the total pressure at the jet location is determined by the strength of the nose shock on the windward ray. It is further assumed that the flow at the nose is conical. When the vehicle is confined to small angles of attack and the flow near the sharp nose (half angle =  $\delta$ ) is assumed to be conical, then the shock strength on the windward ray is approximately equal to the strength of the shock produced by a cone of half angle  $\theta_c = \delta + |\alpha|$  at zero angle of attack.

An iterative procedure is required to determine the angle of attack in this case. It is reduced in the current analysis to a binary-chop method of finding the root of the equation

$$H(\alpha) \equiv P_1(\alpha) - P_2(\alpha); \quad -0.3 < \alpha < 0.3 \quad (74)$$

where  $|\alpha| = 0.3$  radians was arbitrarily chosen to be the upper limit on "small angles of attack". The functions  $P_1(\alpha)$  and  $P_2(\alpha)$  are the static pressure ratios determined by shock-expansion theory and a local inclination law. Having guessed an initial value of  $\alpha$ , the functions  $P_1(\alpha)$  and  $P_2(\alpha)$  are calculated and the function  $H(\alpha)$  is evaluated. It can be shown that  $H$  is a monotonic function of  $\alpha$ , so if the function  $H$  has the same sign at  $\alpha \pm 0.3$  radians, there is no root in this interval. In that case, no pressure integration is carried out for the angle of attack corresponding to the local Mach number  $M_1$  at the jet location.

To calculate the function  $P_1(\alpha)$  for a particular angle of attack, the windward-ray shock angle must first be determined. An effective cone half angle  $\theta_c = \delta + |\alpha|$  is calculated, and the shock angle  $\theta_s$  is given by the following relation from Reference 39

$$\sin^2 \theta_s = \frac{1}{M_\infty^2} + \frac{1}{2} \left[ g_2 + g_1 \sin^2 \theta_c - \left\{ (g_2 - g_1 \sin^2 \theta_c)^2 - \left[ (g_3 - g_1) \sin^2 \theta_c \right] \right\}^{1/2} \right] \quad (75)$$

where:

$$g_1 = \frac{\gamma + 1}{2}$$

$$g_2 = 1 - \frac{1}{M_\infty^2}$$

$$g_3 = \gamma \left[ 1 + \frac{1}{M_\infty^2} \right]$$

Using this shock angle, the static pressure ratio  $P_1(\alpha)$  corresponding to the local Mach number  $M_1$  is given by

$$P_1(\alpha) = \left[ 1 + \frac{\gamma - 1}{2} M_1^2 \right]^{-\frac{\gamma}{\gamma - 1}} \left[ \frac{\gamma + 1}{2 \gamma M_\infty^2 \sin^2 \theta_s - \gamma + 1} \right]^{\frac{1}{\gamma - 1}} \left\{ \frac{(\gamma + 1) M_\infty^2 \sin^2 \theta_s \left[ (\gamma - 1) M_\infty^2 + 2 \right]}{2 \left[ (\gamma - 1) M_\infty^2 \sin^2 \theta_s + 2 \right]} \right\}^{\frac{\gamma}{\gamma - 1}} \quad (76)$$

The function  $P_2(\alpha)$  is now obtained from a local inclination law. On the windward side, the pressure is obtained directly from the tangent cone law

$$P_2(\alpha) = 1 + \frac{\gamma}{2} K^2 \left\{ 1 + \left[ \frac{(\gamma + 1) K^2 + 2}{(\gamma - 1) K^2 + 2} \right] \ln \left( \frac{\gamma + 1}{2} + \frac{1}{K^2} \right) \right\} \quad (77)$$

where  $K$  is known for a given  $\alpha$  from the relation

$$K = - \sqrt{M^2 - 1} (n_x \sin \alpha + n_z \cos \alpha) \quad (78)$$

On the leeward side, Prandtl-Meyer hypersonic small disturbance theory is used to yield

$$P_2(\alpha) = \left[ 1 + \frac{\gamma - 1}{2} K \right]^{\frac{2\gamma}{\gamma - 1}} \quad (79)$$

The above analysis was carried out for sharp nosed vehicles assuming an attached shock. To assure consistency, a check is performed to verify that the shock is attached. The new equivalent cone angle is

$$\theta_c = \delta + |\alpha|$$

For a given free-stream Mach number  $M_\infty$ , the shock is attached on cones of half angles  $\theta_c < \theta_M$ . The angle  $\theta_M$  is given in Reference 39 by the equation

$$\theta_M = \frac{1 - \frac{1}{M_\infty^2}}{\gamma \left[ 1 + \frac{1}{M_\infty^2} \right]} \quad (80)$$

If the shock is detached, the windward ray streamline is considered to have passed through a normal shock.

#### 4.4 EQUIVALENT BODY SIZING

The procedure used in sizing the equivalent body is exactly the same as that presented in Reference 19. That is, the radius of the hemisphere-cylinder is assumed to be scaled by one-half the jet-penetration height,  $h_1$ . The height  $h_1$  is given by the expression

$$h_1 = d_t \left[ \left( \frac{2}{\gamma_j + 1} \right)^{\gamma_j / (\gamma_j - 1)} \left[ \frac{\left( \frac{p_{o_j}}{p_\infty} \right) \left( \frac{p_\infty}{p_1} \right)_1}{0.5 \gamma M_1^2 C_{x_1} + 1} \right] \right. \\ \left. \left[ \gamma_j \left( 1 + \frac{v_j}{a_t} + u \phi_j \right) + 1 \right] \right]^{1/2} \quad (81)$$

where  $C_{x_1}$ , the equivalent body drag coefficient at the local Mach number  $M_1$ , is given by

$$C_{x_1} = \frac{1}{\gamma M_1^2} \left[ \left( \frac{\gamma + 1}{2} M_1^2 \right)^{\frac{\gamma}{\gamma - 1}} \left( \frac{\gamma + 1}{2 \gamma M_1^2 - \gamma + 1} \right) - 1 \right] \quad (82)$$

and the jet exit velocity ratio is given by

$$\frac{v_j}{a_t} = \left[ \frac{(\gamma + 1) M_j^2}{2 + (\gamma - 1) M_j^2} \right]^{1/2} \quad (83)$$

The diameter of the equivalent obstacle,  $2S$ , is scaled to be approximately equal to the penetration height when the penetration height is five times larger than the vehicle diameter at the jet. When the jet

penetration height is very small compared to the radius of curvature of the vehicle surface (i. e., approaching the flat-plate case), the drag of the equivalent obstacle is assumed to be associated with half of an axisymmetric shock. Then the equivalent obstacle radius is adjusted so that the cross-sectional area of the obstacle is half that for the diameter equal to the penetration height. Between these two extremes, the ratio between the cross-sectional area of the equivalent obstacle and the vehicle cross-sectional area at the jet,  $A_b$ , is scaled exponentially. The equation employed for the adjustment is

$$S = \frac{h}{Z} \left\{ 1 + \exp \left[ - \xi \left( \frac{A^*}{A_b} \right)^2 \right] \right\}^{1/2}$$

where  $A^* = \pi h^2/4$  and  $\xi = 0.00736$ .

#### 4.5 VEHICLE SURFACE PRESSURE INTEGRATION

As local inclination pressure laws are used, the pressure on a particular mesh element outside the equivalent obstacle shock, depends only on its orientation with respect to the free-stream velocity vector. However, if the element lies within the interaction region, its pressure is multiplied by a static pressure ratio associated with the corresponding point in the equivalent body flow field. To check whether a mesh element with coordinates  $(x, y, z)$  lies within the interaction region, the point must first be transformed into the coordinate system of the equivalent body.

##### 4.5.1 Equivalent Obstacle Coordinate System

In the equivalent body analogy, the hemisphere-cylinder is assumed to lie parallel to the local flow velocity vector. Since the equivalent body flow field data are specified in an axisymmetric coordinate system  $X'-R'$  with the origin at the nose, it is appropriate to place the origin of this coordinate system at a point  $(x_0, y_0, z_0)$  out a distance  $S_1 = 1/2 h_1$  along the unit outer normal  $(n_x, n_y, n_z)$  from the jet location  $(x_j, y_j, z_j)$ , as shown in Figure 39. The  $X'$  axis is aligned with the local flow velocity vector. Since the equivalent body flow field corresponding to a local Mach number  $M_1$  is based on a hemisphere-cylinder of unit radius, all coordinates  $(x, y, z)$  are divided by the scale factor  $S_1$  so the  $X'-R'$  coordinate system is compatible with the equivalent body coordinate system.

The appropriate transformation is derived by first expressing  $X'$  and  $R'$  in terms of the point  $(x_1, y_1, z_1)$  on the  $X'$  axis nearest the desired point  $(x, y, z)$

$$X' = \frac{1}{S} \left[ (x_1 - x_0)^2 + (y_1 - y_0)^2 + (z_1 - z_0)^2 \right]^{1/2} \quad (84)$$

$$R' = \frac{1}{S} \left[ (x - x_1)^2 + (y - y_1)^2 + (z - z_1)^2 \right]^{1/2} \quad (85)$$

The coordinates of the point  $(x_1, y_1, z_1)$  are determined by two conditions: first, that it lies on the  $X'$  axis,

$$\frac{x_1 - x_0}{u_x} = \frac{y_1 - y_0}{u_y} = \frac{z_1 - z_0}{u_z} \quad (86)$$

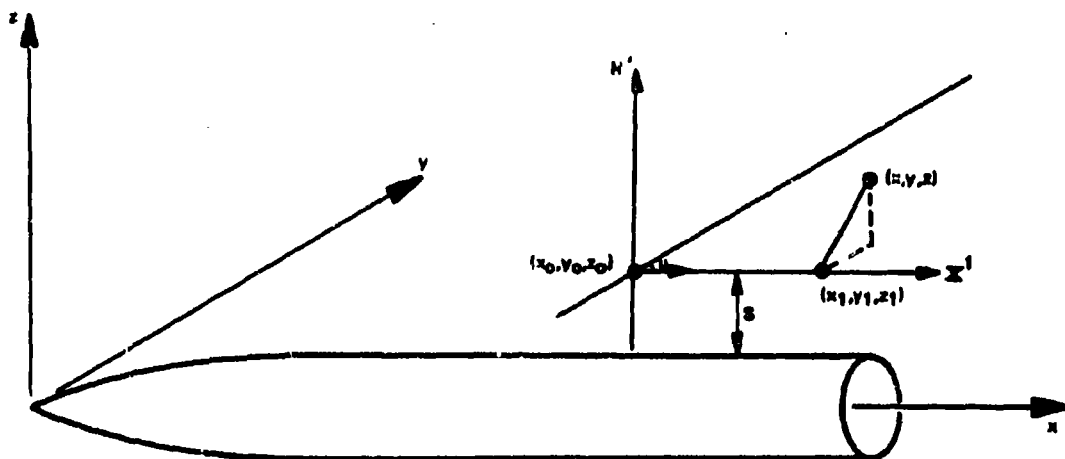


Figure 39. Coordinate System For Equivalent Body Flowfield

and second, that the line from  $(x, y, z)$  to  $(x_1, y_1, z_1)$  is normal to the  $X'$  axis

$$[(x - y_1), (y - y_1), (z - z_1)] \cdot [u_x, u_y, u_z] = 0 \quad (87)$$

Solving these equations simultaneously gives

$$z_1 = \frac{u_x u_z (x - x_0) + u_y y_z (y - y_0) + (u_x^2 + u_y^2) + u_z^2 z}{u_x^2 + u_y^2 + u_z^2} \quad (88)$$

$$y_1 = y_0 + \frac{u_y}{u_z} (z - z_0) \quad (89)$$

$$x_1 = x_0 + \frac{u_x}{u_z} (z - z_0) \quad (90)$$

#### 4.5.2 Inviscid Interaction Region

The interaction region is defined as that part of the vehicle where the surface pressure is affected by the presence of the jet. A purely inviscid analysis would locate this region downstream of the line where the equivalent body shock intersects the vehicle surface. In that case, a considerable portion of the interaction force would be concentrated along this line due to the spike in the resultant surface pressure profile. Experimental data presented in References 16 and 17 show a gradual rise to a peak pressure which is much less than the predicted inviscid value and then a gradual decay to the undisturbed pressure. The effect of viscosity therefore is to "smear out" the spike in the inviscid pressure profile by raising the pressure through shocks associated with boundary-layer interaction and by moving the interaction upstream of the inviscid shock impingement line. In the present version of the analysis, an option is included which simulates the viscous effects of reducing the peak pressure and enlarging the interaction region into an area upstream of the shock impingement line.

In the inviscid case, the interaction region is defined by requiring that the inequalities

$$X'_s \leq X' \leq X'_{\max}$$

$$R' < R'_{\max}$$

be satisfied. The upper bound  $X'_{\max}$  is the known limit of the equivalent-body flow field and  $R'_{\max}$  is the shock radius at that  $X' = X'_{\max}$ . The shock abscissa  $X'_s$  is given by the equation

$$X'_s(R') = \sum_{m=1}^9 C_m R'^{m-1} \quad (91)$$

In the program operation, Equation (91) represents an empirical fit of the shock shape from the method of characteristics solutions.

If the point  $(X', R')$  is found to lie within the interaction region, the pressure assigned to the associated incremental surface area is determined by scaling the undisturbed pressure at  $(X', R')$  by the pressure at the nearest point in the equivalent obstacle pressure distribution. With the undisturbed (jet off) pressure at the point  $(X', R')$  on the missile surface denoted  $\bar{p}(X', R')$ , the disturbance pressure at  $(X', R')$  is given by

$$p(X', R') = \bar{p} P_c$$

where

$$P_c = \frac{P_c}{P_1} = P_c(M, X', R', S)$$

is the pressure ratio in the equivalent obstacle pressure distribution at the point  $(X', R')$ . The nearest point in the characteristics pressure distribution is found by a hunting procedure based on the fact that the characteristics points are arranged in order of ascending x-coordinate. Hunting for the nearest point may therefore be confined to a circle of radius

$$d = \min \left\{ \begin{array}{l} |R' - R'_{\min}| \\ |X' - X'_s| \end{array} \right\}$$

around the point  $(X', R')$ . The relatively small amount of computing time required with this streamlined hunting procedure made surface fitting the equivalent-body pressure field unnecessary.

An empirical adjustment has been made in the program that limits the extent of the interaction region in the vehicle cross-sectional plane. The limitation is on the radial angle from the jet, in the cross-sectional plane. No pressure scaling because of the disturbance is done beyond an angle of  $150^\circ$  away from the jet. This adjustment was made because it is known from flow visualization in wind-tunnel tests that the jet bow shock dissipates in the cross-sectional plane.



#### 4.5.3 Boundary-Layer Separation Effects

The interaction of the jet-induced bow shock with the boundary layer is shown schematically in Figure 40. The flow geometry and the corresponding pressure distribution are shown for a longitudinal plane located some distance laterally from the jet nozzle. The geometry of the lambda-type shock pattern shown is quite speculative as there is no direct way of actually observing these details in a three-dimensional experiment. The details of the interaction phenomena must, therefore, be surmised from the measured pressure distributions. The interaction of a swept planar shock with a laminar boundary layer is analyzed in some detail in Reference 40. It is reported there that at least two plausible flow models can be postulated which will produce the observed results. Further, it is possible that either type of shock structure may exist, depending upon the state of the boundary layer, the Mach number, the shock strength, and other parameters.

As indicated by comparing the viscous and inviscid pressure distributions illustrated in Figure 40, the primary effect of the boundary layer is to reduce the peak pressure and to distribute the load over a greater area. The initial pressure rise occurs as a result of either a thickening or separation of the boundary layer ahead of the shock location. A fully separated boundary layer with reverse flow probably occurs only quite close to the jet, where the local pressure gradients are high. Over much of the disturbed area only a local thickening of the boundary layer occurs.

The maximum pressure at the wall probably occurs just downstream of the main shock at the location of the rear leg of the lambda shock pattern. The pressure decay downstream of the peak then follows quite close to the inviscid pressure profile, because there is no mechanism in this region to support a large pressure gradient normal to the wall.

The interaction force is dependent upon the distance that the boundary layer is affected ( $X_2 - X_1$  in Figure 40) as well as the peak pressure. Numerous attempts have been made to correlate this or related distances with the pressure rise for two-dimensional separated boundary layers. For example, the results of Needhan and Stollery in Reference 41 are correlated by Equations 13 of Reference 19. In another analysis more applicable to the present situation, Hakkinen, et al., in Reference 42 correlate the extent of boundary-layer separation produced by two-dimensional incident shocks. They conclude that the extent of the separation should correlate with the "driving pressure" which induces the separation. The driving pressure is taken to be the difference between the "final" pressure and the pressure required for incipient separation. In the two-dimensional separation analysis of Reference 42, the final pressure is equal to the inviscid pressure behind the shock. Though their correlation is not directly applicable to the present analysis, it is reasonable to expect that somewhat similar trends may exist. In their analysis (which they verified by experiment) they showed that the separated length varied almost linearly with the difference between the final or inviscid pressure and the

plateau pressure. Assuming a similar behavior may exist for the more complex three-dimensional case of interest here, the distance  $(X_s - X_1)$  in Figure 40 should increase as the pressure difference  $(p_{inv} - p_{exp})$  increases.

An empirical hyperbolic curve fit for the shape of the bow shock caused by jets exhausting transverse to a flat plate is presented in Reference 19. The equation for the shock radius  $(R)$  normalized with respect to the jet height  $(h)$  is

$$\left(\frac{R}{h}\right)^2 \frac{1}{\beta} = \left[ \left(\frac{x}{h}\right) \beta^{-3/2} + 2.5 \right]^2 - 6.25 \quad (92)$$

where

$$\beta = \sqrt{M_\infty^2 - 1}$$

and  $x$  is the distance downstream of the shock apex. Differentiating the above equation provides the local shock angle  $(\theta)$ , in the form

$$\beta^2 \tan^2 \theta = 1 + \frac{6.25 \beta}{(R/h)^2} \quad (93)$$

The shock angle, combined with the expression describing the pressure rise across an oblique shock in air, yields an equation for the pressure  $(p_{inv})$  immediately behind the shock, in the form

$$\left( \frac{p_{inv} - p_1}{p_N - p_1} \right) = \left[ \left(\frac{R}{h}\right)^2 \frac{M^2}{6.25\beta} + 1 \right]^{-1} \quad (94)$$

where  $p_N$  is the pressure behind a normal shock. This expression provides the pressure which would exist immediately behind the shock  $(p_{inv}$  in Figure 40) in the absence of any viscous effects and is the pressure immediately behind the main incident shock outside of the shear layer illustrated in Figure 40.

The measured surface peak pressure must be closely related to the pressure which exists behind the shock outside the shear layer. Therefore, one would expect that experimental data should correlate

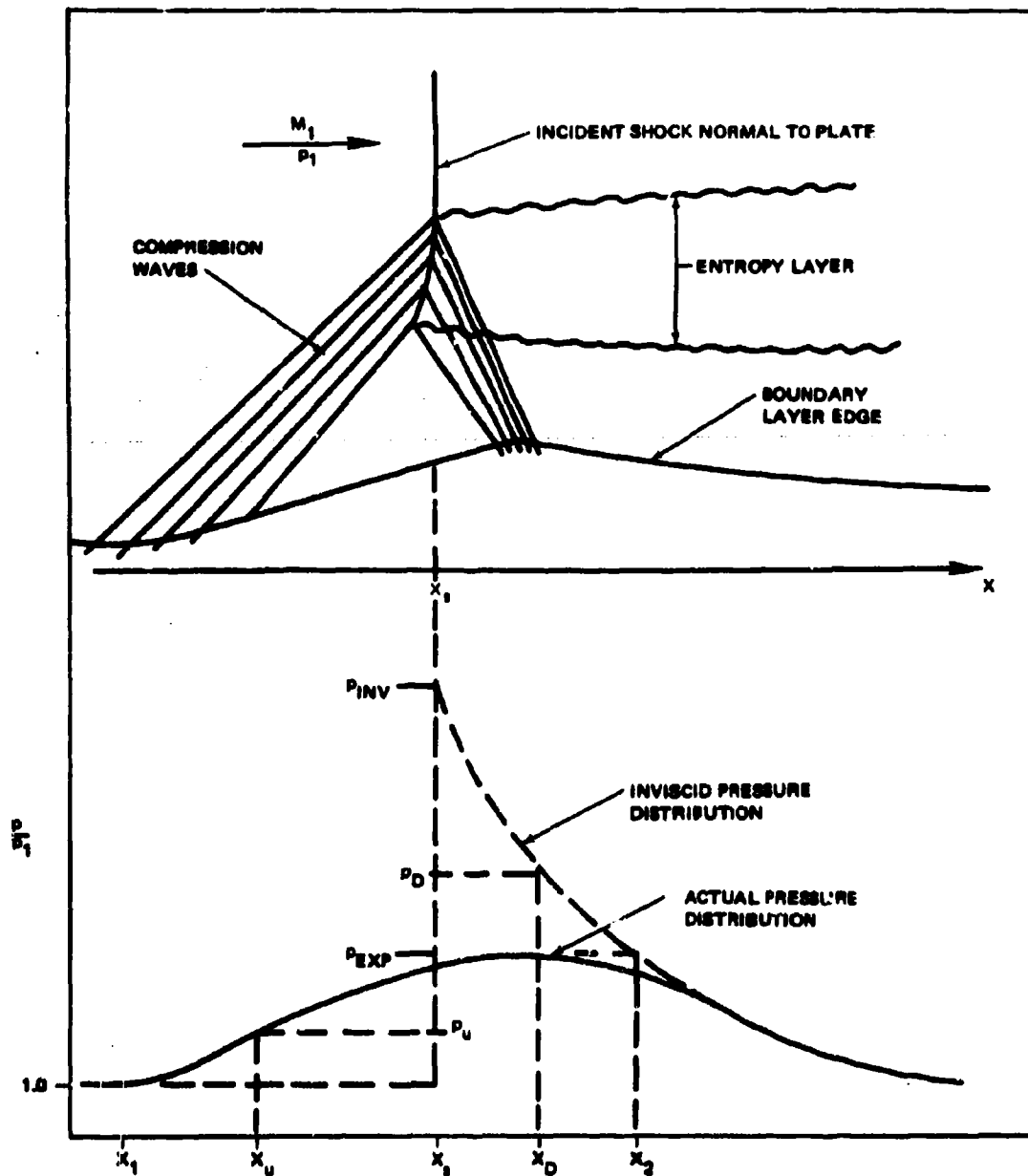


Figure 40. Bow Shock/Boundary Layer Interaction Approximation

with the same parameter which governs the inviscid pressure rise. Experimental values of the peak pressure are presented in Figure 41 in terms of the parameters suggested by the form of Equation 94. The inviscid pressure computed from Equation 94 is also presented for comparison. As shown, the experimental pressures are small compared to the predicted inviscid values. The characteristic plateau pressure for a two-dimensional turbulent separation is also shown on Figure 41 for the Mach numbers of the test data from References 16 and 43. It is seen that the maximum pressure can exceed the two-dimensional plateau pressure near the jet; these points correspond to the "second peak" pressure which occurs immediately upstream of the jet. In general, however, the pressures are substantially less than the two-dimensional values. A curve fit of the experimental data is provided by

$$\left( \frac{p_{\text{exp}} - p_1}{p_N - p_1} \right) = 0.4e^{-0.8(R/h)M\beta^{-1/2}} \quad (95)$$

In the equivalent obstacle analogy computer program, Equation (95) is used to account for the effect of boundary layer separation on the interaction control moment. The inviscid flow pressure distribution downstream of the bow shock is distributed over a distance extending from  $X_1$  upstream of the shock to  $X_2$  downstream of the shock, as shown in Figure 40.

The distance  $X_1$  is determined by truncating the inviscid spike in the pressure profile at the experimentally observed value determined from Equation (96) and redistributing the remaining interaction force into a region of constant pressure gradient upstream of the shock impingement line. The value of the constant pressure gradient, and, hence, the distance  $X_1$  upstream of the shock, is fixed by the requirement that the interaction force due to the spike

$$\Delta F_i = \frac{1}{2} (p_{\text{inv}} - p_{\text{exp}})(X_2 - X_s) \quad (96)$$

equal the area under the upstream triangle. This requirement gives the nondimensional ratio

$$\frac{X_2 - X_s}{X_s - X_1} = \left[ \frac{p_{\text{inv}} - p_1}{p_{\text{exp}} - p_1} - 1 \right]^{-1} \quad (97)$$

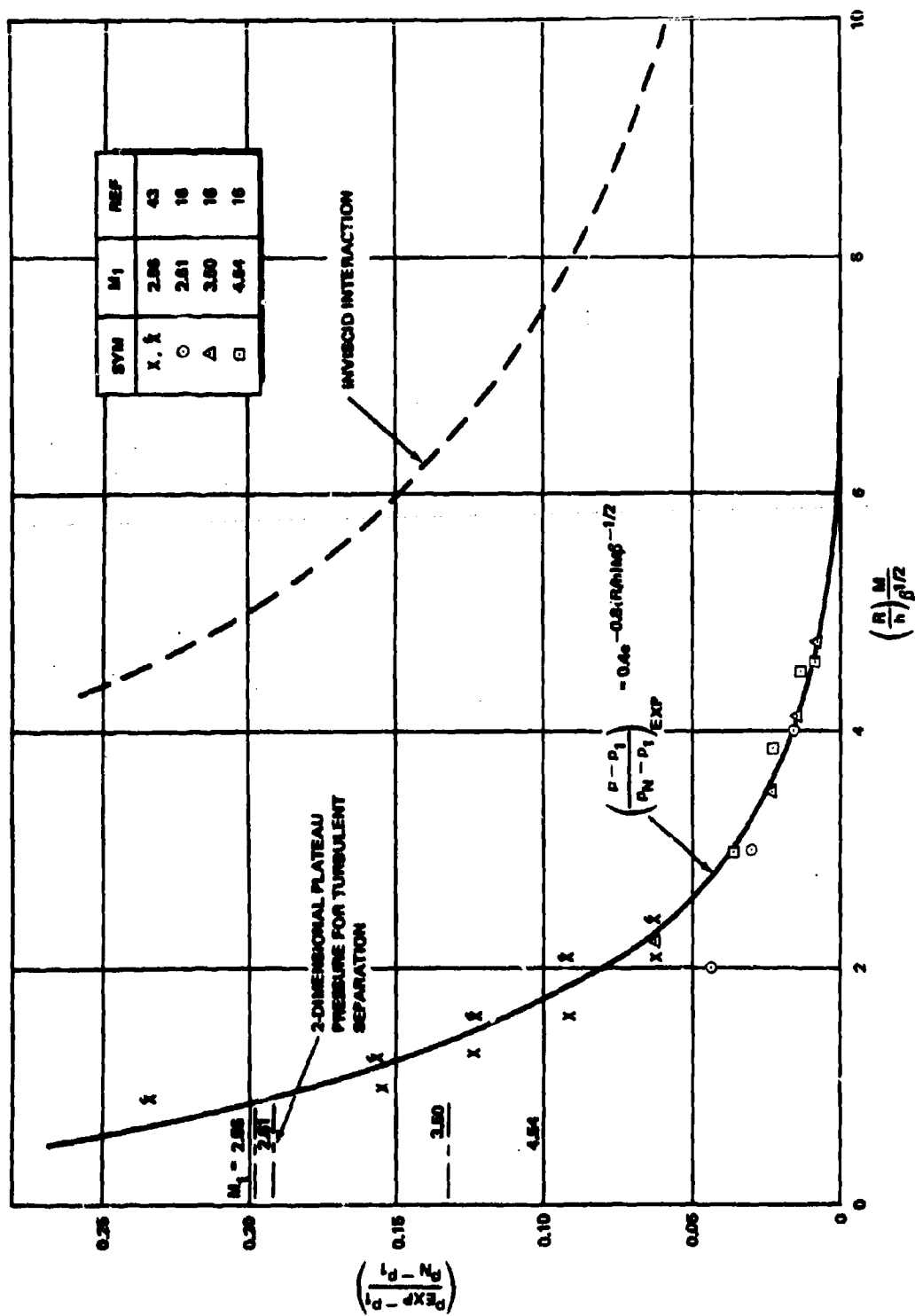


Figure 41. Correlation of Pressure at X<sub>5</sub> for Turbulent Separation

where  $p_{inv}$  is the calculated inviscid flow pressure and  $p_{exp}$  is the experimentally determined value as given by Equation (95). By definition then, any point with coordinates  $(X'_1, R')$  such that

$$X'_1 < X'_u \leq X'_s$$

where  $R'_u < R'_{max}$ , has a pressure ratio  $P_u = p_u/p_1$  associated with it. The pressure ratio,  $P_u$ , is given by

$$P_u = P_{exp} + \frac{X'_s - X'_u}{X'_s - X'_1} (1 - P_{exp}) \quad (98)$$

For any point  $(X'_D, R'_D)$  such that

$$X'_s < X'_D \leq X_2$$

and  $R'_D < R'_{max}$ , the associated pressure is given by Equation 95 as

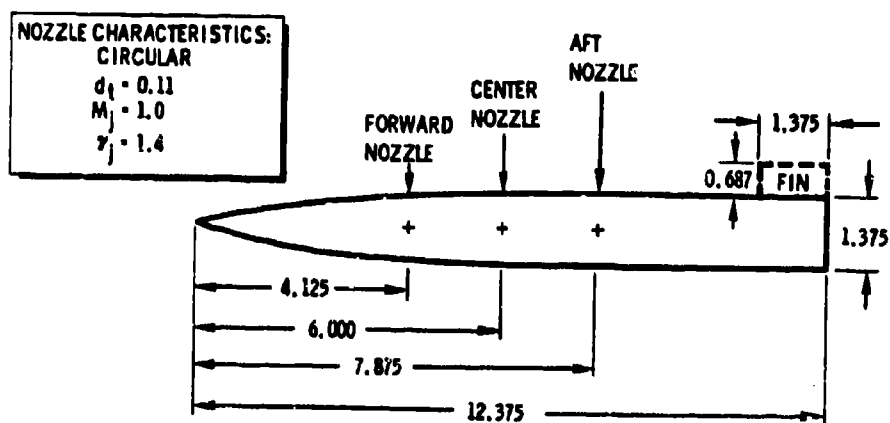


Figure 42. AMICOM Reaction Jet Force Model

$$P_D - P_{exp} = 1 + 0.4 (P_N - 1) \exp \left\{ -0.4 R_D' M_1 / \sqrt{M_1^2 - 1} \right\} \quad (99)$$

For points in the interaction region downstream of  $X_2$ , the inviscid pressure scaling method discussed in Subsection 4.5.2 is employed.

#### 4.6 EQUIVALENT OBSTACLE PROGRAM RESULTS

The equivalent obstacle analogy program has been used to predict amplification factors for a variety of configurations and flow conditions for which wind tunnel data are available. The only check on the validity of the analogy is the accuracy of such force and moment data comparisons, since details of the flow are not simulated. In Figures 43 to 50, some data comparisons are shown for the AMICOM wind tunnel model illustrated in Figure 42 (for details of the model see Reference 31). These comparisons are representative of the general accuracy level achieved with the computer program applied to other flow conditions and missile geometry. Results are generally better for aft located jets and higher freestream Mach numbers. For all the following data comparisons, the jet is at the center location indicated in Figure 42. All moments are referred to the nose and the jet is on the leeside of the model at positive angle of attack.

The basic normal force and pitching moment coefficients are shown versus angle of attack for  $M_\infty = 3.0$  in Figures 43 and 44. For these coefficients, the variation with pressure ratio is due principally to increasing jet thrust. The basic accuracy level of the jet-off aerodynamics predictions at low Mach numbers is shown in these figures. Better accuracy is achieved at higher Mach numbers.

In Figures 45 and 46, force and moment amplification factors are shown as functions of angle of attack and Mach number. As indicated, the accuracy of the prediction method is worse for lower pressure ratios, particularly when interaction forces are negative. This is believed due to lack of proper compensation for low pressures aft of the jet on the missile surface. The angle of attack effects are difficult to generalize because of limited extent of the data.

Prediction of force and moment amplification factor sensitivities to jet thrust are shown in Figures 47 and 48. Again, the low accuracy level at low thrust can be observed.

At a constant pressure ratio, the sensitivities of amplification factors to Mach number are shown in Figures 49 and 50. The general accuracy level indicated for this relatively high pressure ratio is believed to be as good as can be expected from the analogy, for this type of configuration (i. e., forward jets).

It is believed by the authors that progress must be made in basic understanding of three dimensional effects due to JI bow shock dissipation and viscous effects downstream of the jet plume before significant increases in the accuracy level of amplification factor predictions can be made. In the interim, the equivalent obstacle analogy method appears to offer as accurate a prediction scheme as is available.

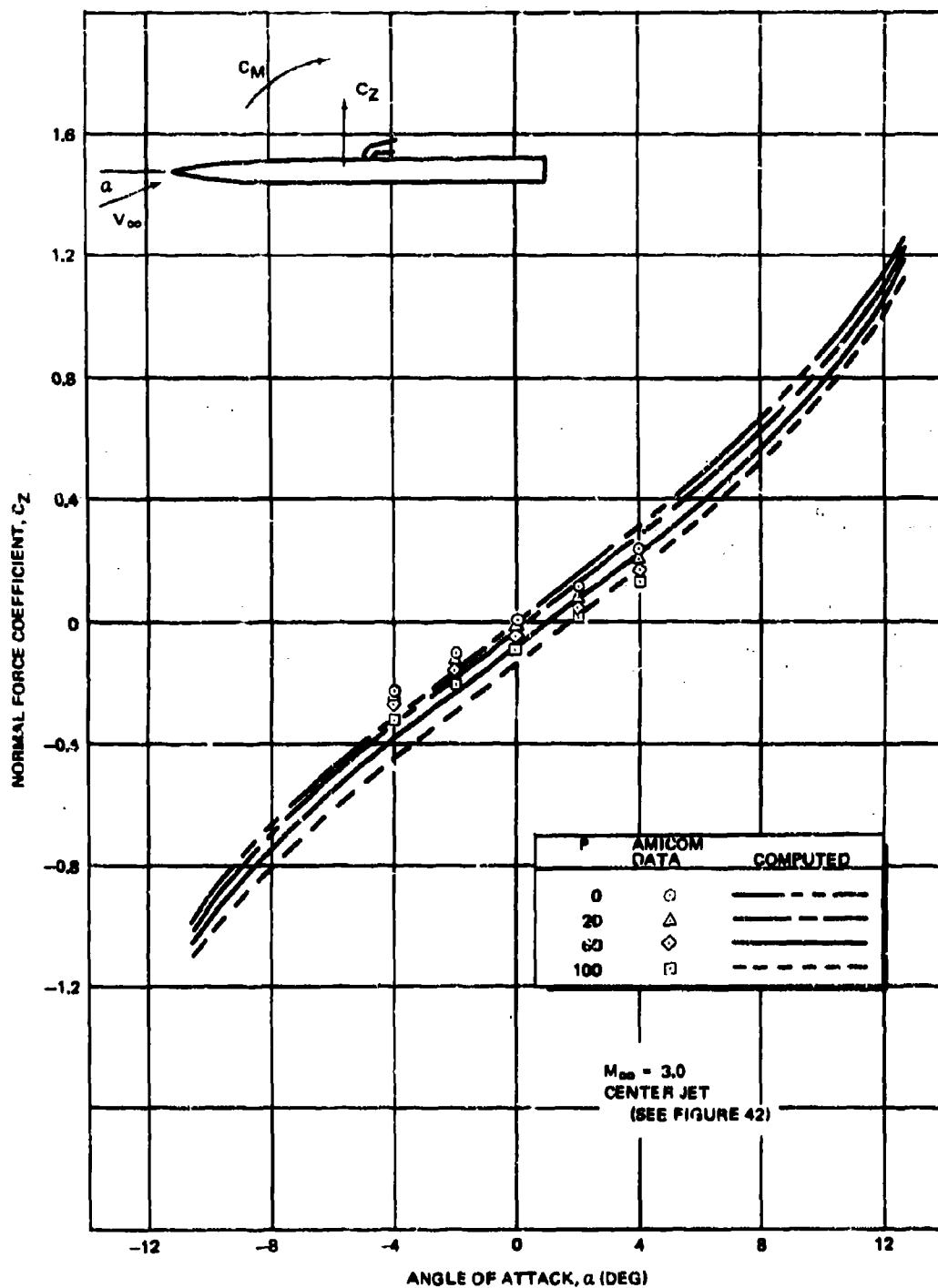


Figure 43. Equivalent Obstacle Analogy Prediction of Normal Force



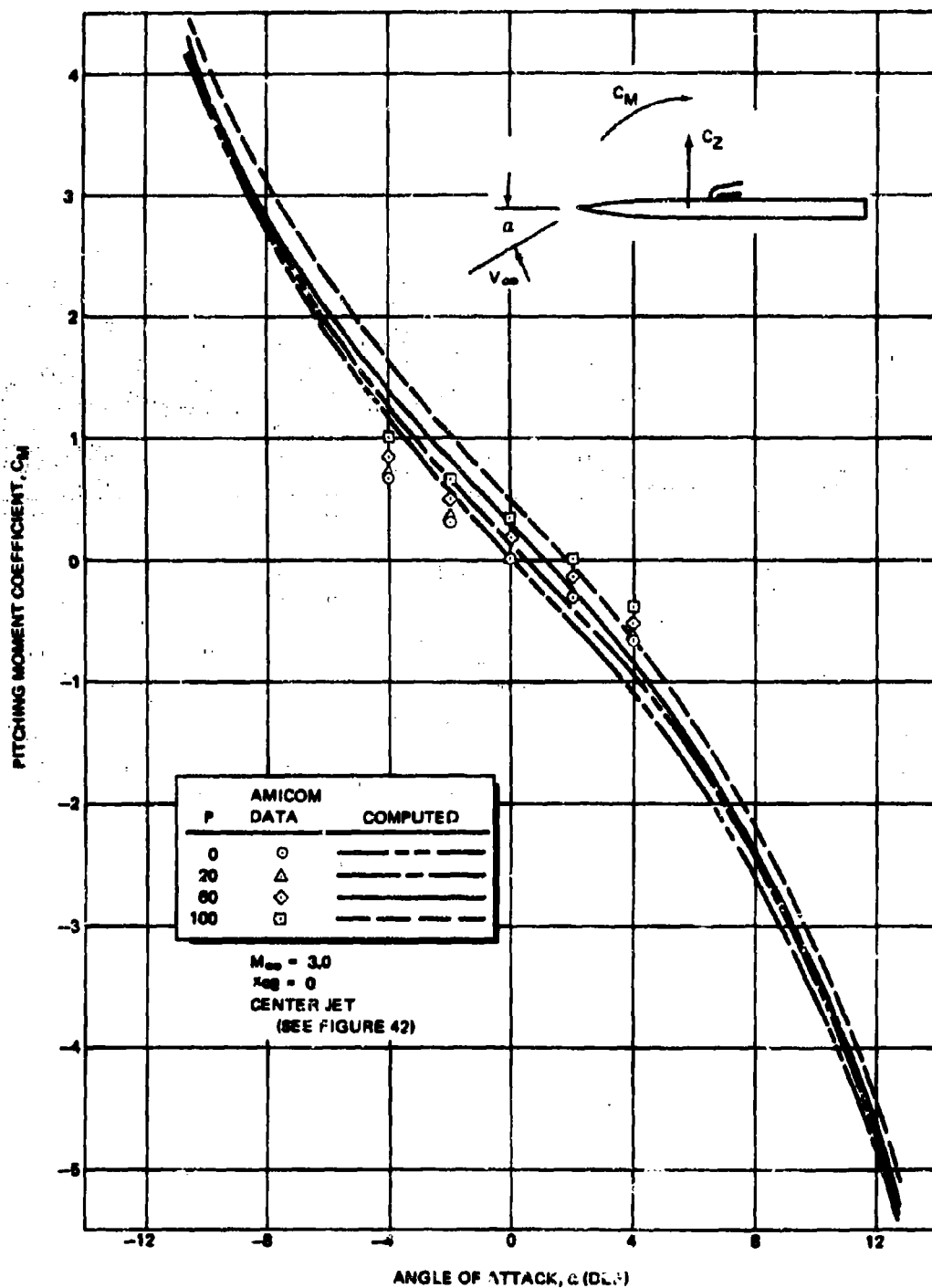


Figure 44. Equivalent Obstacle Analogy Prediction of Pitching Moment

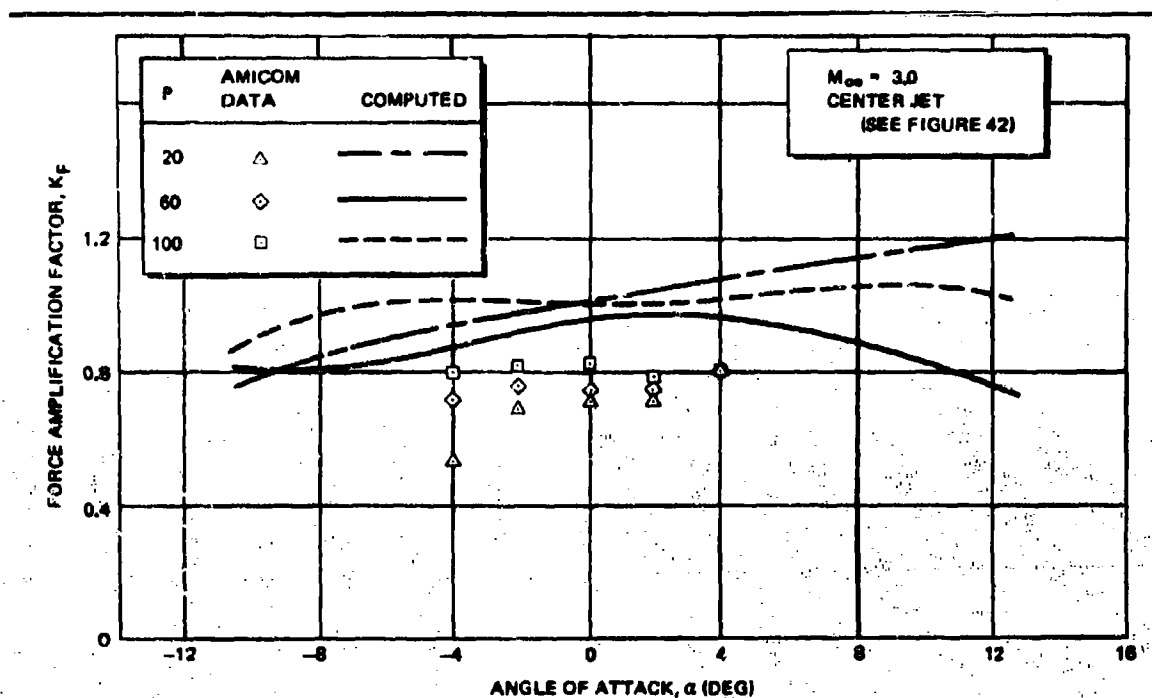


Figure 45. Equivalent Obstacle Analogy Prediction of  $K_F$  Versus  $\alpha$

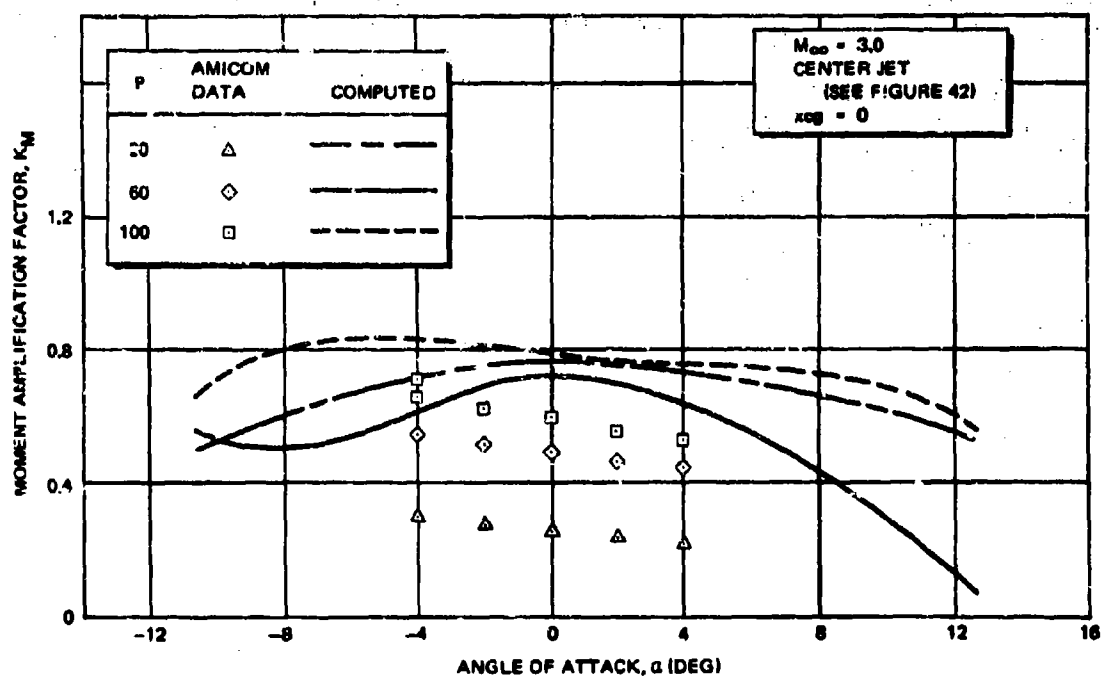


Figure 46. Equivalent Obstacle Analogy Prediction of  $K_M$  Versus  $\alpha$

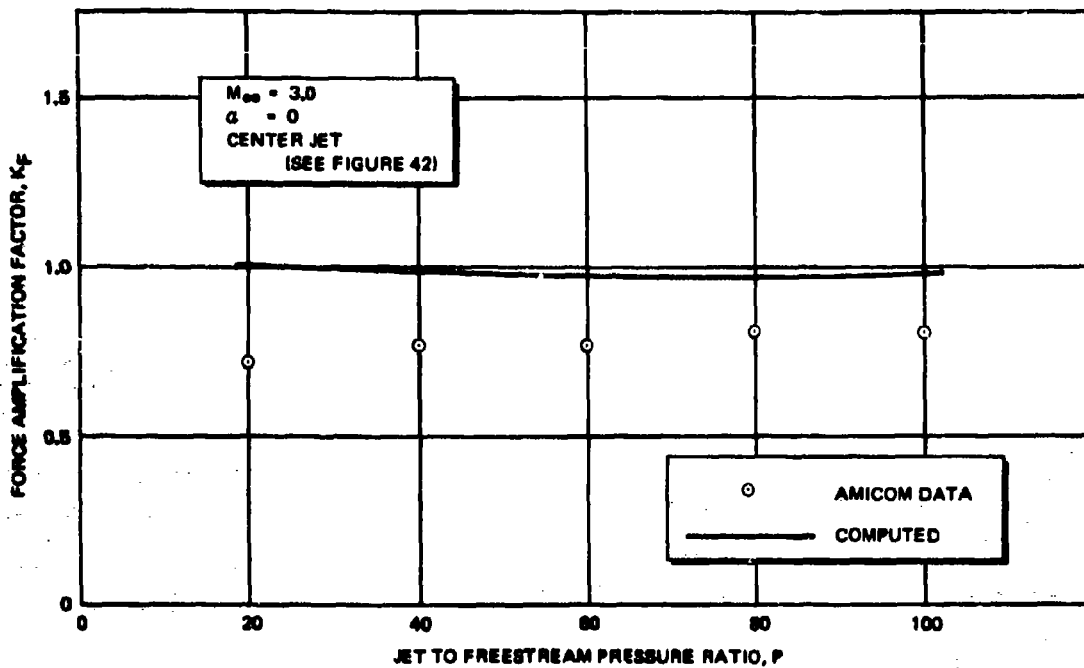


Figure 47. Equivalent Obstacle Analogy Prediction of  $K_F$  Versus  $P$

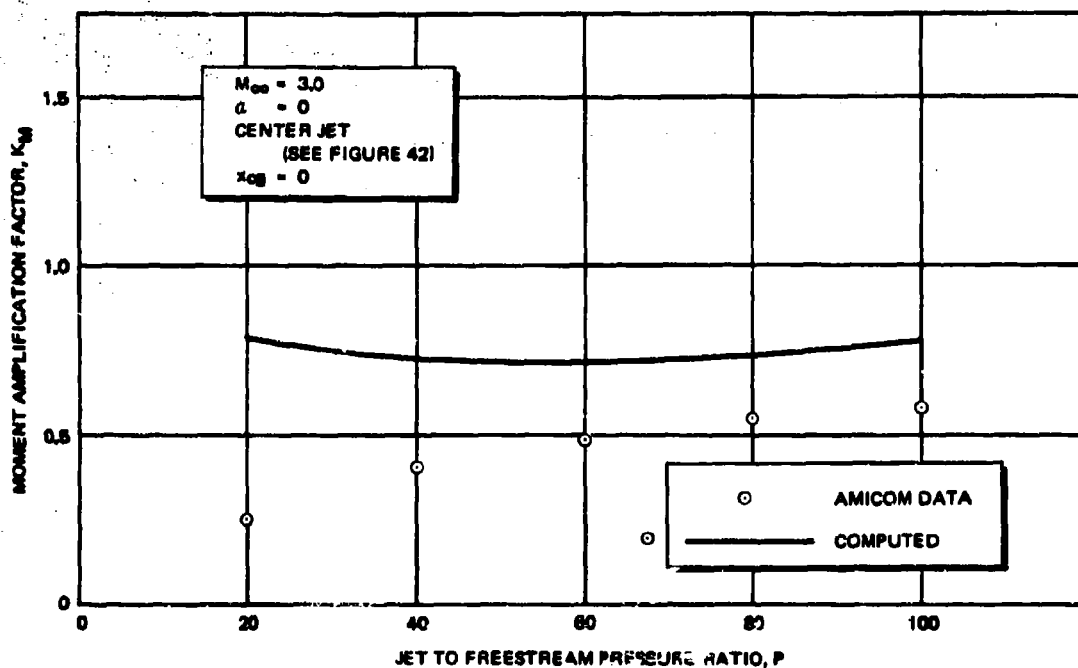


Figure 48. Equivalent Obstacle Analogy Prediction of  $K_M$  Versus  $P$

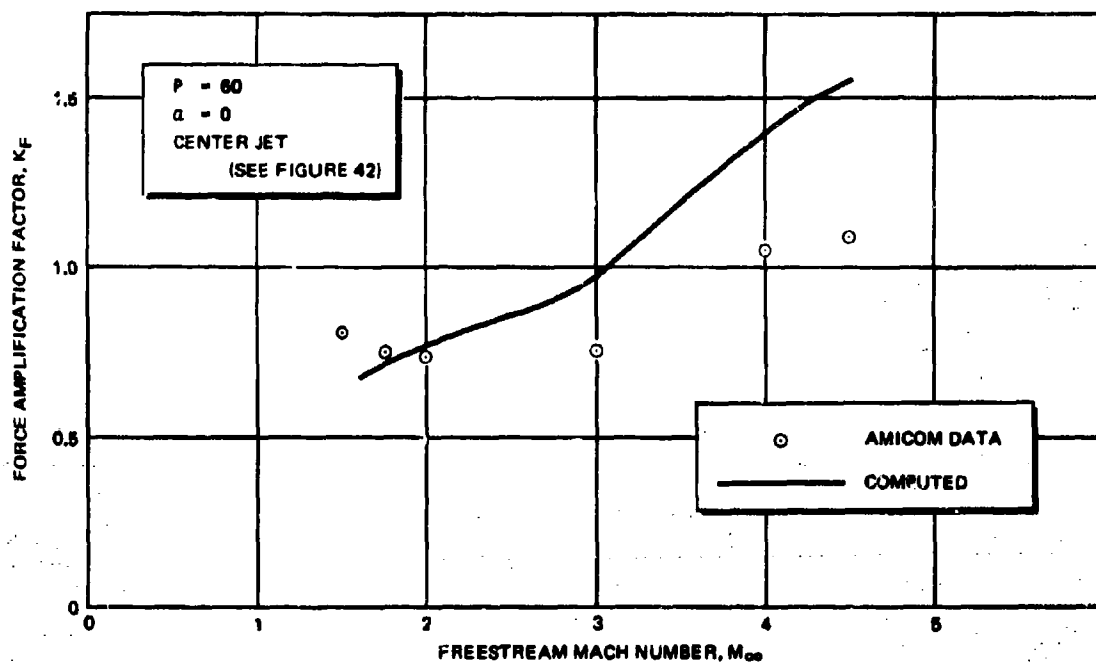


Figure 49. Equivalent Obstacle Analogy Prediction of  $K_F$  Versus  $M_\infty$

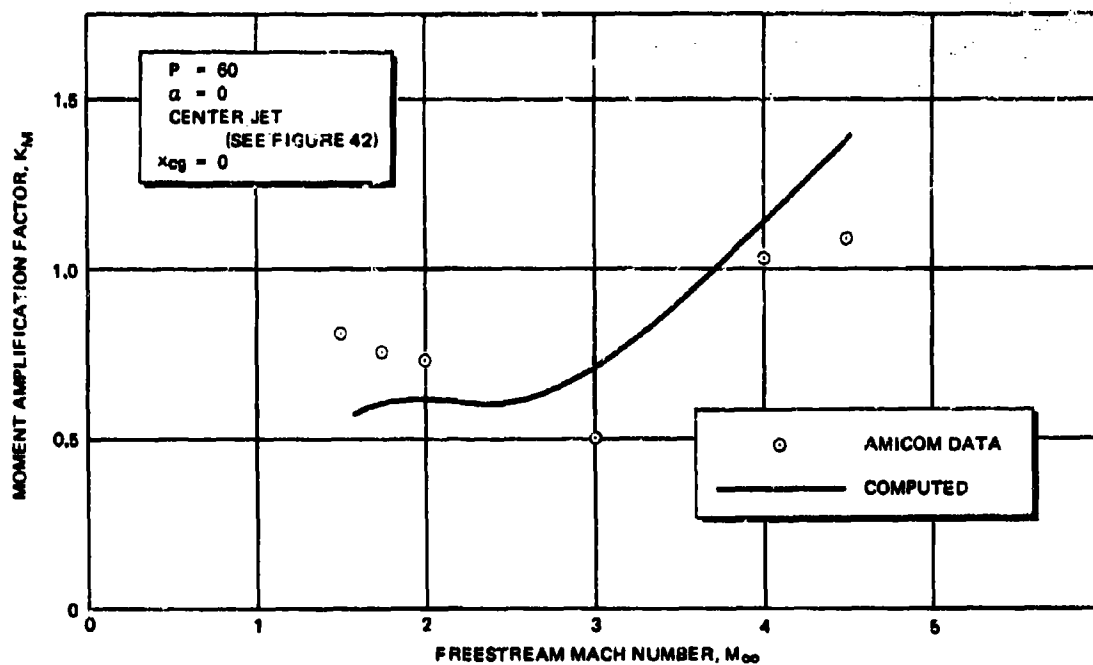


Figure 50. Equivalent Obstacle Analogy Prediction of  $K_M$  Versus  $M_\infty$

**BLANK PAGE**

## Section 5

### JET-FIN INTERFERENCE EFFECTS

Transverse jet-induced interference effects in subsonic or supersonic mainstreams have been divided into the two general categories, near-field effects and fin-interference effects. Near-field effects are confined to the neighborhood of the nozzle and represent the direct JI effect in amplifying or degrading the force and moment which the jet thrust would produce in still air. In the category of fin-interference effects are phenomena assumed to occur many nozzle diameters downstream, where the deflected jet may interact with aerodynamic control fins. The discussions in Sections 2 through 4 pertain to the near-field category of JI effects.

The calculation of fin interference effects has been restricted to vehicle configurations where the fins lie at a considerable distance downstream of the transverse jet nozzle exit. It is assumed that at these downstream distances, the jet is almost aligned with the free stream. It is further assumed that the jet has been reduced to two counterrotating vortices and a region of turbulence whose average axial velocity is almost equal to the free stream velocity. Models have been developed that predict the variation of vortex strength with distance from the nozzle exit and other jet and free stream parameters, for both subsonic and supersonic free-stream Mach numbers. With the strengths and location of the jet-induced vortices known, interference forces and moments due to far downstream interactions between the jet and fins can be calculated. The methods developed in this study are applicable to cruciform missiles at arbitrary flight Mach numbers and attitudes.

A complete solution of the interference problem requires a knowledge of fin-jet interference effects as well as of jet-fin interference effects. That is, the effects of the body and fins upon the jet trajectory, vortex strengths, etc. should be estimated. However, it is assumed here that fin-jet interference effects are small, and that the jet behaves at all times as if it were exhausting into a uniform, infinite crossflow. With this restriction, the calculation of jet-fin interference effects is broken into two parts. First, a semi-empirical model of the jet in an infinite crossflow, valid at large distances from the orifice, is developed. Second, the interference forces induced by the jet are calculated.

#### 5.1 GENERAL CONSIDERATIONS

For subsonic Mach numbers, data such as those shown in Figures 7 and 8 indicate that the major interference pressure disturbances are confined to a distance of five or six Mach disk heights from the

centerline of the nozzle. For supersonic flight Mach numbers, data such as those shown in Figure 51 indicate the major interference normal force occurs less than ten penetration heights downstream of the jet exit. In Figure 51, the normal force increment is defined as

$$\Delta C_Z = (C_Z)_{\text{fin on}} - (C_Z)_{\text{fin off}}$$

with the jet and mainstream flow conditions the same with fin on and fin off. The configuration is described in Reference 19 or 31. The conclusion to be drawn from the limited extent of the major interaction disturbances in either subsonic or supersonic mainstreams is that fins located downstream of this region will encounter relatively small pressure disturbances. However, the resultant interference control moment due to fin interference may still be large.

Some of the data from the AMICOM-CAL tests (References 27 and 28) were obtained with instrumented, cruciform rectangular fins on the model to measure interference forces on the fins. The configuration shown in Figure 4 corresponds to the tests in Reference 27, and for this case the sensitivity of the fin force and moment balance was apparently too small to detect the interference forces. For the tests described in Reference 28, however, a more sensitive balance was used, and significant interference forces were measured.

The data of Burt and Dahlke in Reference 44 show that, for a configuration with opposed transverse jets, the strongest fin interference effects occurred when the fins nearest the jet plumes were placed in a slightly asymmetric position relative to the plume. The most significant fin interference effects appear to be caused by the two counterrotating vortices created by the interaction of the jet and the cross flow. In References 45 and 46, Dahlke has measured the strength of these vortices at one station downstream of the nozzle, based on flow field surveys conducted with a special probe.

In the present study, several assumptions have been made, based on the available experimental data, to derive a semi-empirical mathematical model for jet-fin interference. It is assumed that, in the region where the fins lie, the jet is almost aligned with the free stream. Indeed, it will be assumed that the fins lie within the "vortex zone" of the jet, which has been discussed at the end of Subsection 2.1. Restricting the analysis to small missile angles of attack then permits bringing the entire fin interference problem within the context of the slender-body approximation (i.e., of crossflow velocities that are much smaller than the free-stream velocity). The above restrictions are satisfied by configurations of practical interest, as examination of

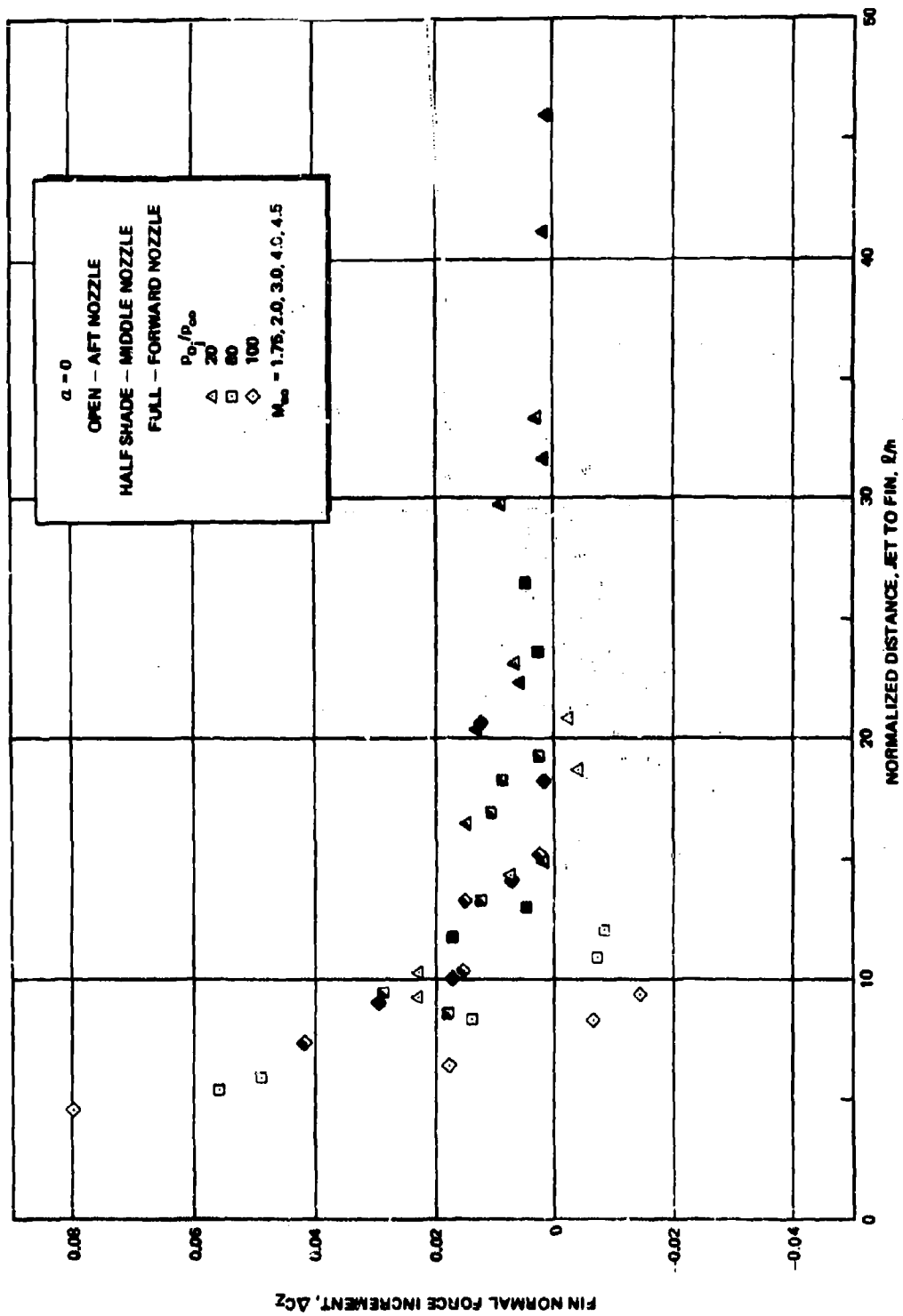


Figure 51. Scale of Fin Interference With Penetration Height



Figure 52 as well as the configurations tested in References 31 and 44 will reveal. Some of the data leading to the assumptions will be illustrated below.

## 5.2 JET PROPERTIES AT LARGE DISTANCES FROM THE NOZZLE

It is known that a jet in a subsonic or supersonic crossflow contains two counterrotating vortices. This is true of subsonic (References 21, 22, and 23), as well as sonic or supersonic, highly underexpanded jets (References 16 and 46). For example, Figure 52, which has been taken from Dahlke's report (Reference 46) clearly shows the two vortex regions. The vectors in the figure represent the Mach number component in a plane perpendicular to the body axis. The circulatory nature of the flow is clearly visible. For subsonic jets, Pratte and Baines in Reference 22 indicate that at large distances from the nozzle the axial velocity in the jet is almost equal to the free stream velocity. Further, the vortices are effectively convected at this velocity, while their strength decays because of viscous dissipation. It is assumed that highly underexpanded sonic or supersonic jets exhausting into subsonic or supersonic streams exhibit similar behavior at large distances from the nozzle.

### 5.2.1 Vortex Strengths in a Subsonic Jet

A semi-empirical model to predict the variation in vortex strength with distance is postulated in this section. It is first assumed that the jet is everywhere subsonic, but similarities between subsonic jets and highly underexpanded jets in subsonic or supersonic crossflows are formulated, which allow the results obtained for subsonic jets to be extended to the latter cases.

The vortices are assumed to be convected downstream at  $U_\infty$  (Figure 53), and the flow is analyzed as an unsteady flow in the  $y$ - $z$  plane. This is consistent with the assumption of crossflow velocities which are small compared to  $U_\infty$ . In the  $y$ - $z$  plane, the jet is represented by two counterrotating vortices located at  $(-y_0, z_0)$  and  $(y_0, z_0)^*$ , and connected by a vortex sheet of vanishing strength as illustrated in Figure 54. The vortex positions and strengths are assumed to depend on time. From one instant of time to another, impulsive pressures of different magnitude would have to be applied across the vortex sheet to generate the fluid motion instantaneously from rest. The resulting impulse  $\underline{I}$  may be calculated from the relation

$$\underline{I} = - \oint_C \rho \phi \underline{n} ds \quad (100)$$

\*As before, these coordinates have been normalized by the nozzle exit diameter.

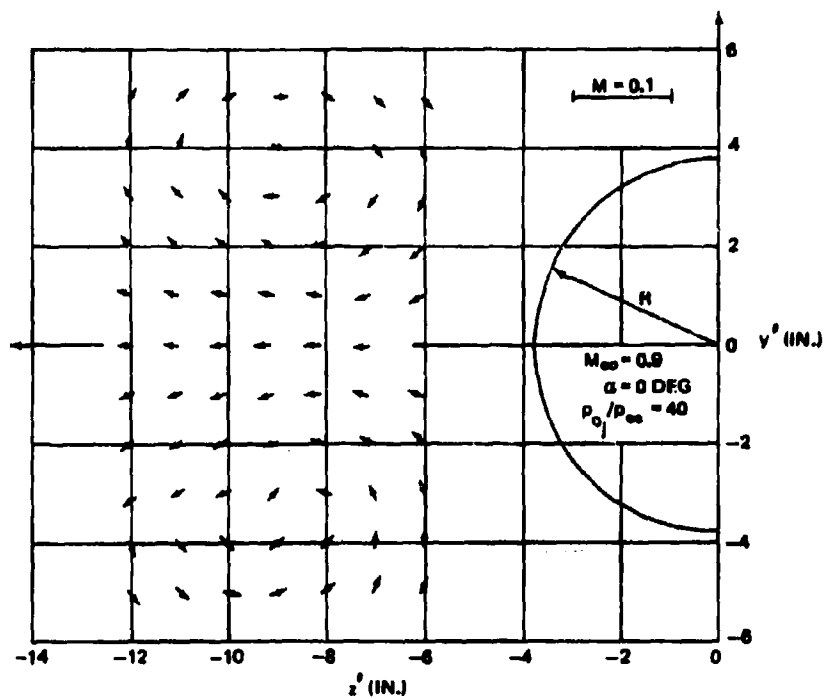


Figure 52. Jet Wake in Free Stream Flow Field at Mach 0.9 and Zero Angle of Attack

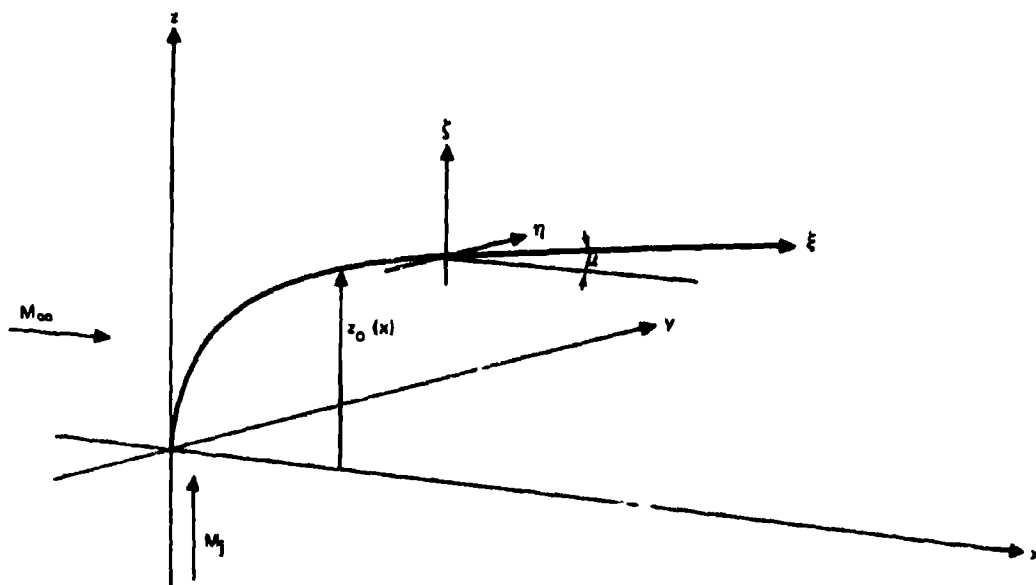


Figure 53. Jet-Oriented Coordinate System

where  $\Phi$  is the potential of the fluid motion, and  $\rho$  is the fluid density. The integral in Equation (100) is evaluated on a path  $C$  enclosing both vortices and their connecting sheet as discussed in Reference 37. For the vortices shown in Figure 54, the potential may be written as:

$$\Phi = \frac{\Gamma}{2\pi} \left\{ \tan^{-1} \left( \frac{z - z_0}{y + y_0} \right) - \tan^{-1} \left( \frac{z - z_0}{y - y_0} \right) \right\} \quad (101)$$

Substituting Equation (101) into Equation (100) and performing the integration, yields:

$$\underline{\Gamma} = \underline{k} (2\rho \Gamma y_0) \quad (102)$$

where  $\underline{k}$  is a unit vector in the  $z$  direction. The rate of change of  $\underline{\Gamma}$  with respect to time is equal to the net force which must be applied to the vortices and connecting sheet system to generate the fluid motion instantaneously from rest, as discussed in Reference 37. This force is given by

$$\underline{\dot{F}} = \frac{d\underline{\Gamma}}{dt} = \underline{k} (2\rho) \frac{d}{dt} (\Gamma y_0) \quad (103)$$

In the present development, it will be assumed that vortex strength and separation must vary in such a way that the net force on the system of vortex sheet and vortices is zero. This assumption has been made by Bryson in Reference 47, in computing lift forces on slender bodies at high angles of attack. Then Equation (103) requires that

$$\frac{d}{dt} (\Gamma y_0) = 0$$

so that

$$\Gamma = \frac{K'}{y_0} \quad (104)$$

where  $K'$  is constant for fixed  $U_\infty/U_j$  and  $d_j$ . Equation (104) implies that if the vortices draw apart their strength must decrease. If viscous dissipation is included, it seems reasonable that the vortex strengths should decay; this model, however, is inviscid, so it is

difficult to explain what happens to the vorticity caused by the decrease in vortex strength. In Bryson's model of separated flow about a body of revolution at high incidence, vorticity generated in the boundary layer about the body is assumed to be "fed" to the separation vortices through the intervening connecting sheets. No such mechanism may be used to account for vorticity lost in the present model, since no external boundaries are present. The only explanation to account for the "lost vorticity" is that as the vortex on one side decays in strength, a small amount of vorticity is carried via the connecting sheet to the plane of symmetry, to be cancelled there by the vorticity of opposite sign arriving from the vortex on the other side.

The vortices shown in Figure 54 will convect upward at the velocity induced by one vortex at the location of the other. This velocity is given by

$$\frac{dz_o}{dt} = \frac{\Gamma}{4\pi y_o d_j}$$

and, since the vortices were assumed to convect downstream at  $U_\infty$ ,

$$\frac{dz_o}{dx} = \tan \mu = \frac{\Gamma}{4\pi U_\infty y_o d_j}$$

where the angle  $\mu$  is defined in Figure 53.

If  $\mu$  is assumed to be small so that

$$\tan \mu \sim \mu \sim \sin \mu$$

then

$$\frac{dz_o}{d\xi} = \frac{\Gamma}{4\pi U_\infty y_o d_j} \quad (105)$$

Given the dependence of  $y_o$  on  $\xi$ , Equations (104) and (105) may be used to calculate the change in  $\Gamma$  and the vortex trajectory.

In Reference 22, Pratte and Baines find that they can correlate their data for jet trajectory and thickness by the use of variables scaled by the jet to free-stream velocity ratio such as

$$\chi = \sigma \xi$$

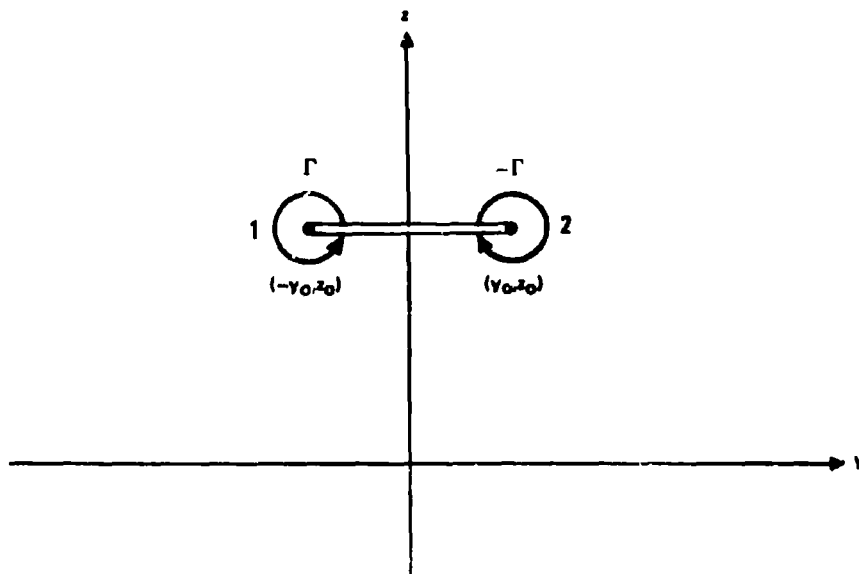


Figure 54. Jet-Induced Vortices in the Crossflow Plane

where  $\xi$  is the coordinate along the jet trajectory shown in Figure 53 and

$$\sigma = \frac{U_{\infty}}{U_j}$$

Pratte and Baines also find that, in the vortex region, the jet cross-section grows as  $\chi^{1/3}$ , apparently in self-similar fashion (Reference 22). This is the same behavior exhibited by turbulent jets in coaxial external streams, when the difference between jet and free stream velocities is small (Reference 48). In the present case it will be assumed that the vortices also spread as  $\chi^{1/3}$ , so that

$$Y_o = Y_v \chi^{\frac{1}{3}} \quad (106)$$

where

$$Y_o = \sigma y_o$$

and  $Y_v$  is a constant which has the same value for all velocity ratios and jet diameters.

Substituting Equation (104) into Equation (105) yields

$$\frac{dz_o}{d\xi} = \left( \frac{K'}{4\pi U_\infty d_j} \right) \frac{1}{y_o^2}$$

Written in terms of similarity variables  $\chi$ ,  $Y_o$ , and

$$Z_o = \sigma z_o,$$

this becomes

$$\frac{dZ_o}{d\chi} = \left[ \frac{K' \sigma^2}{4\pi U_\infty d_j} \right] \frac{1}{Y_o^2}$$

and substitution of Equation (106) then yields

$$\frac{dZ_o}{d\chi} = \left[ \frac{K' \sigma^2}{4\pi U_\infty d_j} \right] \frac{1}{Y_v^2 \chi^{2/3}} \quad (107)$$

The data of Pratte and Baines show that  $Z_o$  is a universal function of  $\chi$ , and consequently it follows from Equation (107) that

$$\frac{K' \sigma^2}{4\pi U_\infty d_j} = K \quad (108)$$

where  $K$  is a universal constant which has the same value for all velocity ratios. Furthermore, it is possible to integrate Equation (107) and obtain

$$Z_o = \frac{3K}{Y_v^2} \chi^{1/3} \quad (109)$$

The behavior predicted by Equation (109) for the jet trajectory is verified by the data of Pratte and Baines, who measured:

$$Z_0 = (\text{const.}) \chi^{1/3}$$

as shown in Figure 5 of Reference 22. Finally, writing Equation (104) in terms of similarity variables leads to the result

$$\Gamma^* = \frac{K}{Y_v \chi^{1/3}} \quad (110)$$

where

$$\Gamma^* \equiv \left( \frac{\Gamma}{4\pi U_\infty d_j} \right) \sigma \quad (111)$$

Equations (110) and (111) state that the product of normalized vortex strengths  $(\Gamma/4\pi U_\infty d_j)$  and velocity ratio is a universal function of the similarity variable  $\chi$ .

In summary, the postulated variation in vortex spacing  $Y_0$ , leads to a vortex strength variation which can be used to predict the correct form for the jet trajectory. Indirectly, at least, this appears to verify the proposed relation between vortex strength and spacing. The results derived are expected to hold in the vortex zone, which has been found to lie downstream of the value  $\chi = 5$ , as shown in Reference 22. Two empirical constants have been introduced,  $K$  and  $Y_v$ . These will be calculated using Dahlke's measurements of vortex strength and positions. Before this can be done, it is necessary to postulate the equivalence between the subsonic and a sonic, highly underexpanded jet.

### 5.2.2 Equivalence Between Subsonic and Sonic Underexpanded Jets

The equivalence between the subsonic and sonic jets is formulated in terms of a scaling length. For underexpanded jets, the scale chosen is proportional to the Mach disk height or jet penetration height, depending on whether the free stream is subsonic or supersonic.

Equivalent similarity variables are defined as follows:

$$\begin{aligned} X &= \sigma_e \left( \frac{d_j}{d_e} \right) \xi & Y &= \sigma_e \left( \frac{d_j}{d_e} \right) y \\ X &= \sigma_e \left( \frac{d_j}{d_e} \right) x & Z &= \sigma_e \left( \frac{d_j}{d_e} \right) z \end{aligned} \quad (112)$$

where:

$$\sigma_e = \frac{\rho_\infty U_\infty}{\rho_e U_e}$$

$d_e$ : equivalent subsonic jet diameter

$\rho_e U_e$ : equivalent subsonic jet mass flux per unit area

It is assumed that the equivalent subsonic jet and the actual jet have the same mass flux, so that:

$$\rho_e U_e d_e^2 = \rho_j U_j d_j^2$$

Thus,

$$\frac{\sigma_e}{d_e} = \frac{\rho_\infty U_\infty}{\rho_e U_e} \frac{1}{d_e} = \left( \frac{\rho_\infty U_\infty}{\rho_j U_j} \right) \left( \frac{d_e}{d_j} \right) \frac{1}{d_j} \quad (113)$$

If it is assumed that

$$T_{o_j} = T_{o_\infty},$$

the mass flux per unit area ratio may be written in the form



$$\frac{\rho_{\infty} U_{\infty}}{\rho_j U_j} = \left( \frac{P_{oj}}{P_j} \right) \sqrt{\frac{T_j}{T_{oj}}} \left( \frac{P_{\infty}}{P_{oj}} \right) \sqrt{\frac{T_{oj}}{T_{\infty}}} \frac{M_{\infty}}{M_j}$$

and for a sonic nozzle, this becomes:

$$\frac{\rho_{\infty} U_{\infty}}{\rho_j U_j} = \left[ \frac{\gamma + 1}{2} \right]^{\frac{\gamma + 1}{2(\gamma - 1)}} \frac{P_{\infty}}{P_{oj}} \sqrt{\frac{T_{oj}}{T_{\infty}}} M_{\infty} \quad (114)$$

All variables in Equation (114) are known, but in Equation (113) it is necessary to have a relation between the equivalent and actual jet diameters. A plausible characteristic scale is suggested by the behavior of the internal shock system in a highly underexpanded plume.

Considering first the case of subsonic mainstream Mach numbers, it is assumed that the plume behaves as if it were exhausting into still air. Then Reference 30 shows that for high values of the pressure ratio ( $P = P_{oj}/P_{\infty}$ ), the location of the terminal shock or Mach disk is proportional to  $P^{1/2}$  multiplied by the jet exit diameter. Reference 30 also shows that the diameter of the Mach disk varies approximately as  $P^{1/2}$  multiplied by the nozzle exit diameter. Since the equivalent subsonic jet diameter should depend on the subsonic conditions which exist in the jet downstream of the Mach disk, it will be assumed that

$$\left( \frac{d_e}{d_j} \right)_{M_{\infty} < 1} = \delta \sqrt{P} \quad (115)$$

Then, substituting Equations (114) and (115) into Equation (113) leads to the final relation

$$\left( \frac{\sigma_e}{d_e} \right)_{M_{\infty} < 1} = \left[ \frac{\gamma + 1}{2} \right]^{\frac{\gamma + 1}{2(\gamma - 1)}} M_{\infty} \sqrt{\frac{T_{oj}}{T_{\infty}}} \frac{\delta}{d_j \sqrt{P}} \quad (116)$$

where the quantity  $\delta$  is another empirical constant to be obtained from data.

Considering now the case of supersonic free-stream Mach numbers, the relation for the characteristic scale must be changed. As discussed in Reference 19, the flow field to some extent scales with the jet penetration height  $h_s$ . An expression for this quantity is derived in Reference 19. It may be written in the form

$$\left(\frac{h_s}{d_j}\right)^2 = \left(\frac{2}{\gamma+1}\right)^{\frac{1}{\gamma-1}} \left[ \frac{4P}{C_x + \frac{2}{\gamma M_\infty^2}} \right] \frac{1}{\gamma M_\infty^2}$$

where  $C_x$  denotes the drag coefficient of the equivalent obstacle. If, as in Reference 19, it is assumed that:

$$C_x + \frac{2}{\gamma M_\infty^2} \approx 1$$

then the above becomes:

$$\frac{h_s}{d_j} \approx \left[ \frac{2}{\gamma+1} \right]^{\frac{1}{2(\gamma-1)}} \left( \frac{2}{\sqrt{\gamma}} \right) \frac{\sqrt{P}}{M_\infty} \quad (117)$$

It is also shown in Reference 19 that the Mach disk height is directly proportional to the penetration height  $h_s$ . For supersonic free-stream Mach numbers, then, Equation (117) suggests a relationship for the equivalent jet diameter in the form

$$\left(\frac{d_e}{d_j}\right)_{M_\infty > 1} = \frac{\epsilon}{M_\infty} \sqrt{P} \quad (118)$$

where  $\epsilon$  is an empirical constant. For supersonic free streams, Equation (113) then becomes

$$\left(\frac{\sigma_e}{d_e}\right)_{M_\infty > 1} = \left[\frac{\gamma+1}{2}\right]^{\frac{\gamma+1}{2(\gamma-1)}} \sqrt{\frac{T_{o_\infty}}{T_\infty}} \left[\frac{\epsilon}{d_j \sqrt{P}}\right] \quad (119)$$

### 5.2.3 Evaluation of Empirical Constants and Comparisons with Data

Reference 46 contains data on vortex strengths and positions for a sonic, highly underexpanded jet exhausting from an ogive-cylinder for  $M_\infty = 0.9$  and 1.2. The data were obtained by surveying the flow field at a fixed station downstream of the jet nozzle and varying  $(p_{0j}/p_\infty)$  for each value of  $M_\infty$ . In using these results, the effects of the body will be neglected and it will be assumed that the jet behaves as if it were exhausting into an infinite stream.

To calculate the values of  $\delta$  and  $\epsilon$  defined in Subsection 5.2.2, some of the results obtained by Pratte and Baines in Reference 22 will be used.

In particular, if it is assumed that the vortices lie in the same plane as the jet centerline, then the empirical relation in Figure 4 of Reference 22 yields the vortex height as a function of the distance  $X$  from the nozzle centerline (Figure 53) in the form

$$Z_o = (1.76) X^{(0.28)} \quad (120)$$

Using Equation (112), Equation (120) may be written in the form

$$\frac{\sigma_e}{d_e} = (\bar{x})^{0.389} \left[\frac{1.76}{\bar{z}_o}\right]^{1.389}$$

Then substituting for  $(\sigma_e/d_e)$  from Equation (116) in the subsonic case, and from Equation (119) in the supersonic case:

$$\delta|_{M_\infty=0.9} = (0.575) \frac{(\bar{x})^{0.389}}{(\bar{z}_o)^{1.389}} \sqrt{P} \quad (121)$$

$$\epsilon|_{M_\infty=1.2} = (0.492) \frac{(\bar{x})^{0.389}}{(\bar{z}_0)^{1.389}} \sqrt{P} \quad (122)$$

The above relations have been written for the specific cases  $M_\infty = 0.9$  and  $M_\infty = 1.2$ , for which Dahlke surveyed the flow field. Since surveys were conducted at

$$\bar{x} = 47.465 \text{ in.}$$

downstream of the nozzle, substitution of this number in Equations (121) and (122) yields:

$$\delta|_{M_\infty=0.9} = (2.582) \frac{\sqrt{P}}{(\bar{z}_0)^{1.389}}$$

$$\epsilon|_{M_\infty=1.2} = (2.207) \frac{\sqrt{P}}{(\bar{z}_0)^{1.389}}$$

Figure 55 shows graphs of the above relations as calculated from Dahlke's data in Reference 46. Although there is considerable scatter, for pressure ratios greater than 10 the points do seem to lie on a constant line. Based upon Figure 55 for  $P > 10$ , the average values

$$\delta = 1.40 \quad (123a)$$

$$\epsilon = 1.04 \quad (123b)$$

have been chosen.

The theoretical model for the jet vortices implies that certain combinations of parameters should be independent of the pressure ratio. In particular, the product of normalized vortex strength and separation should be constant. From Equation (110)

$$I^* Y_0 = K$$

Using Equations (111) and (112)

$$\left( \frac{\Gamma \bar{Y}_0}{a_\infty} \right) \left[ \frac{1}{4\pi M_\infty} \left( \frac{v_e}{d_e} \right)^2 \right] = K \quad (124)$$

For the subsonic case, Equation (116) is substituted in Equation (124) above. This results in the expression:

$$(K)_{M_\infty < 1} = \left( \frac{\Gamma \bar{Y}_0}{a_\infty P} \right) \left[ \frac{1}{4\pi} \left( \frac{\gamma+1}{2} \right)^{\frac{\gamma+1}{\gamma-1}} M_\infty \left( \frac{T_{0_\infty}}{T_\infty} \right) \left( \frac{\delta}{d_j} \right)^2 \right] \quad (125)$$

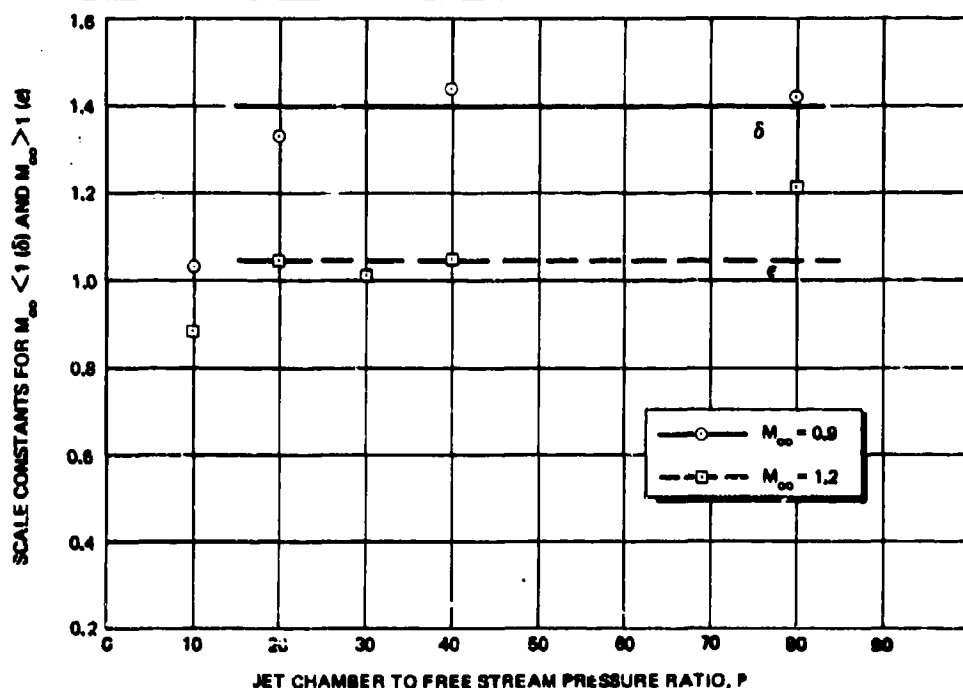


Figure 55. Scale Constants for Equivalent Subsonic Jet Diameters

For supersonic free streams, substitution of Equation (119) into Equation (124) yields

$$(K)_{M_\infty > 1} = \left( \frac{\Gamma \bar{y}_o}{a_\infty P} \right) \left[ \frac{1}{4\pi} \left( \frac{\gamma+1}{2} \right)^{\frac{\gamma+1}{\gamma-1}} \frac{1}{M_\infty} \left( \frac{T_{o_\infty}}{T_\infty} \right) \left( \frac{\epsilon}{d_j} \right)^2 \right] \quad (126)$$

Since the terms in brackets in Equations (125) and (126) are constant for fixed  $M_\infty$ , Dahlke's data should indicate that the term  $(\Gamma \bar{y}_o / a_\infty P)$  is independent of the pressure ratio at each value of  $M_\infty$ . This seems to be the case, as shown in Figure 56; at least to within approximately 11% of the averages indicated by the solid and dotted lines in Figure 56. The values chosen are:

$$\left( \frac{\Gamma \bar{y}_o}{a_\infty P} \right)_{M_\infty < 1} = 0.0615 \quad (127a)$$

$$\left( \frac{\Gamma \bar{y}_o}{a_\infty P} \right)_{M_\infty > 1} = 0.0512 \quad (127b)$$

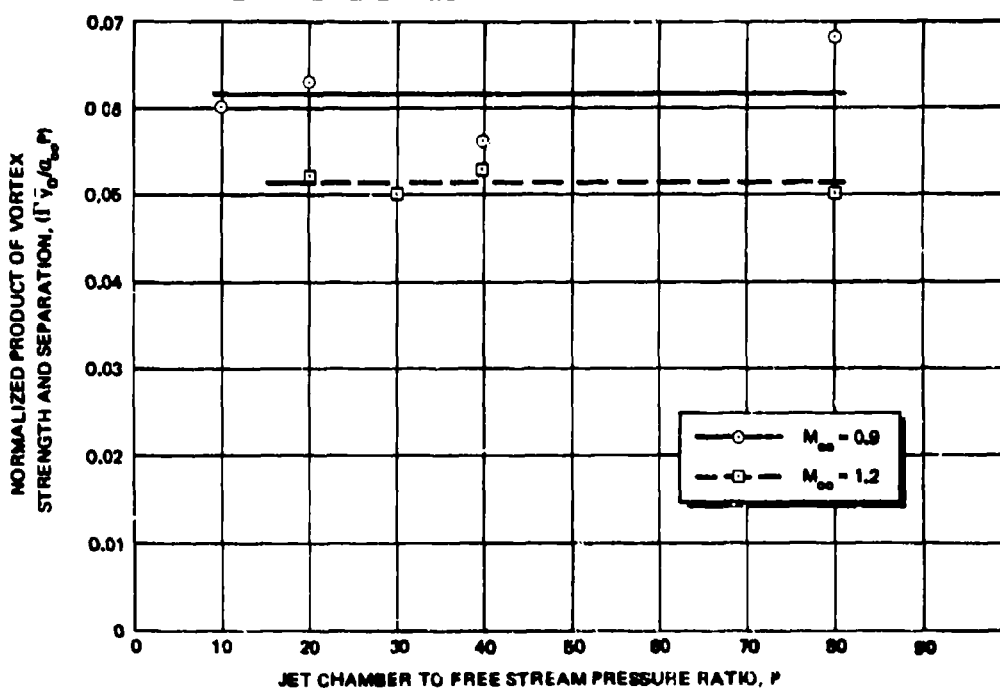


Figure 56. Constant Product of Vortex Strength and Separation

These values, along with  $\delta$  and  $\epsilon$  as given in Equations (123a) and (123b), are substituted into Equations (125) and (126), respectively. The appropriate Mach numbers and  $\gamma = 1.4$  are also substituted. The results are

$$(K)_{M_\infty < 1} = 0.155 \quad (128a)$$

$$(K)_{M_\infty > 1} = 0.073 \quad (128b)$$

Equations (128) point to an inconsistency in the postulated equivalence between subsonic and underexpanded jets. Since the constant  $K$  is presumed to be a universal constant characteristic of the subsonic jet, the values of  $K$  calculated starting from  $M_\infty < 1$  data or  $M_\infty > 1$  data should coincide. Since they do not, it appears that to some extent the postulated equivalences are not valid. Taken individually, however, both the  $M_\infty < 1$  and  $M_\infty > 1$  data indicate that  $K$  is a constant, and using the appropriate value of  $K$  for each case leads to good agreement between predicted and measured vortex strengths, as is shown below. The best way to resolve the above difficulty would be to evaluate  $K$  by using experimentally determined vortex strengths for a subsonic jet directly, but such data are unfortunately not available.

Referring to Equations (106) and (109), the model predicts that the following ratio should be constant.

$$\frac{Y_o}{Z_o} = \frac{\bar{Y}_o}{\bar{Z}_o} = \frac{Y_v^3}{3K}$$

This ratio is shown in Figure 57, for both the  $M_\infty < 1$  and the  $M_\infty > 1$  cases. The data again indicate that for  $P > 10$ , the ratio is approximately independent of  $P$ , as predicted. The average values:

$$\frac{Y_v^3}{3K} \quad M_\infty < 1 = 0.60$$

and

$$\frac{Y_v^3}{3K} \quad M_\infty > 1 = 0.261$$

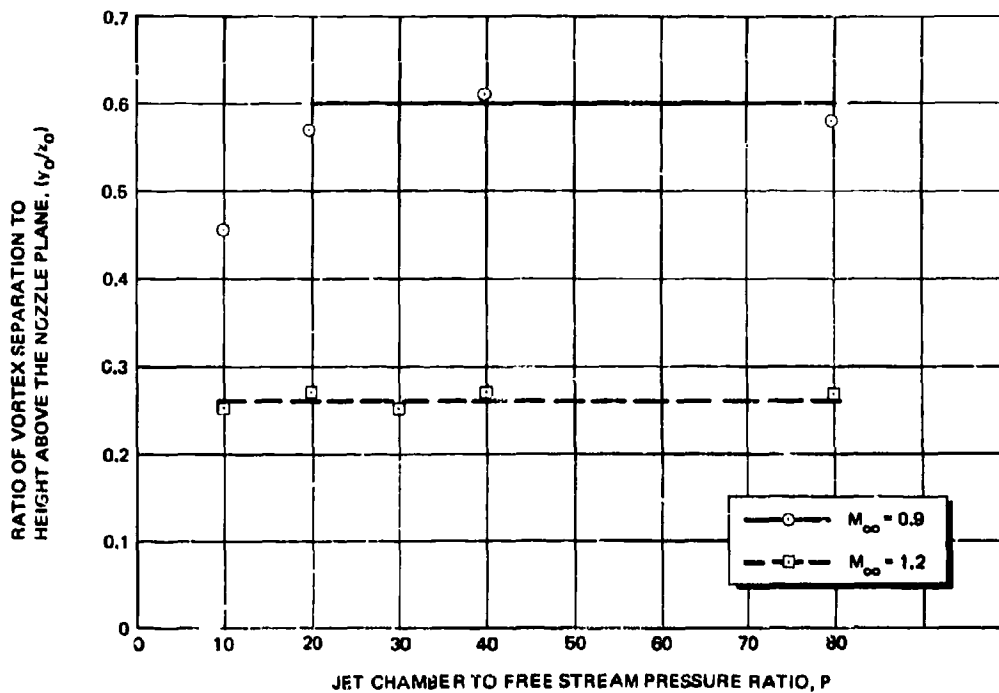


Figure 57. Constant Ratio of Vortex Separation to Height Above the Nozzle Plane

have been chosen. Using Equations (128a) and (128b) these lead to

$$(Y_v)_{M_\infty < 1} = 0.653 \quad (129a)$$

$$(Y_v)_{M_\infty > 1} = 0.385$$

Again, some inconsistency is evident since these are not the same.

The above analysis indicates that vortex strength varies as a function of the similarity variable,  $\chi$ , which is dependent upon distance along the jet axis, pressure ratio  $P$ , and the free-stream Mach number  $M_\infty$ . Dahlke's measurements in Reference 46 were taken at a fixed location downstream of the nozzle, but since the pressure ratio was varied, the similarity variable  $\chi$  has been varied. The model should therefore be able to predict the variation of  $\Gamma$  with pressure ratio. Combining Equations (109), (110), and (120), the following relation is obtained:

$$\Gamma^* = \frac{3K^2}{Y_v^3} \frac{1}{(1.76) \times 0.28}$$



Substituting for  $X$  and  $\Gamma$  from Equations (111) and (112), and substituting the appropriate numerical constants it is possible to arrive at the following expressions:

$$\left(\frac{\Gamma}{a_{\infty}}\right)_{M_{\infty} < 1} = 0.065 P^{0.64} \quad (\text{inches}) \quad (130)$$

$$\left(\frac{\Gamma}{a_{\infty}}\right)_{M_{\infty} > 1} = 0.114 P^{0.64} \quad (\text{inches}) \quad (131)$$

The above results hold for  $\bar{x} = 47.465$  in., which is the station downstream of the orifice at which flow field surveys were conducted in Reference 46. The above equations are compared to the data in Figure 58, and it is evident that the agreement is quite good. The formulas developed above will be used for predicting vortex strengths and positions at the aft fin location, and thus for calculating jet-fin interference forces and moments.

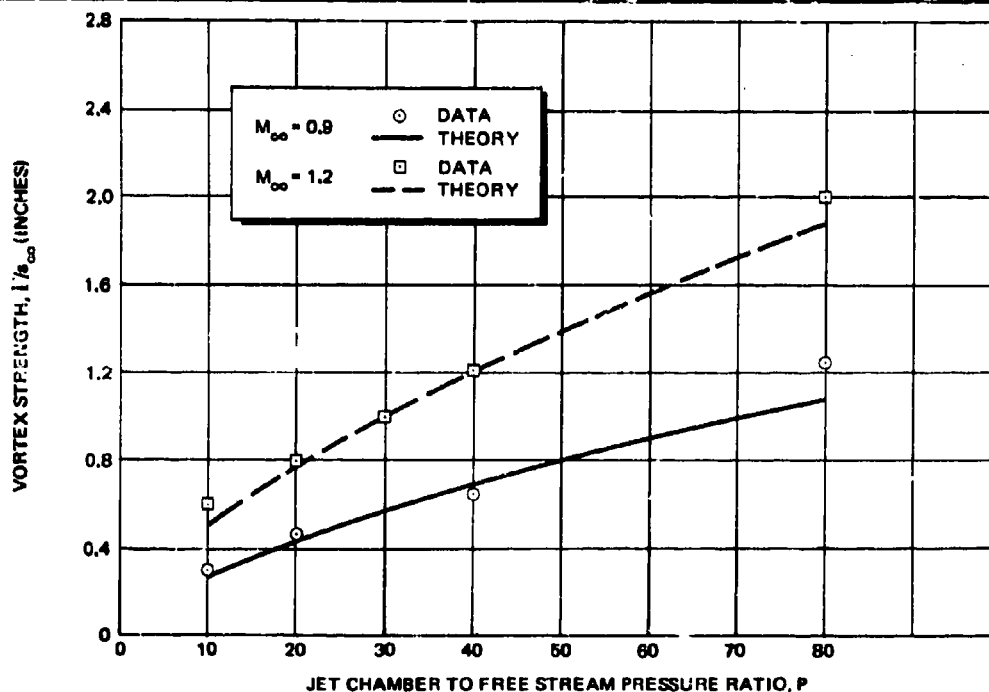


Figure 58. Comparison of Predicted and Experimental Vortex Strengths

### 5.3 JET-FIN INTERFERENCE FORCES AND MOMENTS

The interference effects calculated are the incremental forces and moments acting on the fins alone, which would be produced by turning on a control jet with the missile at given angles of incidence and bank. The general approach is to first obtain the additional upwash which the jet vortices produce at the fin location, and then use simple two-dimensional strip theory for calculating forces and moments on the fins.

Reference axes and angles which are used in the calculation of forces and moments are shown in Figure 59. The missile attitude relative to the free stream coordinates ( $x^*$ ,  $y^*$ ,  $z^*$ ) is defined by the angles of incidence,  $\alpha$ , and of bank,  $\phi$ , as in Reference 49. As noted in the figure, however, the missile is pitched and banked about axes centered at the nozzle station, instead of about the nose. Forces and moments are defined with respect to the body-oriented coordinate system ( $x'$ ,  $y'$ ,  $z'$ ). It will be assumed throughout that only one control jet is turned on; that the jet is sonic; and that the nozzle is aligned with one of four cruciform fins, as shown in Figure 59.

#### 5.3.1 Vortex Strengths and Vortex Locations in the Body-Oriented Coordinate System

Let  $l$  denote the distance along the body axis between the nozzle and the midpoint of the fin's geometric mean chord (assumed to be approximately the fin center of pressure). For purposes of calculating interference effects, it is necessary to know the strength and location of the jet vortices. Consequently, a jet-oriented coordinate system is introduced, with suitable transformations defined below. As the missile pitches and banks, it is assumed that the jet remains aligned with the free stream, although the axis of the nozzle banks with the missile. When the angle of incidence is different from zero, the jet will no longer be normal to the free stream at the nozzle, but this effect is neglected because it is small for small angles of attack.

Coordinate transformations between the ( $x^*$ ,  $y^*$ ,  $z^*$ ) axes and the body-oriented ( $x'$ ,  $y'$ ,  $z'$ ) axes system are given in Reference 49. They are:

$$x' = x^* \cos \alpha - z^* \sin \alpha \quad (132a)$$

$$y' = -x^* (\sin \alpha \sin \phi) + y^* \cos \phi - z^* (\cos \alpha \sin \phi) \quad (132b)$$

$$z' = x^* (\sin \alpha \cos \phi) + y^* \sin \phi + z^* (\cos \alpha \cos \phi) \quad (132c)$$

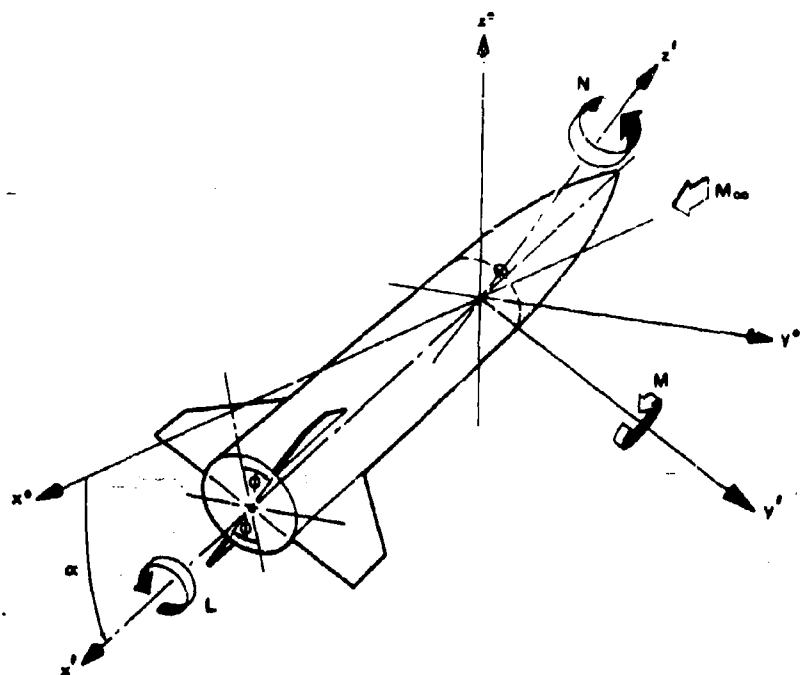


Figure 59. Reference Axes for Fin Interference Calculations

New reference axes are now introduced, denoted by  $(x'', y'', z'')$ . These are also centered along the body centerline, at the nozzle station. The  $x''$  coordinate is aligned with the free-stream direction, and one plane of the system coincides with the plane defined by the free-stream (or  $x^*$ ) direction and the nozzle centerline (or  $z'$ ) direction. It is therefore possible to define the unit base vectors ( $\underline{i}''$ ,  $\underline{j}''$ ,  $\underline{k}''$ ) for this new coordinate system as follows:

$$\underline{i}'' = \underline{i}^* \quad (133a)$$

$$\underline{j}'' = \frac{(\underline{k}' \times \underline{i}^*)}{|\underline{k}' \times \underline{i}^*|} \quad (133b)$$

$$\underline{k}'' = \underline{i}'' \times \underline{j}'' = \underline{i}^* \times \left[ \frac{\underline{k}' \times \underline{i}^*}{|\underline{k}' \times \underline{i}^*|} \right] = \frac{\underline{k}' - \underline{i}^* (\underline{i}^* \cdot \underline{k}')}{|\underline{k}' \times \underline{i}^*|} \quad (133c)$$

The  $\underline{i}$ ,  $\underline{j}$ , and  $\underline{k}$  vectors correspond to the  $x$ ,  $y$ , and  $z$  directions, respectively, in whatever coordinate system is indicated by the superscript. Equation (133b) defines the  $\underline{j}''$  vector as being normal to the plane defined by the free-stream direction and the nozzle centerline, and Equation (133c) defines the  $\underline{k}''$  vector as being normal to the  $\underline{i}''$  and

$\underline{j}''$  vectors. Using the transformation in Equations (132), it is possible to derive the relations between the  $(x^*, y^*, z^*)$  axis base vectors and the  $(x', y', z')$  axis base vectors. These are:

$$\underline{i}^* = \underline{i}' (\cos\alpha) - \underline{j}' (\sin\alpha \sin\phi) + \underline{k}' (\sin\alpha \cos\phi) \quad (134a)$$

$$\underline{j}^* = \underline{j}' (\cos\phi) + \underline{k}' (\sin\phi) \quad (134b)$$

$$\underline{k}^* = -\underline{i}' (\sin\alpha) - \underline{j}' (\cos\alpha \sin\phi) + \underline{k}' (\cos\alpha \cos\phi) \quad (134c)$$

Substitution of Equations (134) into Equations (133) then gives:

$$\underline{i}'' = \underline{i}' (\cos\alpha) - \underline{j}' (\sin\alpha \sin\phi) + \underline{k}' (\sin\alpha \cos\phi) \quad (135a)$$

$$\underline{j}'' = \underline{i}' \left[ \frac{\sin\alpha \sin\phi}{\sqrt{1 - \sin^2\alpha \cos^2\phi}} \right] + \underline{j}' \left[ \frac{\cos\alpha}{\sqrt{1 - \sin^2\alpha \cos^2\phi}} \right] \quad (135b)$$

$$\begin{aligned} \underline{k}'' = & -\underline{i}' \left[ \frac{\sin\alpha \cos\alpha \cos\phi}{\sqrt{1 - \sin^2\alpha \cos^2\phi}} \right] + \underline{j}' \left[ \frac{\sin^2\alpha \sin\phi \cos\phi}{\sqrt{1 - \sin^2\alpha \cos^2\phi}} \right] \\ & + \underline{k}' \sqrt{1 - \sin^2\alpha \cos^2\phi} \end{aligned} \quad (135c)$$

With the base vector transformation given by Equations (135), it is easy to arrive at the coordinate transformations:

$$\begin{aligned} x' = & x'' [\cos\alpha] + y'' \left[ \frac{\sin\alpha \sin\phi}{\sqrt{1 - \sin^2\alpha \cos^2\phi}} \right] - \\ & - z'' \left[ \frac{\sin\alpha \cos\alpha \cos\phi}{\sqrt{1 - \sin^2\alpha \cos^2\phi}} \right] \end{aligned} \quad (136a)$$

$$y' = -x'' [\sin\alpha \sin\phi] + y'' \left[ \frac{\cos\alpha}{\sqrt{1 - \sin^2\alpha \cos^2\phi}} \right] + z'' \left[ \frac{\sin^2\alpha \sin\phi \cos\phi}{\sqrt{1 - \sin^2\alpha \cos^2\phi}} \right] \quad (136b)$$

$$z' = x'' [\sin\alpha \cos\phi] + z'' \sqrt{1 - \sin^2\alpha \cos^2\phi} \quad (136c)$$

Finally, the jet-oriented  $(\bar{x}, \bar{y}, \bar{z})$  coordinate system is defined. It is the same as the  $(x'', y'', z'')$  axis system, but its origin is located at the nozzle exit instead of at the axis of the body. Letting  $R$  denote the radius of the missile at the nozzle location, the transformation between jet-oriented and body-oriented coordinates is:

$$x' = \bar{x} [\cos\alpha] + \bar{y} \frac{\sin\alpha \sin\phi}{\sqrt{1 - \sin^2\alpha \cos^2\phi}} - \bar{z} \frac{\sin\alpha \cos\alpha \cos\phi}{\sqrt{1 - \sin^2\alpha \cos^2\phi}} \quad (137a)$$

$$y' = -\bar{x} [\sin\alpha \sin\phi] + \bar{y} \frac{\cos\alpha}{\sqrt{1 - \sin^2\alpha \cos^2\phi}} + \bar{z} \frac{\sin^2\alpha \sin\phi \cos\phi}{\sqrt{1 - \sin^2\alpha \cos^2\phi}} \quad (137b)$$

$$z' = \bar{x} [\sin\alpha \cos\phi] + \bar{z} \sqrt{1 - \sin^2\alpha \cos^2\phi} + R \quad (137c)$$

The equations for vortex strengths and positions derived in Subsection 5.1 are based upon the  $(\bar{x}, \bar{y}, \bar{z})$  coordinate system. For purposes of computing fin interference forces and moments, it is desired to know the location and strengths of the jet vortices at the body station located at distance  $l$  downstream of the nozzle station, and in a plane perpendicular to the body axis. The coordinates of the fin station in the body-fixed system are:

$$\begin{aligned} x' &= l \\ y' &= 0 \\ z' &= 0 \end{aligned}$$

Letting the subscript  $f$  denote the coordinates of this same point in the jet-oriented system, Equations (137) may be inverted to obtain the result:

$$\bar{x}_f = l \cos \alpha - R \sin \alpha \cos \phi \quad (138a)$$

$$\bar{y}_f = \frac{l \sin \alpha \sin \phi}{\sqrt{1 - \sin^2 \alpha \cos^2 \phi}} \quad (138b)$$

$$\bar{z}_f = -l \frac{\sin \alpha \cos \alpha \cos \phi}{\sqrt{1 - \sin^2 \alpha \cos^2 \phi}} - R \sqrt{1 - \sin^2 \alpha \cos^2 \phi} \quad (138c)$$

The equation for a plane normal to the missile centerline at  $l$  has the following vector form

$$(\underline{r} - \underline{r}_f) \cdot \underline{i}' = 0 \quad (139)$$

Equation (135) may be inverted to obtain  $\underline{i}'$  in terms of the base vectors ( $\underline{i}''$ ,  $\underline{j}''$ ,  $\underline{k}''$ ), which are identical to the jet-oriented base vectors ( $\underline{i}$ ,  $\underline{j}$ ,  $\underline{k}$ ), with the result:

$$\underline{i}' = \underline{i} [\cos \alpha] + \underline{j} \frac{\sin \alpha \sin \phi}{\sqrt{1 - \sin^2 \alpha \cos^2 \phi}} - \underline{k} \frac{\sin \alpha \cos \alpha \cos \phi}{\sqrt{1 - \sin^2 \alpha \cos^2 \phi}}$$

When this is substituted into Equation (139), the expression obtained for the plane in terms of jet-oriented coordinates is

$$\begin{aligned} & [\cos \alpha] (\bar{x} - \bar{x}_f) + \left[ \frac{\sin \alpha \sin \phi}{\sqrt{1 - \sin^2 \alpha \cos^2 \phi}} \right] (\bar{y} - \bar{y}_f) - \\ & - \left[ \frac{\sin \alpha \cos \alpha \cos \phi}{\sqrt{1 - \sin^2 \alpha \cos^2 \phi}} \right] (\bar{z} - \bar{z}_f) = 0 \end{aligned} \quad (140)$$

The intersection of this plane with the jet trajectory must now be found, in order to determine the point at which jet properties should be calculated. This is done by noting that the jet trajectory may be defined by the relations:

$$\bar{x} = \bar{x}_j \quad (141a)$$

$$\bar{y} = 0 \quad (141b)$$

$$\bar{z} = \bar{z}_j (\bar{x}_j) \quad (141c)$$

Substitution of these and the relations of Equations (138) into Equation (140) yields

$$l = \bar{x}_j \cos \alpha - \bar{z}_j (\bar{x}_j) \frac{\sin \alpha \cos \alpha \cos \phi}{\sqrt{1 - \sin^2 \alpha \cos^2 \phi}} \quad (142)$$

Equation (142) may be written in terms of the similarity variables defined in Equations (106) by simply multiplying by  $(\sigma_e/d_e)$  to yield

$$X_j \cos \alpha - Z_j (X_j) \frac{\sin \alpha \cos \alpha \cos \phi}{\sqrt{1 - \sin^2 \alpha \cos^2 \phi}} = L \quad (143)$$

where

$$L = \frac{\sigma_e l}{d_e}$$

Finally, using the empirical Equation (120), Equation (143) may be written as

$$X_j - (1.76) X_j^{(0.28)} \frac{\sin \alpha \cos \phi}{\sqrt{1 - \sin^2 \alpha \cos^2 \phi}} = \frac{L}{\cos \alpha} \quad (144)$$

Solution of this equation for  $X_j$ , yields the location along the jet trajectory at which vortex strengths and spacing should be calculated. It should be noted that Equations (141) refer to the centerline of the jet

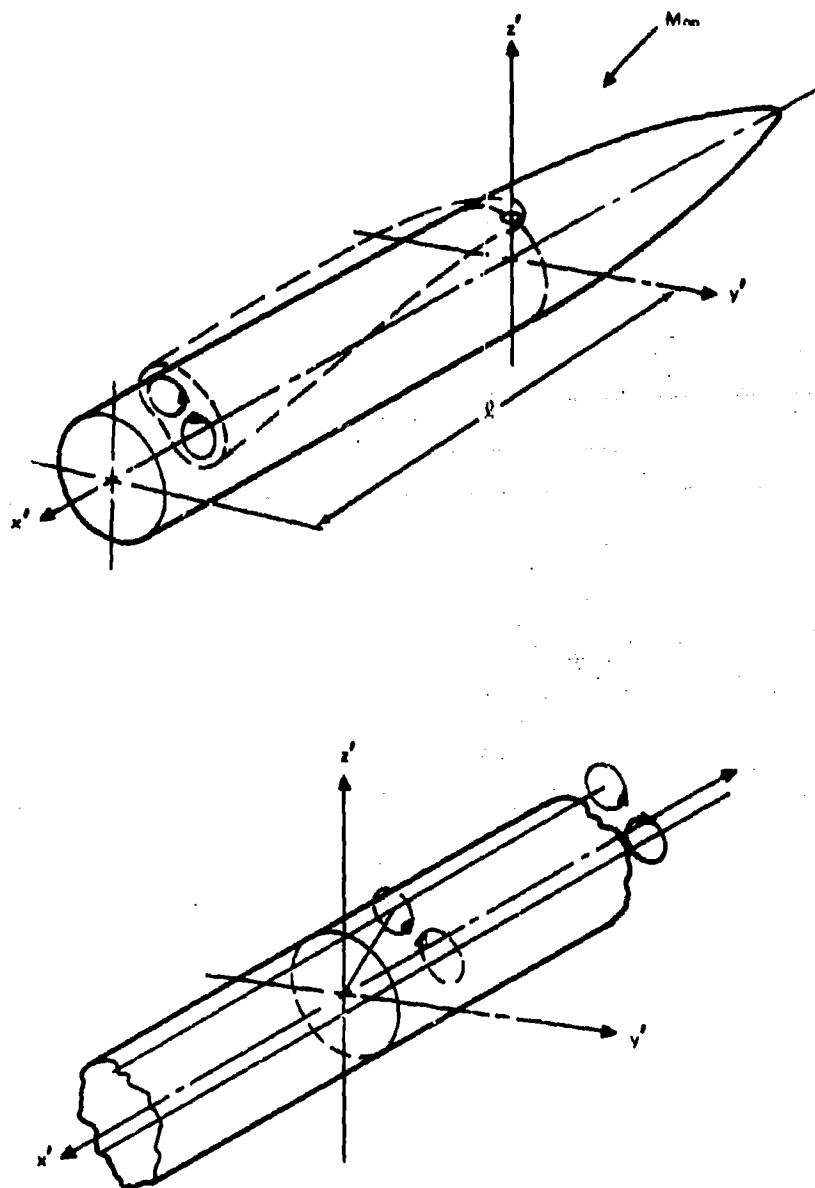


Figure 60. Actual Jet Plume and Theoretical Model for Calculating Induced Velocities at the Fin Location



trajectory, so that the distance at which the jet vortices intersect the plane will be somewhat different from that given by Equation (144). This effect, however, is neglected.

The formulas obtained in Subsection 5.2 may be used to calculate the location and strength of the jet vortices. The transformation Equations (137) will then give their location in the body-oriented coordinate system, at a station located a distance  $l$  downstream of the nozzle, and in a plane normal to the body axis

### 5.3.2 Jet Fin Interference Forces and Moments

As previously mentioned, it is assumed that crossflow velocities are much smaller than the free-stream velocity. Further, it is assumed that the body cross-section does not change at the fin location,  $l$ , and that the vortex strength does not change very much over the space of a body radius. Consequently, the flow induced by the jet vortices about the missile body is equivalent to the incompressible flow induced about an infinite circular cylinder by two infinite counterrotating vortices, as illustrated in Figure 60. The strength and location of the vortices are taken to be those at a distance  $l$  downstream of the nozzle. They are calculated by methods described in Subsections 5.2 and 5.3.1. The angles of attack and side slip induced by the vortices at the fin locations are calculated. It is assumed that the fins are flat plates of high aspect ratio, so that simple strip theory may be used to calculate the induced forces and moments, as described in Reference 50. Figure 61 shows schematically the upwash and sidewash induced

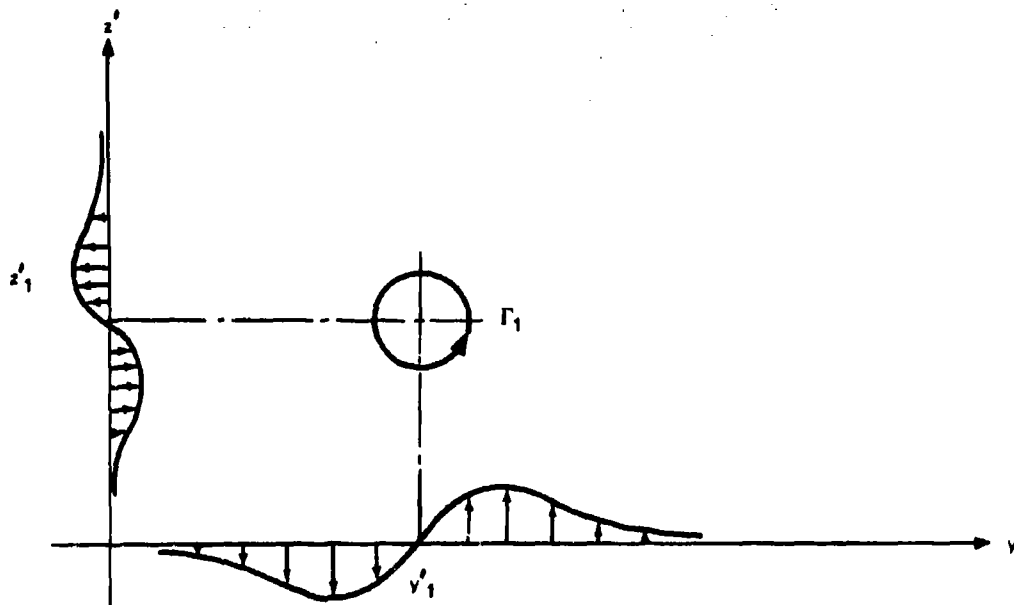


Figure 61. Upwash and Sidewash Produced by a Single Vortex

by a positive vortex of strength  $\Gamma$ , at the planes  $z' = 0$  and  $y' = 0$ , respectively. The complete vortex system contributing to interference effects consists of the two jet vortices,  $\Gamma_1$ , and  $\Gamma_2$ , as well as their images inside the cylinder. Since all vortices have the same strength, a positive strength  $\Gamma$  is introduced such that

$$\Gamma_1 = \Gamma$$

$$\Gamma_2 = -\Gamma$$

$$\Gamma_{1_i} = -\Gamma$$

$$\Gamma_{2_i} = \Gamma$$

where the subscript (i) denotes the image vortex inside the cylinder. The vortex system is depicted in Figure 62.

Following Appendix B of Reference 50, the upwash produced by these vortices at the  $y'$  axis is:

$$w_1 = \frac{\Gamma}{2\pi} \left[ \frac{(y' - y'_1)^2}{(y' - y'_1)^2 + z'^2_1} \right] \quad (145a)$$

$$w_2 = -\frac{\Gamma}{2\pi} \left[ \frac{(y' - y'_2)^2}{(y' - y'_2)^2 + z'^2_2} \right] \quad (145b)$$

$$w_{1_i} = -\frac{\Gamma}{2\pi} \left[ \frac{(y' - y'_{1_i})^2}{(y' - y'_{1_i})^2 + z'^2_{1_i}} \right] \quad (145c)$$

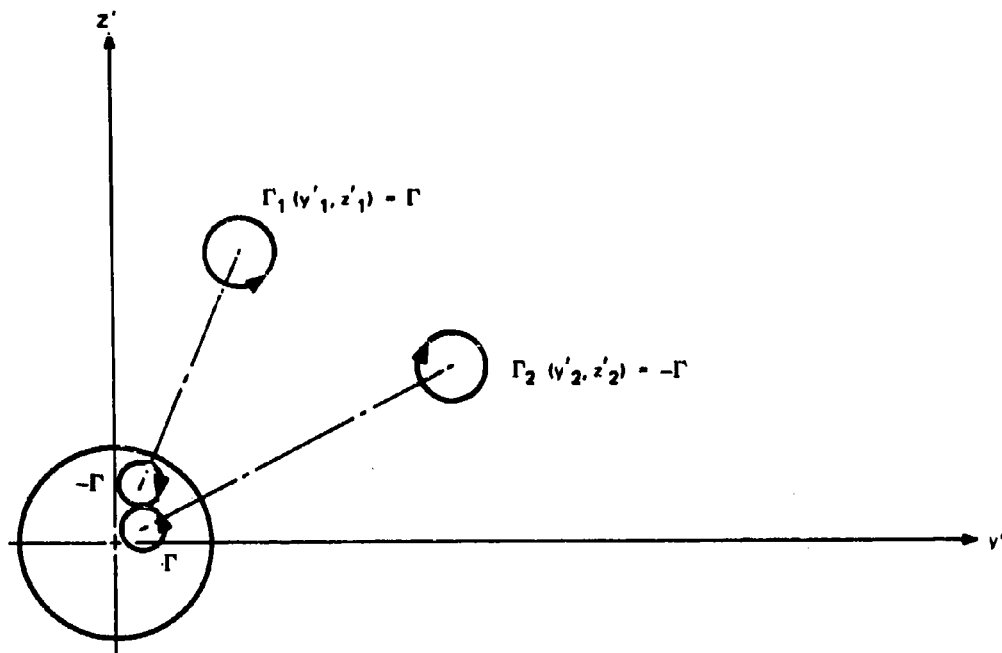


Figure 62. Vortex System Contributing to Total Induced Velocities

$$w_{2_i} = \frac{\Gamma}{2\pi} \left[ \frac{(y' - y'_{2_i})}{(y' - y'_{2_i})^2 + z'_{2_i}{}^2} \right] \quad (145d)$$

where

$$y'_{1_i} = \frac{R^2}{y'^2_1 + z'^2_1} y'_1 \quad z'_{1_i} = \frac{R^2}{y'^2_1 + z'^2_1} z'_1 \quad (146)$$

and

$$y'_{2_i} = \frac{R^2}{y'^2_2 + z'^2_2} y'_2 \quad z'_{2_i} = \frac{R^2}{y'^2_2 + z'^2_2} z'_2 \quad (147)$$

Also, the sidewash induced on the  $z'$  axis is given by

$$v_1 = -\frac{\Gamma}{2\pi} \left[ \frac{(z' - z'_1)}{y'^2_1 + (z' - z'_1)^2} \right] \quad (148a)$$

$$v_2 = \frac{\Gamma}{2\pi} \left[ \frac{(z' - z'_2)}{y'^2_2 + (z' - z'_2)^2} \right] \quad (148b)$$

$$v_{1_i} = \frac{\Gamma}{2\pi} \left[ \frac{(z' - z'_{1_i})}{y'^2_{1_i} + (z' - z'_{1_i})^2} \right] \quad (148c)$$

$$v_{2_i} = -\frac{\Gamma}{2\pi} \left[ \frac{(z' - z'_{2_i})}{y'^2_{2_i} + (z' - z'_{2_i})^2} \right] \quad (148d)$$

The fin geometry is depicted in Figure 63. The variation of chord  $c$  with distance from the axis may be written in the general form

$$c = c_r - \left[ \frac{c_r - c_t}{s - R} \right] (y' - R) \quad (149)$$

or, normalized by the cylinder radius  $R$ , in the equivalent form

$$C = C_r \left[ 1 - \left( \frac{1 - \lambda}{S - 1} \right) (Y' - 1) \right] \quad (150)$$

where:

$C_r$  = normalized root chord ( $c_r/R$ )

$\lambda$  = taper ratio ( $c_t/c_r$ )

$S$  = normalized semi-span ( $s/R$ )

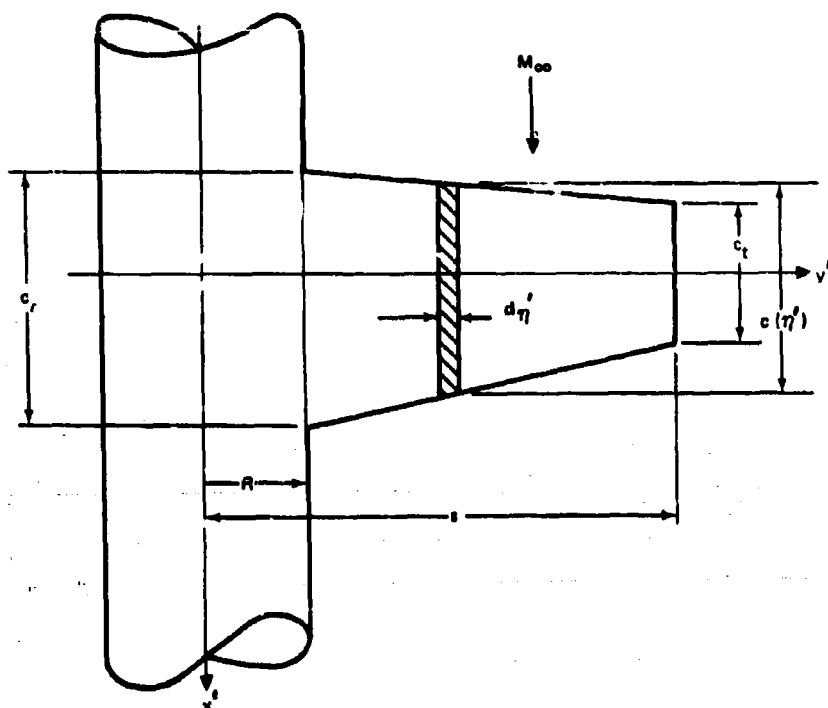


Figure 63. Fin Geometry

$Y' = \text{normalized coordinate } (y'/R)$

To compute the induced angles of attack and sideslip, the induced velocities given by Equations (145) and (149) are to be divided by the component of free-stream velocity along the  $x'$  axis. For small angles of attack,  $\alpha$ , this component is approximately equal to  $U_\infty$ . The total induced angle of attack along the  $y'$  axis is therefore

$$\alpha_i = \frac{1}{U_\infty} [w_1 + w_2 + w_{1_i} + w_{2_i}] \quad (151)$$

and the sideslip angle along the  $z'$  axis is

$$\beta_i = \frac{1}{U_\infty} [v_1 + v_2 + v_{1_i} + v_{2_i}] \quad (152)$$

Using strip theory, then, the normal force on the horizontal fins is

$$F_Z = q_\infty \left\{ \int_R^s C_{L_i}(\eta) c(\eta) d\eta + \int_{-s}^{-R} C_{L_i}(\eta) c(\eta) d\eta \right\} \quad (153)$$

the side force on the vertical fins is

$$F_Y = q_\infty \left\{ \int_R^s C_{L_i}(\zeta) c(\zeta) \zeta d\zeta + \int_{-s}^{-R} C_{L_i}(\zeta) c(\zeta) \zeta d\zeta \right\} \quad (154)$$

and the rolling moment on the fins is

$$M_L = q_\infty \left\{ \int_R^s C_{L_i}(\eta) c(\eta) \eta d\eta + \int_{-s}^{-R} C_{L_i}(\eta) c(\eta) \eta d\eta \right. \\ \left. - \int_R^s C_{L_i}(\zeta) c(\zeta) \zeta d\zeta - \int_{-R}^{-s} C_{L_i}(\zeta) c(\zeta) \zeta d\zeta \right\} \quad (155)$$

Pitching and yawing moments are obtained by multiplying  $F_Z$  and  $F_Y$  respectively, by  $l$ . In the above equations,  $C_{L_i}$  represents the two-dimensional lift coefficient for a flat plate at an angle of incidence. It should be noted that the above equations assume that the fins are independent of each other (i. e., fin-fin interference effects are neglected). Also, any forces induced by the vortices on the cylindrical portion of the body are not included.

The relation between  $C_{li}$  and the induced angles of attack or sideslip depends on whether the free stream is subsonic or supersonic. In the subsonic case, Reference 51 gives the following relation:

$$(C_{li})_{M_\infty < 1} = \frac{2\pi}{\beta} \begin{Bmatrix} \alpha_i \\ \beta_i \end{Bmatrix} \quad (156)$$

and for supersonic free streams

$$C_{li} \quad M_\infty > 1 = \frac{4}{\beta} \begin{Bmatrix} \alpha_i \\ \beta_i \end{Bmatrix} \quad (157)$$

where

$$\beta = \sqrt{|1 - M_\infty^2|}$$

The derivation of final results for the induced normal force in the subsonic case will now be carried out in detail. With

$$C_{li} = \frac{2\pi}{\beta U_\infty} [w_1 + w_2 + w_{1i} + w_{2i}]$$

and Equation (145), and Equation (153) may be written in the form:

$$\begin{aligned}
 C_{Z_{M_\infty < 1}} = \frac{\Gamma}{\pi R^2 \beta U_\infty} & \left\{ \int_R^s \frac{(\eta - y'_1) c(\eta) d\eta}{(\eta - y'_1)^2 + z'_1{}^2} \right. \\
 & - \int_R^s \frac{(\eta - y'_2) c(\eta) d\eta}{(\eta - y'_2)^2 + z'_2{}^2} - \int_R^s \frac{(\eta - y'_{1i}) c(\eta) d\eta}{(\eta - y'_{1i})^2 + z'_{1i}{}^2} \\
 & + \int_R^s \frac{(\eta - y'_{2i}) c(\eta) d\eta}{(\eta - y'_{2i})^2 + z'_{2i}{}^2} + \int_{-s}^{-R} \frac{(\eta - y'_1) c(\eta) d\eta}{(\eta - y'_1)^2 + z'_1{}^2} \\
 & - \int_{-s}^{-R} \frac{(\eta - y'_2) c(\eta) d\eta}{(\eta - y'_2)^2 + z'_2{}^2} - \int_{-s}^{-R} \frac{(\eta - y'_{1i}) c(\eta) d\eta}{(\eta - y'_{1i})^2 + z'_{1i}{}^2} \\
 & \left. + \int_{-s}^{-R} \frac{(\eta - y'_{2i}) c(\eta) d\eta}{(\eta - y'_{2i})^2 + z'_{2i}{}^2} \right\} \quad (158)
 \end{aligned}$$

where  $C_Z$  is the normal force coefficient defined by

$$C_{Z_{M_\infty < 1}} = \frac{F_Z}{\pi R^2 q_\infty} \quad (159)$$

If all lengths in Equation (158) are normalized by the cylinder radius,  $R$ , and the symmetry of the fins is utilized, so that:

$$C(\eta) = C(-\eta)$$



Then it is possible to write Equation(158) in the following form:

$$\begin{aligned}
 C_{Z_{M_\infty < 1}} = & \left[ \frac{\Gamma}{\pi R \beta U_\infty} \right] \left\{ \int_1^S C(\eta) \left[ \frac{(\eta - Y'_1)}{(\eta - Y'_1)^2 + Z'_1{}^2} \right. \right. \\
 & - \left. \frac{(\eta + Y'_1)}{(\eta + Y'_1)^2 + Z'_1{}^2} \right] d\eta - \int_1^S C(\eta) \left[ \frac{(\eta - Y'_2)}{(\eta - Y'_2)^2 + Z'_2{}^2} \right. \\
 & - \left. \frac{(\eta + Y'_2)}{(\eta + Y'_2)^2 + Z'_2{}^2} \right] d\eta - \int_1^S C(\eta) \left[ \frac{(\eta - Y'_{1_i})}{(\eta - Y'_{1_i})^2 + Z'_{1_i}{}^2} \right. \\
 & - \left. \frac{(\eta + Y'_{1_i})}{(\eta + Y'_{1_i})^2 + Z'_{1_i}{}^2} \right] d\eta + \int_1^S C(\eta) \left[ \frac{(\eta - Y'_{2_i})}{(\eta - Y'_{2_i})^2 + Z'_{2_i}{}^2} \right. \\
 & \left. \left. - \frac{(\eta + Y'_{2_i})}{(\eta + Y'_{2_i})^2 + Z'_{2_i}{}^2} \right] d\eta \right\} \quad (160)
 \end{aligned}$$

where  $C(\eta)$  is given by Equation(150).

The integrals in Equation(160) are evaluated by standard techniques, and the final result is:

$$\begin{aligned}
 C_{Z_{M_\infty < 1}} = & \left[ \frac{\Gamma}{\pi R \beta U_\infty} \right] \left\{ I(Y'_1, Z'_1; S, \lambda) - I(Y'_2, Z'_2; S, \lambda) \right. \\
 & \left. - I(Y'_{1_i}, Z'_{1_i}; S, \lambda) + I(Y'_{2_i}, Z'_{2_i}; S, \lambda) \right\} \quad (161)
 \end{aligned}$$

where:

$$\begin{aligned}
 I(Y'_1, Z'_1; S, \lambda) = C_r \left\{ \frac{1}{2} \left[ \left( \frac{S-\lambda}{S-1} \right) - \left( \frac{1-\lambda}{S-1} \right) Y'_1 \right] \log \left[ \frac{(S-Y'_1)^2 + Z'^2_1}{(1-Y'_1)^2 + Z'^2_1} \right] \right. \\
 - \frac{1}{2} \left[ \left( \frac{S-\lambda}{S-1} \right) + \left( \frac{1-\lambda}{S-1} \right) Y'_1 \right] \log \left[ \frac{(S+Y'_1)^2 + Z'^2_1}{(1+Y'_1)^2 + Z'^2_1} \right] \\
 + \left( \frac{1-\lambda}{S-1} \right) Z'_1 \left[ \tan^{-1} \left( \frac{S-Y'_1}{Z'_1} \right) - \tan^{-1} \left( \frac{S+Y'_1}{Z'_1} \right) \right. \\
 \left. \left. - \tan^{-1} \left( \frac{1-Y'_1}{Z'_1} \right) + \tan^{-1} \left( \frac{1+Y'_1}{Z'_1} \right) \right] \right\} \quad (162)
 \end{aligned}$$

and

$$Y'_{1i} = \frac{Y'_1}{Y'^2_1 + Z'^2_1} \dots, \text{ etc.}$$

The side force and rolling moment coefficients are defined:

$$C_Y = \frac{F_Y}{\pi R^2 q_\infty} \quad (162a)$$

$$C_L = \frac{M_L}{\pi R^3 q_\infty} \quad (162b)$$

Integrations similar to those carried out for the normal force lead to the following results for the subsonic side force coefficient

$$C_{Y_{M_\infty < 1}} = \left[ \frac{\Gamma}{\pi R \beta U_\infty} \right] \left\{ -G(Y'_1, Z'_1; S, \lambda) + G(Y'_2, Z'_2; S, \lambda) \right. \\ \left. + G(Y'_{1_i}, Z'_{1_i}; S, \lambda) - G(Y'_{2_i}, Z'_{2_i}; S, \lambda) \right\} \quad (163)$$

where, for example,

$$G(Y'_1, Z'_1; S, \lambda) = I(Z'_1, Y'_1; S, \lambda) \quad (164)$$

(i.e.,  $G$  is obtained by interchanging  $Y'_1$  and  $Z'_1$  in Equation (162), as might have been expected from the symmetry of the situation).

Finally, carrying out the integrations indicated in Equation (155), leads to the following results for the subsonic rolling moment coefficient.

$$C_{L_{M_\infty < 1}} = \left[ \frac{\Gamma}{\pi R \beta U_\infty} \right] \left\{ H(Y'_1, Z'_1; S, \lambda) + H(Z'_1, Y'_1; S, \lambda) \right. \\ - H(Y'_2, Z'_2; S, \lambda) - H(Z'_2, Y'_2; S, \lambda) \\ - H(Y'_{1_i}, Z'_{1_i}; S, \lambda) - H(Z'_{1_i}, Y'_{1_i}; S, \lambda) \\ \left. + H(Y'_{2_i}, Z'_{2_i}; S, \lambda) + H(Z'_{2_i}, Y'_{2_i}; S, \lambda) \right\} \quad (165)$$

where:

$$\begin{aligned}
 \frac{H}{C_r} = & \left\{ (S-\lambda) - (1-\lambda S) \right\} + \frac{1}{2} \left\{ \left( \frac{S-\lambda}{S-1} \right) Y_1' - \left( \frac{1-\lambda}{S-1} \right) Y_1'^2 \right. \\
 & + \left( \frac{1-\lambda}{S-1} \right) \frac{Z_1'^2}{2} \left. \right\} \log \left[ \frac{(S-Y_1')^2 + Z_1'^2}{(1-Y_1')^2 + Z_1'^2} \right] - \frac{1}{2} \left\{ \left( \frac{S-\lambda}{S-1} \right) Y_1' \right. \\
 & + \left( \frac{1-\lambda}{S-1} \right) Y_1'^2 - \left( \frac{1-\lambda}{S-1} \right) \frac{Z_1'^2}{2} \left. \right\} \log \left[ \frac{(S+Y_1')^2 + Z_1'^2}{(1+Y_1')^2 + Z_1'^2} \right] \\
 & - Z_1' \left\{ \left( \frac{S-\lambda}{S-1} \right) - 2 \left( \frac{1-\lambda}{S-1} \right) Y_1' \right\} \left\{ \tan^{-1} \left( \frac{S-Y_1'}{Z_1'} \right) \right. \\
 & - \tan^{-1} \left( \frac{1-Y_1'}{Z_1'} \right) \left. \right\} - Z_1' \left\{ \left( \frac{S-\lambda}{S-1} \right) + 2 \left( \frac{1-\lambda}{S-1} \right) Y_1' \right\} \\
 & \left\{ \tan^{-1} \left( \frac{S+Y_1'}{Z_1'} \right) - \tan^{-1} \left( \frac{1+Y_1'}{Z_1'} \right) \right\} \quad (166)
 \end{aligned}$$

Comparison of Equations (156) and (157) indicates that the interference coefficients for supersonic free streams may be obtained from subsonic results by simply multiplying by  $(2/\pi)$ .

#### 5.4 RESULTS OF JET-FIN INTERFERENCE CALCULATIONS

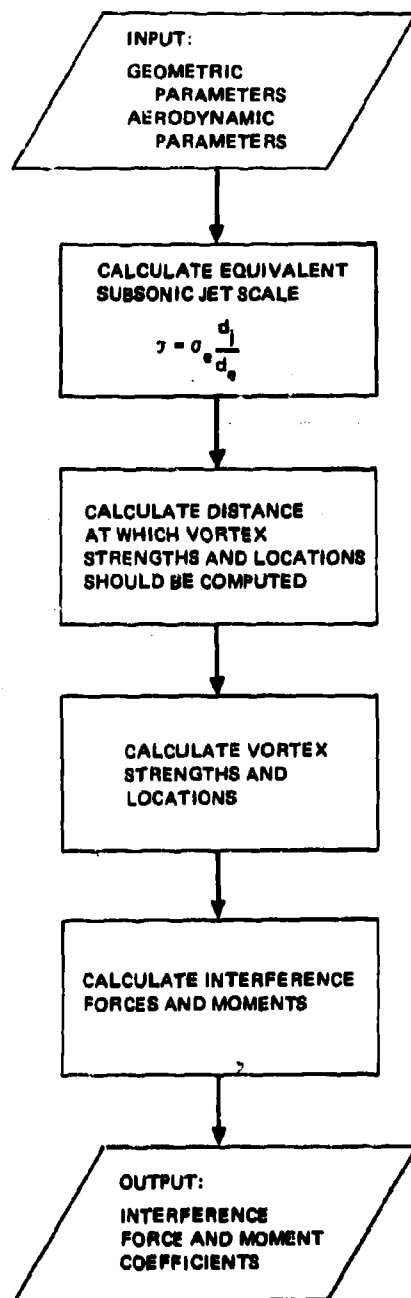
The formulas derived in Subsection 5.3, in conjunction with the methods for predicting vortex strengths and positions described in Subsection 5.2, have been used in two computer programs for calculating jet-fin interference forces and moments on a cruciform missile. One of these programs is valid for subsonic free-stream Mach numbers, and the other for supersonic free-stream Mach numbers. As previously mentioned, the interference effects calculated are the incremental force and moment coefficients which are induced on the fins alone by the presence of the jet vortices.

A brief description of the programs is now given, with reference to the flow chart and tables of Figure 64.

Given the geometric and aerodynamic input parameters listed in Figure 64, the program first calculates the appropriate equivalent subsonic jet scale, using Equation (116) in the subsonic case, and Equation (119) in the supersonic case. For specific angles of attack  $\alpha$  and bank  $\phi$ , the program then calculates the value of  $X$  at which vortex properties are to be computed by solving Equation (144) numerically.

At this point, a check is made to ensure that the resulting  $X$  corresponds to a value of  $X$  which is greater than 5. This is done to ensure that the fins lie within the "vortex region" of the jet as defined in Reference 22. The restriction is necessary because the model for the jet vortices is only valid in this region. The program is terminated if the condition  $X > 5$  is not met.

If the above test is passed, the formulas derived in Subsection 5.2 are used for computing the strength of the vortices and their position relative to the jet-oriented ( $\bar{x}$ ,  $\bar{y}$ ,  $\bar{z}$ ) coordinate system. Using the transformation Equation (137), the vortex positions relative to the body fixed ( $x'$ ,  $y'$ ,  $z'$ ) coordinate system are finally calculated. After suitable normalization of the vortex coordinates, the formulas derived in Subsection 5.3.2 are used for calculating interference forces and moments. At this stage, it is again necessary to discriminate between sonic and supersonic free-stream Mach numbers, as described in Subsection 5.3.2. For each value of the free stream Mach number,  $M_\infty$ , and pressure ratio,  $P$ , the program prints all the interference coefficients listed in Figure 64 as functions of the bank angle  $\phi$ , for each value of the angle of incidence  $\alpha$ . The results of some sample computations are shown in Figures 65 through 67. As indicated in the figures, the free-stream Mach number is 0.8 and the angle of incidence is  $2^\circ$ .



#### GEOMETRIC PARAMETERS

JET DIAMETER	$d_j$
DISTANCE BETWEEN NOZZLE CENTERLINE AND FIN HALF CHORD LOCATION	$l$
FIN SEMISPAN	$s$
BODY CROSS-SECTIONAL RADIUS	$R$
FIN ROOT CHORD	$c_r$
FIN TIP CHORD	$c_t$

#### AERODYNAMIC PARAMETERS

FREE-STREAM MACH NO.	$M_\infty$
ANGLE OF ATTACK	$\alpha$
JET-CHAMBER-TO- FREE-STREAM PRESSURE RATIO	$P$

#### INTERFERENCE COEFFICIENTS

NORMAL FORCE	$C_Z$
SIDE FORCE	$C_Y$
ROLLING MOMENT	$C_L$
PITCHING MOMENT	$C_M$
YAWING MOMENT	$C_N$

#### NOTE:

JET EXIT MACH NUMBER IS  
ASSUMED TO BE UNITY.  
GEOMETRIC PARAMETERS MUST  
HAVE CONSISTENT DIMENSIONS.

Figure 64. Flowchart for Fin Interference Force and Moment Computations

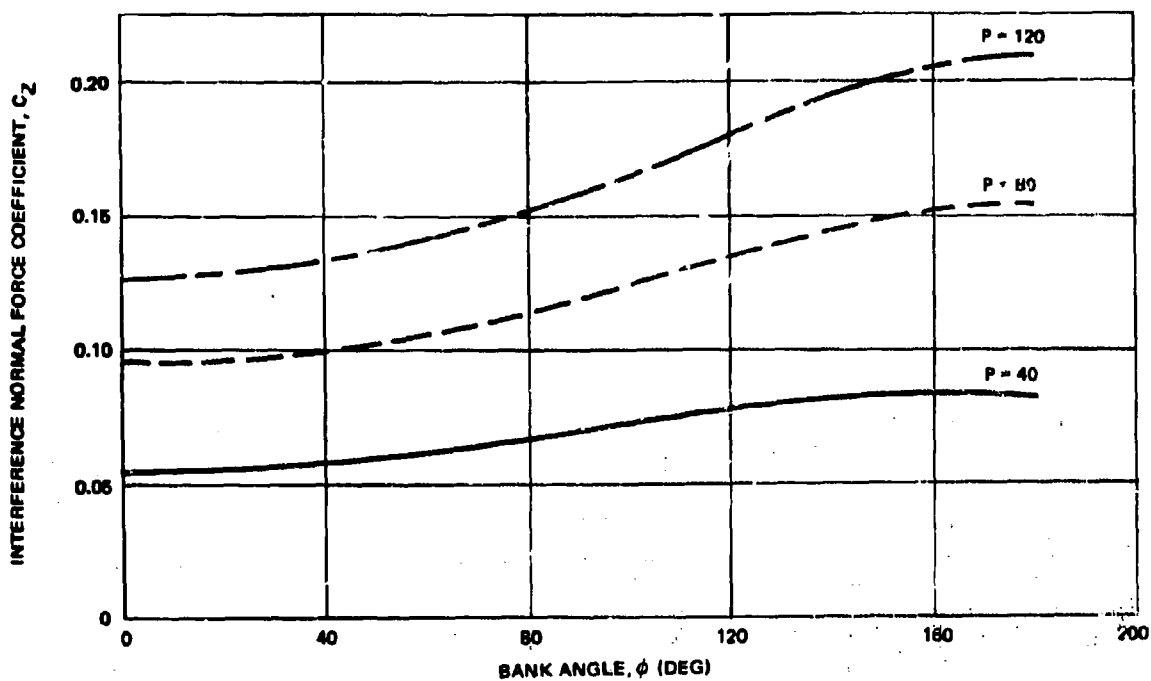


Figure 65. Fin Interference Normal Force Coefficient ( $M_\infty = 0.8$ ,  $\alpha = 2^\circ$ )

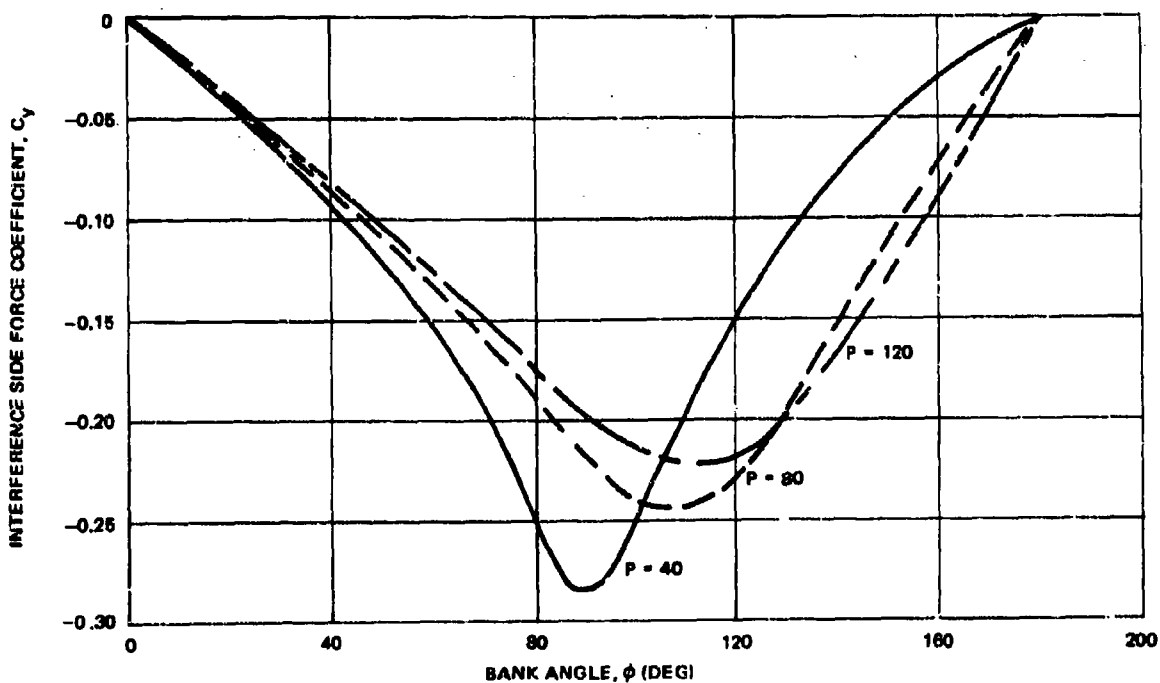


Figure 66. Fin Interference Side Force Coefficient ( $M_\infty = 0.8$ ,  $\alpha = 2^\circ$ )

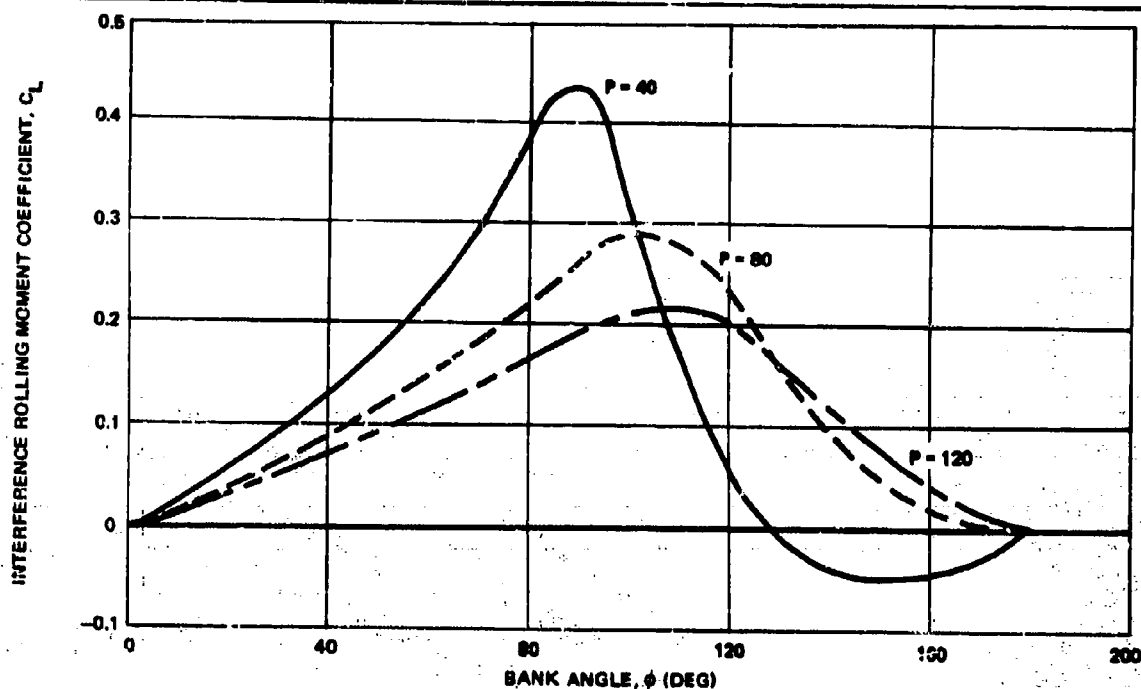


Figure 67. Fin Interference Rolling Moment Coefficient ( $M_\infty = 0.8$ ,  $\alpha = 2^\circ$ )

The missile and fin geometries correspond roughly to the configuration tested in Reference 27 and depicted in Figure 4. The specific values used for the geometric parameters are:

$$l = 57.405 \text{ in.}$$

$$s = 6.855 \text{ in.}$$

$$R = 2.75 \text{ in.}$$

$$c_r = c_t = 5.5 \text{ in.}$$

The nozzle is assumed to be sonic, as the program requires, and to have a diameter

$$d_j = 0.22 \text{ in.}$$

Pitching and yawing moment coefficients about the nozzle station may be obtained from Figures 65 and 66 by simply multiplying  $C_z$  and  $C_y$  by the normalized moment arm ( $l/R$ ).

The behavior of the curves in Figures 65 through 67 may be explained as follows. The equations of Subsection 5.2 as well as the data of Reference 46 indicate that the vortex spacing  $\bar{y}_0$ , vortex height above the exit plane  $\bar{z}_0$ , and vortex strength  $\Gamma$  increase with increasing pressure ratio  $P$ , for a fixed  $M_\infty$  and a fixed station downstream of the nozzle. Generally,  $\Gamma$  grows with  $P$  at a faster



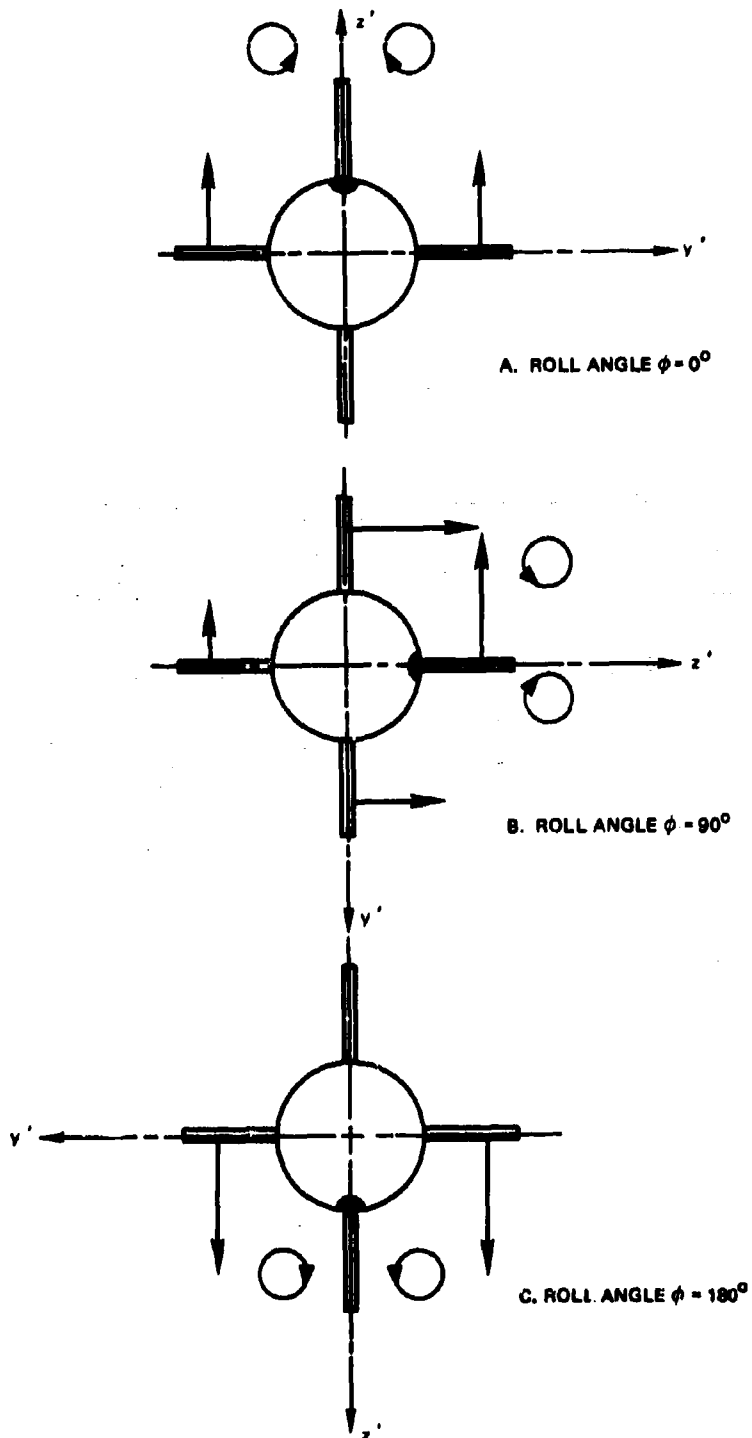


Figure 88. Schematic Diagram of Vortex Locations and Interference Forces for Various Roll Angles

rate than either  $\bar{y}_0$  or  $\bar{z}_0$ . In a sense, then, an increase in  $P$  will produce two counteracting effects on the fin interference forces and moments. As the vortices move farther away with increasing  $P$ , interference effects should decrease; on the other hand, an increase in  $P$  also tends to increase interference effects by increasing  $\Gamma$ . Unless the vortices are quite close to the fin, the latter effect predominates, since  $\Gamma$  increases at a faster rate with  $P$  than either  $\bar{y}_0$  or  $\bar{z}_0$ . However, forces induced on fins located near the vortices are more sensitive to vortex position, and an increase in  $P$  may well decrease interference effects. These trends are reflected in Figures 65 through 67. Figure 65 indicates an increase in  $C_z$  with pressure ratio. (It is recalled that the nozzle centerline is aligned with the  $Z$ -axis.) On the other hand, side force and rolling moment coefficients, which are primarily governed by the upwash induced by the vortices on fins that lie near the vortices, may either decrease or increase with  $P$ , depending on the bank angle  $\phi$ . The trends obtained when  $\phi$  is varied may be explained with the aid of Figure 68. Because of symmetry, side force and rolling moment coefficients must be zero at  $\phi = 0^\circ$  and at  $\phi = 180^\circ$ . The normal force coefficient must be greater at  $\phi = 180^\circ$  than at  $\phi = 0^\circ$ , since for a positive  $\alpha$  the vortices lie closer to the fins at the former roll angle. From Figure 68b it is evident that the side force should be negative at  $\phi = 90^\circ$ , and the side force may further be expected to peak near  $\phi = 90^\circ$ . Figure 68 also indicates that at  $\phi = 90^\circ$  the contribution of the horizontal fins to the rolling moment is positive (counterclockwise), while that of the vertical fins is negative. Consequently, it is not surprising that under certain conditions the interference rolling moment coefficient changes sign as  $\phi$  is varied. This effect is evident in Figure 67, for the case  $P = 40$ . As previously mentioned, fin interference forces for subsonic  $M_\infty$  have been measured during the AMICOM-CAL tests described in Reference 28. A sample case for the configuration tested yielded large errors in the magnitude of the theoretical interference forces, although the measured trends were predicted correctly. The configuration tested in Reference 28, however, had a very low fin panel aspect ratio--one half of that shown in Figure 4. Consequently the simple strip theory used in calculating interference forces would not be expected to apply to this configuration.

Experimental data are available for supersonic free stream Mach numbers, and a comparison has been made using the supersonic fin interference program. The geometry chosen corresponds to the configuration tested in Reference 31 for the center nozzle location. The geometric parameters have the following values

- $d_j = 0.11$  in.
- $l = 5.688$  in.
- $s = 1.375$  in.

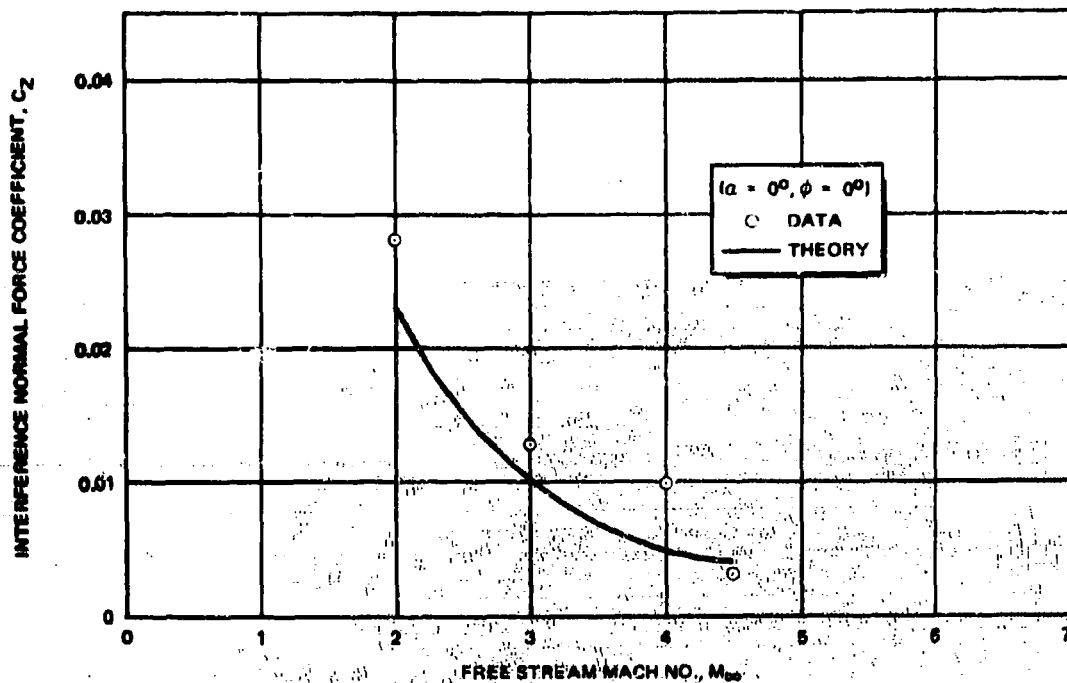


Figure 69. Comparison of Interference Normal Force Coefficient With Data  $P = 60$

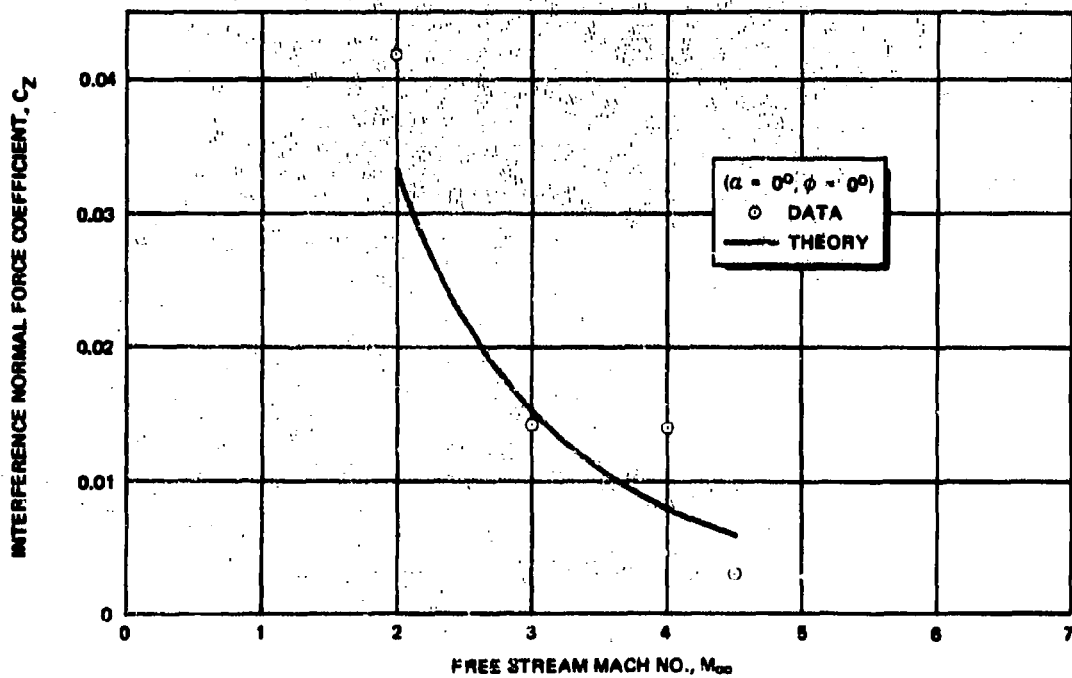


Figure 70. Comparison of Interference Normal Force Coefficient With Data  $P = 100$

$$R = 0.687 \text{ in.}$$

$$c_r = 1.375 \text{ in.}$$

$$c_t = 1.375 \text{ in.}$$

The relevant experimental interference normal force coefficient has been obtained from data by the operation.

$$C_z = (C_z)_{\text{fins on}} - (C_z)_{\text{fins off}}$$

Theoretical and experimental results are compared in Figures 69 and 70, for pressure ratios of 60 and 100, respectively. The agreement appears to be satisfactory.

**BLANK PAGE**

## Section 6

### CONCLUSIONS

After extensive study of the problem of JI with a subsonic mainstream, it appears evident that adequate analytical models can be formulated from potential flow theory; however, more accurate models will have to be based on viscous flow analysis. In general, the adequacy of any analytical methods developed will remain unknown until more detailed experimental data are available.

Very few measurements of the behavior of an underexpanded jet plume exhausting into a subsonic cross flow have been conducted. Measurements of the jet vortex strengths have so far been limited to the results described in References 45 and 46, and these were only obtained at one station downstream of the nozzle. Measurements of the flowfield in the viscous wake-like region on the leeward side of an underexpanded jet have not been made, although it appears that this region influences the interference pressure distribution very strongly. Tests of an underexpanded jet exhausting from a flat plate have been conducted by AMICOM concurrently with this study. Data resulting from these experiments will provide a basis for evaluating the analytical models developed in this study and others reported in the VTOL-related literature.

Based upon data concerning subsonic jets in subsonic mainstreams and the limited underexpanded jet data available, the behavior of the JI interference pressure distribution appears amenable to empirical description. The Fourier series empirical fit method developed in this study is expected to provide a relatively convenient and accurate empirical description of the interference pressure distribution. It has been shown in this study that a characteristic dimension of the underexpanded jet plume will scale the interference pressure distribution as the jet exit dimension does for subsonic jets. Consequently, it is expected that data from tests involving an underexpanded jet will be easily fit by the Fourier series method, with jet exit Mach number replacing the velocity ratio ( $U_\infty/U_j$ ) as a parameter.

Several semi-empirical models of the interference pressure distribution due to a jet in a subsonic mainstream have been developed in this study. Generally, the approach taken has been to postulate equivalent flowfields which appear plausible either on physical grounds, or from a qualitative knowledge of the behavior of the induced pressure on a flat plate. These flow models contain empirical constants which are determined by matching to experimental pressure distributions in some region. The validity of a particular model is then judged by how well the pressure distribution is represented in other regions. The model flows postulated have been assumed to be inviscid. Reasonably good representation of the pressure coefficient distribution has been achieved with some of these models. Close agreement

with data is usually restricted to a particular range in the azimuthal angle. Unfortunately, the models which give best overall agreement with data are those which seem most unrealistic on physical grounds. This difficulty is tied to the assumption of a model flow which is inviscid. On the lee side of the jet, a realistic model must include viscous effects.

The equivalent solid obstacle analogy provides a basis for calculating approximate JI control effectiveness in supersonic flight. In general, the behavior of amplification factor with angle of attack and flight Mach number, as well as with jet thrust, can be predicted. Accounting for the effects of boundary layer separation by redistributing the pressures due to the inviscid flow about the equivalent obstacle does not appear to increase the accuracy of the prediction method. The effects of equivalent obstacle shock reflection from the vehicle surface should be accounted for to improve the accuracy and general validity of the prediction method. Equivalent obstacle flowfield analyses which admit nonaxisymmetric shocks are required in order to account for this shock interaction.

Methods for calculating jet-fin interference effects for subsonic and supersonic mainstreams have been developed. They are based upon a simple, semi-empirical model of the jet-induced vortices which is valid at large distances from the nozzle. An equivalence between sonic, highly underexpanded jets and subsonic jets has been postulated, and data for both situations are used in evaluating universal empirical constants. The resultant vortex strength variation has been shown to agree quite well with the limited data available. For given vortex strengths and locations, simple schemes for computing the induced load on control fins placed well aft of the jet nozzle have been developed. One of these is valid for subsonic free stream Mach numbers, and the other for supersonic freestream. Results of sample calculations show that for a fixed Mach number, increasing the jet chamber pressure may increase or decrease fin interference effects, depending upon the relative location of the jet-induced vortices and the fins which contribute to the interference force or moment. Limited data comparisons for supersonic mainstreams have been made, and the agreement between calculations and experiment has been found to be satisfactory.

## Appendix A

### TERMINAL SHOCK LOCATION FOR SUPERSONIC NOZZLES

In this appendix, a formula is derived for calculating the location of the terminal shock or Mach disk in a highly under expanded rocket plume exhausting into still air. The approach is the analytical equivalent of a graphical method developed by Adamson and Nicholls in Reference A-1. The expression for the terminal shock location for a nozzle with exit Mach number,  $M_j$ , greater than unity, is based upon a simple, semi-empirical representation of the Mach number distribution along the centerline of the plume of a sonic nozzle.

#### A.1 SONIC NOZZLE

For a sonic nozzle exhausting into still air, it has been shown in Reference A-2 that the Mach number distribution along the centerline of the plume may be represented by the flow from a compressible source whose sonic sphere radius is given by

$$r^* = (0.61) d_j^* \quad (\text{A-1})$$

(Starred quantities will refer to conditions for the sonic nozzle.)

Flow continuity for a compressible source requires that

$$\rho_1^* u_1^* r^{*2} = \rho^* u z^{*2}$$

where  $( )_1$  denotes conditions at the sonic radius  $M^* = 1$

$z^*$  is a coordinate with origin at the nozzle exit plane (See Figure A-1b)

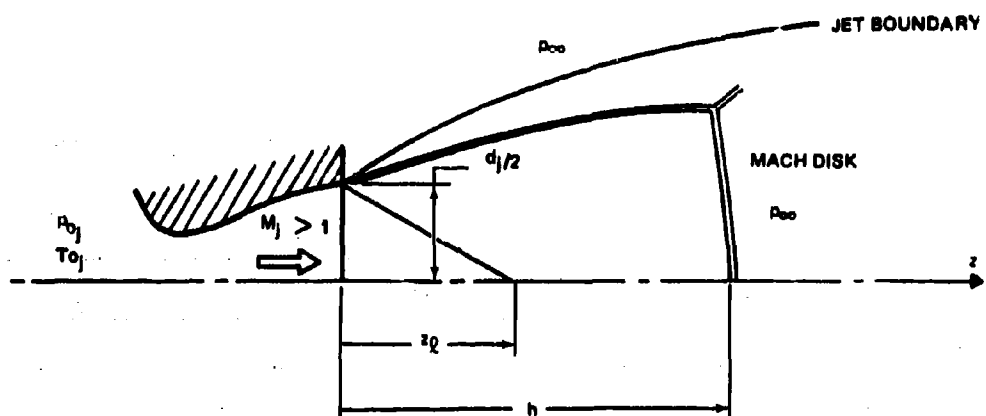
The above relation can be written in terms of stagnation conditions as

$$\left(\frac{z^*}{r^*}\right)^2 = \left(\frac{\gamma+1}{2}\right)^{-\frac{\gamma+1}{2(\gamma-1)}} \left(\frac{p_{o,j}^*}{p^*}\right) \left(\frac{T^*}{T_{o,j}^*}\right)^{1/2} \frac{1}{M^*} \quad (\text{A-2})$$

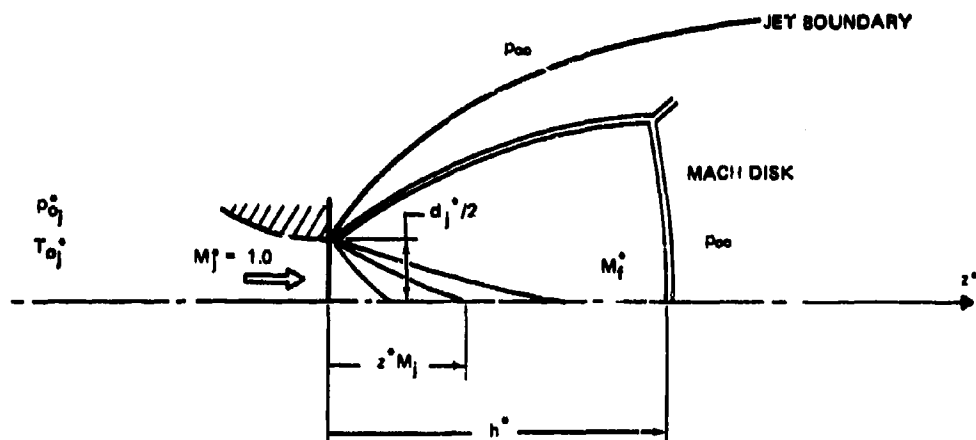
Using isentropic flow relations and Equation (A-1), Equation (A-2) can be written in the form

$$\frac{z^*}{d_j^*} = (0.61) \left[\frac{2}{\gamma+1}\right]^{\frac{\gamma+1}{4(\gamma-1)}} \left\{ \frac{1}{\sqrt{M^*}} \left[ 1 + \left(\frac{\gamma-1}{2}\right) M^{*2} \right]^{\frac{\gamma+1}{4(\gamma-1)}} \right\} \quad (\text{A-3})$$





a. SUPERSONIC NOZZLE



b. SONIC NOZZLE

Figure A-1. Mach Disk Height for a Supersonic Nozzle Based on Sonic Nozzle Results

Figure A-2 compares Equation (A-3) for  $\gamma = 1.4$  with the results of a method of characteristics solution reported in Reference A-3. Evidently the agreement is excellent, except in the immediate neighborhood of the orifice.

With the subscript  $f$  denoting flow conditions just upstream of the terminal shock, Equation (A-1) and Equation (A-2) can be combined to yield

$$\frac{h^*}{d_j^*} = (0.61) \left(\frac{\gamma+1}{2}\right)^{-\frac{\gamma+1}{4(\gamma-1)}} \left(\frac{p_{o_j}^*}{p_f^*}\right)^{1/2} \left(\frac{T_f^*}{T_{o_j}^*}\right)^{1/4} \frac{1}{\sqrt{M_f^*}}$$

The final pressure and temperature,  $p_f^*$  and  $T_f^*$ , are determined by the condition that the pressure across the Mach disk rise to the external pressure,  $p_\infty$ . Using normal shock relations, then, the above equation may be written as

$$\frac{h^*}{d_j^*} = (0.61) \left(\frac{\gamma+1}{2}\right)^{-\frac{\gamma+1}{4(\gamma-1)}} \left(\frac{p_{o_j}^*}{p_\infty}\right)^{1/2} \left(\frac{T_\infty}{T_{o_j}^*}\right)^{1/4} \left\{ \frac{2\gamma M_f^{*2} - (\gamma-1)}{(\gamma-1)M_f^{*2} + 2} \right\}^{1/2} \quad (A-4)$$

The final Mach number,  $M_f^*$ , may also be determined by the condition that the pressure immediately downstream of the terminal shock be equal to  $p_\infty$  and normal shock relations then yield the equation

$$\frac{p_\infty}{p_{o_j}^*} = \left[ \frac{2\gamma M_f^{*2} - (\gamma-1)}{\gamma+1} \right] \left[ \frac{2}{(\gamma-1)M_f^{*2} + 2} \right]^{\frac{\gamma}{\gamma-1}} \quad (A-5)$$

It is not possible to invert Equation (A-5) to obtain  $M_f^*$  for a given pressure ratio, but it is possible to obtain this quantity from Figure A-3, which is a plot of Equation (A-5) for  $\gamma = 1.4$ . Figure A-3 indicates that for moderately high pressure ratios  $M_f^*$  is large, and it is therefore possible to write Equation (A-4) in the approximate form

$$\frac{h^*}{d_{o_j}^*} \approx (0.61) \left(\frac{\gamma+1}{2}\right)^{-\frac{\gamma+1}{4(\gamma-1)}} \left(\frac{2\gamma}{\gamma-1}\right)^{1/4} \left(\frac{T_\infty}{T_{o_j}^*}\right)^{1/4} \left(\frac{p_{o_j}^*}{p_\infty}\right)^{1/2} \quad (A-6)$$

If it is further assumed that  $T_\infty = T_{o_j}$ , and that  $\gamma = 1.4$ , Equation (A-6) becomes

$$\frac{h^*}{d_j^*} = (0.755) \sqrt{\frac{p_{o_j}^*}{p_\infty}} \quad (A-7)$$

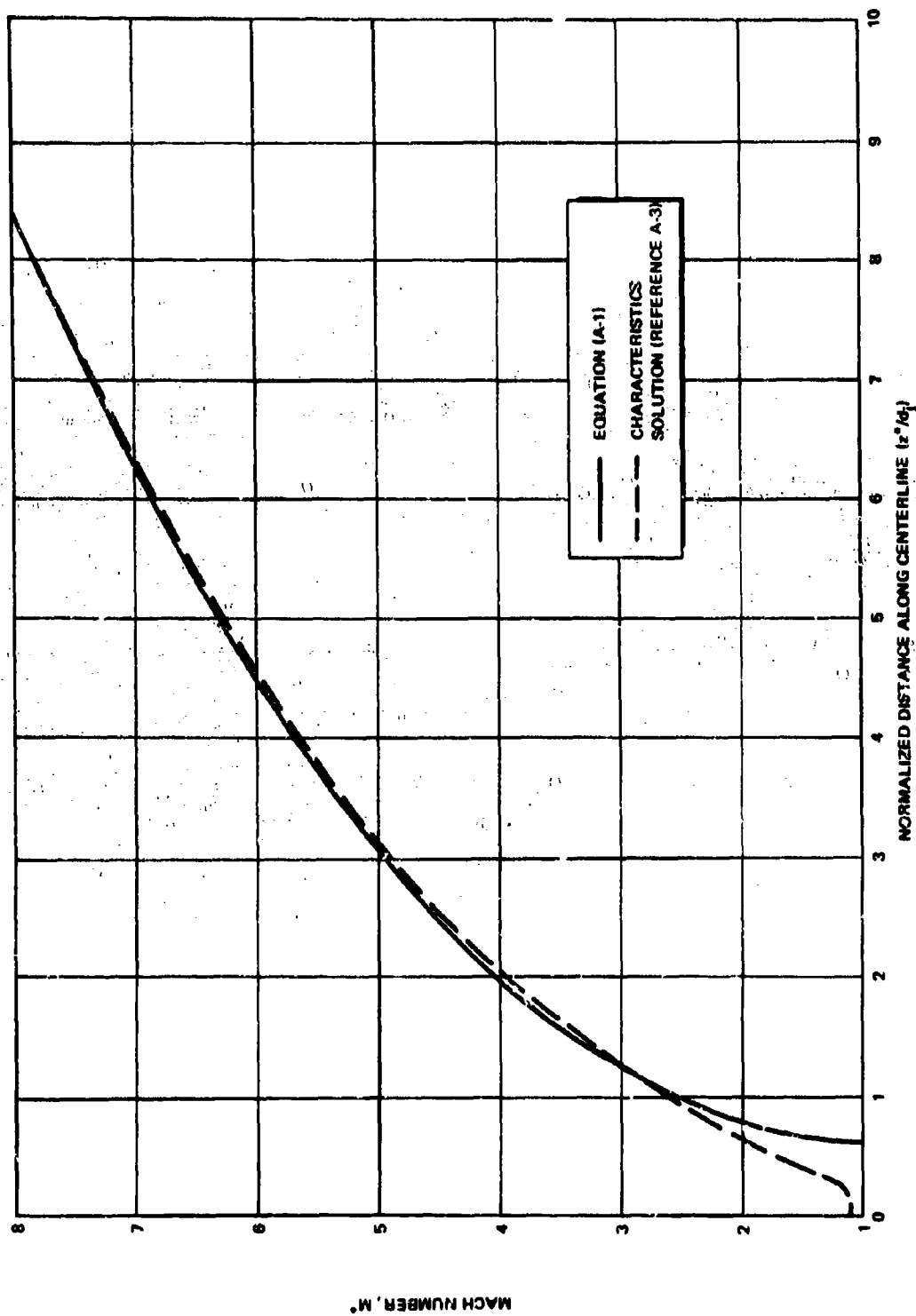


Figure A-2. Mach Number Distribution for Sonic Nozzle Plume

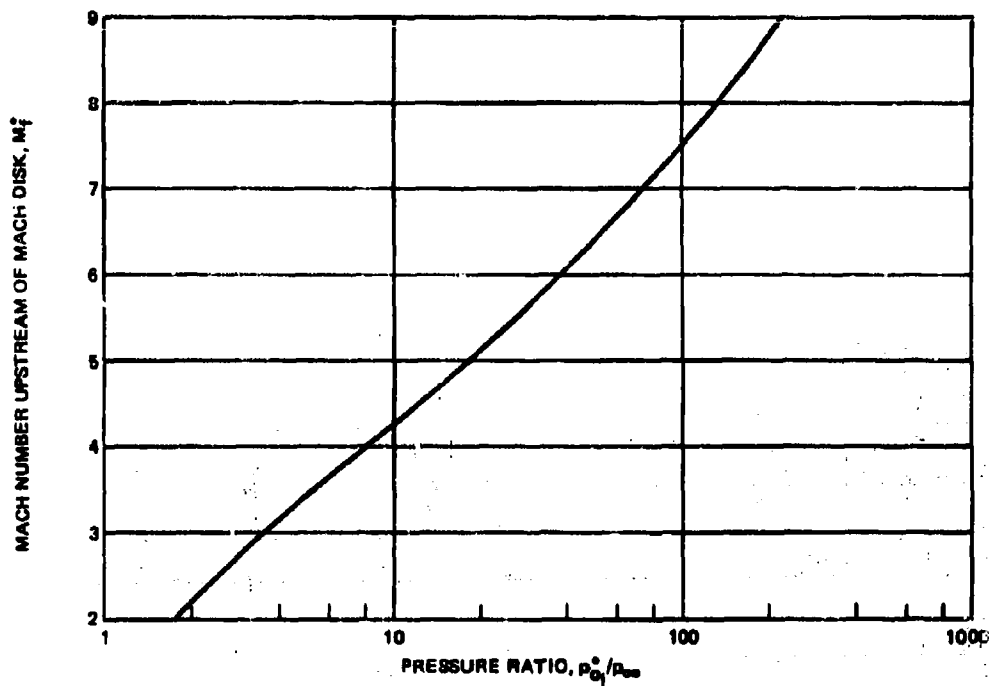


Figure A-3. Mach Number Upstream of the Mach Disk

This may be compared with the empirical formula derived by Crist, Sherman, and Glass in Reference A-4

$$\frac{h_j^*}{d_j^*} = (0.645) \sqrt{\frac{p_{0j}^*}{p_{\infty}}} \quad (\text{A-3})$$

Equation (A-4) predicts that the effects of varying  $\gamma$  and the temperature ratio ( $T_{\infty}/T_{0j}^*$ ) will be small. This general trend has been observed experimentally in Reference A-4.

## A.2 SUPERSONIC NOZZLE

Following the method of Adamson and Nicholls in Reference A-1, the terminal shock location for a supersonic nozzle will now be derived based on the sonic nozzle results of the previous section. Referring to Figure A-1a, it is evident that the flow along the centerline of the supersonic nozzle plume will remain undisturbed until the first expansion fan from the nozzle lip strikes the axis. Let the distance from the exit to the point at which this happens be denoted by  $z_f$ . In Figure A-1b, the distance  $z_{M_j}^*$  denotes the point at which the expanding flow in the subsonic nozzle plume reaches a Mach number equal to the exit Mach number of the supersonic nozzle. Adamson and Nicholls

have assumed that the Mach number distribution between  $h$  and  $z_f$  is the same as the Mach number distribution between  $h^*$  and  $z_{M_j}^*$ . Assuming once again that the flow then crosses the Mach disk to achieve a pressure equal to  $p_\infty$ , it follows that

$$h = z_f + h^* - z_{M_j}^*$$

Normalizing by the exit diameter of the supersonic nozzle yields

$$\frac{h}{d_j} = \left( \frac{A_j^*}{A_j} \right)^{\frac{1}{2}} \left( \frac{h}{d_j^*} - \frac{z_{M_j}^*}{d_j^*} \right) + \frac{z_f}{d_j} \quad (A-9)$$

Equation (A-4) may be used for  $h^*/d_j^*$ , and Equation (A-3) will give, for  $z_{M_j}^*/d_j^*$

$$\frac{z_{M_j}^*}{d_j^*} = (0.61) \left[ \frac{2}{\gamma+1} \right]^{\frac{\gamma+1}{4(\gamma-1)}} \left\{ \frac{1}{\sqrt{M_j}} \left[ 1 + \frac{\gamma-1}{2} M_j^2 \right]^{\frac{\gamma+1}{4(\gamma-1)}} \right\} \quad (A-10)$$

It will now be required that the sonic and supersonic nozzles have the same stagnation conditions

$$p_{o_j}^* = p_{o_j}$$

$$T_{o_j}^* = T_{o_j}$$

and then isentropic streamtube ; yield

$$\left( \frac{A_j^*}{A_j} \right)^{\frac{1}{2}} = \left( \frac{\gamma+1}{2} \right)^{\frac{\gamma+1}{4(\gamma-1)}} \sqrt{1 + \left( \frac{\gamma-1}{2} \right) M_j^2}^{-\frac{\gamma+1}{4(\gamma-1)}} \quad (A-11)$$

Furthermore, it is evident from Figure A-1a that if the initial characteristic is assumed to be straight, the ratio  $(z_f/d_j)$  is just equal to one half the cotangent of the Mach angle.

Thus,

$$\frac{z_f}{d_j} = \frac{1}{2} \sqrt{M_j^2 - 1} \quad (A-12)$$

Substituting Equations (A-4), (A-11) and (A-12) into Equation (A-9) yields the final expression for the Mach disk location for a supersonic nozzle as

$$\frac{h}{d_j} = (0.61) \left\{ \sqrt{\frac{p_{o_j}}{p_\infty}} \left( \frac{T_\infty}{T_{o_j}} \right)^{\frac{1}{4}} \left[ \frac{2\gamma M_f^{*2} - (\gamma - 1)}{(\gamma - 1) M_f^{*2} + 2} \right]^{\frac{1}{4}} \right. \\ \left. \left[ \frac{\sqrt{M_j}}{\left[ 1 + \left( \frac{\gamma - 1}{2} \right) M_j^2 \right]^{\frac{\gamma + 1}{4(\gamma - 1)}}}} - 1 \right] + \frac{1}{2} \sqrt{M_j^2 - 1} \right\} \quad (A-13)$$

Again,  $M_f^*$  may be obtained from Figure A-3 for a given pressure ratio (and for  $\gamma = 1.4$ ) or if  $M_f^*$  is assumed to be large an approximation is

$$\frac{h}{d_j} = (0.61) \left\{ \left( \frac{2}{\gamma - 1} \right)^{\frac{1}{4}} \sqrt{\frac{p_{o_j}}{p_\infty}} \left[ \frac{\sqrt{M_j}}{\left[ 1 + \left( \frac{\gamma - 1}{2} \right) M_j^2 \right]^{\frac{\gamma + 1}{4(\gamma - 1)}}}} - 1 \right] + \right. \\ \left. + \frac{1}{2} \sqrt{M_j^2 - 1} \right\} \quad (A-14)$$

(where it has again been assumed that  $T_\infty = T_{o_j}$ ).

It is evident that Equation (A-13) does not reduce to the sonic nozzle result when  $M_j = 1$  (due to the second term in the braces). This discrepancy is caused by the fact that the compressible source model does not represent the Mach number distribution near the exit correctly (see Figure A-2).

### A.3 COMPARISON WITH DATA

Figures A-4, A-5, and A-6 compare the above formulae to the experimental results of Love, et al. (Reference A-5). For  $M_j = 1$ , some discrepancy is evident in Figure A-4. Figure A-4 also illustrates the difference between taking the limit of Equation (A-13) as  $M_j \rightarrow 1$  and using the sonic nozzle results of Equation (A-4). In both instances, the approximate formulas obtained by assuming  $M_j^* \gg 1$  give results which are in close agreement with those obtained by using the actual value of  $M_j$  given by Figure A-3. The discrepancies for  $M_j = 1$  due to the fact that supersonic source flow does not accurately represent the Mach number distribution in the immediate neighborhood of the nozzle plane, as shown in Figure A-2. Since this region of discrepancy is removed by the method of calculating  $h$  for supersonic nozzles, the agreement with data improves at higher nozzle Mach numbers. Figure A-5 compares theory and experiment for  $M_j = 2$ , and the agreement is very good. The more complicated Equation (A-13) gives slightly better agreement with data but the difference with the results obtained by assuming  $M_j^* \gg 1$  does not appear to be significant. Figure A-6 compares theory and experiment for  $M_j = 3$ . It should be noted that for this Mach number, the terminal shock does not exist for pressure ratios of less than 90. The points shown in the figure below this value correspond to the distance from the exit to the first intersection of a diamond shock pattern. The unshaded data points on the figure are true Mach disk locations, and the theory again predicts them quite accurately.

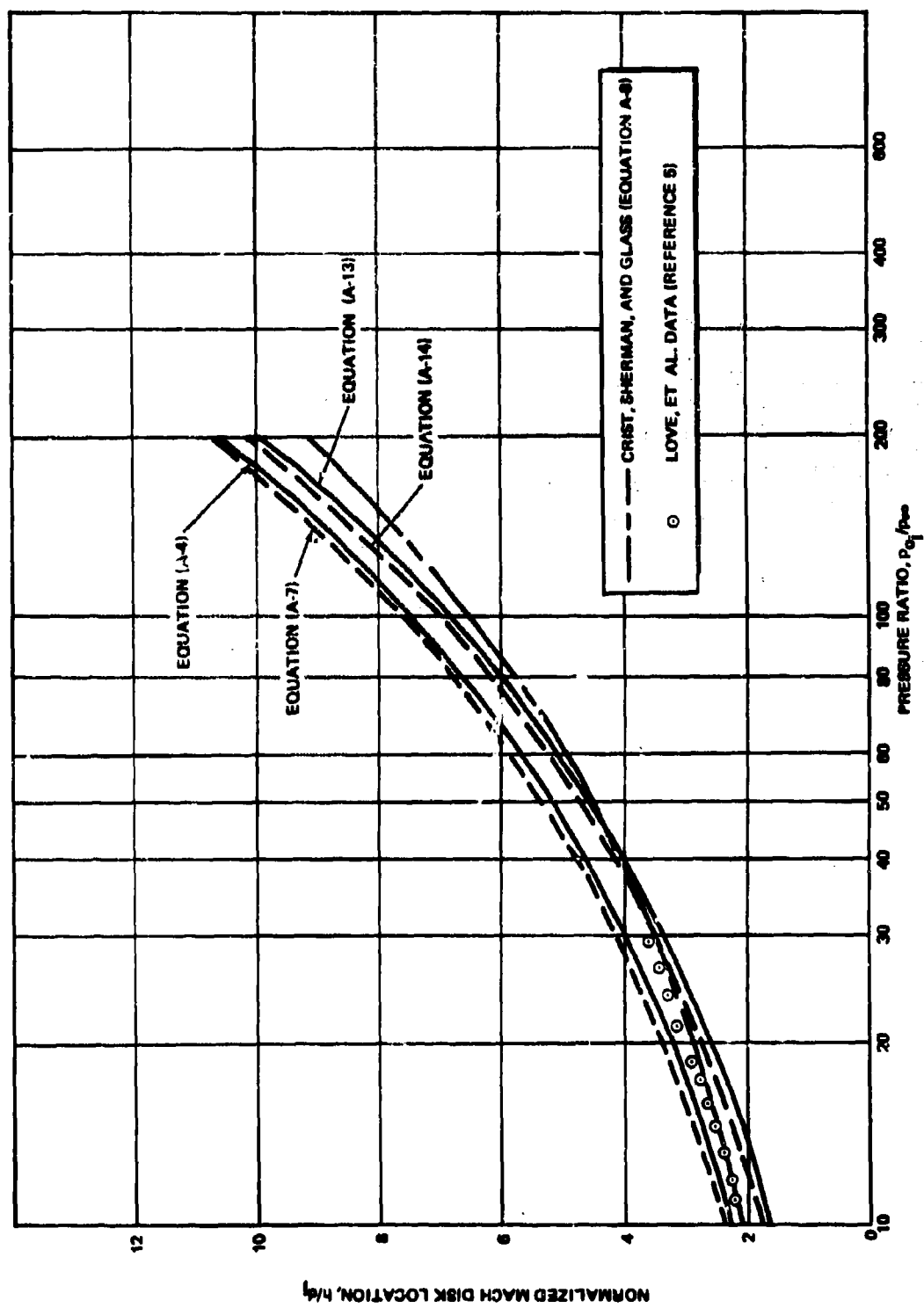


Figure A-4. Comparison of Theory and Data for  $M_1 = 1.00$



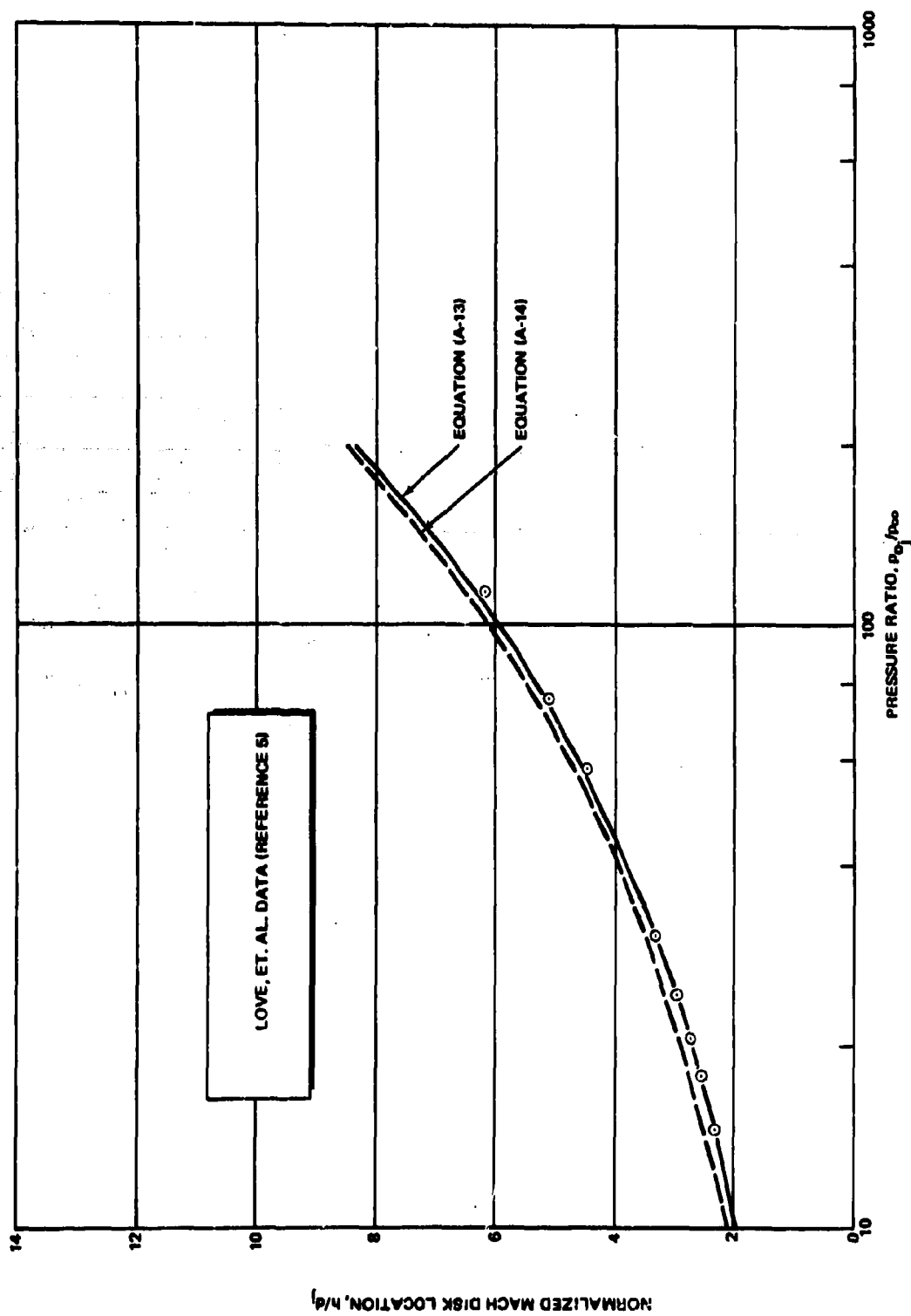


Figure A-5. Comparison of Theory and Data for  $M_j = 2.00$

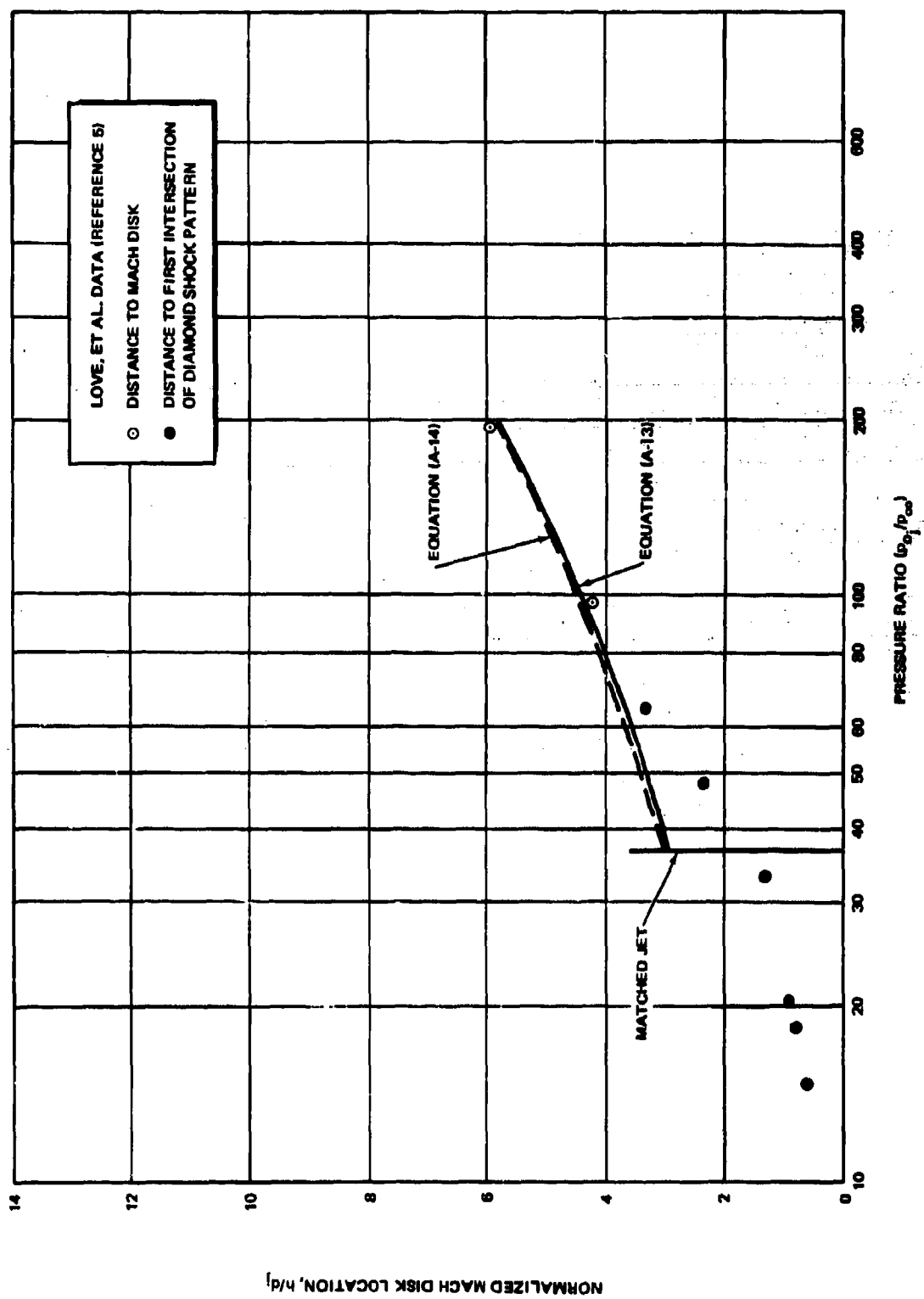


Figure A-6. Comparison of Theory and Data for  $M_j = 3.00$

**BLANK PAGE**

## Appendix B

### SINGULARITY STRENGTHS FOR VORTEX MODEL

#### B.1 DERIVATION OF FOURIER COEFFICIENTS

As discussed in Section 3.2.2, the vortex model leads to the following expression for the pressure coefficients

$$\begin{aligned}
 C_p = A_2 \left[ \frac{1}{\zeta^2} + \frac{1}{\bar{\zeta}^2} \right] - \left[ A_1 \left( 1 - \frac{A_2}{r^2} \right) \right] \left[ \frac{1}{\zeta} + \frac{1}{\bar{\zeta}} \right] - \left[ \frac{A_1^2}{r^2} + \frac{A_2^2}{r^4} \right] - \\
 - iA_3 (\zeta_0 - \bar{\zeta}_0) \left[ \frac{\zeta^2 + A_1 \bar{\zeta} - A_2}{\zeta^2 (\zeta - \zeta_0)(\zeta - \bar{\zeta}_0)} + \frac{\bar{\zeta}^2 + A_1 \zeta - A_2}{\bar{\zeta}^2 (\bar{\zeta} - \zeta_0)(\bar{\zeta} - \bar{\zeta}_0)} \right] + \\
 + A_3^2 (\zeta_0 - \bar{\zeta}_0)^2 \left[ \frac{\zeta^2}{r_0^2 (\zeta - \zeta_0)(\bar{\zeta} - \bar{\zeta}_0) \left[ \zeta - (r^2/\zeta_0) \right] \left[ \bar{\zeta} - (r^2/\bar{\zeta}_0) \right]} \right]
 \end{aligned}
 \tag{B-1}$$

The objective is to obtain the first three terms in the Fourier series representation for Equation (B-1) by means of the relations:

$$c_0(r) = \frac{1}{\pi} \int_0^\pi C_p(r, \theta) d\theta
 \tag{B-2}$$

$$c_n(r) = \frac{2}{\pi} \int_0^\pi C_p(r, \theta) \cos n\theta d\theta \quad (B-3)$$

$$(n = 1, 2)$$

(The symmetry of the model about the plane  $\theta = 0$  insures that all sine terms in the series will be identically zero.) Since pressure coefficients predicted by the model and determined from experiment are to be matched at  $r = 1$ , it is simpler to start out with Equation (B-1) written for  $r = 1$ . Written in real variables, Equation (B-1) takes the form.

$$\begin{aligned} C_p(1, \theta) = & - \left\{ A_1^2 + A_2^2 \right\} + \frac{A_3^2 (\zeta_o - \bar{\zeta}_o)^2}{F(\theta)} - \left\{ 2A_1 (1 - A_2) \right\} \cos \theta - \\ & - \left\{ 2A_2 \right\} \cos 2\theta + \left\{ \frac{2iA_3 (\zeta_o - \bar{\zeta}_o)}{F(\theta)} \right\} \left\{ \left[ 1 - A_2 r_o^2 \right] \cos 2\theta + \right. \\ & + \left[ A_1 (1 + r_o^2) + (\zeta_o + \bar{\zeta}_o) (A_2 - 1) \right] \cos \theta + \\ & \left. + \left[ r_o^2 - A_1 (\zeta_o + \bar{\zeta}_o) - A_2 \right] \right\} \end{aligned} \quad (B-4)$$

where

$$F(\theta) = a_0 + a_1 \cos \theta + a_2 \cos 2\theta \quad (B-5)$$

and:

$$a_0 = (1 + \zeta_o \bar{\zeta}_o)^2 + \zeta_o^2 + \bar{\zeta}_o^2 \quad (B-6a)$$

$$a_1 = -2 (1 + \zeta_o \bar{\zeta}_o) (\zeta_o + \bar{\zeta}_o) \quad (B-6b)$$

$$a_2 = 2 \zeta_0 \bar{\zeta}_0$$

(B-6c)

Then the integral in Equation (B-2) yields

$$-c_0(1) = (A_1^2 + A_2^2) - A_3^2 (\zeta_0 + \bar{\zeta}_0)^2 \frac{I_{02}}{\pi} +$$

$$+ \left[ \frac{2iA_3(\zeta_0 - \bar{\zeta}_0)}{\pi} \right] I_{01} \quad (B-7)$$

where

$$I_{02} = \int_0^\pi \frac{d\theta}{a_0 + a_1 \cos \theta + a_2 \cos 2\theta} \quad (B-8)$$

and

$$I_{01} = \int_0^\pi \left( \frac{b_0 + b_1 \cos \theta + b_2 \cos 2\theta}{a_0 + a_1 \cos \theta + a_2 \cos 2\theta} \right) d\theta \quad (B-9)$$

and

$$b_0 = \zeta_0 \bar{\zeta}_0 - A_1 (\zeta_0 + \bar{\zeta}_0) - A_2 \quad (B-9a)$$

$$b_1 = A_1 (1 + \zeta_0 \bar{\zeta}_0) + (\zeta_0 + \bar{\zeta}_0) (A_2 - 1) \quad (B-9b)$$

$$b_2 = 1 - A_2 (\zeta_0 \bar{\zeta}_0) \quad (B-9c)$$

Evaluating  $I_{o_2}$  first, it is advantageous to make the substitution:

$$x = \cos \theta$$

So that the integral becomes, with some rearranging

$$I_{o_2} = -\frac{i}{2a_2} \int_{-1}^{+1} \frac{dx}{\sqrt{1-x^2} \left[ x^2 + \left(\frac{a_1}{2a_2}\right)x + \frac{(a_0 - a_2)}{2a_2} \right]}$$

or, factoring the quadratic in the denominator

$$I_{o_2} = -\frac{i}{2a_2} \int_{-1}^{+1} \frac{dx}{\sqrt{1-x^2} (x-c)(x-\bar{c})} \quad (B-10)$$

where it may be shown (using Equation B-6), that

$$c = \frac{\zeta_o^2 + 1}{2\zeta_o} \quad (B-11a)$$

$$\bar{c} = \frac{\zeta_o^2 + 1}{2\zeta_o} \quad (B-11b)$$

The integral in Equation (B-10) may be evaluated as follows: Consider a complex  $z$  plane, slit along the real axis from  $-1$  to  $+1$ . In this plane, consider the contour integral

$$\oint_C \frac{dz}{\sqrt{z^2-1} (z-c)(z-\bar{c})} \quad (B-12)$$

where  $C$  is the contour shown in Figure B-1

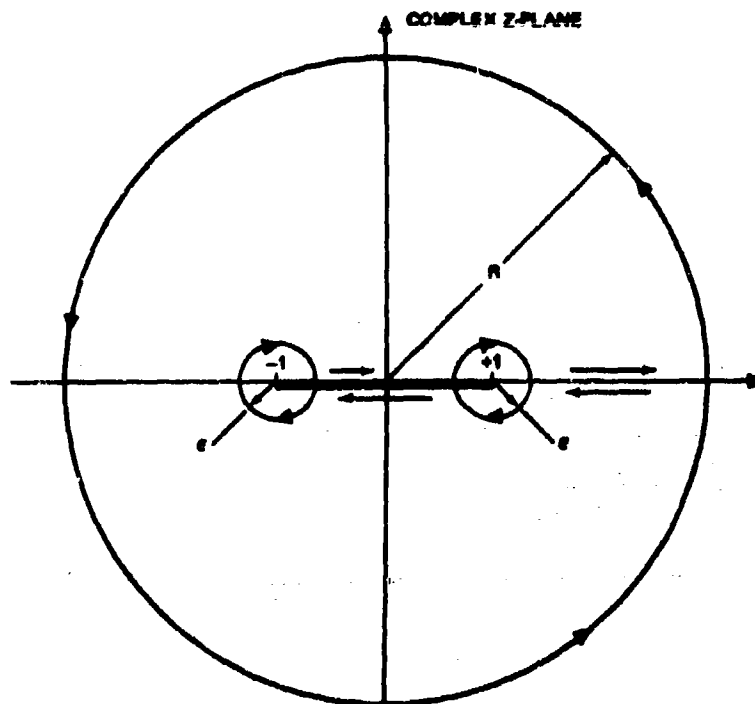


Figure B-1. Integration Contour for Equation (B-12)

It is assumed that the poles  $c$  and  $\bar{c}$  do not lie on the contour, and that the circle of radius  $R$  is large enough to enclose both singularities. In that case, the use of the Residue Theorem as discussed in Reference B-1 yields

$$J = \frac{2\pi i}{(c - \bar{c})} \left\{ \frac{1}{\sqrt{c^2 - 1}} - \frac{1}{\sqrt{\bar{c}^2 - 1}} \right\} \quad (\text{B-13})$$

Writing the different parts of the integral along  $C$ , and then allowing

$$R \rightarrow \infty$$

and

$$\epsilon \rightarrow 0$$



it is possible to show that

$$\vartheta = \frac{2}{i} \int_{-1}^{+1} \frac{dx}{\sqrt{1-x^2} (x-c) (x-\bar{c})} \quad (\text{B-14})$$

Then Equations (B-13) and (B-14) lead to the final result

$$I_{02} = - \frac{\pi}{2a_2 (c-\bar{c})} \left[ \frac{1}{\sqrt{c^2-1}} - \frac{1}{\sqrt{\bar{c}^2-1}} \right] \quad (\text{B-15})$$

The integral  $\int_{-1}^c$

$I_{01}$

in Equation (B-9) may be evaluated in an analogous fashion, as may the other integrals which arise from the application of Equation (B-3). The final equations obtained for the three Fourier coefficients at  $r = 1$  are:

$$A_1^2 + A_2^2 - a_{33} A_3^2 - a_{23} A_2 A_3 + c_0(1) = 0 \quad (\text{B-16})$$

$$b_{33} A_3^2 + b_{23} A_2 A_3 + b_{12} A_1 A_2 - b_{13} A_1 A_3 - \beta_1 A_1 - c_1(1) = 0 \quad (\text{B-17})$$

$$c_{33} A_3^2 + c_{23} A_2 A_3 - c_{13} A_1 A_3 + \gamma_2 A_2 - \gamma_3 A_3 - c_2(1) = 0 \quad (\text{B-18})$$

where:

$$a_{33} = \frac{(\zeta_0 - \bar{\zeta}_0)}{(\zeta_0 \bar{\zeta}_0 - 1)} \left[ \frac{\zeta_0}{\zeta_0^2 - 1} - \frac{\bar{\zeta}_0}{\bar{\zeta}_0^2 - 1} \right] \quad (\text{B-19a})$$

$$a_{23} = 2i (\zeta_0 - \bar{\zeta}_0) \quad (\text{B-19b})$$

$$b_{33} = \frac{(\zeta_o - \bar{\zeta}_o)}{(\zeta_o \bar{\zeta}_o - 1)} \left[ \frac{\zeta_o^2 + 1}{\zeta_o^2 - 1} - \frac{\bar{\zeta}_o^2 + 1}{\bar{\zeta}_o^2 - 1} \right] \quad (\text{B-20a})$$

$$b_{23} = 2i (\zeta_o^2 - \bar{\zeta}_o^2) \quad (\text{B-20b})$$

$$b_{12} = \beta_1 = 2 \quad (\text{B-20c})$$

$$b_{13} = a_{23} = 2i (\zeta_o - \bar{\zeta}_o) \quad (\text{B-20d})$$

$$c_{33} = \frac{(\zeta_o - \bar{\zeta}_o)^2}{\zeta_o \bar{\zeta}_o} \left\{ 1 + \frac{1}{(\zeta_o - \bar{\zeta}_o)(\zeta_o \bar{\zeta}_o - 1)} \right.$$

$$\left. \left[ \frac{\bar{\zeta}_o (\zeta_o^4 + 1)}{\zeta_o^2 - 1} - \frac{\zeta_o (\bar{\zeta}_o^4 + 1)}{\bar{\zeta}_o^2 - 1} \right] \right\} \quad (\text{B-21a})$$

$$c_{23} = 2i (\zeta_o^3 - \bar{\zeta}_o^3) \quad (\text{B-21b})$$

$$c_{13} = b_{23} = 2i (\zeta_o^2 - \bar{\zeta}_o^2) \quad (\text{B-21c})$$

$$\gamma_2 = 2 \quad (\text{B-21d})$$

$$\gamma_3 = a_{23} = 2i (\zeta_o - \bar{\zeta}_o) \quad (\text{B-21e})$$

## B.2 SOLUTION OF THE EQUATIONS

Substituting numerical values for  $c_0(1)$ ,  $c_1(1)$ , and  $c_2(1)$  evaluated using Vogler's data from Reference (B-2) will yield the five simultaneous equations for the five unknowns  $A_1$ ,  $A_2$ ,  $A_3$ ,  $r_0$ , and  $\theta_0$ . These are Equations (31) and (32), in Section 3.2.2, (B-16), (B-17), and (B-18), with the supplemental Equations (B-19a) through (B-21e), in which it is recalled that

$$\zeta_0 = r_0 e^{i\theta_0}, \quad \bar{\zeta}_0 = r_0 e^{-i\theta_0}$$

It is possible to combine the above set of equations into another set which is more suitable for numerical calculation. After a considerable account of algebra, the results are:

$$Q_4 A_3^4 + Q_3 A_3^3 + Q_2 A_3^2 + Q_1 A_3 + Q_0 = 0 \quad (\text{B-22})$$

where

$$Q_4 = b_{33} \beta_3^2 + \left[ 4(r_0^2 - 1) \sin 2\theta_0 \right] c_{33} \beta_3 + \left[ \frac{4 \cos \theta_0}{r_0} \right] c_{33}^2 \quad (\text{B-23a})$$

$$Q_3 = 4b_{33} \beta_3 + \left[ 8(r_0^2 - 1) \sin 2\theta_0 \right] \left[ c_{33} + 2\beta_3 r_0 \sin \theta_0 \right] + 4c_{33} \beta_3 \left( \frac{\cos \theta_0}{r_0} \right) + 16c_{33} \sin 2\theta_0 \quad (\text{B-23b})$$

$$Q_2 = 4b_{33} - [4(r_o^2 - 1) \sin 2\theta_o] [\beta_3 c_2(1) - 8r_o \sin \theta_o] +$$

$$+ \left[ \frac{8 \cos \theta_o}{r_o} \right] [c_{33} + 2\beta_3 (r_o \sin \theta_o)] - c_1(1) \beta_3^2 -$$

$$- \left[ \frac{8 \cos \theta_o}{r_o} \right] [c_{33} c_2(1) - 8r_o^2 \sin^2 \theta_o] \quad (B-23c)$$

$$Q_1 = - [8(r_o^2 + 1) \sin 2\theta_o] c_2(1) - \left[ \frac{4 \cos \theta_o}{r_o} \right] [\beta_3 c_2(1) - 8r_o \sin \theta_o]$$

$$- 4\beta_3 c_1(1) \quad (B-23d)$$

$$Q_o = \left[ \frac{4 \cos \theta_o}{r_o} \right] c_2^2(1) - 4c_1(1) - \left[ \frac{8 \cos \theta_o}{r_o} \right] c_2(1) \quad (B-23e)$$

an expression for  $b_{33}$  is given by Equation (B-20a). Written in real variables this has the form

$$b_{33} = \frac{16r_o^3 \sin^2 \theta_o \cos \theta_o}{(r_o^2 - 1) [r_o^4 - 2r_o^2 \cos 2\theta_o + 1]} \quad (B-24)$$

The variable  $\beta_3$  is given by

$$\beta_3 = - (4r_o \sin \theta_o) \left[ (r_o^2 - 1) (1 + 2 \cos 2\theta_o) - 1 \right] \quad (B-25)$$

The variable  $c_{33}$  has been defined in Equation (B-12a), and in terms of real variables it has the form

$$c_{33} = -4 \sin^2 \theta_o \left\{ 1 + \frac{1}{(r_o^2 - 1)} \left[ \frac{r_o^6 - r_o^2(r_o^2 + 1) [1 + 2\cos 2\theta_o] + 1}{r_o^4 - 2r_o^2 \cos 2\theta_o + 1} \right] \right\} \quad (\text{B-26})$$

Note that if values of  $r_o$  and  $\theta_o$  are assumed, Equation (B-22) becomes a fourth order polynomial for  $A_3$ . The other equations in the set are:

$$A_2 = \frac{c_2(1) - 4A_3(r_o \sin \theta_o) - c_{33}A_3^2}{\beta_3 A_3 + 2} \quad (\text{B-27})$$

$$A_1 = 2A_2 \left[ \frac{\cos \theta_o}{r_o} \right] \quad (\text{B-28})$$

$$\tan^3 \theta_o - \left( \frac{A_3}{A_1} \right) \tan^2 \theta_o + \left[ \frac{4A_2}{A_1^2} + 1 \right] \tan \theta_o - \left( \frac{A_3}{A_1} \right) = 0 \quad (\text{B-29})$$

and

$$\begin{aligned}
& \{4A_2A_3\sin\theta_o\} r_o^7 + \{A_1^2 + A_2^2 + c_o(1)\} r_o^6 \\
& - \left[ \left[ 4A_2A_3\sin\theta_o \right] \left[ 1 + 2\cos 2\theta_o \right] \right] r_o^5 - \\
& - \left\{ A_1^2 + A_2^2 + c_o(1) \right\} \left[ 1 + 2\cos 2\theta_o \right] + \\
& + 4A_3^2 \sin^2 \theta_o \left\{ r_o^4 + \left[ \left[ 4A_2A_3\sin\theta_o \right] \left[ 1 + 2\cos 2\theta_o \right] \right] r_o^3 + \right. \\
& + \left. \left[ \left[ A_1^2 + A_2^2 + c_o(1) \right] \left( 1 + 2\cos 2\theta_o \right) - \right. \right. \\
& - 4A_3^2 \sin^2 \theta_o \left. \right\} r_o^2 - \left[ 4A_2A_3\sin\theta_o \right] r_o - \\
& - \left\{ A_1^2 + A_2^2 + c_o(1) \right\} = 0 \tag{B-30}
\end{aligned}$$

Equations (B-22) through (B-30) have been used in a numerical scheme to obtain solutions. Starting with assumed values for  $r_o$  and  $\theta_o$ , the coefficients of the fourth-order polynomial in Equation (B-22) are calculated using Equations (B-23a) through (B-26). All roots of this polynomial are then obtained numerically, and any complex roots discarded. The remaining values of  $A_3$  are used to calculate corresponding values  $A_2$  and  $A_1$  by means of Equations (B-27) and (B-28). The cubic in Equation (B-29) is then solved numerically to obtain new values for  $\theta_o$ ; and, finally, the seventh-order polynomial in Equation (B-30) is solved for  $r_o$ . Any complex roots are again discarded.

Note that if all roots in the above scheme are real, for each initial value of  $r_o$  and  $\theta_o$  there exist the following possibilities:

4 possible  $A_1, A_2, A_3$ 's

12 possible  $\theta_o$ 's

84 possible  $r_o$ 's

In practice, however, very few roots turn out to be real. In addition to requiring that all variables be real, two more constraints are imposed on the results. It is known physically that the vortices must lie in the leeward quadrants, and consequently the requirement

$$0^\circ \leq \theta_o \leq 90^\circ \quad (\text{B-31})$$

is imposed. Since it is also known that the vortices lie near the jet, it is also required that

$$0 < r_o < 1 \quad (\text{B-32})$$

### B.3 NUMERICAL RESULTS

The validity of the vortex model as tested by carrying through a complete case for  $U_o/U_j = 0.4$ , based upon the data of Vogler in Reference B-2. A direct iterative scheme as suggested by the discussion above was unsuccessful because in many cases an input  $(r_o, \theta_o)$  pair which satisfied the constraints of Equations (B-31) and (B-32), did not lead to any calculated  $(r_o, \theta_o)$  values which satisfied this constraint. Therefore, it was decided to search the matrix to acceptable  $r_o$  and  $\theta_o$  inputs for those values which led to new values which also satisfied constraints of Equations (B-31) and (B-32). A flow chart for this scheme is shown in Figure B-1. Briefly, the program takes input initial values for the components of the vortex position vector  $(r_o, \theta_o)$  which satisfy the constraints of Equations (B-31) and (B-32), and searches for solutions to the set of five nonlinear equations which also satisfy the above constraints. The most relevant input-output diagram is depicted in Figure B-2. The diagram indicates how the acceptable output varies as the input  $\theta_o$  is varied for a fixed value of the input  $r_o$ . The input values vary over the entire acceptable range (solid lines), but only those input values which lie within the regions shown by dotted boundaries lead to output  $r_o$  and  $\theta_o$  which satisfy the constraints of Equations (B-31) and (B-32). For the cases shown in Figure B-3, the first input values (solid points)

$$r_o = 0.65$$

$$\theta_o = 5^\circ$$

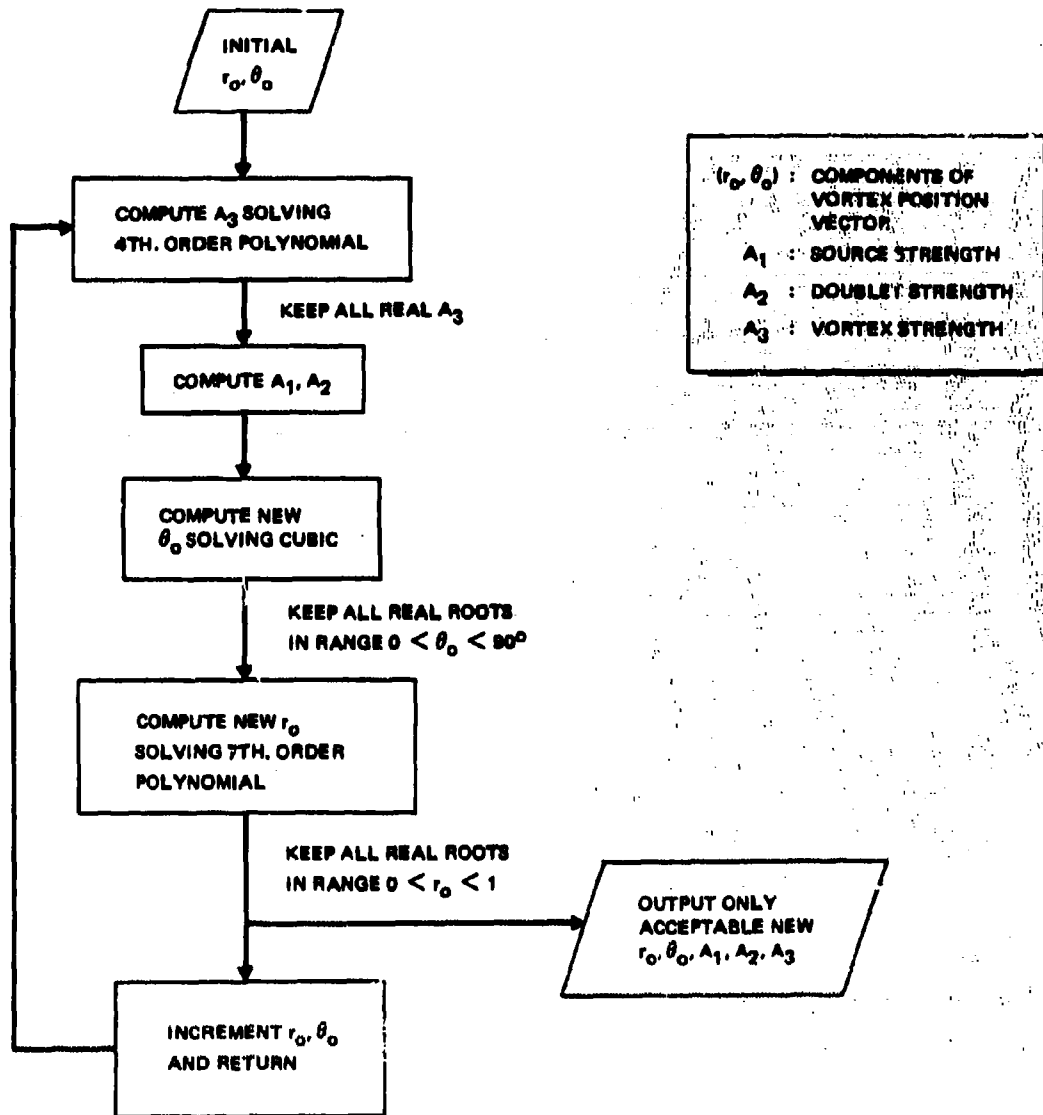


Figure B-2. Search for Solutions to Set of Five Simultaneous Equations for Vortex Model



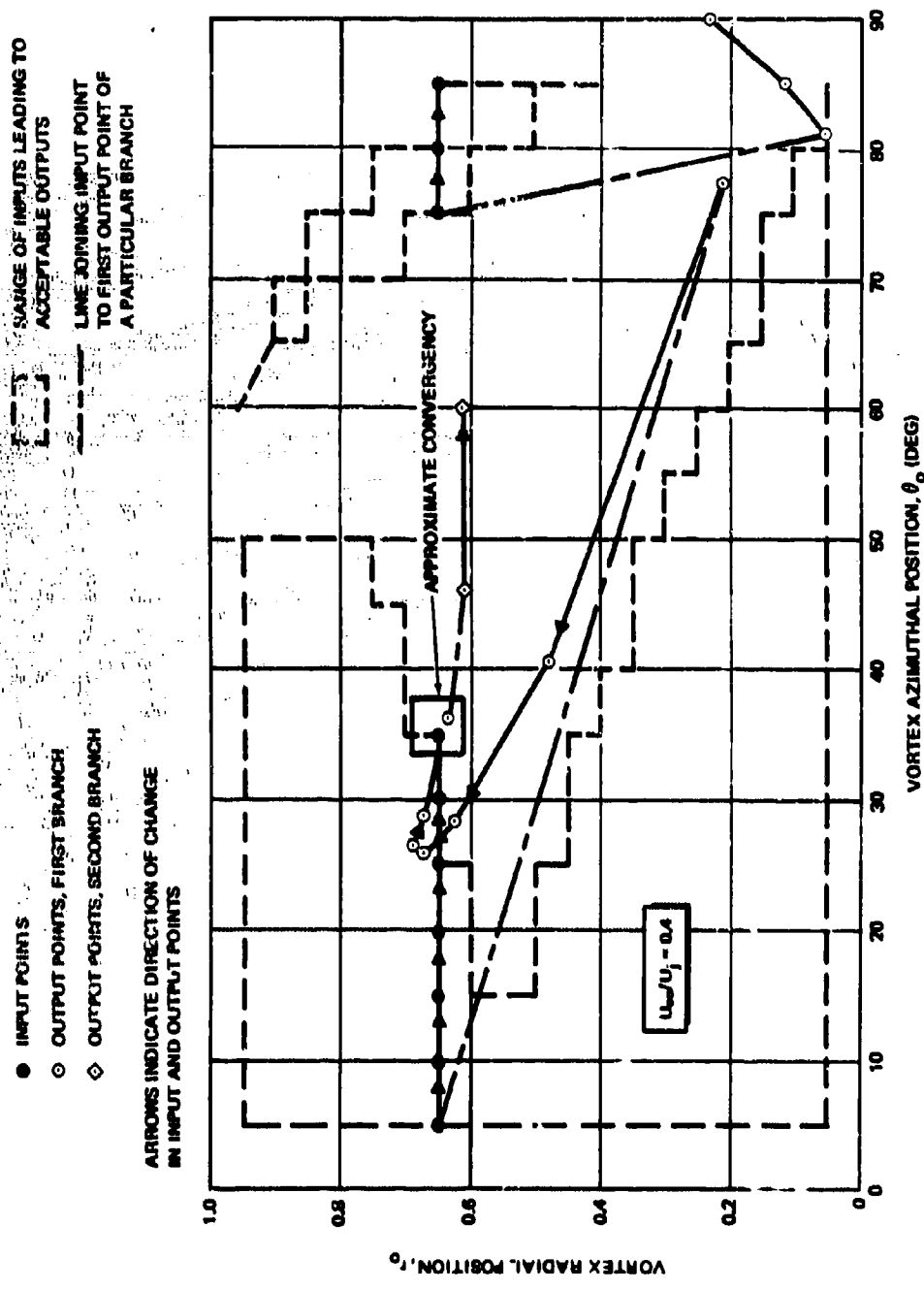


Figure B-3. Result of Search for Solutions to Vortex Model

lead to an output (open point) of

$$r_o = 0.21$$

$$\theta_o = 77.5^\circ$$

As the input  $\theta_o$  is increased, the output points approach the input points, until at input point  $r_o = 0.65$ ,  $\theta_o = 35^\circ$ ; the corresponding output point is  $r_o = 0.64$ ,  $\theta_o = 36.5^\circ$ . Since the system of equations is nonlinear, more than one output may correspond to a single input point. This fact is illustrated in Figure B-2 by the points labeled "second branch". As the input  $\theta_o$  is increased beyond  $35^\circ$ , the output values no longer satisfy the constraints (B-31) and (B-32), and are therefore ignored. At  $r_o = 0.65$ ,  $\theta_o = 75^\circ$ , satisfactory output values are again obtained, and they are shown in the lower right-hand corner of Figure B-1. Exact equality of input and output would signify that a solution to the set of equations has been found. This has obviously not yet been achieved by the above results, and iterations in the neighborhood of the points labeled "approximate convergence" would be necessary to obtain a more accurate answer. However, it was felt that the above results were accurate enough to allow an overall evaluation of the model. Examination of diagrams analogous to Figure B-2 has shown that convergence is not approached at any other point. The final results for this case are taken as:

$$A_1 = -0.1207$$

$$A_2 = -0.0478$$

$$A_3 = 0.668$$

$$\theta_o = 36.31^\circ$$

$$r_o = 0.64$$

Substitution of these values into the set of Equations (B-22) through (B-30) verifies that they are approximately satisfied. These are the values which have been used for plotting the model three term Fourier series representation shown in Figures 20 to 26.

**BLANK PAGE**

## Appendix C

### EQUIVALENT SOLID OBSTACLE ANALOGY COMPUTER PROGRAM

#### C.1 MAIN PROGRAM

##### C.1.1 Input Tape

The first task performed by the main program is that of reading the input tape. The input tape is an even-parity BCD tape, density 800 bits per inch, which contains the images of punched output from a method of characteristics analysis of the flow fields around a unit hemisphere-cylinder at various Mach numbers  $\{M_i\}$ . The input tape contains the images of the following cards:

1. The first card contains JMACH, the number of Mach numbers in the sequence  $\{M_i\}$ . (For operation on the IBM 7094, JMACH=6.)

2. The next JMACH cards contain

$j, n_j, M_j, X_{j\min}, X_{j\max}$

where  $j = 1, 2, \dots, JMACH$ ;  $n_j$  is the number of net points in the  $j$ th flow field;  $M_j$  is the Mach number,

$X_{j\min}$  and  $X_{j\max}$

denote the limits of the stored flow field data.

$(M_j, X_{j\min}, X_{j\max})$

are stored in the arrays AMLOC(6), XMINC(6), and XMAXC(6) respectively.

3. The next cards contain the actual net point data

$j, i, X_{ji}, R_{ji}, P_{ji} \quad \begin{array}{l} j = 1, 2, \dots, JMACH \\ i = 1, 2, \dots, n_j \end{array}$

where  $(X_{ji}, R_{ji}, P_{ji})$  are the longitudinal and radial coordinates, and the associated pressure ratio,  $p/p_1$ .

4. The next 9 x (JMACH) cards contain the coefficients  $C_{jm}$  of the set of equations

$$X = \sum_{m=1}^9 C_{jm} R^{m-1}; \quad j = 1, 2, \dots, JMACH$$

describing the shock shape associated with the Mach number  $M_j$ . These coefficients are stored in the array COEF(6, 9).

All data read from the input tape is stored in COMMON/BLK2/ so it is available to the integration subroutine (INTEG). The input tape is read first, and none of the information in BLK2 is altered during the execution of the program. Thus it is necessary to read this tape only once, regardless of the number of cases to be run. COMMON/BLK2/ accounts for 11,773 storage locations in the program when JMACH = 6.

#### C. 1.2 Input Cards

After the input tape has been read and COMMON/BLK2/ filled, the input cards for the first case are read. The data on the cards fill the input array RR (100), which contains jet and free-stream data described in Table C-1 in locations 1-19 and vehicle geometry specifications in locations 20-99. Each ( $K = 1-100$ ) input card contains five combinations ( $K$ , RR ( $K$ )) in a format specification (1X, 5 (I3, E9.4)) where only nonzero values RR ( $K$ ) need be input. The input cards for each case must be preceded by a card containing the number of cards, NCARD, to be read for that particular case punched in an (I10) format.

#### C. 1.3 Program Logic

The logic involved in the main program is summarized by listing the four main subroutines in the following manner:

##### 1. SUBROUTINE KWKBOD(NC, RR)

Inputs via calling arguments: Component type flags,  
Component end points

Inputs via COMMON: None

Outputs via calling arguments: None

Outputs via COMMON: All integration mesh data transferred to integration subroutine through COMMON/MAIN/.

Table C-1  
INPUT LOCATIONS FOR VEHICLE GEOMETRY SPECIFICATIONS

Location	Quantity	Item
1	$M_\infty$	Free stream Mach number
2	LBLSEP	Flag $\begin{cases} 0 & \text{No} \\ 1 & \text{Yes} \end{cases}$
3	NCOMP	Number of vehicle components
4	$D_B$	Vehicle diameter
5	$L_B$	Vehicle length
6	$\delta$	Nose half angle (degrees)
7	$x_{cg}$	Vehicle c. g. location
8	$y_{cg}$	Vehicle c. g. location
9	$z_{cg}$	Vehicle c. g. location
10	$x_j$	Jet location
11	$z_j$	Jet location
12	CDIS	Nozzle discharge coefficient
13	NPJ	Jet patch number
14	$d_t$	Jet diameter
15	$\phi$	Nozzle cant angle
16	$M_e$	Jet exit Mach number
17	$\gamma_j$	Jet specific heat ratio
18	$p_{0j}/p_\infty$	Jet pressure ratio
19	NEWTPM	Flag $\begin{cases} 0 & \text{Newtonian theory on lee side} \\ 1 & \text{Prandtl-Meyer theory on lee side} \end{cases}$

(Locations 20 - 100 contain the body section inputs as described in Section C.2.)

External references: Several other subroutines are called by KWKBOD during vehicle geometry calculations. Since these require no special inputs or handling by the user, a detailed description of them is omitted here.

2. SUBROUTINE LOCFLO (AMLOC, JMACH, ALPHA, NPJ, GAMINF, AMINF, CONANG)

Inputs via calling arguments: Number of local Mach numbers, JMACH. Sequence of local Mach numbers  $[M_i]$ . Jet patch number, NPJ. Nose half angle,  $\delta$ .

Inputs via COMMON: None

Outputs via calling arguments: Sequence of angles of attack

Outputs via COMMON: Pressure ratios

$$[P_i] \equiv \left[ \left( \frac{P_i}{P_\infty} \right)_i \right] \text{ at jet location.}$$

Local flow direction vectors  $[u_{x_i}]$   $[u_{y_i}]$ ,  $[u_{z_i}]$

Angle of attack flags  $[(JFLAG)_i]$

Unit outer normal at jet  $\hat{n}_j$

3. SUBROUTINE JETHIT (AMLOC, GAMINF, GAMJET, POJFIN, DT, JMACH, THRUST, PHI, AME)

Inputs via calling arguments: Jet data

$$\gamma_j, \frac{P_{oj}}{P_\infty}, d_t, \phi, M_e, CDIS$$

Sequence of Mach numbers  $[M_i]$

Inputs via COMMON: Pressure ratios  $[P_i]$

Angle of attack flags  $[(JFLAG)_i]$

Outputs via calling arguments: Jet thrusts  $[T_i]$  and normal, sonic, vacuum thrust  $[T_s]$ .

Outputs via COMMON: Sequence of equivalent body radii  $[S_i]$ .

4. SUBROUTINE INTEG (JMACH, CGX, NPJ, AMINF, GAMINF, ALPHA, AREF, DREF, TC)

Inputs via calling arguments: Number of local Mach Numbers, JMACH.

Free stream  $M_\infty$ .

Vehicle c. g. location  $x_{cg}$ ,  $y_{cg}$ ,  $z_{cg}$

Reference area and length  $A_{ref}$ ,  $d_{ref}$

Vehicle angles of attack  $[\alpha_i]$

Jet patch number, NPJ

Jet thrust  $[T_i]$

Inputs via COMMON: Angle of attack flags  $[(JFLAG)_i]$

Outputs via COMMON: Vehicle force and moment coefficients

External references: Another subroutine, PRESS, is called by INTEG during the integration procedure.

5. SUBROUTINE WRITR (ALPHA, DREF, AREF, AMINF, N)

Inputs via calling arguments: Vehicle angles of attack  $[\alpha_i]$

Reference length and area, DREF, AREF

Free stream  $M_\infty$

Number of local Mach numbers (N)

Inputs via COMMON: Jet-off and jet-on aerodynamic coefficients

Jet thrusts  $[T_i]$

Jet pressure ratio  $(p_{oj}/p_\infty)$

Unit outer normal at jet  $(\hat{n}_j)$

Outputs: All aerodynamic coefficient and JI amplification factor outputs are printed by this subroutine.

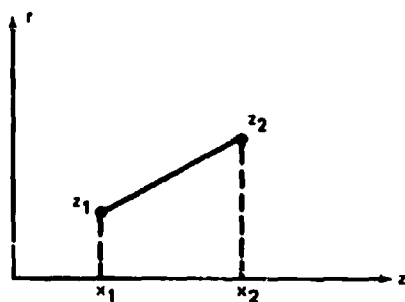
## C.2 VEHICLE GEOMETRY

The vehicle is assumed to be fixed in the coordinate system xyz with its nose at the origin and with the positive x-axis as the axis of symmetry. The cross section of the vehicle can be made up of N components, where N lies in the range  $1 \leq N \leq 8$ . Thus, the input scheme requires that each component be described by a separate curve in the x-z plane. The curves may be one of three types: straight line, circular arc, or arbitrary curve. The input data for the first curve is entered in locations 20-29 of the input array, RR, the second curve in locations 30-39, etc. A summary of the inputs required for each type of curve is shown in Figure C-1.

It should be noted that the flag denoting the type of curve (1, 2, or 3) must be entered in locations 20, 30, 40, etc., and the coordinates entered in the following four to eight locations.

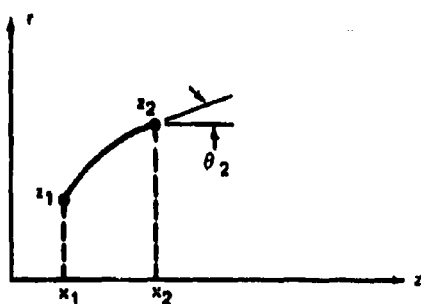
After the vehicle shape is read in, the integration mesh is set up. Each component is divided into four patches, each subtending a  $45^\circ$  angle on the surface. As is also indicated in Figure 4.1, the free stream velocity vector is assumed to lie in the x-z plane, so consideration of the half-space  $y \leq 0$  is sufficient for vehicle geometry considerations. A 16 rectangle per patch mesh is constructed on all the patches upstream of the jet. Aft of and including the patch NPJ on which the jet is located, the mesh fineness is chosen to be 64 rectangles per patch. The patch number of the jet is an input quantity and can be determined readily from the numbering system indicated in Figure 4.1. If an even finer mesh is desired in the vicinity of the jet, the region may be constructed of several short components.





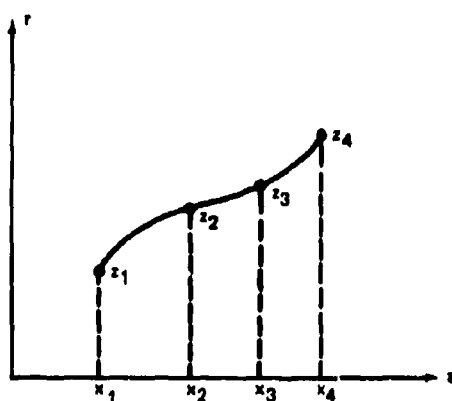
a. STRAIGHT-LINE SEGMENT

INPUT	LOCATION
FLAG = 1	10 + 10N
x <sub>1</sub>	11 + 10N
z <sub>1</sub>	12 + 10N
x <sub>2</sub>	13 + 10N
z <sub>2</sub>	14 + 10N



b. CIRCULAR ARC

FLAG = 2	10 + 10N
x <sub>1</sub>	11 + 10N
z <sub>1</sub>	12 + 10N
x <sub>2</sub>	13 + 10N
z <sub>2</sub>	14 + 10N
θ <sub>2</sub> (DEGREES)	16 + 10N



c. ARBITRARY CURVE

FLAG = 3	10 + 10N
x <sub>1</sub>	11 + 10N
z <sub>1</sub>	12 + 10N
x <sub>2</sub>	13 + 10N
z <sub>2</sub>	14 + 10N
x <sub>3</sub>	15 + 10N
z <sub>3</sub>	16 + 10N
x <sub>4</sub>	17 + 10N
z <sub>4</sub>	18 + 10N

Figure C-1. Vehicle Profile Description Options

The coordinate system described above is a standard aerodynamic coordinate system for the user's benefit. Inside the program, however, a transformation is made to another coordinate system in which:

X (INPUT/OUTPUT) = X(3) or operating z axis  
Y (INPUT/OUTPUT) = -X(2) or operating negative y axis  
Z (INPUT/OUTPUT) = X(1) or operating x axis

for the purpose of internal program operation. The user should bear this in mind when consulting the flow charts.

### C.3 LOCAL FLOW SUBROUTINE (LOCFLO)

In this subroutine, where the angles of attack  $\{\alpha_i\}$  corresponding to local Mach numbers  $\{M_i\}$  at the jet location are calculated, several algebraic equations are solved numerically. The schemes used (binary chop and regula falsi) are straightforward and should present no problem to the user. The convergence criteria and basic logic are readily apparent from the flow charts, so no further discussion is necessary here.

Although the program has the capability of using either Newtonian or Prandtl-Meyer lee side aerodynamic theories, the Prandtl-Meyer theory is used for determining the angles of attack  $\{\alpha_i\}$ .

For every angle of attack,  $\alpha_k$ , corresponding to a local Mach number,  $M_k$ , at the jet location, the flag  $(JFLAG)_k$  is set equal to zero. If no  $\alpha_k$  is found corresponding to a particular Mach number,  $(JFLAG)_k$  is set equal to 1 indicating to the integration subroutine that no pressure integration is to be carried out at this angle of attack.

If the input nose half-angle is less than  $85^\circ$ , the attached shock version of LOCFLO is executed. If the angle of attack corresponding to a particular local Mach number is greater than 0.3 radian, an appropriate message is printed. If data is desired for larger angles of attack for a vehicle with a sharp nose, it is recommended that the program be rerun for a slightly blunted vehicle of the same overall dimensions. In this case the input nose half-angle will be  $90^\circ$  and the detached shock option will be executed.

### C.4 PRESSURE INTEGRATION SUBROUTINE

The pressure integration over the vehicle surface is carried out by subroutine INTEG. This subroutine uses the integration mesh constructed by subroutine KWKBOD. The integration is performed for the vehicle at those angles of attack,  $\alpha_k$ , of the sequence,  $[\alpha_i]$ , for which the flag,  $(JFLAG)_k$ , of the sequence,  $[(JFLAG)_i]$ , was set equal to zero in subroutine LOCFLO.

At each mesh element, before calculating the surface pressure, another subroutine, PRESS, is called. This subroutine tests to see if the mesh element lies within the region of influence of the jet. If it does, the pressure used in the integration scheme is calculated by the

method described in section C.4.1. If the mesh element lies outside the region of influence of the jet, control is returned to subroutine INTEG where the pressure is computed without regard for the jet.

In subroutine INTEG, the pressure on each mesh element outside the region of influence of the jet is determined by a local inclination pressure law. On the windward side, tangent-cone theory is used. On the lee side, depending on the value of the input flag NEWTPM, either Newtonian or Prandtl-Meyer hypersonic small disturbance theory is used.

SUBROUTINE PRESS (X, Y, Z, J, KFLAG, PEPI, KPRESS) is given below.

#### Inputs and Outputs

##### Inputs through calling arguments:

X, Y, Z are the coordinates of the mesh element in question.  
J is the index denoting an angle of attack of the sequence  $\{\alpha_i\}$ .

KPRESS(6) is an array zeroed in INTEG and used to count the times PRESS is called.

##### Outputs through calling arguments:

KFLAG is set equal to one if the point (X, Y, Z) is inside the region of influence of the jet, and set equal to zero otherwise.

##### Inputs through COMMON/BLK1/:

PIPINF (6) contains the pressure  $[P_i]$  at the jet location.

XYZJ(3) contains the coordinates  $(X_j, Y_j, Z_j)$  of the jet location.

UNJ(3) contains the components  $(n_x, n_y, n_z)$  of the unit outer normal  $\hat{n}$  at the jet location.

UX(6), UY(6), UZ(6) contain the components of the series of unit vectors  $[\hat{u}_i]$  aligned with the local flow at the jet location.

SCALE(6) contains the scale factors  $[S_i]$  which are calculated as described in Section 4.

NEWTPM is the input lee side aerodynamic theory flag.  
(0 - Newtonian, 1 - Prandtl-Meyer).

IBLSEP is the input boundary layer separation flag.  
(0 - Inviscid pressure profile, 1 - Modified pressure profile).

Inputs through COMMON/BLK2/:

NCHAR(6) contains the numbers  $[N_{c_i}]$  of characteristic net points in the equivalent body flow field at local Mach numbers  $[M_i]$ .

XCHAR(6,650), RCHAR(6,650), PCHAR(6,650) contain the coordinates  $[X_{c_{ji}}]$ ,  $[R_{c_{ji}}]$ , of the net points and their associated pressure ratios  $[P_{c_{ji}}]$ .

XMINC(10) contains the abscissas  $[X_{c_{min}}]$  of the most forward net point.

XMAXC(10) contains the abscissas  $[X_{c_{max}}]$  of the farthest aft net point.

Beyond this point the pressure perturbation due to the hemisphere-cylinder is negligible. The pressure perturbation is ignored at radial angles in body cross-section larger than  $\pm 150$  degrees from the jet centerline.

COEF(10, 9) contains the coefficients  $C_{jk}$  in the equations

$$X'_{shock} = \sum_{k=1}^9 C_{jk} R_{shock}^{k-1} \quad j = 1, 2, \dots, JMACH$$

for the shock shapes in the equivalent body coordinate system.

In this subroutine, the coordinates of a point  $(x, y, z)$  are transformed into the equivalent body coordinate system  $(X', R')$  and examined to determine whether they lie within the region of influence of the jet. The limits of the interaction region depend on whether the boundary layer separation simulation option is being exercised. In the inviscid case, the upstream limit is the equivalent body shock wave. In the case of the modified pressure profile, the problem is reduced to determining whether a hypothetical point  $(X^*, R')$  has an inviscid pressure ratio associated with it greater than the experimentally observed plateau pressure.

The logic involved in this subroutine may be considered as consisting of three main parts. First, the limits of the interaction region are calculated; second, it is determined whether the point in question lies within the interaction region; and finally, the appropriate pressure ratio is assigned to the point  $(X', R')$ .

An array of counters KPRESS(6) zeroed in subroutine INTEG indicates when PRESS is being called for the first time. The first time it is called for a given angle of attack (i. e., a particular local Mach number and equivalent body flow field) the limits  $R'_{min}$  and

$R'_{\max}$  corresponding to the shock end points  $X'_{\min}$  and  $X'_{\max}$  read in on the input tape must be determined. The numerical methods used to solve the equation

$$X' = \sum_{n=1}^9 C_n R'^{(n-1)}$$

are unique. Because of the unknown nature of the above curve fit outside the interval  $(X'_{\min}, X'_{\max})$ , the iteration schemes were designed to converge to the end points of the interval  $(R'_{\min}, R'_{\max})$ , from the interior. To find  $R'_{\max}$ , an initial  $R' = 15$  is guessed, and the iteration proceeds outward in steps of size

$$DR = \frac{X'_{\max} - X'_s(R')}{\sqrt{M^2 - 1}}$$

The resulting sequence  $\{R' + n DR\}$  approaches  $R'_{\max}$  monotonically because the Mach angle  $\mu = \tan^{-1} (M^2 - 1)^{-1/2}$  is always smaller than the shock angle at any point  $X'_s(R')$ . To find  $R'_{\min}$ , an initial value of  $R' = 10$  is guessed and the iteration proceeds toward the  $X'$  axis in steps of size

$$DR = \frac{X'_s(R') - X'_{\min}}{\frac{dX'_s}{dR'}}$$

The resulting sequence  $\{R' - n DR\}$  approaches  $R'_{\min}$  monotonically because the shock angle  $\beta = \tan^{-1} \frac{dX'_s}{dR'}$  is a monotonic increasing function of  $R'$  and always greater than zero. The pattern of iteration in both the above cases should be clear from Figure C-1. An examination of the flow charts for subroutine PRESS will show that there are safeguards in the event of a numerical overshoot of an end point.

The second task of the subroutine is to determine whether a point lies inside the interaction region. Clearly, if  $X' > X'_{\max}$  or if  $R' > R'_{\max}$ , the point in question is outside the region and control is returned to INTEG with KFLAG set equal to zero, indicating that the surface pressure at the point  $(x, y, z)$  is unaffected by the presence of the jet. Next, the shock abscissas are found for the particular value of  $R'$  in question. If  $R' > R'_{\min}$ , it is clear that the shock station is given by

$$X'_s = \sum_{n=1}^9 C_n R'^{(n-1)}$$

If  $R' < R'_{\min}$ , a normal shock is assumed (since the point  $(X', R')$  is near the sonic line on the equivalent body) and  $X'_s$  is set equal to  $X'_{\min}$ . The inviscid pressure ratio  $P_{\text{inv}}$  across the shock is then calculated for the appropriate shock angle  $\beta$ .

$$\beta = \frac{\pi}{2}$$

$$R' < R'_{\min}$$

$$\beta = \tan^{-1} \left( \sum_{n=2}^9 C_n R'_n{}^{(n-2)} \right) \quad R'_{\min} \leq R' \leq R'_{\max}$$

If the boundary layer separation simulation is being exercised ( $\text{'BLSEP} = 1$ ), a new abscissa

$$X'_D = (X'_2 - X'_J) \frac{(X'_2 - X'_s)}{(X'_s - X'_1)} + X'_s, \text{ is computed for every}$$

point upstream of  $X'_s$ . The original value  $X'_u$  is stored in XTEMP and the flag LFLAG is set equal to one to indicate to later sections of the subroutine that the point  $(X', R')$  is an image of an upstream point. In the inviscid case, KFLAG is zeroed and control returned to INTEG if  $X' < X'_s$ .

The pressure perturbation ratio  $P$  associated with a point  $(X', R')$  is found by locating the nearest characteristics net point  $(XCHAR(J, I_c), RCHAR(J, I_c))$  in the stored equivalent body flow field and using its associated pressure ratio  $PCHAR(J, I_c)$ . The index  $J$  indicates the local Mach number, and  $I_c$  the  $I_c^{\text{th}}$  net point, when arranged in order of ascending  $X'$  coordinates. Instead of searching all  $NCHAR(J)$  points for the nearest one, searching is confined to a circle of radius

$$d = \min \begin{Bmatrix} |R' - R'_{\min}| \\ |X' - X'_s| \end{Bmatrix}$$

around the point  $(X', R')$ . This is accomplished by determining the index  $I_s$  corresponding to the net point with the largest  $XCHAR(J, I) < X' - d$  and the index  $I_e$  corresponding to the point with the smallest  $XCHAR(J, I) > X' + d$ . Then, the search for the nearest point need take place

only among  $XCHAR(J, I)$  with  $I_s < I < I_L$ . If no points in the interval

$$[XCHAR(J, I_s), XCHAR(J, I_L)]$$

lie within the circle of radius  $d$ , the procedure is repeated in a circle of radius

$$d = \frac{1}{2} [XCHAR(J, I_L + 1) - XCHAR(J, I_s - 1)]$$

until the nearest point is found.

## REFERENCES

1. Vinson, P. W., Amick, J. L., and Liepmann, H. P. Interaction Effects Produced by Jet Exhausting Laterally Near Base of Ogive-Cylinder Model in Supersonic Mainstream. NASA Memo 12-5-58W, February 1959.
2. Amick, J. L. and Hays, P. B. Interaction Effects of Side Jets Issuing from Flat Plates and Cylinders Aligned with a Supersonic Stream. WADD TR-60-329, June 1960.
3. Phinney, R. E., Werle, M. J., Knott, J., and Volz, W. C. Slot Jet Interaction Studies of an Ogive-Cylinder at  $M_\infty = 4$  and 5. NOLTR-68-143, September 1968.
4. Spring, D. J., Street, T. A., and Amick, J. L. Transverse Jet Experiments and Theories--A Survey of the Literature, Part I. U. S. Army Missile Command, Redstone Arsenal, Report RD-TR-67-4, June 1967.
5. Barnes, J. W., Davis, J. G., and Tang, H. H. Control Effectiveness of Transverse Jets Interacting With a High-Speed Free Stream. AFFDL-TR-67-90, Vol. 1, July 1967.
6. Carvalho, G. F. and Hays, P. B. Jet Interference Experiments Employing Body-Alone and Body-Fin Configurations at Supersonic Speeds. University of Michigan Technical Report 03942-7-T, GM-979, December 1970.
7. Swanson, R. S. Parametric and Preliminary Design Comparison of Transverse Jet Controls and Flap-Type Aerodynamic Controls for Re-entry Vehicles and High Speed Cruise Aircraft. AFFDL-TR-68-98, December 1968.
8. Spring, D. J. and Street, T. A. Experimental Investigation of the Pressure Distributions Induced Upon a Body of Revolution by Several Transverse Jets at Low Speeds. U. S. Army Missile Command Report No. RD-TM-68-7, August 1968.
9. Kuiper, R. A. Control Jet Effectiveness in the Subsonic and Transonic Flight Regimes. Philco Aeronutronic Division Publication No. U. 2932, December 1964.



10. Heyser, A. and Maurer, F. Experimental Investigations on Solid Spoilers and Jet Spoilers at Mach Numbers of 0.6 to 2.8. Translation No. 32, Jet Propulsion Laboratory, 21 February 1964.
11. Vinson, P. R. Prediction of Reaction Control Effectiveness at Supersonic and Hypersonic Speeds. Martin-Orlando Report OR-6487, March 1965.
12. Seid, F. W. and Zukoski, E. E. A Study of the Interaction of Gaseous Jets from Transverse Slots with Supersonic External Flow. AIAA Journal, Vol. 6, No. 2, February 1968.
13. Werle, M. J. A Critical Review of Analytical Methods for Estimating Control Forces Produced by Secondary Injection. NOLTR 68-5, January 1968.
14. Kaufman, H. L. G. Hypersonic Flows Past Transverse Jets. Presented at the AIAA Fifth Aerospace Sciences Meeting, Paper No. 67-190, New York, New York, 23 to 26 January 1967.
15. Strike, W. T. Analysis of the Aerodynamic Disturbances Generated on a Flat Plate Containing Lateral Jet Nozzles Located in a Hypersonic Stream. AEDC-TR-67-158, January 1968.
16. Spaid, F. W., Zukoski, E. E., and Rosen, R. A Study of Secondary Injection of Gases Into a Supersonic Flow. Jet Propulsion Laboratory TR 32-834, 1 August 1966.
17. Street, T. A. and Spring, D. J. Experimental Investigation of a Transverse Jet Injecting From a Flat Plate into a Mach Number 5.0 Free Stream. U. S. Army Missile Command Report No. RD-TM-68-6, August 1968.
18. Leiko, W. Loads Induced on a Flat Plate at a Mach Number of 4.5 with a Sonic or Supersonic Jet Exhausting Normal to the Surface. NASA TN-D-1935, July 1963.
19. Cassel, L. A., Davis, J. G., and Engh, D. P. Lateral Jet Control Effectiveness Prediction for Axisymmetric Missile Configurations. U. S. Army Missile Command Report No. RD-TR-68-5, June 1968.
20. Lee, Jr., E. E. and Willis, C. M. Interaction Effects of a Control Jet Exhausting Radially from the Nose of an Ogive-Cylinder Body at Transonic Speeds. NASA TN-D-3752, January 1967.

21. Jordinson, R. Flow in a Jet Direct Normal to the Wind  
Gt. Brit. Aero. Res. Council. R&M No. 3074, 1958.
22. Pratte, B. D., and Baines, W. D. Profiles of the Round  
Turbulent Jet in a Crossflow. Jour. of the Hydraulic Div.,  
Proc. of the ASCE, November 1967.
23. Keffer, J. F. and Baines, W. D. The Round Turbulent  
Jet in a Crosswind. Jour. of Fluid Mech., Vol. 15,  
pp. 481-496. 1963.
24. Abranovich, G. N. Theory of Turbulent Jets. Reproduced  
by the Armed Services Technical Information Agency,  
Arlington, Va.
25. Reichenau, D. E. A. Interference Effects Produced by a  
Cold Jet Issuing Normal to the Airstream from a Flat Plate  
at Transonic Mach Numbers. AEDC-TR-67-220, Arnold  
Air Force Sta., Tenn., October 1967.
26. Reichenau, D. E. A. Interference Effects of Cold and Hot  
Rocket Exhaust Issuing Normal to the Airstream from a Flat  
Plate at Free Stream Mach Numbers from 0.6 to 1.4.  
AEDC-TR-66-127, Arnold Air Force Sta., Tenn., June 1966.
27. Reid, C. F., Jr. The Effect of Several Forward-Mounted  
Control Jet Nozzles on a Typical Missile Configuration at  
Transonic Speeds. Cornell Aero. Lab., Inc. Report  
No. AA-2234-W-1 (Vols. I and II), Buffalo, N. Y.,  
January 1967.
28. Reid, C. F., Jr. The Effect of Several Forward-Mounted  
Control Jet Nozzles on a Typical Missile Configuration at  
Transonic Speeds. Cornell Aero. Lab., Inc. Report  
No. AA-2267-W-3, July 1967.
29. Love, E. S., Grigsby, G. E., Lee, L. P., and Woodling, M. J.  
Experimental and Theoretical Studies of Axisymmetric Free  
Jets. NASA TR-R-6, 1959.
30. Crist, S., Sherman, P. M., and Glass, D. R., Study of the  
Highly Underexpanded Sonic Jet. AIAA Journal, Vol. 4,  
No. 1, January 1966.
31. Spring, D. J. An Experimental Investigation of the Interference  
Effects Due to a Lateral Jet Issuing from a Body of Revolution  
Over the Mach Number Range 0.8 to 4.5. U. S. Army Missile  
Command, Redstone Arsenal, Report RD-TR-68-10  
August 1968.

32. Vogler, R. D. Surface Pressure Distributions Induced on a Flat Plate by a Cold Air Jet Issuing Perpendicularly from the Plate and Normal to a Low-Speed Free-Stream Flow, NASA TN-D-1629. March 1963.
33. Bradbury, L. J. S. and Wood, M. N. The Static Pressure Distribution Around a Circular Jet Exhausting Normally from a Plane Wall into an Airstream. Gt. Brit. Aero. Res. Council, C. P. No. 822, 1965.
34. Martin, W. and Gelb, G. An Experimental Investigation of the Flow Field About a Subsonic Jet Exhausting into a Low Velocity Airstream. Northrop Corp., Norair Div. NOR-65-229, August 1965.
35. Peake, D. J. The Pressures on a Surface Surrounding a Jet Issuing Normal to a Mainstream. Natl. Res. Council of Canada. Aero. Rept. LR-410. Ottawa, November 1964.
36. Wooler, P. T., Burghart, G. H., and Gallagher, J. T. Pressure Distribution on a Rectangular Wing With a Jet Exhausting Normally into an Airstream. Jour. of Aircraft Vol. 4., No. 6. November - December 1967.
37. Milne-Thompson, L. M. Theoretical Hydrodynamics, 3rd Edition. The MacMillan Co., New York, 1955.
38. Timmer, H. G. and Stokes, T. R. Rapid Prediction of Hypersonic Aerodynamic Characteristics - Computer Program F218. McDonnell Douglas Astronautics Company--Western Division, DAC-62432, December 1968.
39. Simon, W. E. and Walter, L. A. Approximations for Supersonic Flow Over Cones. AIAA Journal, Vol. No. 7, July 1963.
40. Martellucci, A. and Libby, P. A. Supersonic Flow About General Three-Dimensional Blunt Bodies (Volume II). Aeronautical Systems Division, Air Force Systems Command Report No. ASD-TR-61-727 (Vol. II), October 1962.
41. Needham, D. A. and Stollery, J. L. Boundary Layer Separation in Hypersonic Flow. AIAA Paper No. 66-455, June 1966.
42. Hakkinen, R. J., Greber, I., Trilling, L. and Abarbanel, S. S. The Interaction of an Oblique Shock Wave With a Laminar Boundary Layer. NASA Memo. 2-18-59W, March 1959.

43. Street, D. R. Effects of Injection Nozzle Configuration on Secondary Injection Into Supersonic Flow. California Institute of Technology Mechanical Engineering Degree Thesis, 1956.
44. Burt, J. R., Jr., and Dahlke, C. W. Effects of Spin and Vent Tube Jet Flow on Lance Missile Aerodynamic Coefficients from Analysis of Wind Tunnel Test, LTV Test 246 (U). U. S. Army Missile Command Report No. RF TM-67-4, Redstone Arsenal, Ala. June 1967, (Confidential).
45. Dahlke, C. W. An Experimental Investigation of Downstream Flow-Field Properties Behind a Forward Located Sonic Jet Injected into Transonic Freestream from a Body of Revolution. U. S. Army Missile Command Report No. RD-TM-68-2, Redstone Arsenal, Ala., January 1968.
46. Dahlke, C. W. An Experimental Investigation of Downstream Flow-Field Properties Behind a Sonic Jet Injected into Transonic Free Stream from a Body of Revolution (Series II). U. S. Army Missile Command Report No. RD-TM-69-2, Redstone Arsenal, Ala., February 1969.
47. Bryson, A. E. Symmetric Vortex Separation on Circular Cylinders and Cones. Journal of Applied Mechanics, Trans. of ASME, December 1959.
48. Hinze, O., Turbulence. McGraw-Hill Book Co., Inc., New York, 1959.
49. Nielsen, J. N. Missile Aerodynamics, McGraw-Hill Book Co., Inc., New York, 1960.
50. Pitts, W. D., Nielsen, J. N. and Kaatari, G. E. Lift and Center of Pressure of Wing-Body-Tail Combinations at Subsonic, Transonic, and Supersonic Speeds. NASA Report 1307, July 1953.
51. Landahl, M. and Ashley, H. Aerodynamics of Wings and Bodies. Addison Wesley, 1964.
- A-1. Adamson, T. C. and Nicholls, J. A. On the Structure of Jets from Highly Underexpanded Nozzles into Still Air. Journal of the Aero. Sciences, Vol. 26, 1959, pp 16-24.
- A-2. Ashkenas, H. and Sherman, F. S. The Structure and Utilization of the Supersonic Free Jet in Low Density Wind Tunnels. Rarefied Gas Dynamics, J. H. DeLeeuw (ed.) Academic Press, Vol. 2, 1965.

- A-3. Owen, P. L. and Thornhill, G. K. The Flow in an Axially-Symmetric Supersonic Jet From a Nearly-Sonic Orifice Into a Vacuum. Aero. Res. Council R&M 2616, Gt. Brit., 1952.
- A-4. Crist, S., Sherman, P. T. and Glass, D. R. Study of the Highly Underexpanded Sonic Jet. AIAA Journal, Vol. 4, No. 1, January 1966.
- A-5. Love, E. S., et al. Experimental and Theoretical Studies of Axisymmetric Free Jets. NASA TR-R-6, 1959.
- B-1. Morse, P. M. and Feshbach, H. Methods of Theoretical Physics, Volume I. McGraw-Hill Book Company, 1953.
- B-2. Vogler, R. D. Surface Pressure Distributions Induced on A Flat Plate by a Cold Air Jet Issuing Perpendicular From the Plate and Normal to a Low Speed Free-Stream Flow. NASA TN-D-1629, March 1963.

UNCLASSIFIED

Security Classification

DOCUMENT CONTROL DATA - R & D		
(Security classification of title, body of abstract and indexing annotation must be entered when the overall report is classified)		
1. ORIGINATING ACTIVITY (Corporate author) McDonnell Douglas Astronautics Company Western Division 3000 Ocean Park Blvd., Santa Monica, California		2a. REPORT SECURITY CLASSIFICATION <b>UNCLASSIFIED</b>
		2b. GROUP N/A
3. REPORT TITLE Jet Interaction Control Effectiveness for Subsonic and Supersonic Flight		
4. DESCRIPTIVE NOTES (Type of report and inclusive dates) Final Report--Lateral Jet Interaction Study-- Phase II, 1 June 1968 - 30 September 1969		
5. AUTHOR(S) (First name, middle initial, last name) Louis A. Cassel, Norbert A. Durando, Clark W. Bullard, James M. Kelso		
6. REPORT DATE September 1969	7a. TOTAL NO. OF PAGES 182	7b. NO. OF REFS 58
8a. CONTRACT OR GRANT NO. DAAH01-68-C-1919	9a. ORIGINATOR'S REPORT NUMBER(S) MDAC-G1164	
b. PROJECT NO. DA Project Number 1M2623XXA206		
c. AMC Management Structure Code	9b. OTHER REPORT NO(S) (Any other numbers that may be assigned this report) U. S. Army Missile Command Report RD-TR-69-21	
d. No. 522C.11.148		
10. DISTRIBUTION STATEMENT This document is subject to special export controls and each transmittal to foreign governments or foreign nationals may be made only with prior approval of C. G., U. S. Army Missile Command, ATTN: AMSMI-RD		
11. SUPPLEMENTARY NOTES None	12. SPONSORING MILITARY ACTIVITY Advanced Systems Laboratory Research and Engineering Directorate U. S. Army Missile Command Redstone Arsenal, Alabama 35809	
13. ABSTRACT Interference effects between a highly underexpanded, sonic or supersonic jet in a subsonic or supersonic crossflow, and the surface from which the jet exhausts are examined. For subsonic freestream Mach numbers, existing data is examined and correlated. Various semi-empirical models to represent the interference pressure distribution on flat plates are then developed. For supersonic freestream Mach numbers, a computer program for calculating jet interference effects on axisymmetric bodies at angle of attack is described. Interference effects between the jet plume and control fins on a cruciform missile are analyzed. A semi-empirical model of the jet in a crossflow, valid at large distances from the nozzle is developed. The results of this model are then used to compute interference forces and moments on fins located aft of the nozzle, both for subsonic and for supersonic freestream Mach numbers.		

UNCLASSIFIED

Security Classification

14	KEY WORDS	LINK A		LINK B		LINK C	
		ROLE	WT	ROLE	WT	ROLE	WT
	Aerodynamics Fluid Mechanics Gas Dynamics Fluid Injection Gas Injection Secondary Injection Gas-Gas Interaction Surface Interaction Reaction Control Reaction Jet Attitude Control Techniques Control Device Jet Augmented Wing Flap Jet Control Jet Flap Jet Mixing Reaction Jet						

UNCLASSIFIED

Security Classification